The molecular and ionized gas content of low and high redshift galaxies. Understanding the mechanisms regulating star formation.

HUGO MÉNDEZ HERNÁNDEZ

Instituto de Física y Astronomía
Facultad de Ciencias

Universidad de Valparaíso
Doctorado en Astrofísica

January 2022
Valparaíso. Chile.

Declaration of Authorship

This thesis is solely my own composition, except where specifically indicated in the text. Total or partial reproduction, for scientific or academic purposes, is authorised including a bibliographic reference to this document.

Hugo Méndez Hernández
April 14, 2022
Valparaíso, Chile

"Eu não me arrependo de você
Eu não me devia maldizer você assim
Vi você crescer
Fiz você crescer
Vi cê me fazer crescer também
Prá além de mim..."

Caetano Veloso

"Achar
a porta que esqueceram de fechar.
O beco com saída.
A porta sem chave.
A vida. "

P. L.

Abstract

Almost all stars are born within dense molecular clouds and live during most of their lives processing hydrogen into heavier elements. As stars evolve, they deposit these metals in their surroundings and the most massive stars can end their lives with violent supernovae explosions releasing significant fractions of metals into the interstellar medium (ISM). This material is not only contained in the ISM but also mixes with the circumgalactic medium (CGM) and even into the intergalactic medium (IGM). By studying the ionized and neutral gas content of galaxies, and their relationship with events of quenching or triggering of star formation, we will better understand the mechanisms controlling galaxy growth.

The signals coming from the gas located in the ISM and CGM are too weak to reveal in individual galaxies, hence a stacking analysis was adopted to beat down the statistical noise enabling measurements of these weak signals. To perform these analyses I developed the Valparaíso Stacking Analysis Tool (VSAT) . VSAT provides a series of tools to select, pre-process, generate, and analyze composite spectra from VIMOS and ALMA datasets. VSAT was used to analyze two different but complementary samples of galaxies to probe the molecular and ionized gas involved in the star-formation process belonging to the Valparaíso ALMA/APEX Line Emission Survey (VALES) and the Vimos Ultra Deep Survey (VUDS).

I have analyzed the line emission from ^{12}CO$(1-0)$ and its isotopologues ^{13}CO$(1-0)$ and C^{18}O$(1-0)$ ($\nu_{^{12}\mathrm{CO(1\text{-}0)}} = 115.271$ GHz, $\nu_{^{13}\mathrm{CO(1\text{-}0)}} = 110.201$ GHz, and $\nu_{\mathrm{C}^{18}\mathrm{O(1\text{-}0)}} = 109.782$ GHz rest-frame frequencies), in a sample of 27 star-forming galaxies from VALES. I perform a direct comparison of different stacking techniques used with interferometric datasets. I find that galaxies likely undergoing merging activity tend to show a higher $L'(^{12}\mathrm{CO})/L'(^{13}\mathrm{CO})$ ratio by a factor of 2 compared with normal galaxies; similar increased ratios are also found in galaxy samples with higher star formation rates (SFR) or star formation efficiencies (SFE). I find that galaxy samples with high L_{IR}, SFR and SFE show low $L'(^{13}\mathrm{CO})/L'(\mathrm{C}^{18}\mathrm{O})$ line luminosity ratios with high $L'(^{12}\mathrm{CO})/L'(^{13}\mathrm{CO})$ line luminosity ratios, suggesting that these trends are produced by selective enrichment of massive stars in young starbursts.

Additionally, I have studied the metal distribution in the CGM around galaxies at $2< z <6$ by selecting a sample of 238 close galaxy pairs from VUDS. This sample was used to detect the low- (LIS: Si II-λ1526.7, C II-λ1334.4) and high-ionization (HIS: Si IV$-\lambda\lambda$ 1393.8-1402.8, C IV$-\lambda\lambda$ 1548.2-1550.8) absorption features. I detect LIS (C II and Si II) and HIS (Si IV, C IV) up to separations of $\langle b \rangle = 172$ kpc and 146 kpc, respectively. I find that the LIS and HIS rest-frame equivalent width W_0 radial profiles are at the upper envelope of the W_0 measurements at lower redshifts, suggesting a potential redshift evolution for the CGM gas content producing these absorptions. I also find a correlation between C II and C IV with SFR, stellar mass as well as trends with galaxy size (estimated by the effective radius) and azimuthal angle. The stronger CIV line absorptions in the outer regions of these star-forming galaxies could be explained by stronger outflows in galaxies with higher star formation rates and stellar masses, capable of projecting the ionized gas up to large distances, and/or by stronger UV ionizing radiation in these galaxies, able to ionize the gas even at large distances. These results support a scenario where the low-ionization state gas infalling along the major axis of star-forming galaxies provide fuel for new episodes of star formation that will, in turn, produce large-scale outflows along the minor axis, forming bipolar outflows that transport material to the outskirts of star-forming galaxies.

In this thesis I demonstrate that it is possible to detect the weak signal coming from the molecular and ionized gas of star-forming galaxies by using an stacking analysis. In both cases emission/absorption detections from individual sources at these redshifts have not been previously reported and thus these analyses push the limits of current observation capabilities of these type of detections.

Resumen

La mayor parte de las estrellas nacen dentro de nubes de gas molecular denso y frio y durante la mayor parte de sus vidas procesan hidrógeno en elementos más pesados. Mientras envejecen, depositan estos metales en sus alrededores. Las estrellas más masivas pueden terminar sus vidas con violentas explosiones liberando aún más metales al medio interestelar (ISM). Este material no sólo está contenido en el ISM sino que puede mezclarse con el medio circumgaláctico (CGM) inclusive puede alcanzar el medio intergaláctico (IGM). Al estudiar los contenidos de gas neutro e inonizado de las galaxias, así como su relación con eventos que extinguieron o detonaron la formación estelar, podremos entender mejor los mecanísmos que controlan el crecimiento de las galaxias.

La señal proveniente del gas localizado en el ISM y CGM es muy débil para poder ser detectada en objetos individuales, por lo que se adoptó un análisis de *stacking* para reducir el ruido estadístico y poder detectar estas señales. Así, se desarrolló la herramienta VSAT (Valparaíso Stacking Analysis Tool) para seleccionar, pre-procesar y combinar espectros de datos observacionales provenientes de VIMOS y ALMA. VSAT se usó para analizar los gases molecular e ionizado en dos muestras de galaxias pertenecientes a los catálogos: Valparaíso ALMA/APEX Line Emission Survey (VALES) y Vimos Ultra-Deep Survey (VUDS).

Se analizaron las líneas de emisión de los isotopólogos de la mólecula ^{12}CO$(1-0)$: ^{13}CO$(1-0)$ y C^{18}O$(1-0)$ (con frecuencias en reposo: $\nu_{^{12}\mathrm{CO(1\text{-}0)}} = 115.271\,\mathrm{GHz}$, $\nu_{^{13}\mathrm{CO(1\text{-}0)}} = 110.201\,\mathrm{GHz}$, y $\nu_{\mathrm{C}^{18}\mathrm{O(1\text{-}0)}} = 109.782\,\mathrm{GHz}$, respectivamente) en galaxias con formación estelar (*star-forming galaxies (SFG)*) a bajo corrimiento al rojo (*redshift*). Para ello se seleccionó una muestra de 27 *SFG* con *redshifts* en el intervalo $0.02 < z < 0.2$, pertenecientes al catastro de galaxias VALES. Se encontró que aquellas galaxias con evidencias de fusión entre galaxias (*mergers*) muestran una razón de luminosidades $L'(^{12}\mathrm{CO})/L'(^{13}\mathrm{CO})$ mayor hasta por un factor de 2 en comparación con galaxias sin evidencias de *mergers*. Galaxias con altas luminosidades en el infrarrojo (L_{IR}), altas tasas de formación estelar (SFR) y altas eficiencias (SFE) también muestran variaciones similares. Se encontró que galaxias con altas L_{IR}, SFR y SFE muestran una razón de luminosidades $L'(^{13}\mathrm{CO})/L'(\mathrm{C}^{18}\mathrm{O})$ bajas con $L'(^{12}\mathrm{CO})/L'(^{13}\mathrm{CO})$ alta. Lo anterior sugiere que estas tendencias son producidas por un enriquecimiento selectivo del ISM producido por estrellas masivas en brotes de formación estelar jóvenes.

Adicionalmente, se estudió la distribución de metales en el CGM alrededor de *star-forming galaxies* a través de una muestra de 238 pares de galaxias a alto *redshift* ($2< z <6$) pertenecientes al catálogo VUDS. Esta muestra se usó para detectar líneas de absorción de baja (LIS: Si II$-\lambda$1526.7, C II$-\lambda$1334.4) y alta ionización (HIS: Si IV$-\lambda\lambda$ 1393.8-1402.8, C IV$-\lambda\lambda$ 1548.2-1550.8), para así determinar la distribución de metales en el CGM de estas galaxias. Se detectaron LIS (CII y SiII) y HIS (SiIV, CIV) con separaciones de hasta $\langle b \rangle = 172\,\mathrm{kpc}$ y 146 kpc, respectivamente. La dependencia radial de los anchos equivalentes (W_0) de estas líneas se muestran como una envolvente superior a los valores W_0 de galaxias a bajo *redshift*. Además, se encuentra una correlación entre CII y CIV y la tasa de formación estelar y la masa estelar, así como tendencias con el tamaño de las galaxias estimado por el radio efectivo (r_{eff}) y el ángulo azimutal (ϕ). Se detectaron absorciones que son más prominentes en las regiones externas de estas galaxias. Esto se explica por flujos (*outflows*) de gas ionizado en galaxias de alta masa y con tasas de formación estelar mayores capaces de proyectar el gas a grandes distancias o bien por campos de radiación UV capaces de ionizar, inclusive a grandes distancias, el gas de estas galaxias. Estos resultados sugieren un escenario donde afluentes (*inflows*) de gas de baja ionización entran a través del disco galáctico proveyendo el combustible necesario para sostener nuevos brotes de formación estelar (*starburst*). Estos episodios podrían producir eventualmente *outflows* a gran escala a lo largo del eje de rotación de estas galaxias formando *outflows* bipolares transportando material a las regiones externas.

Este trabajo demuestra que es posible detectar las señales débiles provenientes del gas ionizado y molecular de *star-forming galaxies*, utilizando un análisis de *stacking*. En ambos casos, no se han reportado detecciones (emisión y absorción) individuales a estos corrimientos al rojo. Por tanto estos resultados llevan al límite las capacidades observacionales actuales de este tipo de detecciones.

Acknowledgements

First, I would like to thank my supervisors Eduardo Ibar and Paolo Cassata. Without their patience and support this work would not have been possible.

I want to thank Manuel Aravena and Verónica Motta for the revision of this work.

I want to thank Chile and the Universidad de Valparaíso for hosting me in the PhD program and for their support to attend different meetings and conferences to present the results contained in this thesis.

I want to thank all my collegues at Valparaíso and specially to Daniela, Irma and Rosamaria for their support in the last past years.

Thank you Kaê for encouraging me, and your infinite trust in me. You are an important part of this work.

Thank you Théo and Igor, the two papers containing the main results of this work are for you.

Thank you Laura, Hugo, Rodrigo and Maria for coming all the way to Chile from México and Brazil. You arrived at the exact time, when we needed you the most.

I would like to thank Héctor Toledo, who first introduce me into observational astronomy and mesmerized me with awesome galaxy images.

Contents

Declaration of Authorship iii

Abstract vii

Resumen ix

Acknowledgements xi

1 Introduction 1
- 1.1 The Cosmological Scenario . . . 1
- 1.2 The star-formation history of the Universe (SFHU) . . . 1
- 1.3 The inefficient star-formation . . . 3
- 1.4 The baryonic cycle . . . 4
- 1.5 Star-formation related processes . . . 4
  - 1.5.1 The star-formation Rate (SFR) and Efficiency (SFE). . . . 4
  - 1.5.2 The star-formation Modes. . . . 6
  - 1.5.3 Gas accretion. . . . 7
- 1.6 Summarizing . . . 8
- 1.7 This thesis. . . . 9
  - 1.7.1 The stacking technique . . . 9
  - 1.7.2 The interstellar medium and the molecular gas. . . . 9
    - $^{12}C^{16}O$ isotopologues. . . . 10
  - 1.7.3 The circumgalactic medium and the ionized gas. . . . 11

2 Stacking Analysis 13
- 2.1 Historical background . . . 13
- 2.2 Stacking technique . . . 14
- 2.3 Valparaíso Stacking Tool (VSAT) . . . 15
  - 2.3.1 VSAT-3D . . . 15
  - 2.3.2 VSAT-2D . . . 19
  - 2.3.3 VSAT-1D . . . 22
  - 2.3.4 VSAT-Syn . . . 25

3 The ISM of dusty star-forming galaxies at low redshift 27
- 3.1 Introduction . . . 27
- 3.2 Data . . . 28
  - 3.2.1 Sample . . . 28
  - 3.2.2 ALMA $^{13}CO(1-0)$ and $C^{18}O(1-0)$ observations . . . 28
- 3.3 Analysis . . . 29
  - 3.3.1 Image stacking . . . 30
    - 2D-moment-0 stacking . . . 30
    - 3D-image stacking . . . 31
    - Systematic Errors . . . 31

3.3.2 *uv* stacking . . . 34
3.3.3 The differences between the stacking approaches . . . 36
3.3.4 Luminosity measurements . . . 36
3.4 Results . . . 38
3.4.1 The $L'(^{12}CO)/L'(^{13}CO)$ ratio . . . 38
Morphological and environmental dependence . . . 38
The star-formation activity . . . 40
^{13}CO Individual detections . . . 46
110.201 GHz stacked continuum emission. . . . 46
3.4.2 $L'(^{13}CO)/L'(C^{18}O)$ correlations. . . . 46
3.5 Discussion . . . 49
3.5.1 Optical depth, selective photodissociation and chemical fractionation effects. 50
3.5.2 Insights from Galactic Chemical Evolution . . . 51
3.6 Conclusions . . . 51

4 The CMG of star-forming galaxies at $\langle z \rangle \sim 2.6$. 53
4.1 Introduction . . . 53
4.2 Data . . . 56
4.3 Analysis . . . 57
4.4 Results . . . 61
4.4.1 Radial Dependence . . . 64
4.4.2 Star formation and Stellar Mass Dependence . . . 68
4.4.3 Morphological Dependence . . . 71
4.4.4 CII/CIV line ratio . . . 72
4.4.5 Lyα-emission . . . 72
4.5 Discussion . . . 73
4.5.1 LIS/HIS absorption dependencies. . . . 75
4.5.2 C II / C IV line ratio. . . . 78
4.5.3 Lyα-emission. . . . 78
4.6 Conclusions . . . 79

5 Conclusions 81
5.1 Results Paper I . . . 81
5.2 Results Paper II . . . 82
5.2.1 Linking molecular with ionized gas phases. . . . 83
5.3 Future prospects. . . . 83

Bibliography 85

List of Figures

1.1 The mass-energy density content of the Universe. . . . 2
1.2 The star formation history of the Universe . . . 2
1.3 The inefficient star-formation. . . . 3
1.4 Gas matter cycle. . . . 5
1.5 The Kennicutt-Schmidt law. . . . 5
1.6 The star formation efficiency at different redshifts. . . . 6
1.7 Two star formation modes. . . . 7
1.8 Accretion modes. . . . 8
1.9 ISM studies timeline. . . . 11
1.10 CGM studies timeline. . . . 12

2.1 Stacking analysis timeline. . . . 14
2.2 *Shift and Add* technique. . . . 15
2.3 3D stacking scheme. . . . 16
2.4 VSAT-3D ^{12}CO stacked stamps. . . . 17
2.5 3D ^{12}CO stacked spectral line profile. . . . 18
2.6 VSAT-3D ^{12}CO stacked collapsed image. . . . 19
2.7 3D ^{12}CO stacked velocity integrated flux measurement. . . . 19
2.8 *Moment-zero* stacking scheme. . . . 20
2.9 2D ^{12}CO stacked stamps. . . . 21
2.10 2D ^{12}CO stacked velocity integrated flux measurement. . . . 21
2.11 1D *Foreground* galaxy pre-processed spectra. . . . 23
2.12 1D *Foreground* composite spectra. . . . 24
2.13 1D average stacked absorption lines fitting. . . . 25
2.14 VSAT-Syn simulation results. . . . 26

3.1 SNR Optimization. . . . 32
3.2 3D stacking scheme. . . . 33
3.3 Velocity integrated flux density accuracy simulations . . . 35
3.4 ^{12}CO, ^{13}CO and C^{18}O stamps. . . . 37
3.5 $L'(^{12}\mathrm{CO})/L'(^{13}\mathrm{CO})$ vs Morphology . . . 39
3.6 VALES cycle-2 properties distribution. . . . 41
3.7 $L'(^{12}\mathrm{CO})/L'(^{13}\mathrm{CO})$ vs L_{IR} . . . 42
3.8 $L'(^{12}\mathrm{CO})/L'(^{13}\mathrm{CO})$ vs SFR, SFE, Σ_{SFR} and $\Sigma_{\mathrm{H_2}}$ . . . 44
3.9 $L'(^{12}\mathrm{CO})/L'(^{13}\mathrm{CO})$ vs LIR, SFR and SFE (galaxies with C^{18}O observations. . . . 48
3.10 $L'(^{13}\mathrm{CO})/L'(\mathrm{C}^{18}\mathrm{O})$ vs LIR, SFR and SFE (galaxies with C^{18}O observations. . . . 48

4.1 VUDS star-forming galaxies ($1.5 < z < 2.5$) star formation rate vs stellar mass . . . 58
4.2 Projected angular separation (θ), axial ratio (q), effective radius ($\mathrm{r_{eff}}$) and azimuthal angle (ϕ) distributions. . . . 59
4.3 Star-forming galaxy pairs redshift distribution. . . . 60
4.4 Composite spectra shifted to rest-frame of 238 *foreground* galaxies with projected angular separations $< 23''$ . . . 63

4.5 Median absorption lines from the *foreground* (red) and *background* galaxy composite spectra. 65
4.6 Rest equivalent width (W_0) vs mpact parameter (b). 67
4.7 Rest equivalent width (W_0) of the absorption lines as a function of the *foreground* galaxy's stellar mass ($\log[M_\star/M_\odot]$), SFR ($\log[M_\odot yr^{-1}]$), effective radius ($r_{\rm eff}$) and azimuthal angle(ϕ). The W_0 measurements come from composite spectra taking into account galaxy pairs at all projected distances ($b < 23''$) and split by the corresponding galaxy property. 70
4.8 CII/CIV line ratio vs impact parameter b, stellar mass and star formation rate. . . . 73
4.9 Rest equivalent width (W_0) of the Lyα emission line vs impact parameter (b). . . . 74

List of Tables

3.1 ALMA ^{13}CO(1 − 0) and C^{18}O(1 − 0) observations. . . . 29
3.2 ^{13}CO(1 − 0) *moment-zero* detections. . . . 30
3.3 Signal-to-noise Ratio (SNR) detection for ^{12}CO, ^{13}CO and C^{18}O stacked line emission, obtained from three different stacking methods explored. . . . 36
3.4 Average $L'(^{12}\mathrm{CO})/L'(^{13}\mathrm{CO})$ line luminosity ratio vs Morphology. . . . 40
3.5 Average $L'(^{12}\mathrm{CO})/L'(^{13}\mathrm{CO})$ line luminosity ratio vs L_{IR}, SFR, SFE, Σ_{SFR} and $\Sigma_{\mathrm{H_2}}$. . . 43
3.6 Spearman correlation test for L_{IR} vs $L'(^{12}\mathrm{CO})/L'(^{13}\mathrm{CO})$. . . . 44
3.7 Low and high SFR ($\mathrm{M_\odot yr^{-1}}$) galaxy populations average properties: z, $\mathrm{M_{H_2}}$, $\mathrm{M_{H_2}/M_\star}$, $f_{\mathrm{H_2}}$. . . . 45
3.8 ^{13}CO stacked continuum emission for split into low and high SFR ($\mathrm{M_\odot yr^{-1}}$) populations. . . . 46
3.9 Average $L'(^{12}\mathrm{CO})/L'(^{13}\mathrm{CO})$ and $L'(^{13}\mathrm{CO})/L'(\mathrm{C^{18}O})$ line luminosity ratios for 24 VALES galaxies with C^{18}O observations. . . . 47
3.10 Low and high SFR ($\mathrm{M_\odot yr^{-1}}$) galaxy populations average properties: z, $\mathrm{M_{H_2}}$, $\mathrm{M_{H_2}/M_\star}$, $f_{\mathrm{H_2}}$ for 24 galaxies with C^{18}O coverage. . . . 49

4.1 Number of objects belonging: VUDS parent sample, star-forming galaxies at $z > 1.5$, star-forming galaxies with morphological parameters available, close *fg-bg* galaxy pairs, and close *fg-bg* galaxy pairs with morphological parameters available extracted from the VUDS parent sample. . . . 57
4.2 Main spectral features observed in our VUDS stacked spectra in the 1100-2000 Å rest-frame range. . . . 62
4.3 *Foreground-background* (*fg-bg*) galaxy pair statistics. . . . 64
4.4 Median absorption line strengths measured (W_0) in stacked spectra as a function of the average impact parameter ($\langle b \rangle$) of the sample: 68.6 kpc (N=60), 113.5 kpc (N=62), 146.2 kpc (N=60), and 172.8 kpc (N=57). The errors on the equivalent width (W_0) measurements correspond to 1σ confidence intervals based on a Bootstrap analysis (see sec. 4.4.1). . . . 69

List of Abbreviations

AGN	**A**ctive **G**alactic **N**uclei
ALMA	**A**tacama **L**arge **M**illimeter/sub-millimeter **A**rray
CANDELS	**C**osmic **A**ssembly **N**ear-infrared **E**xtragalactic **L**egacy **S**urvey
CASA	**C**ommon **A**stronomoy **S**oftware **A**pplication
CDF-N	**C**handra **D**eep **F**ield **N**orth
CDF-S	**C**handra **D**eep **F**ield **S**outh
CDM	**C**old **D**ark **M**atter
CGM	**C**ircum **G**alactic **M**edium
CMB	**C**osmic **M**icrowave **B**ackground
COSMOS	**COSM**ic ev**O**lution **S**urvey
DEIMOS	**DE**ep **I**maging **M**ulti-**O**bject **S**pectrograph
ECDFS	**E**xtended **C**handra **D**eep **F**ield **S**outh
ELT	**E**xtremely **L**arge **T**elescope
ETG	**E**arly **T**ype **G**alaxy
EVLA	**E**xpanded **V**ery **L**arge **A**rray
FIR	**F**ar **I**nfra**R**ed
FWHM	**F**ull **W**idth **H**eight **M**aximum
GAMA	**G**alaxy and **M**ass **A**ssembly **S**urvey
GMC	**G**iant **M**olecular **C**louds
GMT	**G**iant **M**agellan **T**elescope
H-ATLAS	**H** **A**strophysical **T**erahertz **L**arge **A**rea **S**urvey
HDF	**H**ubble **D**eep **F**ield
HDF-N	**H**ubble **D**eep **F**ield **N**orth
HIS	**H**igh **I**onization **S**tate
HST	**H**ubble **S**pace **T**elescope
ICM	**I**ntra **C**luster **M**edium
IFS	**I**ntegral **F**ield **S**pectra
IGM	**I**nter **G**alactiic **M**edium
IMF	**I**nitial **M**ass **F**unction
ISM	**I**nter **S**tellar **M**edium
JWST	**J**ames **W**ebb **S**pace **T**elescope
KMOS	**K**-band **M**ulti **O**bject **S**pectrograph
LFS	**L**uminosity **F**unction
LIS	**L**ow **I**onization **S**tate
LLS	**L**arge **S**cale **S**tructure
MIR	**M**id **I**nfra**R**ed
MUSE	**M**ulti **U**nit **S**pectroscopic **E**explorer
NOEMA	**NO**rthern **E**xtended **M**illimiter **A**rray
OSIRIS	**O**ptical **S**ystem for **I**maging and low-**I**ntermediate-**R**esolution **I**ntegrated **S**pectroscopy
OTELO	**OSIRIS** **T**unable **E**mission **L**ine **O**bject **survey**
PWV	**P**recipitable **W**ater **V**apour
QSO	**Q**uasi **S**tellar **O**bect

SDSS	**S**loan **D**igital **S**ky **S**urvey
SFD	**S**pectral **E**nergy **D**istribution
SFE	**S**tar **F**ormation **E**fficiency
SFG	**S**tar **F**orming **G**alaxy
SFHU	**S**tar **F**ormation **H**istory of the **U**niverse
SFR	**S**tar **F**ormation **R**ate
SNR	**S**ignal to **N**oise **R**atio
TNO	**T**rans **N**eptunian **O**bject
UDS	UKIDSS **U**ltra **D**eep **S**urvey
ULIRGs	**U**ltra **L**uminous **I**nfra**R**ed **G**alaxies
UKIDSS	**UK**IRT **I**nfra**R**ed **D**eep **S**ky **S**urveys
UKIRT	**United Kindom I**nfra**R**ed **T**elescope
VALES	**V**alparaíso **A**LMA/APEX **L**ine **E**mission **S**urvey
VANDELS	deep **V**IMOS survey of the C**ANDELS** CDF-S and UDS field
VIMOS	**VI**sible **M**ulti **O**bject **S**pectograph
VLT	**V**ery **L**arge **T**elescope
VUDS	**V**imos **U**ltra **D**eep **S**urvey
VSAT	**V**alparaíso **S**tacking **A**nalysis **T**ool
VVDS	**V**imos **V**LT **D**eep **S**urvey

Physical Constants

Hubble constant	$H_0 = 70\,\mathrm{km\,s^{-1}\,Mpc^{-1}}$
Matter density parameter	$\Omega_m = 0.3$
Dark energy density parameter	$\Omega_\Lambda = 0.7$
CO to molecular gas conversion factor	$\alpha_{\mathrm{CO}} = 4.6/0.8$ (mergers) $\mathrm{K\,km\,s^{-1}pc^2}$
Solar mass	$M_\odot = 2\times10^{30}\mathrm{kg}$
Solar luminosiity	$L_\odot = 3.827\times10^{26}\mathrm{W}$

List of Symbols

Å	Angstrom	10^{-9}m
$S\Delta v$	Velocity-integrated flux density	Jy Km s $^{-1}$ pc^2
L'	Velocity-integrated line luminosity	K km s^{-1} pc^2
L_{IR}	Infrared luminosity	$L_{IR}/L_\odot$
z	redshift	$-$
SFR	Star formation rate	$M_\odot yr^{-1}$
SFE	Star formation efficiency	Gyr^{-1}
Σ_{SFR}	Surface star formation rate density	$M_\odot yr^{-1} kpc^{-2}$
Σ_{H_2}	Surface molecular gas density	$M_\odot pc^{-2}$
ϕ	Azimuthal angle	$^\circ$ [degree]
$r_{\rm eff}$	Effective radius	kpc
f_{H_2}	Molecular gas fraction	$f_{H_2} = M_{H_2}/(M_{H_2} + M_\star)$
M_{H_2}	Molecular gas mass	$M_{H_2}/M_\odot$
$M_\star$	Stellar mass	$M_\star/M_\odot$
$M_{H_2}/M_\star$	Molecular gas mass to stellar mass ratio	$-$
D_L	Luminosity distance	Mpc
t	Student's t-test statistic	$-$
D	Kolmogorov-Smirnov statistic	$-$
r_τ	Kendall-Tau correlation coefficient	$-$
p	Statistical test probability	$-$

Para as mulheres da minha vida.

Chapter 1

Introduction

1.1 The Cosmological Scenario

Nowadays the ΛCDM cosmological scenario provides the best description of the Universe. This scenario relies on the Cosmological Principle, that states that "We are not located at any special location in the Universe" (Longair, 2008). It includes i) a cosmological constant Λ (lambda), used to explain the present accelerating expansion of the Universe (space against the attractive effects of gravity, associated with a vacuum energy or dark energy in empty space), and ii) a Cold Dark Matter (CDM) component [1] that accounts for gravitational effects observed in very large-scale structures, (e.g. "flat" rotation curves of galaxies; gravitational lensing of light by galaxy clusters; and enhanced clustering of galaxies) that cannot be accounted for by the quantity of baryonic matter. So far it is the only current cosmological model consistent with i) the observed expansion of space, ii) the observed distribution of lighter elements in the universe (H, He, Li) and iii) the Cosmic Microwave Background (CMB) radiation anisotropies.

From the latest observational results from the Planck mission (Planck Collaboration et al., 2020) we know that, at the present epoch ($z = 0$), the mass-energy density of the universe is composed as follows (see figure 1.4): comprises 67.9% of the dark energy content of the Universe, dark matter accounts an additional 27.2%, and ordinary matter (i.e. chemical elements, gas and plasma) constitutes the remaining 4.9% (free H and He: 4%, stars: 0.5%, heavy elements: 0.03% and neutrinos: 0.3%), material from which visible planets, stars and galaxies are made of. However, a large fraction of this ordinary matter (>90%) is found in a gaseous phase in the Universe (Péroux and Howk, 2020). This cold gas traced by HI and H_2 constitutes the reservoir that fuels star-formation.

1.2 The star-formation history of the Universe (SFHU)

The star-formation rate density of the Universe (see Fig. 1.2) is a measure of how many stars were formed per unit time through the history of the Universe (Madau and Dickinson, 2014). However, we have still a quite superficial understanding of how the processes that regulate star-formation in different galaxies at different epochs really work. The history of star-formation of the Universe can be split into three three main epochs: i) $3< z <8$: a steady increase of the SFR density of the Universe from the end of reionization (z=8) to galaxies first light, ii) $1< z <3$: the star-formation activity of the Universe reaches its peak: nearly 50% of the stars of the present day galaxies were formed and iii) $1< z$: a steep decline of an order of magnitude of the comoving star-formation Rate (SFR) from z$\sim$ 1 to 0.

[1] Dark matter particles are described as cold/hot referring to their velocity at the epoch where matter and radiation were decoupled, and it is described as non-baryonic, dissipation-less (it cannot cool by radiation photons), and collision-less (interaction only through gravitation).

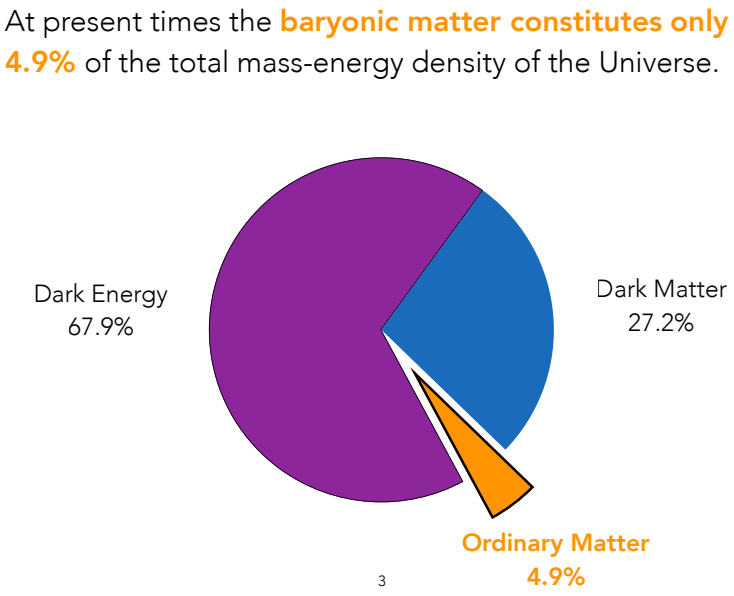

FIGURE 1.1: The mass-energy density content of the ΛCDM cosmological scenario. More than 90% of the ordinary matter is foundto be in the gaseous phase.

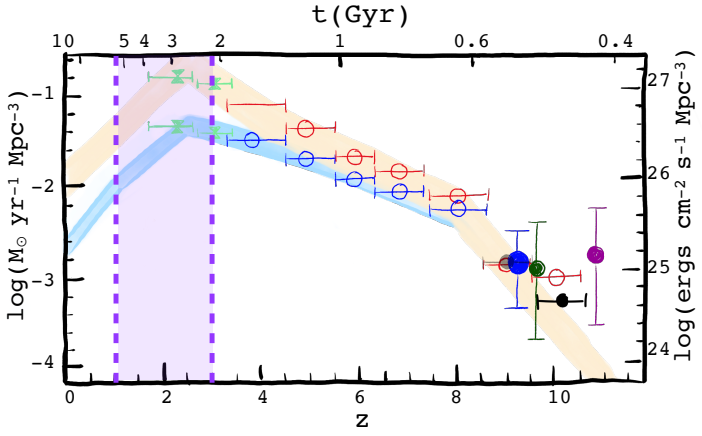

FIGURE 1.2: The UV luminosity (right axis) and SFR density (left) as a function of redshift (Madau and Dickinson, 2014). The upper set of points at every given redshift and orange contour show the dust-corrected SFR densities, while the lower set of points and blue contours show the inferred SFR densities before dust correction. Three main epoochs can be identified: i) a steady increase of the SFR density of the Universe from the end of reionization ($z = 8$), to galaxies first light , ii) the peak of the SFR density between $1 < z < 3$, and iii) a steep decline $0 < z < 1$.

In order to explain the SFHU and understand galaxy formation, we must investigate i) how

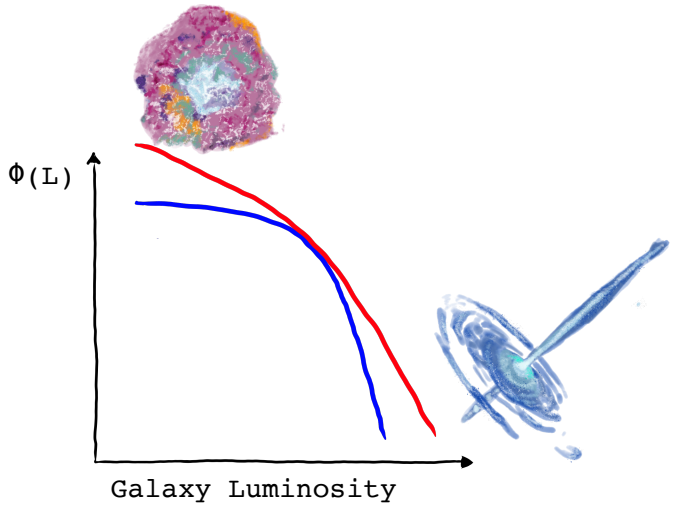

FIGURE 1.3: The inefficient star-formation. Discrepancy between the observed luminossity function and the mass function of dark matter haloes can be alleviated by invoking feedback processes from SNe and AGN at low and high luminosities respectively.

stars and star-formation are distributed over dark matter halos with different masses as a function of time, and ii) identify the mechanisms that influence star-formation (e.g. feedback processes, gas accretion, star-formation rates, star-formation efficiency) and quantify their relative importance. By doing this we will be able to understand how these processes regulate star formation through the cosmic time.

1.3 The inefficient star-formation

The luminosity function (LF) accounts for the number density of galaxies with luminosities in the range $[L, L + dL]$. The LF can be described by a Schechter function [2] and the observed LF of galaxies can be described by a power law truncated by an exponential at large luminosities (see Fig 1.3). However, there is a discrepancy between the observed LF and the mass function of dark matter haloes (Wechsler and Tinker, 2018). Observational and simulated luminosity functions show different shapes suggesting that baryonic mass does not necessarily follows halo mass. Moreover, assuming a constant M/L ratio leads to: i) too many small and big galaxies at z=0, ii) too few massive galaxies and too many baryons within galaxy halos at high z, and iii) missing number of bulgeless/thin disks galaxies and high concentration and cuspiness of c.d.m. in dwarf spiral galaxies. These differences may be related to dynamics of the baryons within dark matter haloes, and probably some feedback processes could reconcile this by lowering SFE: i) SN and ii) AGN on the low (Dekel and Silk, 1986; Hopkins, Quataert, and Murray, 2012) and massive (Silk and Rees, 1998; Croton et al., 2006) ends of the luminosity function.

After an initial population of stars have formed, a fraction of these explode as SN, releasing large amounts of energy into the surrounding medium, that, if accelerated enough ($v > v_{esc}$) material could be injected into the IGM enriching it and suppressing star-formation. However,

[2] $\Phi(L) = (L/L_*)^{\alpha} exp[-L/L_*]$, where α defines the fain-end slope, and L_* is defined by $L/L_* = 10^{-0,4(M_*-M)}$.

this depends on the assumed Initial Mass Function (IMF), the acceleration outflow, and how this energy is deposited and the potential well of the halo. On massive galaxies, SN have little impact, failing to stop the streaming of cold flows to the center, however AGN feedback from Super Massive Black Holes (SMBH) $M \sim \times 10^9 M_\odot$ may provide an effective interaction, which is supported by the Magorrian relation ($M_{BH} - \sigma^{4,5}$ Magorrian et al. 1998; Ferrarese and Merritt 2000; Graham 2012). At late epochs, AGN radio mode drives jets an cocoons that heats halo gas and thus inhibit cooling, resolving: i) the bright-end of the luminosity function, ii) the bimodal color distribution of galaxies, iii) Early-type red colors, iv) the suppression in numbers of intermediate mass and satellite galaxies and also, v) it heats gas that otherwise would be accreted by satellites.

1.4 The baryonic cycle

The gas-matter (Figure 1.4) cycle includes different events (e.g. inflows, outflows) happening within galaxies, which ultimately regulate the formation of new stars. Stars result from the gravitational contraction and collapse of cool and dense gas clouds: 1) if the hydrostatic equilibrium between the self-gravitation of the clouds and the pressure of the surrounding Interstellar Medium (ISM) is broken, an increase of the pressure occurs, leading to an isotropic compression of the cloud and, thus, to star-formation; 2) as stars age, they release dust and deposit metals into the ISM, where dust plays a key role in gas facilitating cooling, moreover 3) stars end up their lives with violent explosions (SNe from massive mass stars) and PNe (intermediate mass stars), adding even larger amounts of dust into the ISM, 4) as gas cools, dust condensates and can expand through shock waves from SNe explosions that sweep the ISM compressing it and forming new clouds again (Finlator and Davé, 2008; Davé, Finlator, and Oppenheimer, 2012).

However, this is not a closed process and interaction with the circumgalactic medium (CGM) and the inter Galactic Medium (IGM) occurs: i) cool flow accretion from the CGM/IGM can enhance star-formation and ii) high velocity flows that can reach the CGM/IGM, enriching it with metals and quenching star-formation (only if the velocities of the gas expelled from stellar outflows are large enough $v > v_{esc}$).

1.5 Star-formation related processes

1.5.1 The star-formation Rate (SFR) and Efficiency (SFE).

The Kennicutt-Schmidt law (Schmidt, 1959; Kennicutt, 1998a; Kennicutt, 1998b) (see Fig 1.5) gives some insight into the processes behind the star-formation. By relating the gas surface density and the star-formation rate density, it measures for the fraction of gas that is being transformed into stars per unit area and it has been found that larger gas contents imply larger star-formation rates and lower gas contents imply lower star-formation rates. From local studies in giant molecular clouds (GMC) in the Milky Way, and by defining star-formation efficiency as the ratio between SFR and gas mass, we know that the star efficiency per free fall time of these systems is $\sim$2%. Moreover this is globally true not only in the Milky Way as it is also observed in nearby disk galaxies (Bigiel et al., 2008). Additionally, a population of galaxies showing a larger star-formation rate is identified: *starbursts* galaxies.

To compare the SFE in different galaxies at different epochs, recent studies (e.g. Krumholz, Dekel, and McKee, 2011; Daddi et al., 2010 see Fig 1.6) Focused their attention in the relationship between gas and star-formation rate at different scales and redshifts, in order to extend the Schmidt-Kennicutt law (Schmidt, 1959; Kennicutt, 1998a; Kennicutt, 1998b) observed at low redshifts. They were able to identified two main populations of galaxies: i) the sequence of disks galaxies and ii) the sequence of starburst galaxies with higher SFR. Later on, Krumholz,

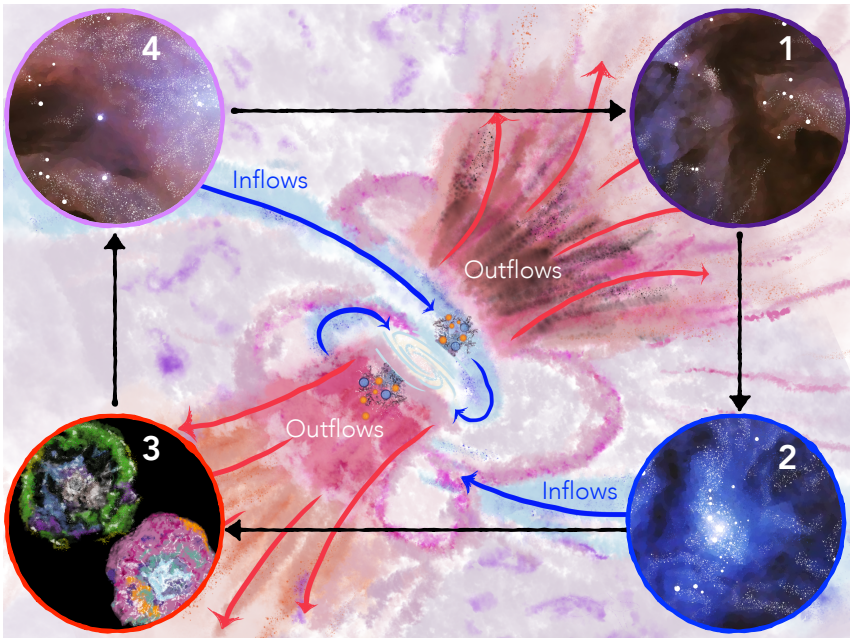

FIGURE 1.4: Gas matter cycle. 1) Stars form in cool dense molecular clouds, 2) as they age deposit metals into the interstellar medium. 3) Stars can end up their lives through violent events depositing more metals and dust in their surrounding medium, which 4) eventually will cool down to form a new generation of stars. However galaxies can accrete/expell material into/from the CGM/IGM.

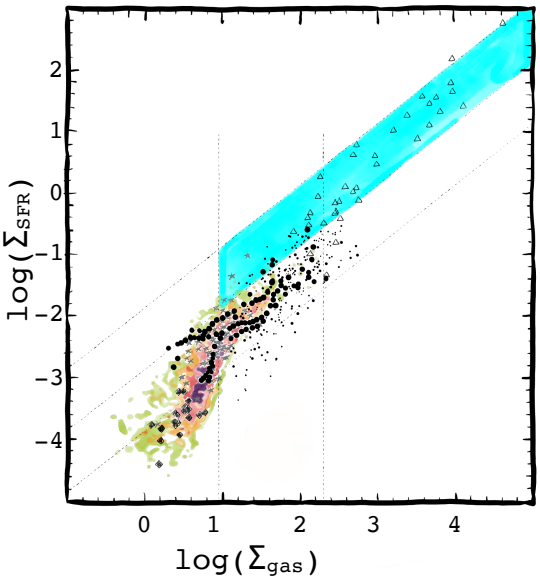

FIGURE 1.5: Σ_{SFR} as a function of Σ gas from giant molecular clouds located in the Milky Way and or individual nearby-galaxies (Bigiel et al., 2008). Stars formed in giant molecular clouds, result in a SFE 2%, which can up-rise up to 30% in dense giant molecular clouds (cyan region).

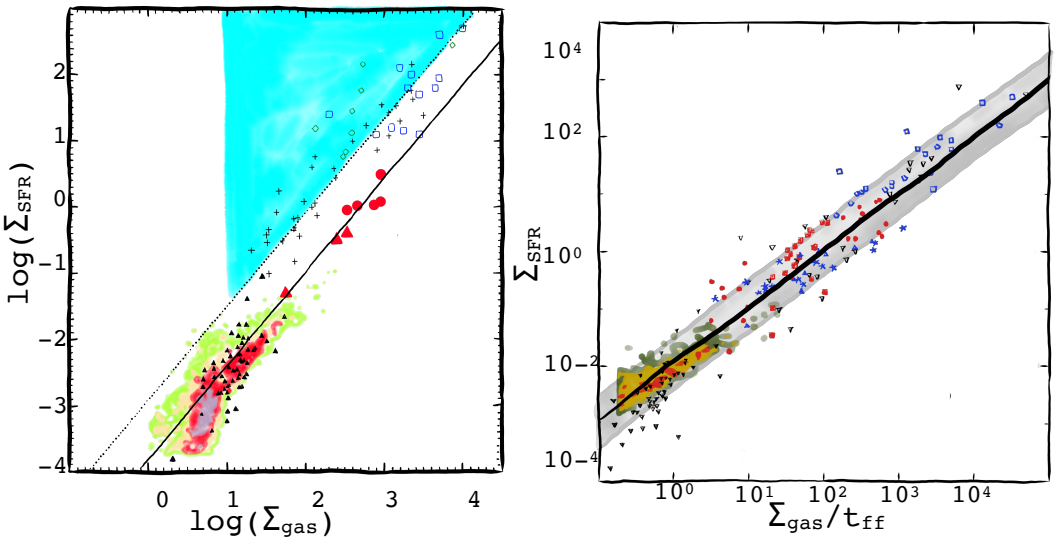

FIGURE 1.6: (Left panel: star-formation surface density Σ_* as a function of observed gas surface density Σ (Daddi et al., 2010), where two main populations of galaxies: i) the sequence of disks galaxies and ii) the sequence of starburst galaxies with higher SFR. Right panel: star-formation surface density Σ_* as a function of observed gas surface density per free-fall time (Σ/t_{ff}) (Krumholz, Dekel, and McKee, 2011), where a single star formation law in which the star formation rate is : (1%) the molecular gas mass per local free-fall time.

Dekel, and McKee (2011) looked for a simple star formation law at all scales and redshifts, by including: i) (resolved observations) Milky Way molecular clouds, ii) (kpc-scale observations) Local Group galaxies, and iii) (unresolved observations) disk and starburst galaxies in the local universe assuming three possible models for the star formation law: i) a local one in which the quantity that matters is the local volume density of gas, ii) a global one in which star-formation occurs on a timescale set by the galactic rotation period, and iii) a model in which the SFR is linearly proportional to the mass of gas above some density threshold. They found that, at low- and high-redshift andin starbursts and disks galaxies the SFR per unit area can be described by a simple law, being the SFE the controlling parameter, and the molecular gas as a controlling ingredient and where the star-formation rate is : 1% the molecular gas mass per local free-fall time.

1.5.2 The star-formation Modes.

Normal star-forming galaxies and starburst galaxies can be identified at all epochs (Elbaz et al., 2011) (Fig. 1.7 right-panel) one with a steady star-formation an another with high star-formation rates. These two modes can also be identified by considering their stellar mass (the gas content already converted into stars, Rodighiero et al. 2011 Fig. 1.7 left-panel). These two star-formation modes are a consequence of how the processes regulating star-formation work: i) occurring without any intervention from Active Galactic Nuclei (AGN) and being characteristic of disk

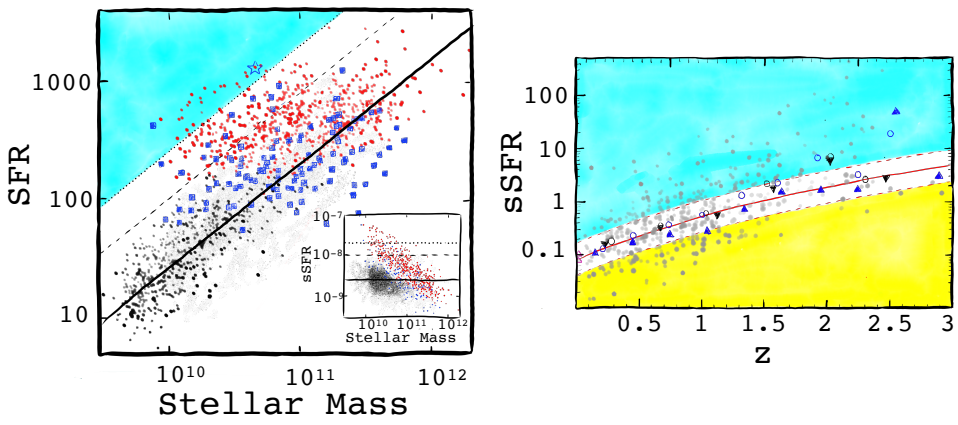

FIGURE 1.7: (Left panel: star-formation surface density Σ_* as a function of stellar mass (Rodighiero et al., 2011), where again two main populations of galaxies: i) a relatively steady one in disk-like galaxies, defining a tight star formation rate (SFR)–stellar mass sequence (soliid black line), and ii) a starburst mode in outliers to such a sequence (cyan shaded region). Right panel: redshift evolution of the median specific SFR (sSFR=SFR/$M_\star$) of star-forming galaxies (Elbaz et al., 2011), main sequence of star-forming and starburst galaxies can be identified at all epochs.

galaxies such as the Milky Way, on a timescale of order at least several galactic rotation times, defining a tight star-formation rate–stellar mass sequence; and ii) a more intense starburst mode, that can be defined as outliers of normal star-forming main sequence, occurring on a relatively rapid time-scale, involving the intervention of AGN (at least for quenching and possibly enhancing or even triggering star-formation) and generally interpreted as driven by merging (accreting hot gas).

1.5.3 Gas accretion.

The main sources of accreting material are the IGM, satellites and recycle feedback gas (see Fig. 1.8). Material infalling onto galxies from the IGM is expected to be the largest source of ongoing accretion for galaxies (Kereš et al., 2005) occuring towards the edges of galaxy disks to avoid feedback from central regions (Stewart et al., 2011; Fernández, Joung, and Putman, 2012) and has been detected indirectly from absorption line experiments (Prochaska et al., 2011; Chen, Lanzetta, and Webb, 2001). Satellite galaxies are expelled from their gas through ram pressure stripping (Tepper-García, Bland-Hawthorn, and Sutherland, 2015; Gatto et al., 2013; Fox et al., 2014). This heated gas cools down and then sinks close to the disk (Heitsch and Putman, 2009; Joung, Bryan, and Putman, 2012; Bland-Hawthorn et al., 2007). Finally, kinematic signatures of feedback mechanisms providing gas to galaxy haloes have been observed (Rubin et al., 2014;

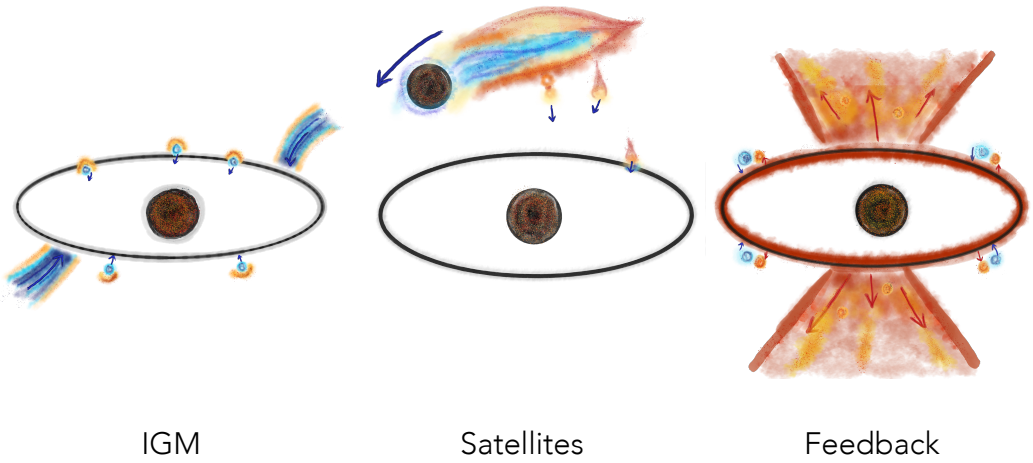

FIGURE 1.8: Different accretion modes supplying gas to sustain star-formation: i) Material infalling onto galxies from the IGM, ii) satellite galaxies and, iii) feedback mechanisms. (Putman, 2017)

Shapley et al., 2003; Chen et al., 2010; Weiner et al., 2009). These observations provide evidence of abundant recycled gas reservoirs that will fuel future episodes of star-formation in these galaxies. The combination of these three accretion modes (gas infall, outflows, and mergers) generates a multi-phase gaseous halo characterized by a highly complex spatial distribution of gas structures of different age and origin (Richter, 2017).

As was mentioned above, the baryonic content of the Universe can be explained by the baryonic cycle in which gas is transformed into stars, including different processes that control it. However, this is not a closed box cycle and interaction with the CGM/IGM is seen (Tumlinson, Peeples, and Werk, 2017). This interaction can be related with these two accretion modes and should be reflected in the number of galaxies observed at any given epoch.

1.6 Summarizing

Our current understanding of galaxy formation is based on studies of i) stars, ii) star-formation and iii) ionized gas, but the link between all these stages is missing, providing us with an incomplete and fragmented view of the processes describing their interplay. For instance, the gas content of cold gas and how it is transformed into stars in high redshift galaxies is still poorly constrained: current studies probe the products of the process of galaxy formation, but miss the actual source. Thus, the next step in the study of galaxy formation is the measurement of the cool gas content of galaxies and, in particular, the molecular ISM out of which stars form as a function of cosmic time.

If we understand the interplay between gas accretion, cooling, star formation, neutral and ionized gas, we may understand why the SFE peaks at a certain halo mass and then declines for more massive systems. Moreover, if we trace the presence of cold neutral and ionized gases, their distribution in different galaxies and different haloes over cosmic time, we might be able to unravel the puzzle of galaxy formation and efficiency of star-formation. However, we need observations of both ends of the star formation process: the fuel (cold molecular gas feeding star-formation), and the products (ionized gas).

1.7 This thesis.

This work made use of two different but complementary samples of galaxies to probe the ionized and the molecular gas involved in the star-formation process: the Vimos Ultra Deep Survey (VUDS, Le Fèvre et al. 2015) and the Valparaíso ALMA/APEX Line Emission Survey (VALES, Villanueva et al. 2017). Since both the line emission and absorptions coming from the cold dense molecular gas and the circumgalactic gas are too weak to achieve individual detections, a stacking analysis was developed to beat down the statistical noise enabling measurements of these weak absorption/emission signals.

1.7.1 The stacking technique

The faint signals coming from the ionized and molecular gas from these two samples are too weak to achieve individual detections. Hence, to overcome these difficulties a stacking analysis has been adopted in order to raise the signal to noise ratio in composite spectra and obtain clear detections. For these purposes the Valparaíso Stacking Analysis Tool (VSAT) has been developed. VSAT provides a series of tools to select, stack and analyze 1D, 2D and 3D data sets from large extragalactic surveys. Although VSAT was specifically designed to co-add VUDS spectral observations and VALES interferometric datasets, VSAT can be also be used to stack observations of diverse astronomical sources coming from different instruments.

1.7.2 The interstellar medium and the molecular gas.

Stars are mostly formed within Giant Molecular Clouds (GMCs), cold dense regions of the interstellar medium (ISM), which are characterized by high densities ($n_{H_2} > 10^4$ cm^{-3}; Gao and Solomon 2004; Bergin and Tafalla 2007) and low temperatures (10–20 K; Evans 1999) that favour the formation of stars. In these regions, the most abundant molecule is molecular hydrogen, H_2, however its lack of a permanent electric dipole makes it difficult to observe in emission. After H_2, the most abundant molecule is carbon monoxide, $^{12}C^{16}O$ (hereafter CO), which easily emits photons from low level rotational transitions in similar ISM conditions as those in which the H_2 molecule resides. Therefore, the CO emission from low-J rotational transitions have become the workhorse tracer of the H_2 gas mass in the local Universe and beyond (Bolatto, Wolfire, and Leroy, 2013). The CO emission is, however, mostly optically thick within GMCs, so isotopologues are usually used to look deeper into GMCs. Accurate determination of the H_2 column densities from $^{12}CO(1-0)$ observations has therefore been a longstanding challenge in distant galaxies (Tan et al., 2011).

^{12}C^{16}O isotopologues.

The abundances of ^{12}C and ^{16}O, together with their isotopes ^{13}C and ^{18}O, are powerful tracers of the evolutionary state of a galaxy, since these are mainly products of primary and secondary stellar nucleosynthesis processing (Milam et al., 2005). It is predicted that ^{12}C is produced in the triple alpha reaction (where three Helium nuclei are fused) in intermediate and high mass stars (Timmes, Woosley, and Weaver, 1995). In the ISM it is expected that ∼50% of ^{12}C would come from massive stars (M>10M$_\odot$) that evolve into Super Nova Type II (SNII) while the remaining half comes from asymptotic giant branch (AGB) stars (1-8M$_\odot$) during the third dredge-up (Pagel, 1997). The isotopologue ^{13}C participates as an intermediary element in the carbon-nitrogen-oxygen (CNO) cycle and is transformed into ^{14}N in the red giant phase of low/intermediate mass stars, whose amounts depend on the available amount of ^{12}C (Prantzos, Aubert, and Audouze, 1996). ^{13}C is brought to the surface during the first and second dredge-up, mixed into the star's atmosphere and finally ejected into the ISM during the third dredge-up (Herwig and Austin, 2004). While enrichment in ^{12}C occurs in rapid timescales, ∼10^6years, ^{13}C enrichment requires longer time-scales ∼10^9years (Vigroux, Audouze, and Lequeux, 1976).

On the other hand, it is known that ^{16}O and ^{18}O are sensitive products of the stellar mass (Kobayashi, Karakas, and Umeda, 2011), and therefore trace differences in the Initial Mass Function (IMF; Milam et al. 2005; Romano et al. 2017). Both ^{16}O and ^{18}O are mainly produced in high mass stars (Tinsley, 1980; Timmes, Woosley, and Weaver, 1995), where ^{16}O is produced during core He-burning in massive stars, and ^{18}O is produced in massive stars during He-burning by addition of an α particle to ^{14}N, resulting from the CNO process (Penzias, 1981; Henkel and Mauersberger, 1993). Both are expelled into the ISM via SNeII explosions (Prantzos, Aubert, and Audouze, 1996). Oxygen isotope ratios can be used to model the evolution of the star-formation activity, where small ^{16}O/^{18}O ratios are interpreted as a common signature of an advanced starburst stage (Henkel and Mauersberger, 1993).

The ^{12}C/^{13}C abundance ratio reflects the relative degree of primary to secondary nucleosynthesis processing, while the ^{18}O/^{16}O abundance ratio traces differences in the IMF (Milam et al., 2005; Romano et al., 2017). In practice, we could assume that the ^{12}C/^{13}C and ^{18}O/^{16}O abundance ratios can be traced by the molecular I(^{12}CO)/I(^{13}CO) and I(^{13}CO)/I(C^{18}O) line intensity ratios respectively. After the first detection of ^{12}CO and its isotopologues in the Milky Way (Wilson, Jefferts, and Penzias, 1970; Penzias, Jefferts, and Wilson, 1971), several works have repeated their detection in nearby galaxies (Rickard et al. 1975; Encrenaz et al. 1979; Rickard and Blitz 1985; Young and Sanders 1986). More recently, several works have proven successfully the usage of I(^{12}CO)/I(^{13}CO) and I(^{13}CO)/I(C^{18}O) line ratio as a chemical evolution tracer in the Galaxy (Halfen, Woolf, and Ziurys, 2017), nearby galaxies (Sliwa et al., 2017; Jiménez-Donaire et al., 2017; Cormier et al., 2018; Sliwa et al., 2017; Brown and Wilson, 2019), and lensed high redshift galaxies (Henkel et al., 2010; Danielson et al., 2013; Spilker et al., 2014; Zhang et al., 2018).

It is known that the ^{12}C/^{13}C abundance ratio changes as a function of distance from the Galactic center of the Milky Way (Langer and Penzias, 1990). This dependency has been confirmed by Halfen, Woolf, and Ziurys (2017) to reflect stellar nucleosynthesis and subsequent Galactic chemical enrichment on the Galaxy disc. An environmental dependence for ^{12}C/^{13}C has been also shown by Alatalo et al. (2015), who found that 17 Early Type Galaxies (ETG) located in the Virgo cluster and groups, show a line intensity ratio about two times smaller than field galaxies. They proposed three different scenarios in which the observed variations could be explained: an extra low-mass stellar enrichment taking place in Virgo cluster galaxies, an increased mid-plane pressure effects of the intracluster medium (ICM) or the survival of only the densest clumps of molecular clouds as galaxies enter the ICM. Additionally, Davis (2014) showed a systematical dependency of I(^{12}CO)/I(^{13}CO) line intensity ratio on star-formation rate surface density (Σ_{SFR}) and gas surface density (Σ_{H_2}) using a sample of nearby starburst and

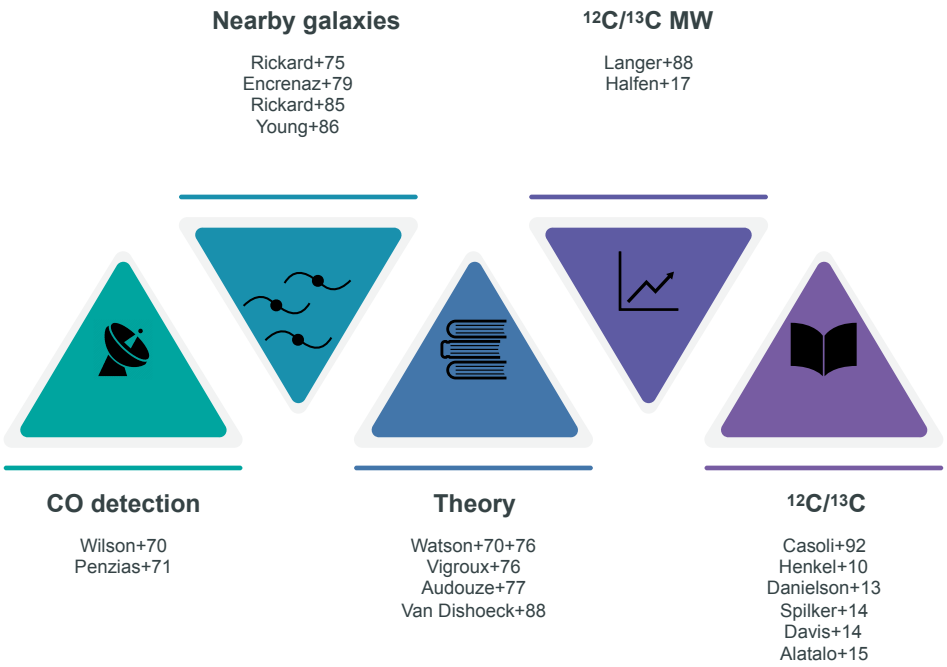

FIGURE 1.9: Evolution on the study of the ISM.

early-type galaxies, suggesting that the observed correlations are caused by the combined action of massive stars heating and/or inducing turbulence in the gas phase on those galaxies with higher Σ_{SFR}. Figure 1.9 shows the evolution on the study of the ISM.

1.7.3 The circumgalactic medium and the ionized gas.

The circumgalactic medium (CGM) is the interface around galaxies where inflowing and outflowing baryonic material is reprocessed. The first evidence of the existence of diffuse material at galactic latitudes in the Milky Way was presented by Münch and Zirin (1961), and suggested the idea of a diffuse gas corona that could be explored by absorption lines in the spectra of background objects. A few years later, Bahcall and Spitzer (1969) proposed that the multiple absorption lines observed in quasi-stellar objects (QSOs) could be associated to gas around nearby galaxies. Later on, this was confirmed by Sargent et al. (1980) and Bergeron (1986) who reported multiple Lyman-α absorption detections at different redshifts in the IGM, and it was demonstrated that these diffuse gas haloes produce strong Lyα, C IV and other lines (Lanzetta et al., 1995; Chen et al., 1998). In an innovative study, Adelberger et al. (2003) successfully used QSOs as backgroud objects to probe the circumgalactic medium of high-redshift galaxies. Since then QSOs have been extensively used to study the CGM at low and high redshifts (e.g. Steidel et al. 2010; Werk et al. 2016; Bouché et al. 2013; Kacprzak et al. 2010). Figure 1.10 shows the evolution on the study of the CGM.

This thesis is organized as follows: in chapter 2 VSAT is introduced, chapter 3 includes the results from the stacking analysis in low redshift star-forming dusty galaxies from VALES, chapter 4 includes the results from the stacking analysis in high redshift galaxies from VUDS, and chapter 5 presents the conclusions and future prospects.

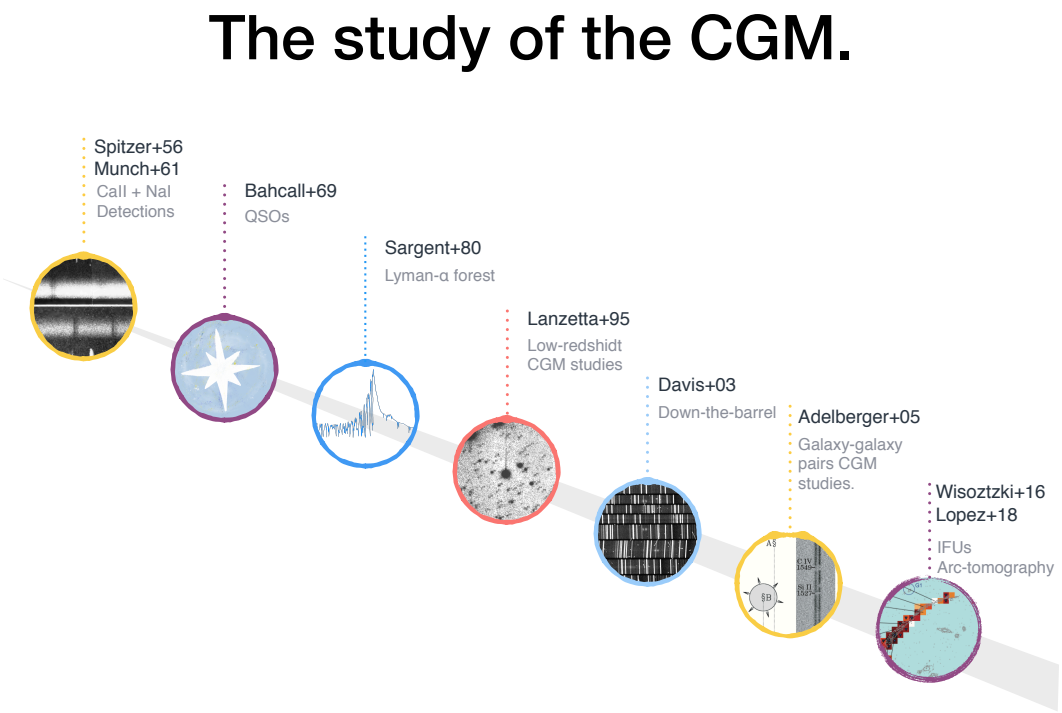

FIGURE 1.10: Evolution on the study of the CGM.

Chapter 2

Stacking Analysis

2.1 Historical background

Astronomical images from large telescopes can be largely affected by atmospheric turbulance which can heavily affect their resolution as light passes through the atmosphere (Fried, 1966). However, as it was proposed by Labeyrie (1970), these nocive effects could be corrected by analysing the interfering effects in the image caused by the atmospheric seeing. This technique was successfully implemented by considering a large number (250) of short exposure ($\lesssim$ .01 seg) images that were uniformly pre-processed and co-added to generate a composite image (Gezari, Labeyrie, and Stachnik, 1972; Lynds, Worden, and Harvey, 1976). This process yielded to a co-added image with a resolution that approached the telescope diffraction limit and improved the signal-to-noise ratio, enabling measurements of stellar diameters and binary structure from stellar systems. Based on these studies, Bates and Cady (1980) created the *shift and add* technique, with a wider applicability compared to the technique used by Lynds, Worden, and Harvey (1976) and useful to detect faint objects. The *shift and add* procedure considers a sequence of images of an astronomical object, where the brightest point in each image is shifted to the centre of the image and then combined. This technique allowed to report experiments where high-quality images of objects viewed under very poor seeing conditions could be formed (Cady and Bates, 1980).

The simplicity of the *shift and add* technique allowed its implementation on different stellar studies: Bagnuolo (1982) and Bagnuolo and McAlister (1983) successfully identified binary star systems, Baba et al. (1985) reconstructed a binary star system (α-Com), Christou et al. (1986) showed the presence of an extended stellar envelope around α-Orionis, and later on it was used to obtain astonishing ground-base images from Io with comparable results as those shown by close-up images taken by Voyager (Kuwamura et al., 2008). More recently, it has been used to find very faint Trans-Neptunian Objects (TNOs) (Fuentes, George, and Holman, 2009; Cochran et al., 1995), monitor geostationary satellites from the ground (Scott and Ellery, 2015), detect faint asteroids (Ashton, 2015) or any other nearby moving objects (Jeong et al., 2019). In extra-galactic astronomy, the *shift and add* (here after *stacking*) technique was first used to co-add the X-ray emission from undetected galaxies at distances up to ($z \sim 4$) in the Chandra Deep Field North (CDF-N) and determine their average emission properties (e.g. Hornschemeier et al. (2000), Brandt et al. (2001b), Brandt et al. (2001a), Nandra et al. (2002), and Seibert, Heckman, and Meurer (2002)). However, stacking analysis has been exploited to extended the detections coming from extra-galactic sources in different wavelength domains: X-ray (Rodighiero et al., 2015; Yang et al., 2018), UV (Rigby et al., 2018), infrared (Dole et al., 2006; Duivenvoorden et al., 2020), sub-mm (Webb et al., 2003; Millard et al., 2020), and radio (Huynh et al., 2005; Perger et al., 2019). Figure 2.1 shows the evolution of the stacking analysis.

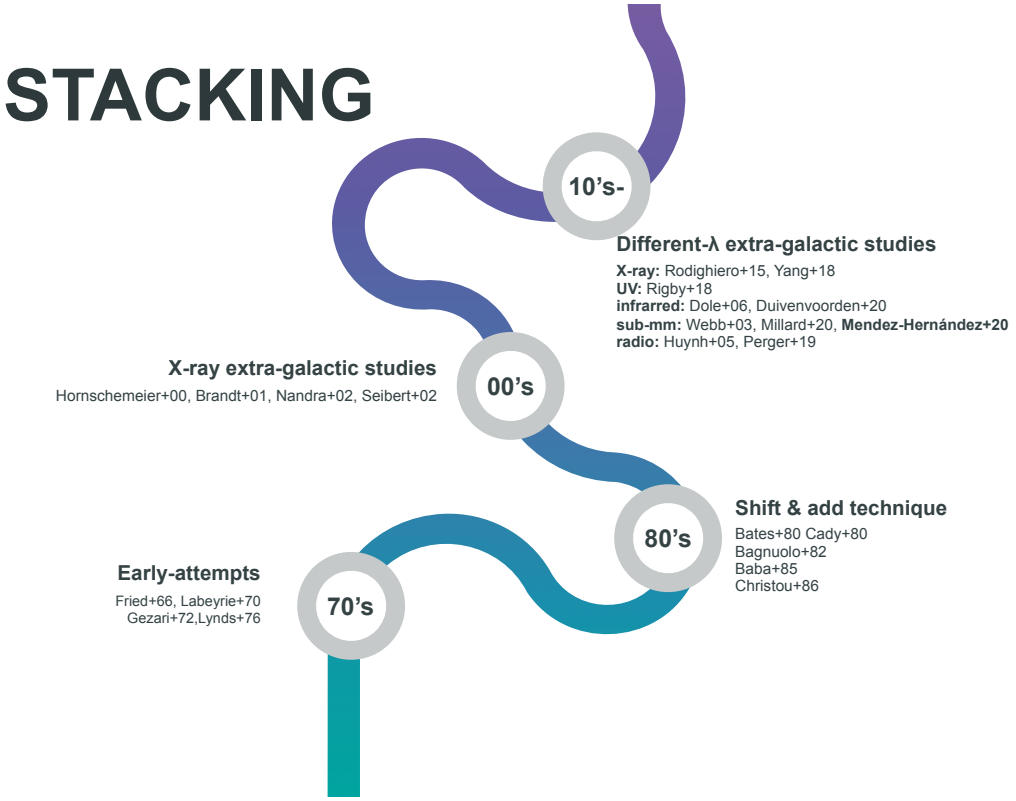

FIGURE 2.1: Evolution of the stacking analysis.

2.2 Stacking technique

The *stacking* analysis provides a statistical approach to measure the average properties of faint targets/sources that are too weak to be individually detected. The average stack will suffer from a noise $\sigma/\sqrt{N_{objects}}$, where σ is the typical noise of the individual data set and $N_{objects}$ is the number of sources to be stacked. Thus, the signal to noise ratio of the resulting image from the *stacking* procedure will be boosted by a factor of $\sim \times\sqrt{N}$. Figure 2.2 schematically shows how two-dimensional (2D) images are co-added. *Stacking* analysis averages the signal from the individual sources in a pixel-by-pixel basis and assuming that the brightest point of all the sources match the center of the individual images. Hence, co-added images can be affected by spatial offsets and have to be taken into account. For example, while optical images trace the stellar component, sub-mm observations can trace dust and molecular gas components. Thus, the location of the peaks does not necessarily match. This can be corrected by applying astrometric corrections, derived from data sets of a bright line emission/absorption with high SNR close to the wavelength/frequency of the data sets to be co-added (Méndez-Hernández et al., 2020).

Similarly, spectral offsets could also affect the location of the signal in the individual sources to be co-added, however the observed location of a bright emission/absorption spectral feature can be used to correct this effect (e.g. Lyα, Berry et al. 2012). Another possibility is to quantify the impact of these harmful effects through statistical analyses. For example, Dole et al. (2006) assessed that *stacking* did not introduce spurious artifacts that could be mimicking a source by adding random or systematic artificial offset to the individual spectral location of their sources in their mid (MIR) and far infra-red (FIR) spectra. Rigby et al. (2018) performed a jackknife analysis by repeating the *stacking* process n times and masking out different spectral regions of the

individual spectra, to guarantee that their composite spectra were free of spurious features produced by intervening absorption systems.

Stacking techniques can be used to perform statistical analyses of well defined samples of galaxies at low- and high-redshifts to infer average flux density of the sample, that then can be used to explore their dependency with other galaxy properties (e.g. star formation rate, stellar mass, luminosity). Thus, *stacking* analyses are a powerful tool to detect the weak signal of faint line absorption/emission of low- and high-redhsift galaxies (Millard et al., 2020; Bera et al., 2018) where detections of individual objects can not be attained. However, this combined signal smears out valuable information about the spatial and kinematic information of the analyzed sources, that otherwise can be deduced from individual source detections. In this work *stacking* analysis are used to detect the faint emission coming from ^{12}CO isotopologues (*i.e.* ^{13}CO, and C^{18}O) in dusty star-forming galaxies at low-redshift and the weak low- and high-ionization metal absorption lines (Si II, C II, Si IV, C IV) in the circumgalactic medium (CGM) in high-redshift galaxies ($\langle z \rangle = 2.6$). In both cases emission/absorption detections from individual sources at these redshifts have not been previously reported and thus these analyses push the limits of current observation capabilities of these type of detections.

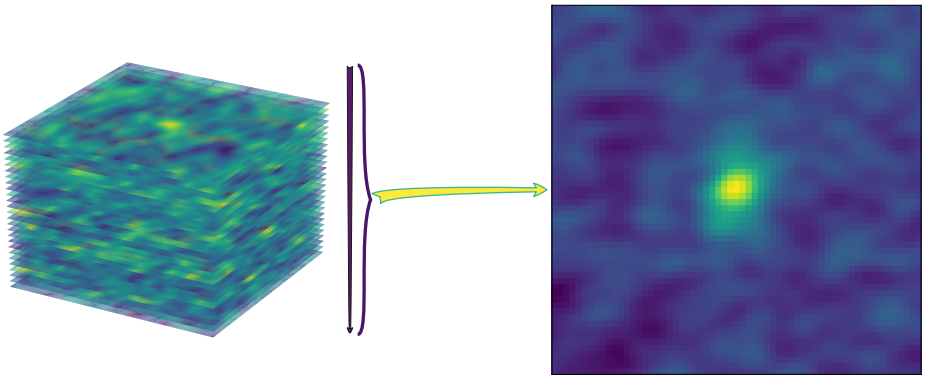

FIGURE 2.2: Co-add scheme where several images previously centered to the pixel with the brightest point (left panel), are combined to produced a composite image (right panel)

2.3 Valparaíso Stacking Tool (VSAT)

For the purposes of this thesis, I have developed the Valparaíso Stacking Tool (VSAT). VSAT provides a series of python tools to stack 1D, 2D and 3D data sets, and analyze the resulting composite spectra/images. It is intended to co-add samples of spectra belonging to large extragalactic catalogs by selecting subsamples of galaxies defined by any particular property (e.g. redshift, stellar mass, star formation rate), with the possibility to generate different (e.g. median, average, weighted average, histogram) composite spectra. The flexibility of VSAT allows to analyze smaller data sets containing any type of astronomical object. The following sections presents the algorithm and examples of its usage.

2.3.1 VSAT-3D

VSAT-3D [1] generates co-added datacubes by combining individual datacubes on a channel by channel and pixel by pixel basis. Figure 2.3 shows the schematic view of the 3D-stacking process. A set of individual datacubes that will be combined are considered to be center in the central

[1] https://github.com/humehe/VSAT-3D

pixel of the channel where the peak of line is observed /expected ($v = 0\,km\,s^{-1}$), and to show variations among their expected fluxes. Although VSAT-3D was created for combining image fits files created with CASA from ALMA interferometric observations, VSAT versatility allows to combine 3D structured data sets from any other instrument.

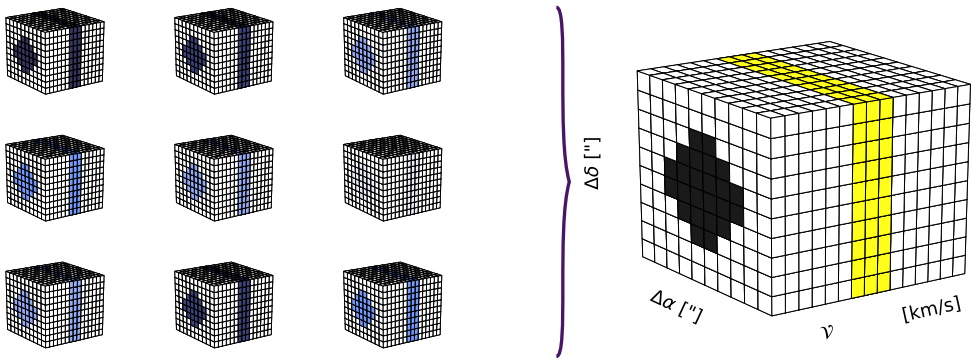

FIGURE 2.3: VSAT-3D co-add scheme of the 3D stacking process following a following a channel by channel pixel by pixel strategy. Note that the datacubes are centered to match the expected frequency in the central channel. The different blue tones indicate variations in the flux intensities among the individual objects to be combined.

VSAT-3D generates *sum, median and average* composite images, although it is possible to generate additional composite datacubes (*i.e. histograms, weighted average, and percentiles*). Then, it is possible to extract the integrated flux densities from the stacked 3D signal, by modeling the source spatial and spectral distribution with a 3D Gaussian profile (equation 2.1)

$$S(x,y,f) = A_0 \exp\left[-\left(\frac{(x-x_0)^2}{2\sigma_x^2} + \frac{(y-y_0)^2}{2\sigma_y^2} + \frac{(f-f_0)^2}{2\sigma_f^2} \right) \right] \tag{2.1}$$

where A_0 is the amplitude of the source, σ_x and σ_y are the source size parameters, and σ_f expresses the width of the line.

For flux measurement purposes, two apertures are defined: inner (*in*), an outer (*ot*). These apertures enclose two different regions: 1) a region where the source's flux will be measured ($\varnothing_{\rm in}$) and 2) a surrounding ring from which noise levels can be estimated ($\varnothing_{\rm in} < \varnothing < \varnothing_{\rm ot}$). For example, Figure 2.4 shows the stamps that are generated for each channel defined within the datacube, adopting $\varnothing_{\rm in} = 10''$ and $\varnothing_{\rm ot} = 20''$. We note that, these apertures can be defined depending on the properties of the observations to be analyzed. From the inner region, a spectral line profile along the velocity/frequency axis can be generated to derive the line width (σ_f) through a one dimensional gaussian fit. To exemplify this, Figure 2.5 shows the spectral line profile constructed from the average and median fluxes per channel, the gaussian fit and the 5σ regions around the ^{12}CO observed frequency, considering a $\varnothing_{\rm in} = 10''$ aperture.

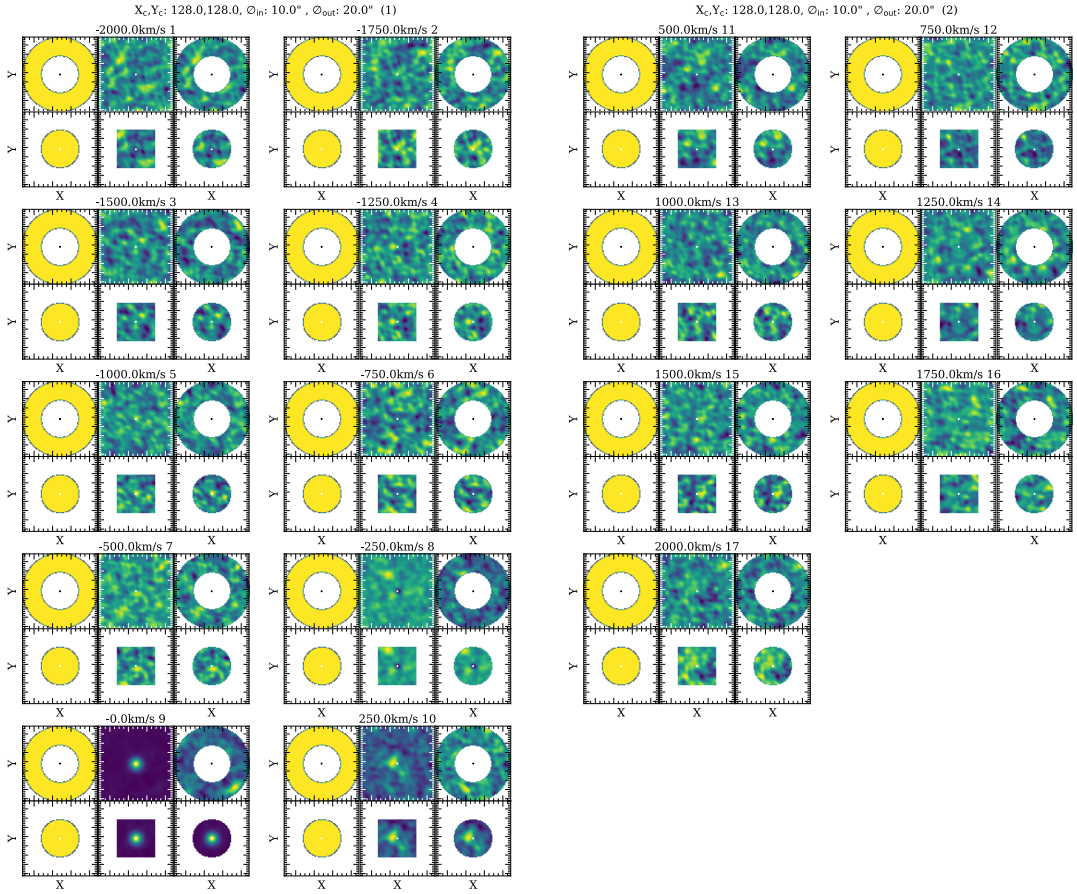

FIGURE 2.4: ^{12}CO composite datacube stamps for the 17 channels corresponding to a $\pm$2000 km s^{-1} width around the central channel. Each channel shows a ring defined between 10″ and 20″ (top panels), surrounding an inner 10″ region where flux measurements are performed (bottom panels). The first column panels show the mask regions, the middle column panels show the original image from the datacube and the third column panels the resulting masked regions from the datacube.

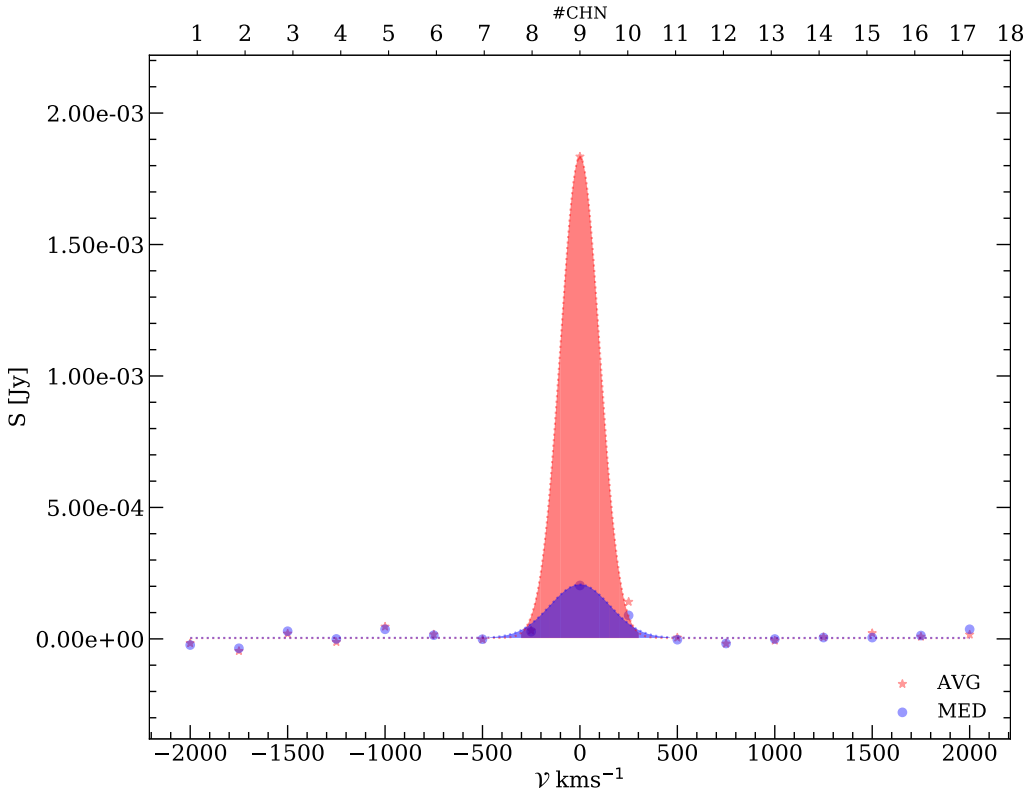

FIGURE 2.5: VSAT-3D ^{12}CO spectral line profile for a 10″ inner aperture, constructed by computing the median (blue) and average (red) flux values within the defined region. Shaded regions correspond to the 5σ CIs around the ^{12}CO observed frequency.

Afterwards, a 2D image of the central channel at which the flux maximum is located (see Fig. 2.6 left panel) and a collapsed image around ($\pm$1fwhm$_f$ [2]) the flux maximum can be created (see Figure 2.6 right panel). From this central channel stamp, a 2D gaussian (eq. 2.2) fit can be performed to derive the amplitude (A_0) and the source size paramters (σ_x, σ_y). Figure 2.7 shows the central channel image with white contours corresponding to the Gaussian fit (left panel), the generated model (middle panel) and the residuals (right panel).

[2] fwhm$_f$ = $\sigma_f \cdot \sqrt{8ln(2)}$, where σ_f, correspond to the fit line width obtained from the corresponding composite stacked spectrum.

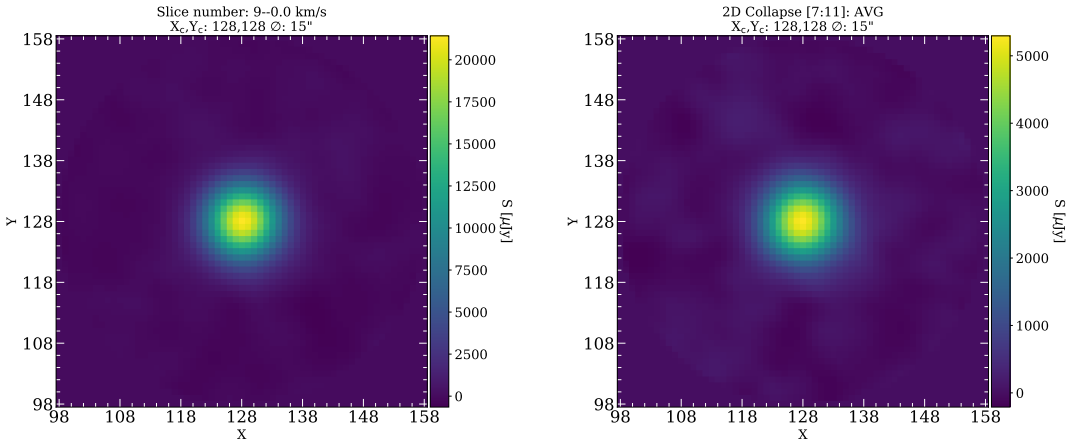

FIGURE 2.6: Central channel (left) and collapsed 2D (right) images for the ^{12}CO composite datacube.

$$S(x,y) = A_0 \exp\left[-\left(\frac{(x-x_0)^2}{2\sigma_x^2} + \frac{(y-y_0)^2}{2\sigma_y^2} \right) \right] \tag{2.2}$$

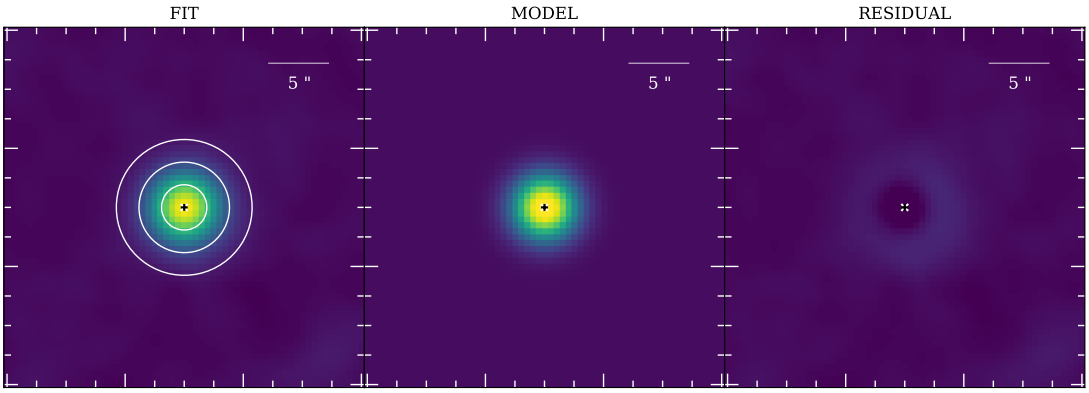

FIGURE 2.7: VSAT-3D central channel 2D image with gaussian fit overlaid in white contours (left-panel), generated 2D gaussian model (middle-panel) and residuals (righ-panel) for ^{12}CO median composite images.

Finally with the fit quantities (A_0, σ_x, σ_y, σ_f) in hand, velocity integrated flux densities computations can be obtained through eq. 2.3

$$S_T = (2\pi)^{3/2} A_0 \sigma_x \sigma_y \sigma_f \tag{2.3}$$

2.3.2 VSAT-2D

VSAT-2D [3] was designed to generate composite 2D images coming from *moment-zero* intensity maps collapsed from interferometric data sets following eq. 2.4.

$$I_{tot}(\alpha,\delta) \; = \; \Delta v \Sigma_{i=1}^{N_{chann}} S_\nu(\alpha,\delta,v_i) \quad [flux - units/km\,s^{-1}] \tag{2.4}$$

[3] https://github.com/humehe/VSAT-2D

where S_ν is the flux dependent the right ascension (α), declination (δ) and velocity (v_i), and Δv is the line width,

However, it can be used to combine images coming from broad-band photometry or X-ray maps. Figure 2.8 shows the channels ($\pm$1FWHM) around the central velocity channel considered to generate a *moment-zero* intensity map.

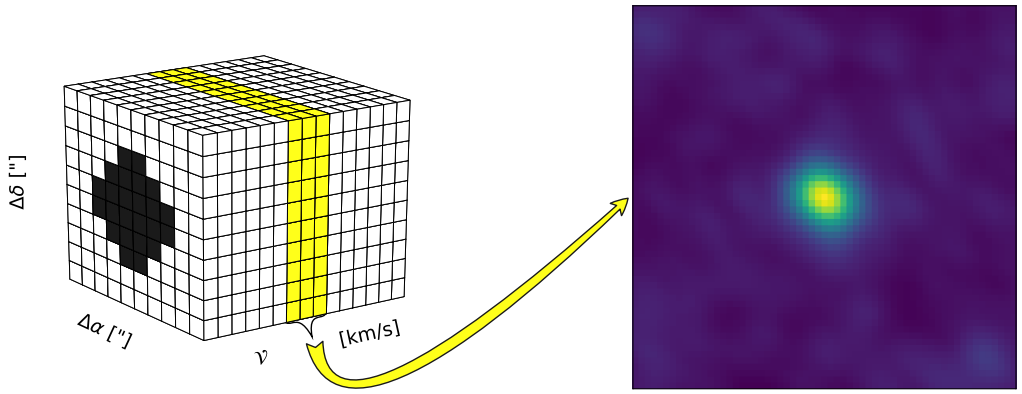

FIGURE 2.8: VSAT-2D moment-zero intesity map generated by collapsing the datacube around $\pm$1FWHM the expected line frequency (yellow).

Similarly to VSAT-3D, three apertures are defined to frame two regions: 1) a region where the source's flux is measured ($\varnothing_{\rm in} = 10''$) and 2) a surrounding ring from which noise levels can be estimated ($\varnothing_{\rm in} < \varnothing < \varnothing_{\rm in}$), and these apertures can be defined depending on the observations to be analyzed. To exemplify its usage, Figure 2.9 shows the stamps that are generated from the *moment-zero* composite image. From the inner region, the integrated flux density is computed through a two dimensional Gaussian fit model (eq. 2.2) of the sources flux distribution. Figure 2.10 shows the *moment-zero* composite image, the flux model and residuals, from which the integrated flux density (S_ν, flux-units/km s^{-1}) is estimated following eq. 2.5.

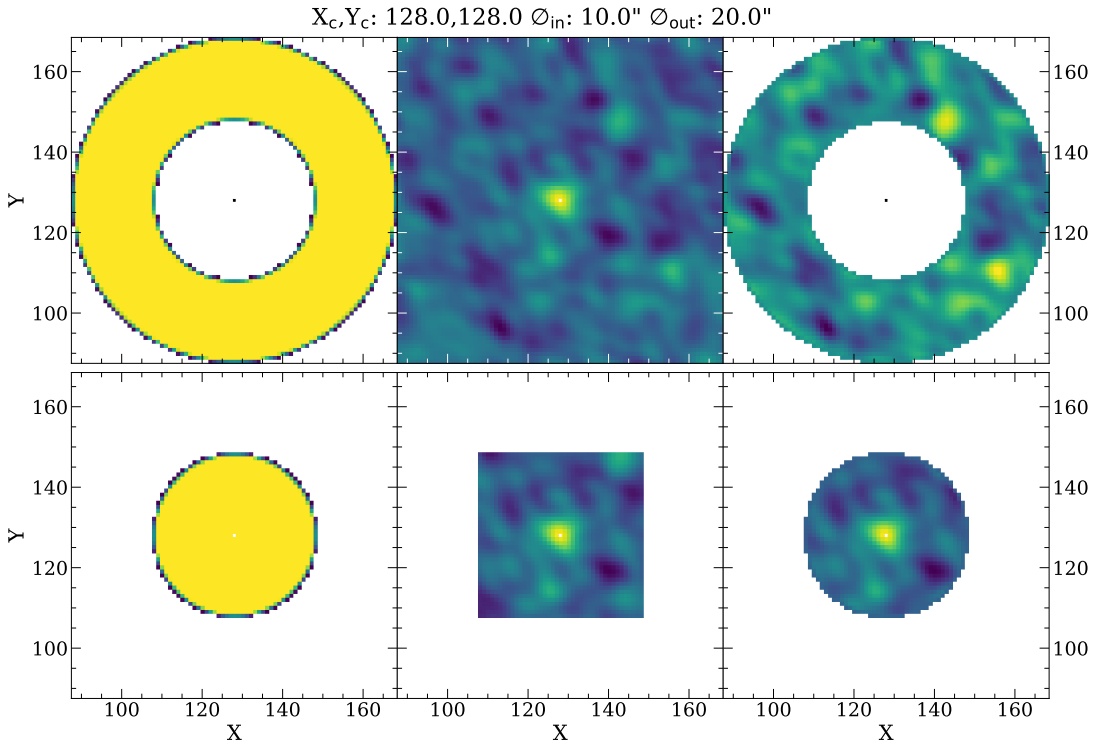

FIGURE 2.9: VSAT-2D ^{12}CO composite *moment-zero* stamps. A ring defined between 10″ and 20″ (top panels), surrounding an inner 10″ region where flux measurements are performed (bottom panels). The first column panels show the mask regions, the middle column panels show the orignal image from the datacube and the third column panels the resulting masked regions from the datacube.

$$S_T = 2\pi\, A_0 \sigma_x \sigma_y \tag{2.5}$$

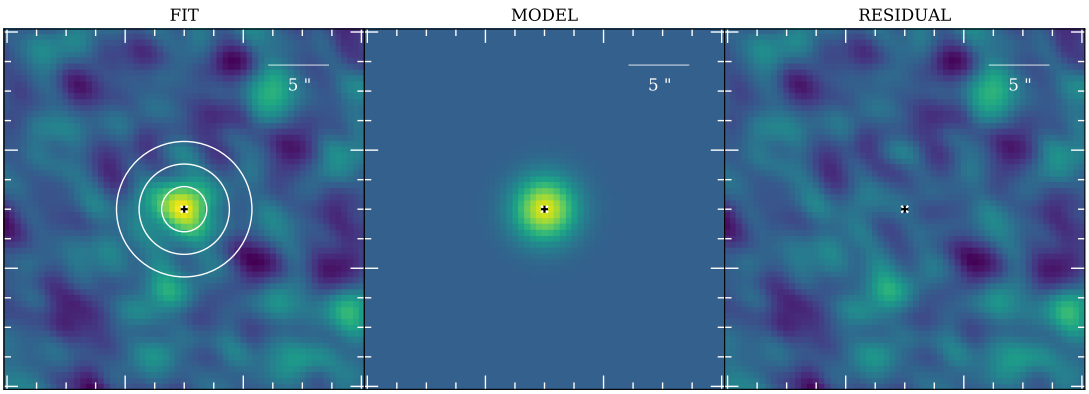

FIGURE 2.10: VSAT-2D ^{12}CO *moment-zero* composite image with gaussian fit overlaid in white contours (left-panel), 2D gaussian generated model (middle-panel) and residuals (righ-panel).

We emphasize that thanks to its flexibility, VSAT-2D can be exploited to analyze collapsed maps around a central frequency / wavelength from any other integral field spectra (IFS, e.g. MUSE, KMOS, JWST).

2.3.3 VSAT-1D

VSAT-1D [4] provides a series of tools for selecting, stacking, and analyzing 1D composite spectra. It is possible to select subsamples of galaxies defined by any particular property (e.g. redshift, stellar mass, star formation rate) and to generate different (e.g. median, average, weighted average, histogram) composite spectra. VSAT-1D was designed to probe the CGM of star-forming galaxies by selecting pairs of close pairs of galaxies, where continuum emission coming from *background* galaxies is absorbed by the CGM of *foreground* galaxies. Therefore, the individual *background* spectra needed to be pre-processed before they could be combined. This includes a shift to the *foreground* rest-frame to succesfully locate the low- and high-ionization absorptions produced by the gas in the CGM. Besides the wavelength shift, this pre-processing also includes continuum fitting, smoothing and line masking. To perform the CGM analysis, composite spectra of both *foreground* and *background* galaxies were generated.

For example, Figure 2.11 illustrate how galaxies can be pre-processed before they are combined. Figure 2.11 shows the spectrum of *foreground* galaxy 5100820808 at z=2.76. The first panel shows the original spectrum with the continuum emission overlaid in green, the second panel shows the continuum normalized spectrum, the third panel shows the rest-frame shifted spectrum, the fourth panel the spectrum smoothed with a Gaussian kernel ($\Delta\lambda \sim 2$ Å) and the fifth panel shows the interpolated spectrum that was used to generate composite spectra.

[4] https://github.com/humehe/VSAT-1D

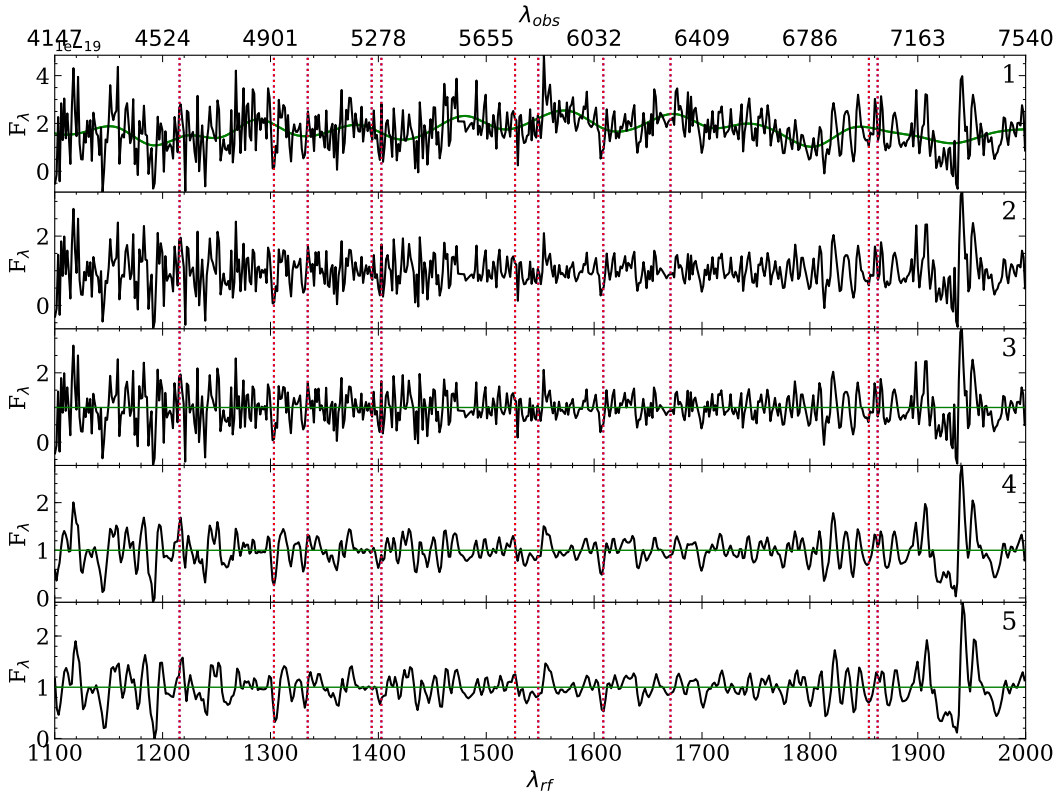

FIGURE 2.11: VSAT-1D spectra corresponding to the *foreground* galaxy 5100820808 at z=2.7698. Each panel shows every step in the *foreground* spectra pre-processing procedure: 1) 5100820808 original spectrum with continuum fit overlaid in green, 2) continuum normalized spectrum, 3) rest-frame shifted spectrum, 4) smoothed spectrum, 5) interpolated spectrum. An auxiliary wavelength axis corresponding to the observed wavelength (λ_{obs} Å) is also included in the top. Red-dotted lines indicate relevant spectral features, from left to right: Lyα-1215, O I+Si II-1303.2, C II-1334.5, Si IV-1393.8/1402.8, Si II-1526.7, C IV-1548.2/1550.8, Fe II-1608, Al II-1670.7, and Al III-1854.7/1862.7

After applying the pre-processing procedures to a set of individual spectra, they can be combined to produce composite spectrum. Figure 2.12 shows in the upper panel the resulting median (dashed-black line) and average (solid-red line) composite spectrum by considering 101 *foreground* galaxies from the COSMOS field, while the lower panel shows the number of galaxies contributing to the coadded spectrum per wavelength element.

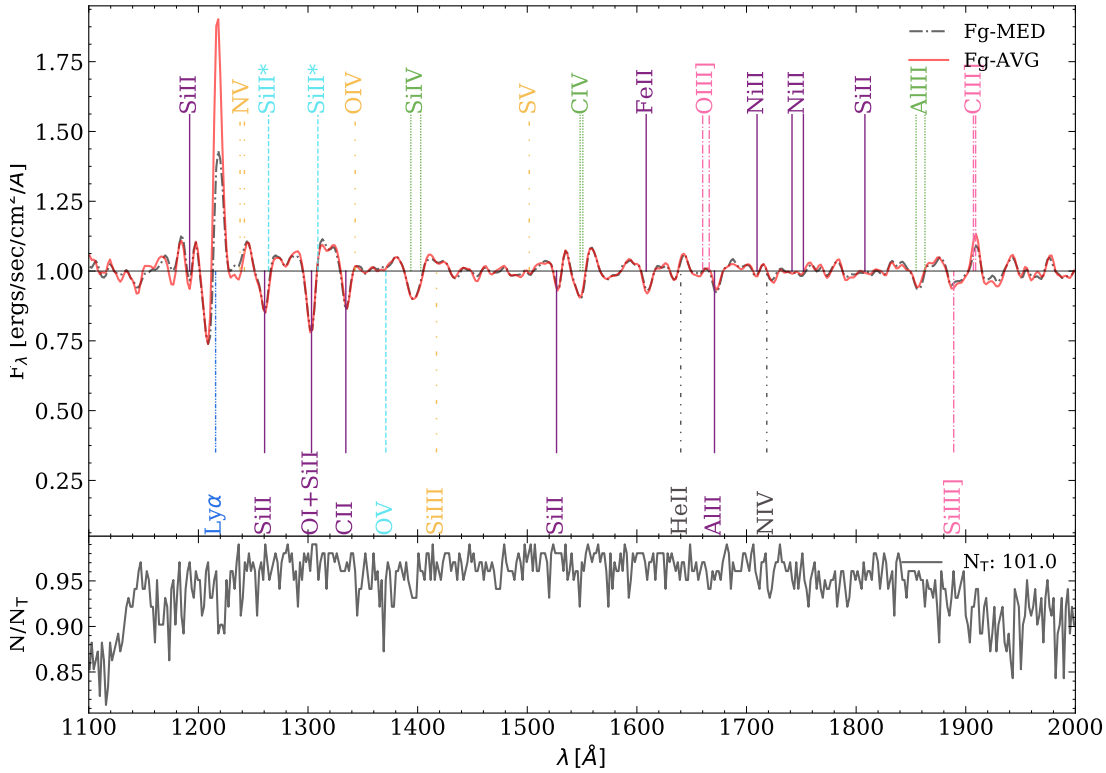

FIGURE 2.12: Top: Median (black) and average (red) composite spectra shifted to rest-frame of 101 *foreground* galaxies belonging to the COSMOS field with projected angular separations $< 23''$ ($b < 121$ kpc at z=2.6). Bottom: The fraction of the contributing individual spectra to the composite spectra per unit wavelength. Several spectral lines of interest are marked: H I (Lyα) emission/absorption (blue), low-ionization interstellar metal absorption lines (solid-purple), high-ionization interstellar metal absorption lines (dotted-green), interstellar fine-structure emission line (dashed-cyan), absorption stellar photospheric lines (dot-dashed-orange) emission nebular lines (dasshed-dotted-magenta), and emission/absorption lines associate with stellar winds (dot-dashed-black).

From this composite spectra it is possible to measure the strength of the spectral line absorption/emission features by fitting a single or multiple Gaussian profiles. Figure 2.13 shows single Gaussian profiles fitted to the central absorption feature for Si II (1526.7 Å) and C IV (1548.2 Å) absorption lines. Equivalent widths (EW) estimations are given in the rest frame and are obtained by integrating each composite spectrum around the central wavelength restframe of an spectral line adopting a 5σ integration window.

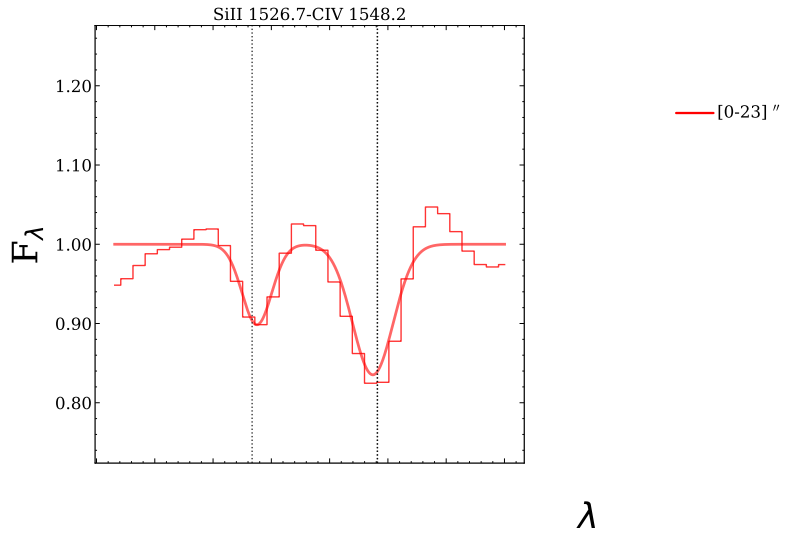

FIGURE 2.13: VSAT-1D median Si II (1526.7 Å) and Ci IV (1548.2 Å) absorption lines detected from the *foreground* galaxy composite spectra The solid lines correspond to a one dimensional Gaussian fit.

2.3.4 VSAT-Syn

To estimate the systematic errors of the stacked velocity-integrated line flux measurements `VSAT-Syn`[5] was created. This tool to simulate the ALMA Band-3 observations used in the ^{12}CO, ^{13}CO and C^{18}O stacking analyses. Each galaxy was modeled as a point-like source described by 2D circular Gaussian profile and its spectral flux distribution is described by a 1D Gaussian profile centred at 0 km s^{-1}. These sources are summed on top of random, normally distributed background noise that has been convolved to the scale of the synthesized beam [6] of the observations. Then, the stacking process was simulated by considering the same number of objects during the experiment and fixing their signal-to-noise ratios ($\langle \mathrm{SNR_{in}} \rangle$) and velocity line widths. Next, these simulated sources are stacked and the velocity-integrated line flux densities are gauge as described above (see 2.3.1 and 2.3.2). This process is then repeated 1000 times, by considering fixed values of amplitudes and velocity widths. Finally, the extracted velocity-integrated line flux densities (S_{out}) are measured and compared to the input values.

[5] https://github.com/humehe/VSAT-Syn

[6] Spatial resolution of the array used to observe a a given interferometric data-sets defined by $\theta_{syn} \sim 1.2\lambda/d$, where d is the base line of the array defined by distance between a pairs of antennas. It is the analogous of the point-spread function of optical telescopes.

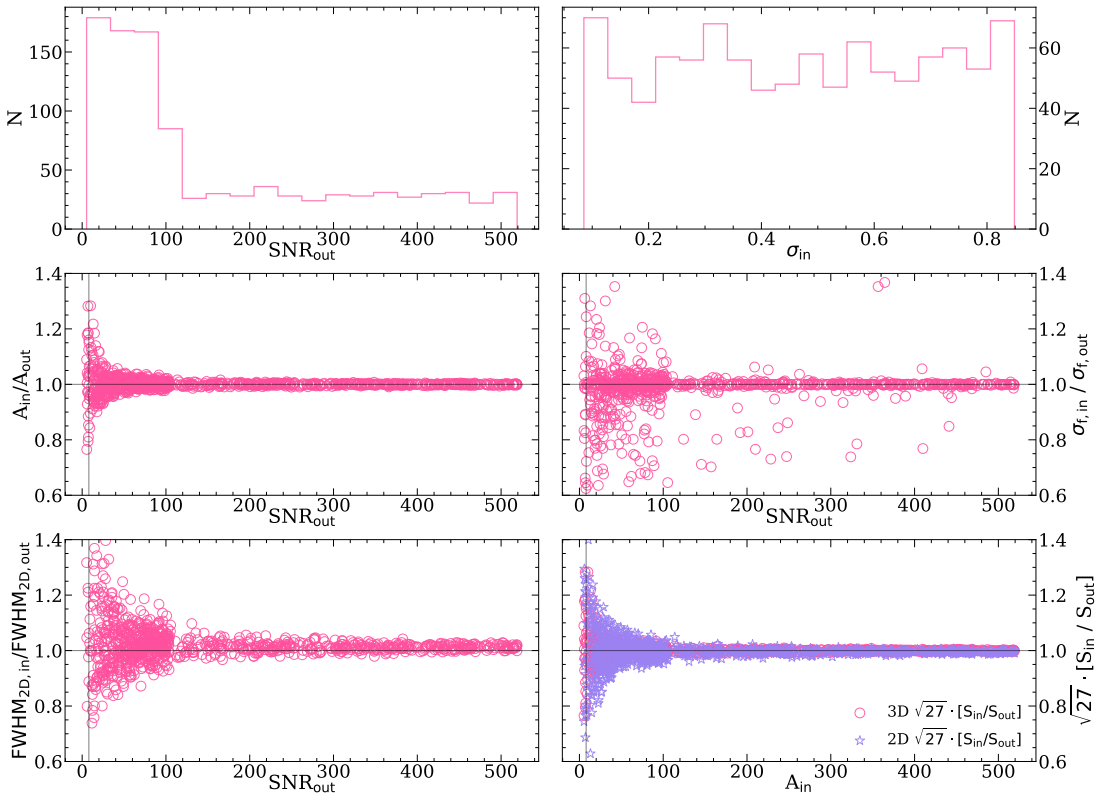

FIGURE 2.14: Simulated accuracy of the velocity-integrated flux density measurements (S_{in}/S_{out}) after stacking 27 galaxies for 2D and 3D stacking methods considering 1000 repetitions. The top-left panel shows the distribution of the simulated galaxies according to their SNR_{out} stacked detection. Top-right panel shows the distribution of the line velocity width (σ_{in}) adopted for the simulations between 50 kms^{-1}(0.08) and 500 kms^{-1} (0.85). The second-row panels show the spectral line profile amplitude (A_{in}/A_{out}-left) and line velocity width (σ_{in}/σ_{out}-right) accuracies. The bottom-left panel shows the source size ($FWHM_{2D,in}/FWHM_{2D,out}$) accuracy. The 2D flux measurements were obtained from the same simulated datacubes by collapsing them around $\pm 3\sigma_{out}$ of the central channel. The bottom-right panel shows the 2D (stars) and 3D (circles) velocity-integrated flux density measurements. Stacked detections with high SNR_{out} have clearly better accuracy for the velocity-integrated flux density measurements. S_{in} refers to the average velocity-integrated flux densities of the simulated sources used for the stacks, while S_{out} refers to the measured velocity-integrated flux density on the composite stacked images.

Fig. 2.14 shows the simulated accuracy of the velocity-integrated flux density measurements with respect to the stacked spectra (S_{in}/S_{out}) after stacking 27 galaxies for 2D (open stars) and 3D (open circles) stacking methods considering 1000 repetitions. The first row panels show the distribution of the simulated galaxies according to their SNR_{out} stacked detection (left), and the distribution of the line velocity width (σ_{in}) adopted for the simulations (right) between 50 kms^{-1}(0.08) and 500 kms^{-1} (0.85). The second row panels show the spectral line profile amplitude (A_{in}/A_{out}-left) (left) and line velocity width (σ_{in}/σ_{out}), (right) acuracies. The third row panels show the source size ($FWHM_{2D,in}/FWHM_{2D,out}$) accuracy (left), and the 2D (purple stars) and 3D (pink circles) velocity-integrated flux density measurements (right). Although **VSAT-Syn** was created to match the ALMA Band-3 observations, it can be used to mimic different observing conditions by varying the background noise level or the properties of the modelled source (e.g. velocity width, shape, size or orientation).

Chapter 3

The ISM of dusty star-forming galaxies at low redshift

The following chapter presents the results on the stacking analysis on 27 star-forming galaxies from the Valparaíso ALMA/APEX Line Emission Survey. These results have been published in the Monthly Noticies of the Royal Astronomical Society journal (Méndez-Hernández et al., 2020).

3.1 Introduction

Stars are mostly formed within Giant Molecular Clouds (GMCs), cold dense regions of the interstellar medium (ISM), which are characterized by high densities ($n_{H_2} > 10^4$ cm^{-3}; Gao and Solomon 2004; Bergin and Tafalla 2007) and low temperatures (10–20 K; Evans 1999) that favour the formation of stars. In these regions, the most abundant molecule is molecular hydrogen, H_2, however its lack of a permanent electric dipole makes it difficult to observe in emission. After H_2, the next most abundant molecule is carbon monoxide, $^{12}C^{16}O$ (hereafter CO), which easily emits photons from low level rotational transitions in similar ISM conditions as those in which the H_2 molecule resides. Therefore, the CO emission from low-J rotational transitions have become the workhorse tracer of the H_2 gas mass in the local Universe and beyond (Bolatto, Wolfire, and Leroy, 2013).

After the first detection of ^{12}CO and its isotopologues in the Milky Way (Wilson, Jefferts, and Penzias, 1970; Penzias, Jefferts, and Wilson, 1971), several works have repeated their detection in nearby galaxies (Rickard et al. 1975; Encrenaz et al. 1979; Rickard and Blitz 1985; Young and Sanders 1986). More recently, several works have proven successfully the usage of $I(^{12}\mathrm{CO})/I(^{13}\mathrm{CO})$ and $I(^{13}\mathrm{CO})/I(\mathrm{C}^{18}\mathrm{O})$ line ratio in nearby galaxies (Sliwa et al., 2017; Jiménez-Donaire et al., 2017; Cormier et al., 2018; Sliwa et al., 2017; Brown and Wilson, 2019), and lensed high-redshift galaxies (Henkel et al., 2010; Danielson et al., 2013; Spilker et al., 2014; Zhang et al., 2018).

An environmental dependence for $^{12}C/^{13}C$ has been shown by Alatalo et al. (2015), who found that 17 Early Type Galaxies (ETG) located in the Virgo cluster and groups, showed a line intensity ratio about two times lower than field galaxies. They proposed three different scenarios in which the observed variations could be explained: an extra low-mass stellar enrichment taking place in Virgo cluster galaxies, an increased mid-plane pressure effects of the intracluster medium (ICM) or the survival of only the densest clumps of molecular clouds as galaxies enter the ICM. Additionally, Davis (2014) showed a systematic dependence of the $I(^{12}\mathrm{CO})/I(^{13}\mathrm{CO})$ line intensity ratio on the star formation rate surface density (Σ_{SFR}) and the molecular gas surface density (Σ_{H_2}) using a sample of nearby starburst and early-type galaxies. They suggest that the observed correlations are caused by the combined action of massive stars heating and/or inducing turbulence in the gas phase on those galaxies with higher Σ_{SFR}.

Recent works have reported $I(^{13}CO)/I(C^{18}O)$ line intensity ratios for different galaxy types. Danielson et al. (2013) showed a low $I(^{13}CO)/I(C^{18}O)$ line intensity ratio ($\sim$1) in a high redshift lensed galaxy suggesting the presence of a significant fraction of high-mass stars. Sliwa et al. (2017) reported a simultaneous high $I(^{12}CO)/I(^{13}CO)$ ($\gg$60) intensity ratio with a low $I(^{13}CO)/I(C^{18}O)$ ($\lesssim$ 1) intensity ratio consistent with an ISM enrichment by the presence of a young starburst, a top-heavy IMF or their combined action. Jiménez-Donaire et al. (2017) presented a $I(^{13}CO)/I(C^{18}O)$ line intensity ratio dependency with Σ_{SFR} and galactocentric distance in nine nearby spiral galaxies due to the selective enrichment of the ISM by massive stars. More recently, Zhang et al. (2018) showed high $I(^{12}CO)/I(^{13}CO)$ line intensity ratios with a simultaneous low $I(^{13}CO)/I(C^{18}O)$ line intensity ratios in four gravitationally lensed sub-millimetre galaxies (SMGs) at z $\sim$2-3, and claimed this to be caused by a change of the IMF where there is a higher number of massive stars in high-z starburst galaxies than in typical galaxies.

For galaxies beyond the Local Universe, the observation of faint emission lines as ^{13}CO or $C^{18}O$ is usually challenging. The abundances of ^{13}CO and $C^{18}O$ are typically 50 and 500 times lower than ^{12}CO (Jiménez-Donaire et al., 2017) and their flux density ratios usually range between 20 to 100 for I(^{12}CO)/I(^{13}CO) and between 20-140 for I(^{12}CO)/I(C^{18}O) (Aalto et al., 1991; Casoli, Dupraz, and Combes, 1992b; König et al., 2016; Sliwa et al., 2017). For individual detections in nearby local ULIRGs, ^{13}CO and $C^{18}O$ observations need to be at least four times deeper than ^{12}CO observations to yield line detections (Sliwa et al., 2017; Brown and Wilson, 2019). In this work, we propose an alternative way to overcome sensitivity limitations by stacking the signals of the $^{12}CO(1-0)$, $^{13}CO(1-0)$ and $C^{18}O(1-0)$ lines ($\nu_{^{12}CO(1\text{-}0)} = 115.271$ GHz, $\nu_{^{13}CO(1\text{-}0)} = 110.201$ GHz, and $\nu_{C^{18}O(1\text{-}0)} = 109.782$ GHz rest-frame frequencies, respectively) from individual star-forming galaxies to produce a statistically robust study for the content of these isotopologues up to $z = 0.2$.

3.2 Data

3.2.1 Sample

In this work, we present ^{13}CO(1-0) and $C^{18}O$(1-0) line measurements for 27 and 24 galaxies, respectively, which were previously detected by *Herschel* in [C II] (Ibar et al. 2015) and with ALMA in ^{12}CO (Villanueva et al. 2017). The sample is part of the Valparaíso ALMA/APEX Line Emission Survey (VALES; Villanueva et al. 2017; Cheng et al. 2017) designed to characterize the CO emission line of low-J transitions from typical star-forming and starburst galaxies up to z = 0.35. The parent population comes from dusty galaxies taken from the equatorial fields of the *Herschel* Astrophysical Terahertz Large Area Survey (*H*-ATLAS; Eales et al. 2010.) Galaxies were selected using a spectroscopic redshift at $0.02 < z < 0.2$, and a *Herschel* detection near the peak of the spectral energy distribution (SED) of a normal star-forming galaxy ($S_{160\mu m} > 150\mu$Jy). All galaxies have an unambiguous optical counterpart in the Sloan Digital Sky Survey (SDSS; Adelman-McCarthy et al. 2008), have high-quality spectra from the Galaxy and Mass Assembly survey (GAMA [1]; Liske et al. 2015; Driver et al. 2016 $z_{QUAL} \geq 3$), and show a Petrosian SDSS radii smaller than 15″ (see Ibar et al. 2015 for more details).

3.2.2 ALMA $^{13}CO(1-0)$ and $C^{18}O(1-0)$ observations

Observations with ALMA in band-3 were performed as part of project 2013.1.00530.S (P.I. E. Ibar), targeting the redshifted $^{12}CO(1-0)$, $^{13}CO(1-0)$ and $C^{18}O(1-0)$ emission lines for 27 VALES galaxies. The $^{12}CO(1-0)$ observations reached a root mean square (rms) of 2 mJy beam^{-1}

[1] http://www.gama-survey.org/

TABLE 3.1: New ALMA ^{13}CO(1 − 0) and C^{18}O(1 − 0) observations (Project ID: 2013.1.00530.S) presented in this work. 'PWV' is the average precipitable water vapour estimate for the observations. All data were taken using 32 12-m ALMA antennas. One observation taken on 24 January 2015 failed to run through the pipeline due to unknown reasons, so we have arbitrarily removed it from this work. Note that ^{12}CO(1 − 0) observations can be found in Villanueva et al. (2017).

Target names HATLAS	Observation Date	Flux Calibrator	Bandpass Calibrator	Phase Calibrator	PWV [mm]
J085340.7+013348, J085405.9+011130 J085356.4+001255, J083601.5+002617	2015 January 24 (1/3)	Ganymede	J1058+0133	J0909+0121	5.9
J085112.9+010342, J090949.6+014847 J085450.2+021208, J091205.8+002655	2015 January 24 (2/3)				5.2
J085346.4+001252, J084428.4+020350 J090005.0+000446, J090532.6+020222	~~2015 January 24 (3/3)~~				4.5
J085111.4+013006, J083745.1-005141, J085828.6+003813, J085233.9+013422	2015 January 25				4.5
J084350.8+005534, J083831.8+000044 J084305.1+010855 J084907.1-005138	2015 January 23 (1/2)	J0750+125	J0909+0121	J0901-0037	3.8
J084217.9+021223 J084139.6+015346 J085748.0+004641, J084428.4+020657	2015 January 23 (2/2)				3.9
J090750.0+010141, J085836.0+013149 J084630.9+005055	2015 January 23	J0854+201	J0750+1231	J0901-0121	3.8

at a spectral resolution of 30 km s^{-1} and are presented in Villanueva et al. (2017). The simultaneous ^{13}CO(1 − 0) and C^{18}O(1 − 0) observations were taken between 23 and 25 January 2015, in compact configuration (maximum baseline of ∼300 m) with precipitable water vapour (PWV) conditions in the range ∼4–6 mm. The observational strategy consisted of grouping sources in terms of redshift, such that we could observe all 27 galaxies using just three spectral setups (each one using four spectral windows to cover 7.5 GHz of bandwidth). The grouped sources are shown in Table 3.1, including the different executions performed by ALMA to reach the requested sensitivity. Unfortunately, the spectral setup missed C^{18}O(1 − 0) coverage in three galaxies.

Data reduction and imaging were performed using the same procedure as in Villanueva et al. (2017), where we developed a common pipeline within the Common Astronomy Software Applications (CASA version 4.4.0) to process all of the science goals. Each source was imaged with the TCLEAN task using a natural weighting. This yielded a restoring beam between 3″ and 4″, nevertheless, for the purposes of this work, we fixed the restoring beam to a common value, at 4.″5, for all sources. The ^{13}CO(1 − 0) and C^{18}O(1 − 0) observations reached rms noise of 0.9 mJy beam^{-1} at 30 km s^{-1} channel width (∼ 2× deeper than ^{12}CO observations). We note that ∼110 GHz continuum emission is undetected at 5σ significance in all sources down to a rms noise of 4μJy beam^{-1}.

3.3 Analysis

Out of the 27 galaxies, 26 have been previously spectrally detected at $> 5\sigma$ significance (signal-to-noise ratio: SNR) in ^{12}CO(1 − 0) (Villanueva et al., 2017). The ^{13}CO line was visually inspected for any individual detection. There were no confident ^{13}CO(1 − 0) emission lines from individual spectra for any of the 27 galaxies. Nevertheless, using the information of the ^{12}CO line widths as priors, we created moment-0 maps by collapsing the cube around ±1× FWHM$_{^{12}CO}$ of the expected ^{13}CO frequencies. In the collapsed images, we identify 7 galaxies with SNR > 5. The remaining 21 galaxies have not been detected above a 5σ significance in their moment-zero

TABLE 3.2: ^{13}CO$(1-0)$ detections from collapsed spectral images using ±FWHM ^{12}CO km s^{-1} line width around ^{13}CO$(1-0)$ expected frequencies. (col 1) ID taken from Villanueva et al. (2017), (col 2) observed signal-to-noise ratio in moment 0maps, (col 3) velocity integrated line flux densities with error measurements, (col 4) ^{13}CO$(1-0)$ luminosity with error measurements.

ID HATLAS	$SNR_{^{13}CO}$	$S_{^{13}CO}\Delta v$ mJy km s^{-1}	$L'_{^{13}CO}$ K km s^{-1}pc^2
J090949.6+014847	5.6	490 ± 90	68.0 ± 12.1
J085346.4+001252	5.7	225 ± 40	2.9 ± 0.5
J084139.6+015346	6.1	206 ± 33	5.4 ± 0.9
J084350.8+005534	6.2	458 ± 73	11.9 ± 2.0
J083831.8+000044	6.4	147 ± 22	4.3 ± 0.7
J085748.0+004641	5.9	343 ± 58	8.9 ± 1.5
J090633.6+001526	7.0	710 ± 100	9.6 ± 1.4

maps. Table 3.2 shows the SNRs, velocity integrated line flux densities and luminosities of these individual ^{13}CO detections. With respect to the C^{18}O emission line, we do not identify any detection in the spectra nor in the individual moment-0 maps using the same approach mentioned above.

Different techniques have been proposed to detect the emission of faint emission lines, falling below the detection limits. For example, Loomis et al. (2018) proposed a matched filtering method that uses a previously identified high signal-to-noise emission line as a kernel for filtering the *uv* signal and, thereby, facilitate the detection of any contiguous faint emission line. Similarly, Yen et al. (2016) proposed an image-plane line detection technique tailored to boost the SNR of faint emission lines in Keplerian disks. An independent approach has been the development of stacking techniques. This has been successful to detect the combined signal of faint emission coming from multiple objects of the same population over the electromagnetic spectrum, including the X-ray (Bartelmann and White, 2003; Rodighiero et al., 2015; Yang et al., 2018), UV (Berry et al., 2012; Rigby et al., 2018), infrared (Dole et al., 2006; Duivenvoorden et al., 2020), submm (Webb et al., 2003; Knudsen et al., 2005; Ibar et al., 2013; Millard et al., 2020), and radio (Miller et al., 2013; Bera et al., 2018; Perger et al., 2019) regimes. Moreover, stacking techniques have proven to be a robust method for line and continuum detections of high redshift galaxies (Scoville et al., 2007; Lehmer et al., 2007; Schinnerer et al., 2007; Miller et al., 2008). In order to compute stacked line ratios, in this study we explore three different techniques: two of them in the image plane: i) stacking all the moment-0 maps, ii) stacking all the frequency channels of all sources following a channel by channel basis, and additionally by iii) stacking the individual *uv*-plane average signals.

3.3.1 Image stacking

2D-moment-0 stacking

Based on the previously detected ^{12}CO line widths and intensity peaks, we collapsed the datasets to create moment-0 maps. For this, we measure ^{12}CO line widths using 20 km s^{-1} channel for all galaxies. Using the IMMOMENTS CASA task, we collapse each galaxy cube to create moment-0 maps for all ^{12}CO, ^{13}CO and C^{18}O datasets, around ($\pm 1\times$ FWHM$_{^{12}CO}$) the ^{12}CO, ^{13}CO and C^{18}O expected frequencies. We visually inspected all of the 27 collapsed ^{12}CO images to correct for any possible spatial offsets with respect to the intensity peak. Such offsets exist; optical and submm observations trace the stellar and the molecular gas content of galaxies respectively, and thus the location of the peaks do not necessarily match. Given that the reference coordinates

of our ALMA observations were obtained from optical images, we apply astrometric corrections to our ^{12}CO intensity maps, in order to correct any discrepancy between optical and ^{12}CO images. These corrections are on average of the order of $\sim$ 1.″4 in random directions (smaller than the synthesized beam of 4.″5). Finally, using VSAT, these images were stacked to obtain final collapsed signals reaching rms values of 108 mJy beam^{-1} km s^{-1} for the ^{12}CO line and 18 mJy beam^{-1} km s^{-1} for the ^{13}CO and C^{18}O emission lines. We note that these stacked values are $\sim$ 5 times deeper than individual moment-0 images.

To extract velocity integrated line flux densities from the stacked signals, we create 30″ $\times$ 30″ stamps and model the sources with a 2D Gaussian profile, assuming that the stacked signals are point-like with a FWHM of 4.″5.

3D-image stacking

In this approach, for processing the datacubes, we consider a common spectral channel width for ^{12}CO, ^{13}CO and C^{18}O emission lines. To determine the best common spectral channel width to use, we kept in mind the idea of optimizing the SNR of the final stacked data cubes detections of the lines. For this, datacubes for all of the 27 galaxies were created using CASA task TCLEAN assuming different velocity bin widths: [20, 40, 50, 80, 100, 125, 160, 200, 250, 400, 500, 800] km s^{-1}. After this, we obtained a 3D stacked cube by combining the individual galaxy cubes following a channel by channel and pixel by pixel basis. We then obtained the SNR by measuring the peak at the central image pixel and central velocity channel (0km s^{-1}). We measured the noise in the image excluding the central region. Peak flux densities were recorded for both the mean and median stacked cubes with different velocity width bins and for ^{12}CO, ^{13}CO and C^{18}O data sets. Figure 3.1 shows this central channel SNR as a function of channel velocity width. We find that the ^{12}CO signal maximizes at channel width of 200 km s^{-1} for both the median (SNR$\sim$105.7) and mean (SNR$\sim$96.6). The stacked ^{13}CO line maximizes at 125km s^{-1} (SNR$\sim$8.0) and 500km s^{-1} (SNR$\sim$10.1) for the median and mean, respectively. Finally, the C^{18}O line maximizes at 125km s^{-1} for both the median (SNR$\sim$4.7) and the mean (SNR$\sim$5.5) stacks. Based on these results we decided to use a common spectral channel width of 125 km s^{-1} for ^{12}CO, ^{13}CO and C^{18}O to image all data cubes in order to optimize the signal-to-noise ratio in the final stacked images. We note that the same astrometric offsets used for moment-0 stacking, and described in Section 3.3.1 have been applied here, whilst velocity offsets based on the peak observed in ^{12}CO are applied to all of the independent cubes in order to re-centre the signal. These offsets originate from small differences between the optical and submm redshifts which trace different phases of the ISM.

Using a common channel width of 125 km s^{-1}, a spectral coverage of $\pm$2000km s^{-1}, and a restoring beam with a FWHM of 4.″5, we created the individual datacubes which are then stacked to get a cube containing the average ^{12}CO, ^{13}CO and C^{18}O signals. In order to measure velocity integrated line flux densities, we first created spectral line profiles using a fixed aperture of 15″ radius ($\gtrsim$3$\times$synthesized beam), centred, at the source position. Thereby, we fitted a 1D Gaussian profile to obtain the global stacked velocity line width FWHM$_f$ (see Fig. 3.2 lower panel). Hence, we took the central channel (0km s^{-1}, where the peak in the spectral line profile is located) to fit a 2D Gaussian profile assuming that the signal is point-like (see Fig. 3.2 upper right panel). Finally, the amplitude of the 2D Gaussian fit together with the line width, is used to calculate velocity integrated line flux densities.

Systematic Errors

In order to compute the systematic errors for our stacked velocity integrated line flux density measurements, we ran Monte-Carlo simulations using data cubes with the same physical scales

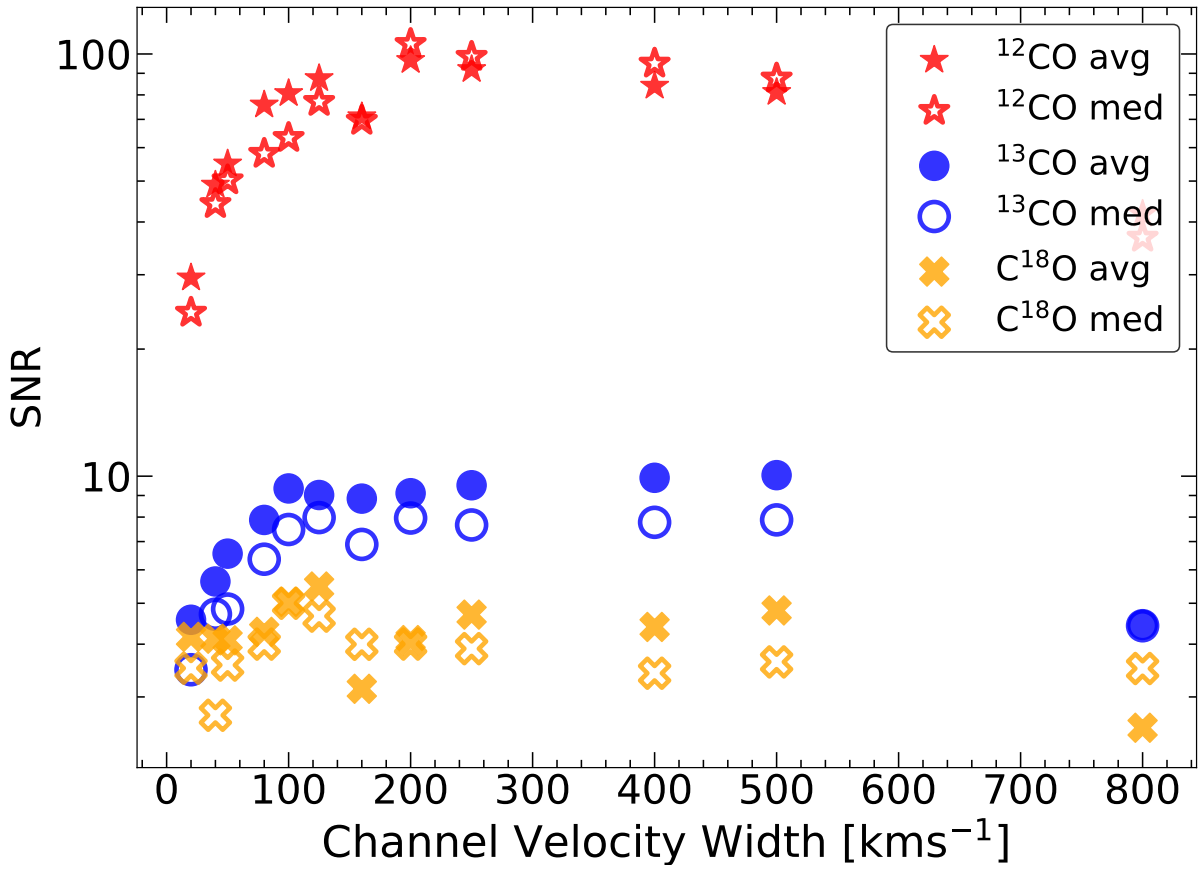

FIGURE 3.1: Stacked signal-to-noise ratios (SNRs) obtained from ^{12}CO (stars), ^{13}CO (circles) and C^{18}O (crosses) using different velocity channel widths, from 20 km s^{-1} to 800 km s^{-1}. Filled symbols correspond to average SNR values while open symbols correspond to median SNR values. These measurements are used to identify the best spectral channel width for 3D stacking (see § 3.3.1).

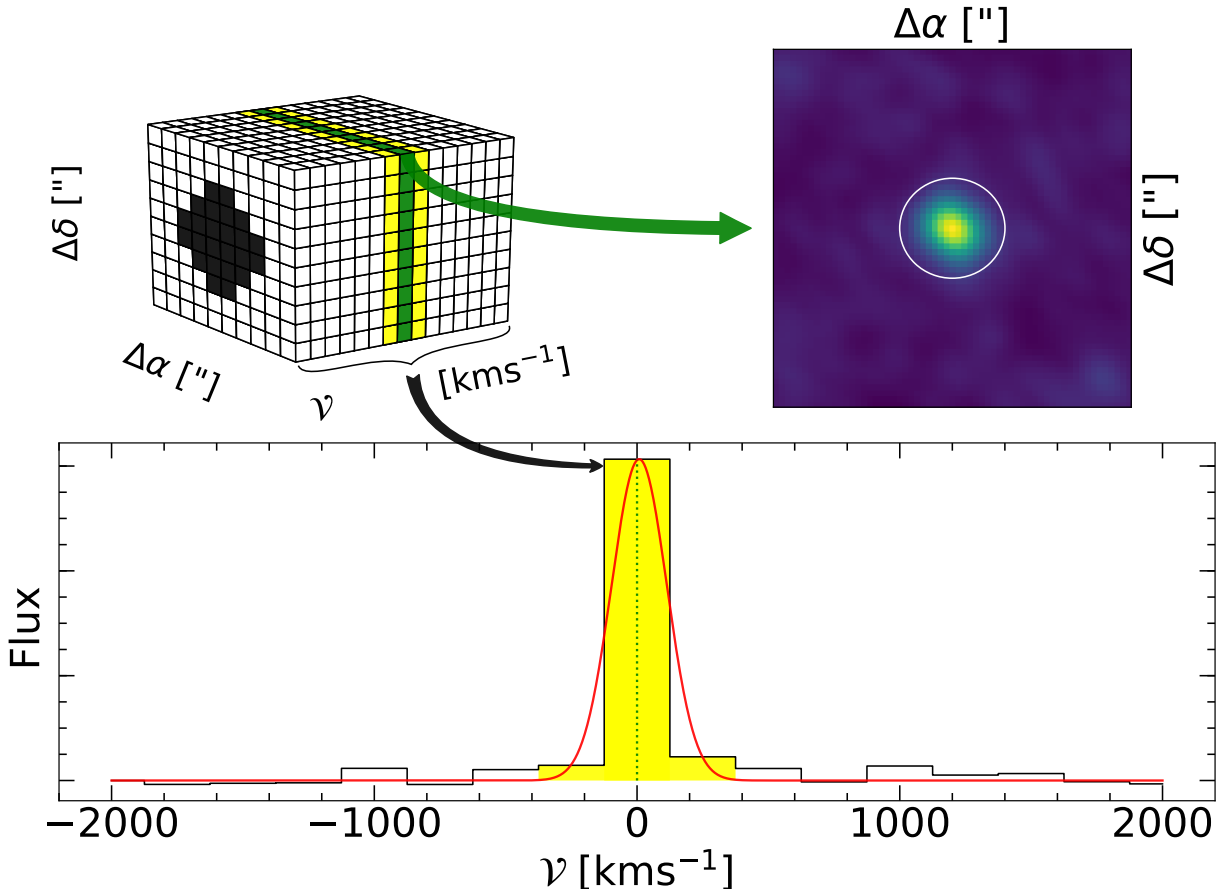

FIGURE 3.2: Velocity integrated flux density measurements on a 3D stacked data cube. Upper left panel: 3D stacked image cube showing the central channel (green) at which the peak of the line is located, the channels covered by the fit FWHM$_f$ line width highlighted in yellow and the 15″ radius aperture (black) used to generate the spectral line profile shown below. The bottom panel shows the spectral line profile (solid black line) and shows the 1D gaussian fit (red line) to obtain the stacked velocity line width FWHM$_f$ highlighted in yellow. The upper right panel shows the central channel where a 2D Gaussian profile is fit (white) to obtain the amplitude of source. Both line width and amplitude are used to compute the velocity integrated line flux densities.

(pixel size, synthesised beam, primary beam) as those covered by the ALMA Band-3 observations.

We model each source as point-like (spatially) using a 2D circular Gaussian profile and spectrally by a 1D Gaussian profile centered at $0\,\mathrm{km\,s^{-1}}$. We simulate a spectral coverage of $\pm 2000\,\mathrm{km\,s^{-1}}$. These sources are added to a random, normally-distributed background noise that has been convolved to the scale of the synthesised beam.

To simulate the stacking, we take 27 data cubes with sources at fixed signal-to-noise ratios (<$\mathrm{SNR_{in}}$>) and fixed velocity line widths. We stacked them and compute the velocity integrated line flux densities as described in Sections 3.3.1 and 3.3.1. We repeat this process 1000 times, where amplitudes and velocity widths are simulated to take fixed values between 0 and 100 times the rms and line FWHMs between 50 and $500\,\mathrm{km\,s^{-1}}$, respectively. The extracted velocity integrated line flux densities (S_{out}) are measured and compared to the input values. Figure 3.3 shows the $<S_{\mathrm{in}}>/S_{\mathrm{out}}$ ratio of 1000 simulated stacked data cubes for both, 2D-moment-0 (open stars) and 3D-image (open circles) stacking methods. The average binned $\overline{<S_{\mathrm{in}}>/S_{\mathrm{out}}}$ ratios (filled symbols in Fig. 3.3) as a function of $\mathrm{SNR_{out}}$ of the composite stack images in the range between zero and 520 ($=100\times\sqrt{27}$). We note that the stacked images have $\mathrm{SNR_{out}}$ that are $\sim\sqrt{27}$ times larger than the average <$\mathrm{SNR_{in}}$> of the individual images given by Poisson factor gained by the stacking approach. For example, if the ^{13}CO stack has a measured $\mathrm{SNR_{out}}$ $\sim$9, then this is produced by individual datacubes with an average <$\mathrm{SNR_{in}}$>$\sim$1.73. Figure 3.3 shows vertical lines indicating three different SNRs values $\sim$6, $\sim$13 and $\sim$18 at which our 3D-stacks show systematic errors of 8%, 3% and 2% while 2D-moment-0 stacks show 5%, 3% and 1%. These results show how typically 2D-stacks show smaller systematic errors than 3D-stacks. These differences tend to become negligible at SNRs>15.

3.3.2 *uv* stacking

Interferometric telescopes provide data that samples the brightness distribution of an observed source in Fourier space, where a point measurement per integration time is provided by a pair of antennas. The location of every point (visibility) in the Fourier space (*uv*-plane) is determined by the separation of a pair of antennas as they trace the track of the source in the Fourier space during integration. The imaging process considers a deconvolution which assumes interpolations made on the *uv*-plane that could lead to artifacts in the extracted images due to the intrinsic non-continuous sampling nature of interferometric datasets (Condon and Ransom, 2016). Interferometric stacking analyses are usually performed using these reconstructed images. Lindroos et al. (2015) developed *stacker* [2], a tool which directly stacks interferometric continuum datasets in the *uv*-plane providing typical signal-to-noise ratios which are 20% higher compared with continuum image stacking. *Stacker* was designed to perform the stacking analysis for continuum *uv*-data, therefore, we mimic continuum maps as the average single channel maps of the ^{12}CO, ^{13}CO and C^{18}O emission lines intensity data of the galaxies. To create individual single channel maps we use the CASA task SPLIT to obtain an average *uv*-data of the channels around the ^{12}CO line observed frequency ($\pm 1\times$ $\mathrm{FWHM_{^{12}CO}}$). As described in Section 3.3.1, ^{12}CO line widths were measured using a $20\mathrm{km\,s^{-1}}$ resolution, and these widths were also used to create the individual single channel maps for the ^{13}CO and C^{18}O datasets. Similarly to previous approaches, we note that we have applied the same astrometric offset corrections to generate the single channel *uv* maps. To measure velocity integrated line flux densities from the *uv* stacks, we create images using CASA task TCLEAN following a similar approach as the images used for 2D and 3D-image stacking procedures. Then, as in 2D-stacks, we model the sources with a 2D Gaussian profile and measured the velocity integrated line flux densities from $30'' \times 30''$ stamps.

[2] https://www.oso.nordic-alma.se/software-tools.php

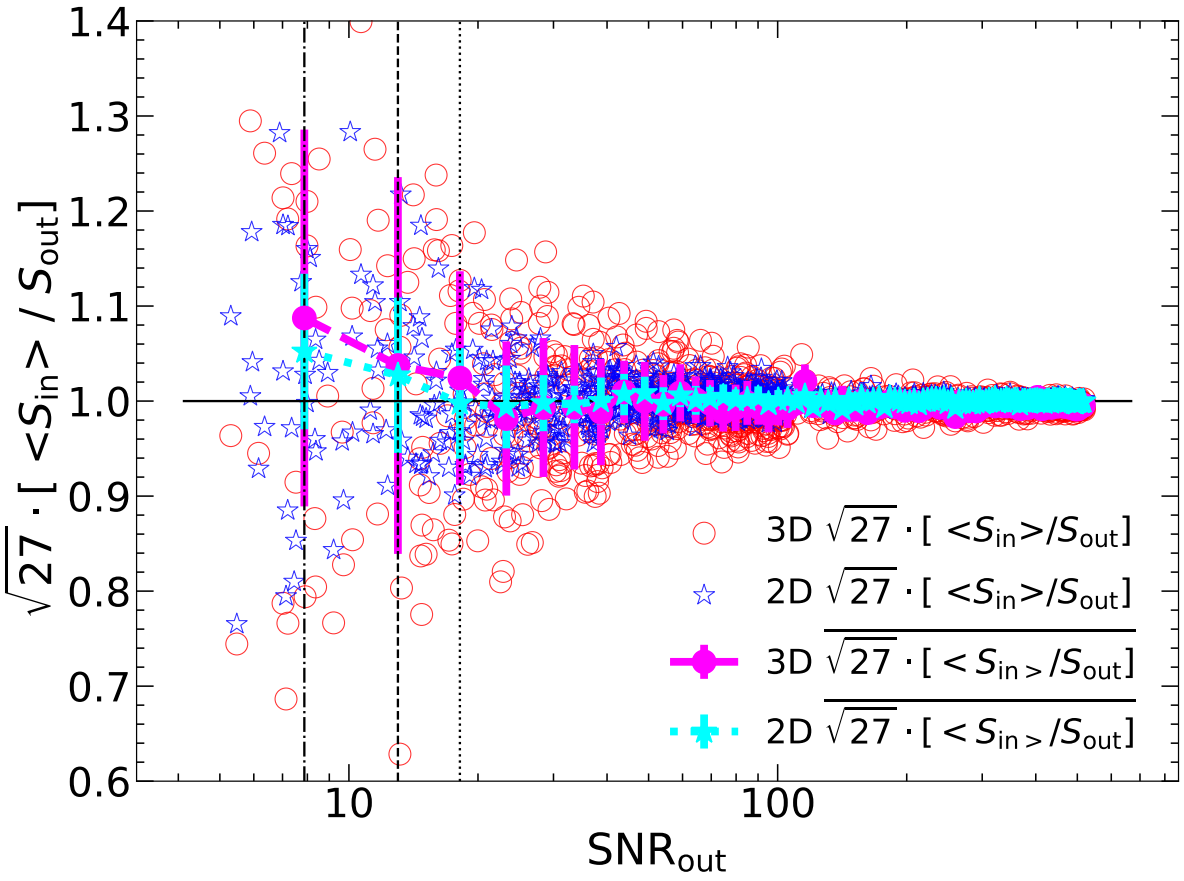

FIGURE 3.3: Simulated accuracy of the velocity integrated flux density measurements ($<S_{in}>/S_{out}$) after stacking 27 galaxies. Stacked detections with high SNR$_{out}$ have clearly better accuracy for the velocity integrated flux density measurements. $<S_{in}>$ refers to the average velocity integrated flux densities of the simulated sources used for the stacks, while S_{out} refers to the measured velocity integrated flux density on the composite stacked images. 3D stacks are shown as open circles, 2D moment-0 stacks are shown as open stars and filled symbols indicate the average $\overline{<S_{in}>/S_{out}}$ binned by SNR$_{out}$. Vertical lines indicate the location of our ^{12}CO, ^{13}CO and C^{18}O SNR$_{out}$ stacked detections at ∼6 (dashed-dotted), ∼13 (dashed) and ∼18 (dotted) where 3D-image stacks show systematic errors of 8%, 3% and 2% while 2D-moment-0 stacks show 5%, 3% and 1% respectively.

TABLE 3.3: Signal-to-noise Ratio (SNR) detection for ^{12}CO, ^{13}CO and C^{18}O stacked line emission, obtained from three different stacking methods explored in this work 1) 2D-moment-0 stacking, 2) 3D-image stacking and 3) *uv* stacking.

SNR	Moment-0	*uv*-stacking	3D-stacking
^{12}CO	41.9	71.1	105.3
^{13}CO	15.1	12.9	9.5
C^{18}O	5.0	5.2	5.4

3.3.3 The differences between the stacking approaches

In this section we discuss the stacking approaches described above in order to decide the most suitable one for our work. As mentioned before, each method is based on different assumptions, therefore, a direct comparison is not entirely trivial. For example, the images obtained from 2D-stacking are generated using CASA task IMMOMENTS which basically sums the intensities of the channels around $\pm 1\times$ FWHM$_{^{12}\mathrm{CO}}$ for the ^{12}CO observed frequency, while the ^{13}CO and C^{18}O lines are blindly extracted at the expected frequencies using the derived ^{12}CO redshifts. The 3D approach concentrates mainly on highlighting the intensities from the central channel of data cubes, where the velocity peak of the flux density profile is located. The case for the stacks obtained from a *uv* approach are constructed starting from CASA task SPLIT, which averages the *uv* intensities of the channels where the lines are located, these channels are exactly the same as those channels used to create the moment-0 maps for 2D-stacking.

In Fig. 3.4 we show 30"×30" image stacks and residuals after point-source extraction for the three methods explored in this work. All three different approaches result in similar velocity integrated line flux densities within the errors. However, we find that for a bright line like ^{12}CO *uv* stacks shows a SNR ∼1.6 times higher than that obtained from 2D stacking method (see Table 3.3). This result is similar to that found by Lindroos et al. (2015), who reported that continuum *uv* stacking signal-to-noise ratio was up to 20% higher than the continuum image stacking. Nevertheless, we find that for ^{12}CO 3D-image stacking shows to be the method with the highest SNR, being 2.5 and 1.6 times higher than 2D-moment-0 stacking and *uv* stacking SNRs respectively. On the other hand, the 3D stacking method shows the lowest SNR for the faint lines like ^{13}CO, while the 2D-moment-0 and *uv* stacking methods show similar SNRs. We note that, all the stacking methods applied on C^{18}O emission line show similar SNRs. Even though *stacker* was specially designed to stack *uv* continuum datasets and it has been successfully applied for *uv* emission line stacking (Fujimoto et al., 2018; Fujimoto et al., 2019; Fudamoto et al., 2020; Carvajal et al., 2020) using a similar procedure as described here, this is the first time that *uv* and image stacking methods for emission line observations are directly compared. Driven by the previously available ^{12}CO data presented in Villanueva et al. (2017), we decide to use the 2D (moment-0) approach to measure values, as this method yields the highest ^{13}CO stacked SNRs that are straightforward to interpret and simple to calculate.

3.3.4 Luminosity measurements

We compute the ^{12}CO, ^{13}CO and C^{18}O luminosities using the velocity integrated line flux densities following (Solomon and Vanden Bout, 2005):

$$L'_{\mathrm{CO}} = 3.25 \times 10^7 S\Delta v \nu_{\mathrm{obs}}^{-2} {D_{\mathrm{L}}}^2 (1+z)^{-3} \tag{3.1}$$

where L'_{CO} is measured in K km s^{-1} pc^2, $S\Delta$v is the velocity integrated line flux density in units of Jy km s^{-1}, ν_{obs} is the observed frequency of the emission line in GHz, D_{L} is the luminosity distance in Mpc, and z is the redshift.

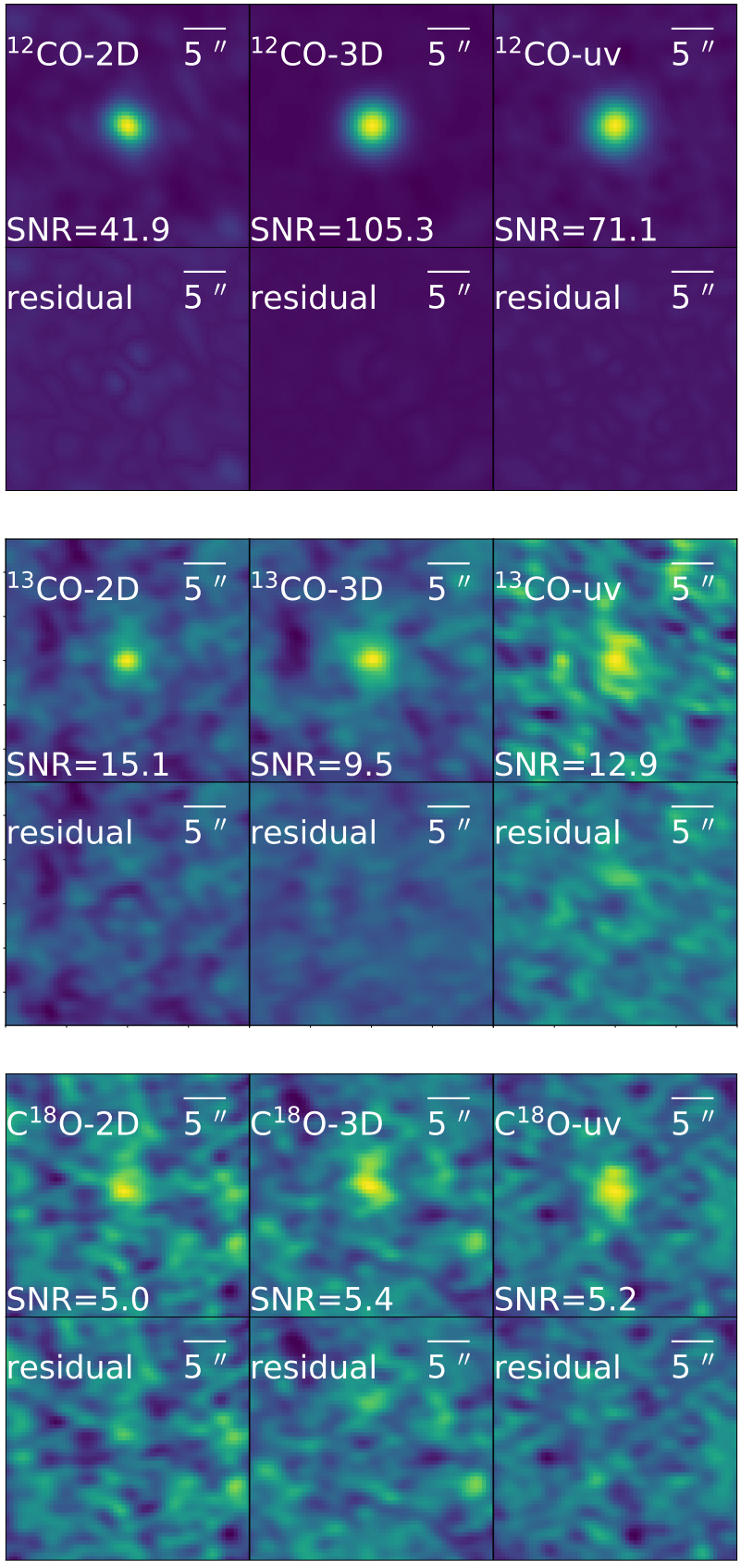

FIGURE 3.4: Final composite 30"×30" stamps stacks (top) and residuals (bottom) from the corresponding flux modelling (see Section 3.3) for ^{12}CO (upper panels), ^{13}CO (middle panels) and C^{18}O (lower panels) emission lines from 2D-moment-0 stack (left column), 3D-image stack (middle column) and *uv* stack (right column).

Considering the fact that we are analysing average properties from galaxies at different redshifts, special consideration should be taken to convert to intrinsic luminosities. To determine the dispersion of the stacked luminosity measurements we have used a Monte Carlo simulation considering that the error from the velocity integrated line flux density measurements is normally distributed and, at the same time, assume a random sampling for the redshift distribution of the parent stacked sample. Repeating this simulation, we get a distribution of luminosities from which we can then infer the 1σ confidence intervals (CI) of our average luminosity measurements. Since each galaxy population has a different redshift distribution, their CIs are independent from one population to another. We note that the differences between intensity and luminosity ratio measurements are negligible. The luminosity ratio of any pair of lines (L'_1, L'_2) comes from converting their fluxes into luminosities following Equation 3.1. Given that the redshifts (z_1, z_2) for both lines are the same, the redshift and luminosity distance dependencies vanish leading to Equation 3.2.

$$\frac{L'_1}{L'_2} = \frac{S_1 \Delta v_1 \nu_1^{-2} D_{L_1}^{-2} (1+z_1)^{-3}}{S_2 \Delta v_2 \nu_2^{2} D_{L_2}^{2} (1+z_2)^{-3}} = \frac{I_1 \nu_1^{-2}}{I_2 \nu_2^{-2}} \tag{3.2}$$

In particular, $L'(^{12}\mathrm{CO})/L'(^{13}\mathrm{CO}) = 0.91 \times I(^{12}\mathrm{CO})/I(^{13}\mathrm{CO})$ and $L'(^{13}\mathrm{CO})/L'(\mathrm{C}^{18}\mathrm{O}) = 0.99 \times I(^{13}\mathrm{CO})/I(\mathrm{C}^{18}\mathrm{O})$, which enable us to make direct comparisons between our results and different intensity and luminosity ratios available in the literature.

3.4 Results

3.4.1 The $L'(^{12}\mathrm{CO})/L'(^{13}\mathrm{CO})$ ratio

The VALES survey provides a wide range of global galaxy properties such as stellar masses, star formation rates, morphologies, luminosities etc. In this section, we present the measured $L'(^{12}\mathrm{CO})/L'(^{13}\mathrm{CO})$ luminosity ratios to search for possible dependencies on different global galaxy parameters.

Morphological and environmental dependence

A morphological and environmental dependence of the $I(^{12}\mathrm{CO})/I(^{13}\mathrm{CO})$ line intensity ratio has been reported by previous studies. While merger systems show a higher $I(^{12}\mathrm{CO})/I(^{13}\mathrm{CO})$ intensity ratio when compared with normal spiral galaxies (Casoli, Dupraz, and Combes, 1992b; Taniguchi and Ohyama, 1998; Taniguchi, Ohyama, and Sanders, 1999), galaxies in dense environments show a lower $I(^{12}\mathrm{CO})/I(^{13}\mathrm{CO})$ intensity ratio (Alatalo et al., 2015). Initially, we explore the morphological and environmental classification available for our sample, according to the most prominent morphological features: Bulge (B), Disc (D), Merger-Irregular (M), and (C) which denotes if the source has multiple projected neighbouring systems ("companions"), as based on a visual inspection presented by Villanueva et al. (2017) to multi-wavelength imaging from the GAMA survey.

We split our sample into 5 different subsets: 0) all galaxies; (n=27; open symbols), 1) all galaxies excluding clear mergers (B, D, BC, DC; n=24); 2) bulge and disc dominated galaxies with projected companions (BC, DC; n=8); 3) bulge and disc dominated galaxies without any companion (B, D; n=16); and 4) mergers (M; n=3) (see Figure 3.5).

In Table 3.4 we present the measured average $L'(^{12}\mathrm{CO})/L'(^{13}\mathrm{CO})$ line luminosity ratio and average <SFR>, <SFE>, and $\langle L_{\mathrm{IR}} \rangle$ values for the five different morphological galaxy populations explored in this work. Using all of the 27 galaxies, we find an average $L'(^{12}\mathrm{CO})/L'(^{13}\mathrm{CO})$ line luminosity ratio of 16.1 ± 2.5. This value is in agreement with the values for mergers (12 ± 3)

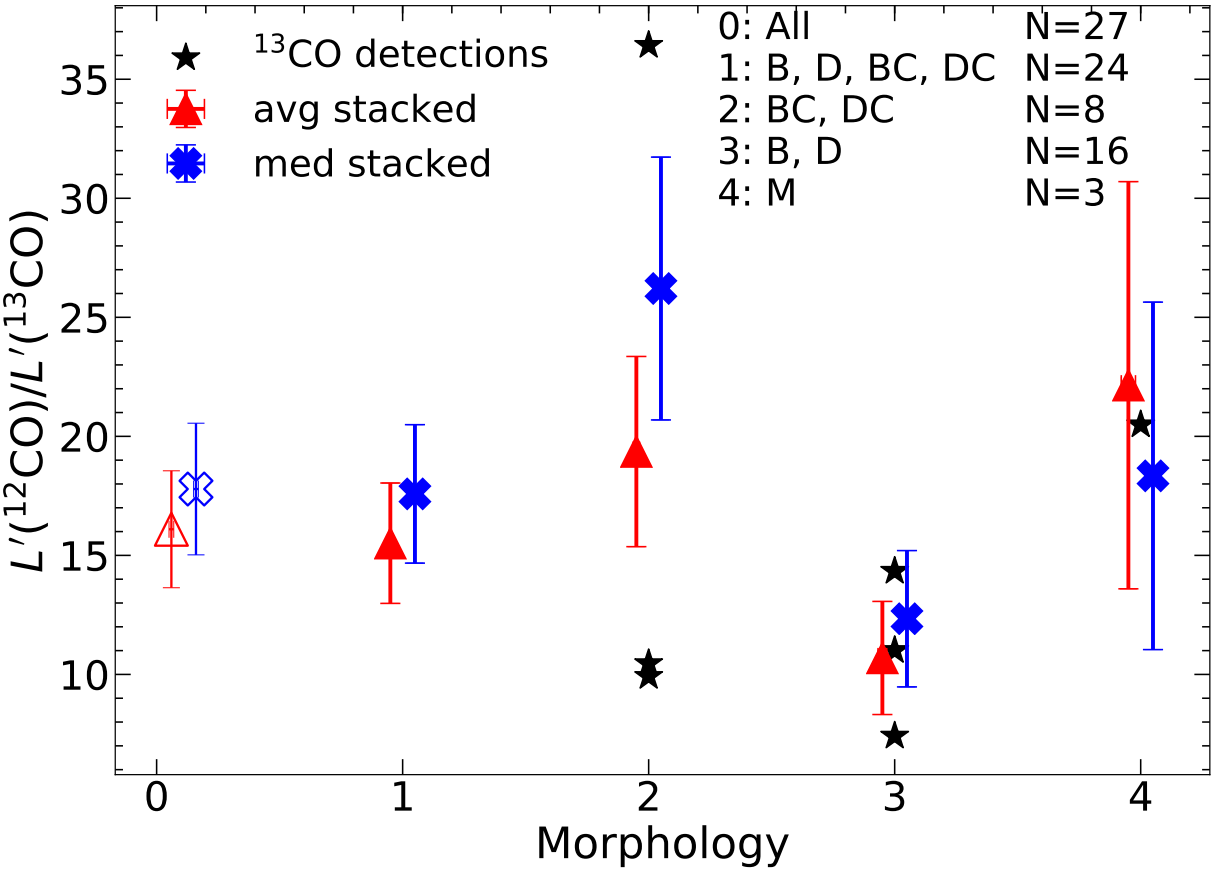

FIGURE 3.5: Average (red triangles) and median (blue crosses) stacked $L'(^{12}CO)/L'(^{13}CO)$ line luminosity ratio values as a function of optical morphological properties as presented in Villanueva et al. (2017): 0) all galaxies (n=27) open symbols, 1) all galaxies excluding mergers (B, D, BC, DC; n=24); 2) bulge and disc dominated galaxies with projected companions (BC, DC; n=8); 3) bulge and disc dominated galaxies without any companion (B, D; n=16); and 4) mergers (M; n=3). Error bars correspond to 1 σ confidence intervals for average ratios.

TABLE 3.4: Average $L'(^{12}CO)/L'(^{13}CO)$ line luminosity ratio and average <SFR>, <SFE> and $<L_{IR}>$ values for different morphological classifications explored in this work (Villanueva et al. 2017; see § 3.4.1 for more details).

ID	Group	N	$L'(^{12}CO)/L'(^{13}CO)$	<SFR> $M_\odot yr^{-1}$	<SFE> Gyr^{-1}	$<\log[L_{IR}/L_\odot]>$
0	All	27	16.1 ± 2.5	14.9 ± 3.8	1.9 ± 0.5	10.9 ± 0.5
1	BC,DC,B,D	24	15.5 ± 2.5	12.7 ± 4.2	0.9 ± 0.1	10.8 ± 0.5
2	BC,DC	16	19.4 ± 4.0	17.6 ± 5.9	1.0 ± 0.1	11.0 ± 0.5
3	B,D	8	10.7 ± 2.4	3.4 ± 0.5	0.8 ± 0.1	10.5 ± 0.2
4	M	3	22.1 ± 8.6	34 ± 6.9	9.6 ± 0.8	11.5 ± 0.2

and interacting early type galaxies (ETGs) (15±5) reported by Alatalo et al. (2015), and to the ratio of nearby spirals, starburst and ETGs (excluding those belonging to the Virgo Cluster used by Alatalo et al. 2015) reported by Davis (2014) (12±1.0). Mergers and galaxies with a visible companion tend to show higher $L'(^{12}CO)/L'(^{13}CO)$ line luminosity ratios. In particular, mergers show the highest <SFR>, <SFE>, and $<L_{IR}>$ average values among the different morphological classifications, and also show a $L'(^{12}CO)/L'(^{13}CO)$ line luminosity ratio 2 times higher than that found in galaxies without a companion. These findings, however, are at low significance (mainly due to the low number statistics). Besides, these ratios are in good agreement with the ratios reported by Alatalo et al. (2015), who found that group galaxies present $L'(^{12}CO)/L'(^{13}CO)$ line luminosity ratios 2 times higher than field galaxies.

The star-formation activity

Villanueva et al. (2017) derived various global galaxy properties, including star formation rate (SFR), star formation efficiency (SFE), molecular gas surface density (Σ_{H_2}), star formation rate surface density (Σ_{SFR}), stellar mass ($M_\star$), gas depletion time (τ), and projected size (R_{FWHM}). The total IR luminosity was obtained as described in Ibar et al. (2015) by integrating the best-fitting SED between 8 and 1000 μm using photometry from IRAS, Wide-field Infrared Survey Explorer (WISE), and *Herschel*. The star formation rate was estimated following SFR ($M_\odot yr^{-1}$) = $10^{-10} \times L_{IR}$ assuming a Chabrier (2003) IMF. The molecular gas mass was computed using L'_{CO} and assuming an α_{CO} conversion factor dependent on the morphological classification ($\alpha_{CO} = 4.6$ K km s^{-1} pc^2 for B and D dominated galaxies and $\alpha_{CO} = 0.8$ K km s^{-1} pc^2 for mergers/interacting galaxies). The SFR and M_{H_2} surface densities were estimated by dividing the measured values by the area of a two-sided disc ($2\pi R^2_{FWHM}$), where R_{FWHM} is the deconvolved FWHM along the semimajor axis obtained through fitting elliptical Gaussian profiles to the ^{12}CO $(1-0)$ moment-0 maps using the CASA task IMFIT. We consider the CO emission to be spatially resolved if the fitted semimajor axis is at least $\sqrt{2}$ times larger than the semimajor axis of the synthesized beam. A more detailed discussion about the computations of these parameters can be found in Villanueva et al. (2017). With these in hand, we looked for possible dependencies of $L'(^{12}CO)/L'(^{13}CO)$ luminosity line ratio on these global galaxy properties by splitting our sample in two bins for each parameter. Figure 3.6 shows the redshift, L_{IR}, SFR, SFE, Σ_{SFR} and Σ_{H_2} distributions, split into low and high values. We find that the most significant trends for the $L'(^{12}CO)/L'(^{13}CO)$ ratios are with L_{IR}, SFR, and SFE (see Figures 3.7 and 3.8). Table 3.5 shows the average $L'(^{12}CO)/L'(^{13}CO)$ line luminosity ratios for low and high L_{IR}, SFR, SFE, Σ_{SFR} and Σ_{H_2} populations.

Figure 3.7 shows a trend of $L'(^{12}CO)/L'(^{13}CO)$ line luminosity ratio with L_{IR} similar to that shown by Taniguchi and Ohyama (1998) who used ^{12}CO and ^{13}CO line data taken from the literature for 61 nearby galaxies, including eight luminous starburst galaxies. They found a correlation between L_{FIR} and $L'(^{12}CO)/L'(^{13}CO)$ line ratio, where starburst galaxies with high infrared luminosities show higher ($L'(^{12}CO)/L'(^{13}CO) \geq 20$) line ratios compared with normal galaxies.

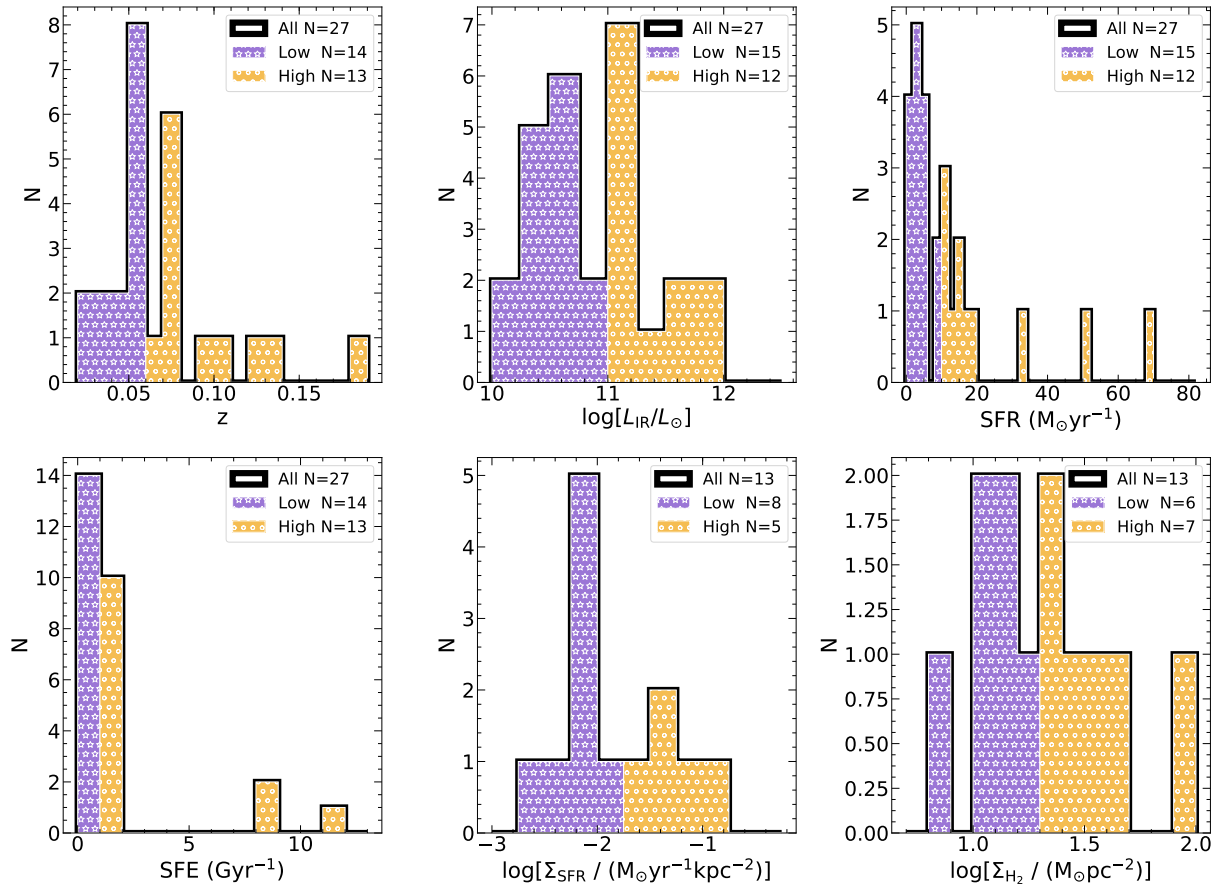

FIGURE 3.6: Redshift, L_{IR}, SFR, SFE, Σ_{SFR} and Σ_{H_2} distributions of the galaxies used in the ^{12}CO and ^{13}CO stacking analysis (solid black line), split into low (purple bars hatched with stars) and high (yellow bars hatched with circles) values.

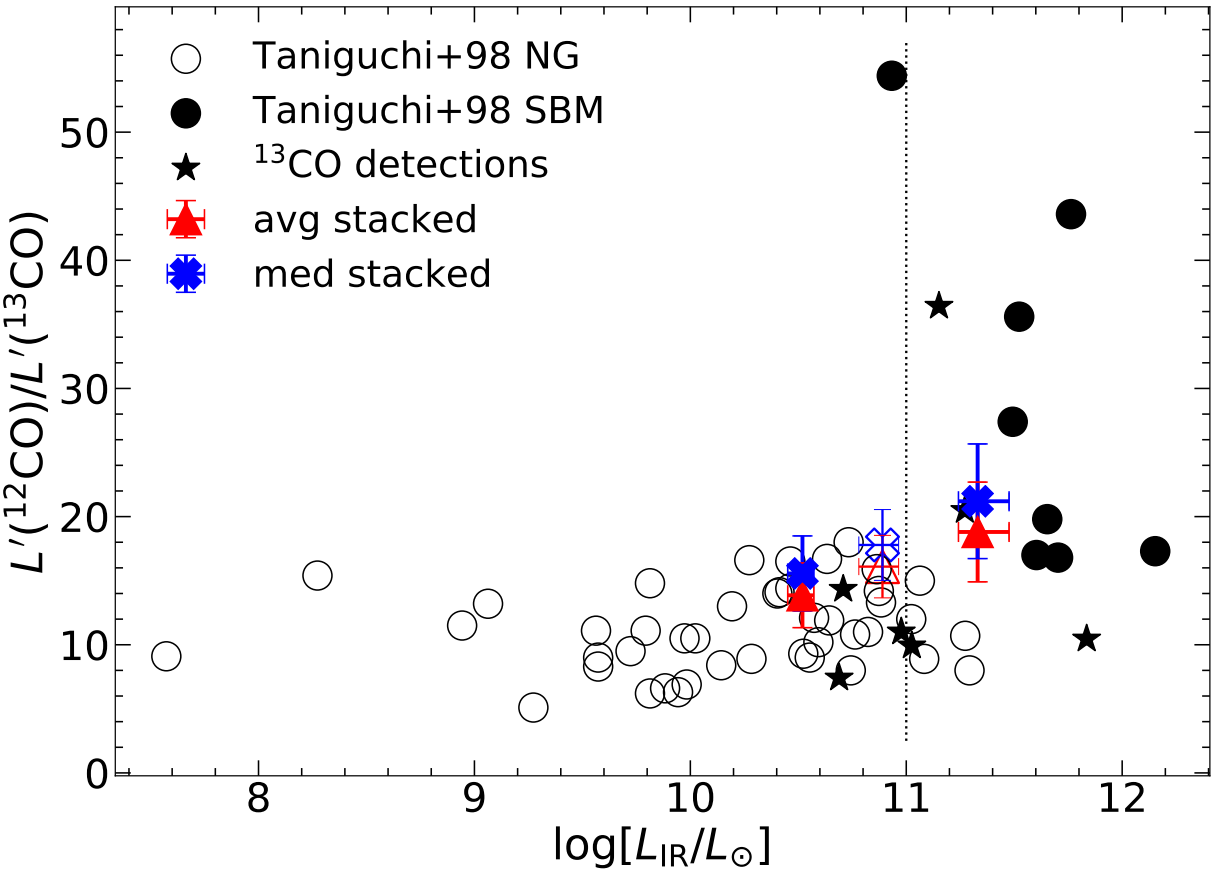

FIGURE 3.7: Average (red triangles) and median (blue crosses) stacked $L'(^{12}CO)/L'(^{13}CO)$ line luminosity ratio for low and high L_{IR} subsets (triangles). A dashed line indicates the boundary between low and high L_{IR} populations. As reference, average and median line luminosity ratio considering all galaxies in open symbols are included. Error bars correspond to 1σ confidence intervals for average or median values based Monte-Carlo simulations. Individual ^{13}CO detections (stars) and $L'(^{12}CO)/L'(^{13}CO)$ line luminosity ratios of normal galaxies (NG open circles) and starburst mergers (SBM filled circles) scaled by a 1.75 factor to convert from far-IR to IR luminosities (see Appendix E from Herrera-Camus et al. 2015) from Taniguchi and Ohyama (1998) are also included.

TABLE 3.5: Average $L'(^{12}CO)/L'(^{13}CO)$ line luminosity ratio for our sample of galaxies split into high and low L_{IR}, SFR, SFE, Σ_{SFR} and Σ_{H_2} values. Column 1: parameter of interest; column 2: range explored; column 3: number of galaxies in the explored range; column 4: average value for parameter of interest; column 5: the average stacked $L'(^{12}CO)/L'(^{13}CO)$ line luminosity ratio; column 6 and 7: student's t-test statistical reports (t, p) to asses the probability (p) that the null hypothesis ($L'(^{12}CO)/L'(^{13}CO)$ line luminosity ratio variations between the low and high SFR populations is not statistically significant), is true.

Parameter	Range	N	Average	$L'(^{12}CO)/L'(^{13}CO)$	t-test	
					t	p
1	2	3	4	5	6	7
$\log[L_{IR}/L_\odot]$	[10.1 - 10.9]	14	10.5 ± 0.1	13.8 ± 2.4	-3.9	0.0006
	[11.0 - 11.9]	13	11.3 ± 0.1	18.7 ± 3.9		
SFR ($M_\odot yr^{-1}$)	[1.8 - 9.5]	15	3.9 ± 0.6	13.3 ± 2.4	-4.3	0.0002
	[10.3 - 83.4]	12	28.6 ± 5.3	18.7 ± 3.8		
SFE (Gyr^{-1})	[0.4 - 0.9]	14	0.6 ± 0.1	12.9 ± 2.7	-4.7	7E-05
	[1 - 11.7]	13	3.3 ± 0.6	19.4 ± 4.2		
$\log[\Sigma_{SFR}$ / $(M_\odot yr^{-1}kpc^{-2})]$	[-2.6 - -1]	13	-1.8 ± 0.1	12.5 ± 2.4	-0.05	0.9
	[-2.6 - -2]	8	-2.2 ± 0.1	12.2 ± 3.1		
	[-2.1 - -1]	5	-1.3 ± 0.1	12.3 ± 3.5		
$\log[\Sigma_{H_2}$ / $(M_\odot pc^{-2})]$	[0.8 - 2.0]	13	1.3 ± 0.1	12.5 ± 2.5	-0.5	0.6
	[0.8 - 1.2]	6	1.0 ± 0.1	11.8 ± 3.2		
	[1.3 - 2.0]	7	1.6 ± 0.2	12.8 ± 3.5		

They dismissed physical gas properties such as density, temperature, or velocity gradients as responsible for the observed high $L'(^{12}CO)/L'(^{13}CO)$ abundance ratio in starburst galaxies and conclude that the only possible mechanism behind the high $^{12}CO/^{13}CO$ abundance ratio in starburst galaxies is an underabundance of ^{13}CO with respect to ^{12}CO. Our stacks (see Figure 3.7) show a trend in which the high L_{IR} sample falls in the starburst region, while the low L_{IR} sample shows an average $L'(^{12}CO)/L'(^{13}CO)$ line luminosity ratio similar to that found in normal galaxies.

To test the significance of the $L'(^{12}CO)/L'(^{13}CO)$-L_{IR} variations we applied a Student's t-test to determine the probability that the $L'(^{12}CO)/L'(^{13}CO)$ line luminosity ratio variations between the low and high L_{IR} populations are not statistically significant. A large p-value indicates that the differences between the two sample means are not statistically significant, while a small one suggests that the differences between the two sample means are significant. Based on this test, we find that the differences in the $L'(^{12}CO)/L'(^{13}CO)$-L_{IR} variations are statistically significant (see Table 3.5). We then implemented a Spearman rank test to investigate a possible $L'(^{12}CO)/L'(^{13}CO)$-L_{IR} correlation, where p-values report the probability of the lack of correlation between the two samples. A large p-value indicates that there is no significant correlation, while a small one suggests a significant correlation. The Spearman rank test was computed considering six galaxies (excluding HATLASJ090949.6 identified as an outlier see Section 3.4.1) with individual ^{13}CO detections, for which we could compute individual $L'(^{12}CO)/L'(^{13}CO)$ luminosity ratios. The Spearman rank test does not provide evidence (see Table 3.6 first row) supporting a significant correlation between $L'(^{12}CO)/L'(^{13}CO)$ and L_{IR}. This might be due to the reduced number (6) of galaxies with individual ^{13}CO detections covering a small range of L_{IR}. However, if we also consider starburst galaxies and normal galaxies covering a wider range of L_{FIR} as reported by Taniguchi and Ohyama (1998), we find (see Table 3.6 second row) evidence supporting a moderate $L'(^{12}CO)/L'(^{13}CO)$-L_{IR} correlation.

TABLE 3.6: Spearman correlation test statistic (ρ, p), to asses the null hypothesis (no significant correlation between $L'(^{12}CO)/L'(^{13}CO)$ and L_{IR}) being true, for 1) 6 galaxies with ^{13}CO individual detections for which we could compute individual $L'(^{12}CO)/L'(^{13}CO)$ luminosity ratios and 2) 6 galaxies with ^{13}CO individual detections plus 61 starburst and normal galaxies reported by Taniguchi and Ohyama (1998).

Sample	N	ρ	p
1) Galaxies with ^{13}CO detections	6	0.71	0.14
2) + Starburst and Normal galaxies	67	0.55	4E-6

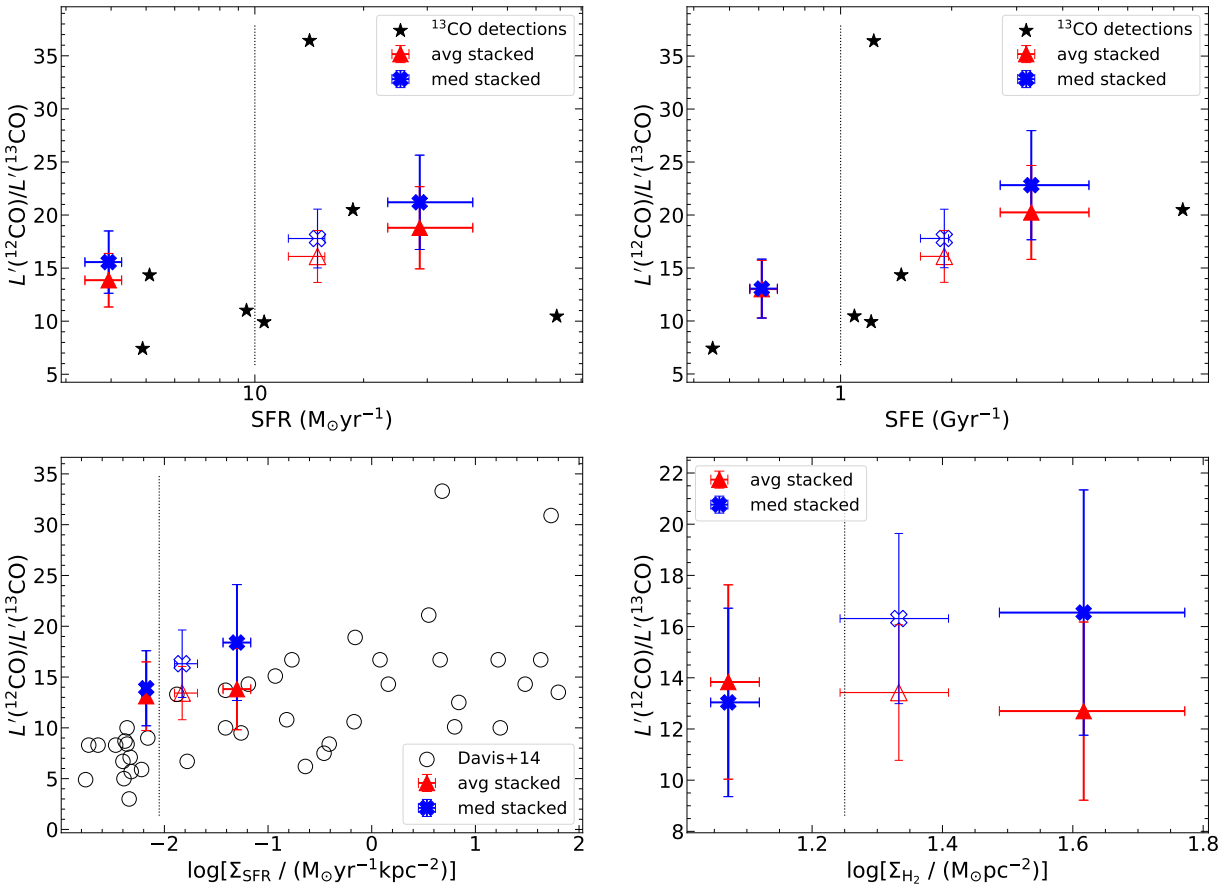

FIGURE 3.8: Average (red triangles) and median (blue crosses) stacked $L'(^{12}CO)/L'(^{13}CO)$ line luminosity ratio for low and high SFR (upper left), SFE (upper right), Σ_{SFR} (lower left) and Σ_{H_2} (lower right) subsets (triangles). As reference, average and median line luminosity ratio considering all galaxies in open symbols and dashed lines indicating the boundary between low and high SFR, SFE, Σ_{SFR} and Σ_{H_2} populations are included. Error bars correspond to 1σ confidence intervals for average or median values based on Monte-Carlo simulations. Individual ^{13}CO detections (stars) and $I(^{12}CO)/I(^{13}CO)$ line intensity ratio of normal galaxies (open circles) from Davis (2014) are also included.

TABLE 3.7: Average values of various galaxy parameters (column 1): redshift, molecular gas mass (M_{H_2}), molecular gas mass to stellar mass ratio ($M_{H_2}/M_\star$), and molecular gas fraction (f_{H_2} = M_{H_2} / (M_{H_2}+$M_\star$)) for the sample after splitting it in low (column 2) and high (columns 3) SFR values. Columns 4 and 5 contain the Kolmogorov-Smirnov statistical reports (D, p) to asses the probability that low and high (z, $M_{H_2}/M_\star$ and f_{H_2}) were drawn from populations with identical distributions.

	SFR [$M_\odot yr^{-1}$]			
Parameter	low	high	KS	
	N = 15 [1.8-9.5]	N = 12 [10.3-83.4]	D	p
1	2	3	4	5
<z>	0.04 ± 0.01	0.10 ± 0.04	0.8	0.0001
<log[$M_{H_2}/M_\odot$]>	8.9 ± 0.6	10.1 ± 0.1	0.5	0.03
<$M_{H_2}/M_\star$>	0.17 ± 0.04	0.53 ± 0.18	0.6	0.02
<f_{H_2}>	0.14 ± 0.06	0.28 ± 0.15	0.55	0.02

Figure 3.8 (upper panels) shows $L'(^{12}CO)/L'(^{13}CO)$ line luminosity ratio trends with SFR and SFE. Considering that SFRs are derived from far-IR luminosities, an expected trend in SFR is also identified (see Fig. 3.7). We also find that the higher the SFE (SFR/M_{H_2}), the higher the $L'(^{12}CO)/L'(^{13}CO)$ line luminosity ratio, following an expected similar trend as with SFR. By looking at the stacked signals, we find significant variations of the $L'(^{12}CO)/L'(^{13}CO)$ line luminosity ratio when we split our sample by low and high SFR values (see Table 3.7). We notice that galaxies with high SFR not only show high $L'(^{12}CO)/L'(^{13}CO)$ luminosity ratio, but also relatively high reservoirs of molecular gas. Table 3.7 shows the average values of redshift, molecular gas mass (M_{H_2}), molecular gas mass to stellar mass ratio ($M_{H_2}/M_\star$), and molecular gas fraction (f_{H_2} = M_{H_2} / (M_{H_2}+$M_\star$)) for our galaxy sample after splitting into low and high SFR values. To estimate the significance of the observed differences between the average properties (M_{H_2}, $M_{H_2}/M_\star$, f_{H_2}) in the low and high SFR populations, we applied a Kolmogorov-Smirnov (KS) test to compute the probability that low and high (z, $M_{H_2}/M_\star$, $M_{H_2}/M_\star$ and f_{H_2}) distributions were drawn from from the same parent population. A large p-value indicates that the distributions are identical, while a small one suggests that the distributions are different. In all cases we find evidence to reject the null hypothesis that the observed properties in the low and high SFR populations were drawn from the same parent population (see Table 3.7).

We perform a similar analysis to the one described by Davis (2014) that reported a positive correlation of the $I(^{12}CO)/I(^{13}CO)$ line intensity ratio with Σ_{SFR} and Σ_{H_2}. In our case, only 13 galaxies are known to be resolved in ^{12}CO, enabling us to derive Σ_{SFR} and Σ_{H_2}. In Figure 3.8 (lower panels) we show the $L'(^{12}CO)/L'(^{13}CO)$ line luminosity ratio as a function of Σ_{SFR} split into high ($10^{-2.1}$–$10^{-1}\,M_\odot yr^{-1}\,kpc^{-2}$) and low ($10^{-2.6}$–$10^{-2}\,M_\odot yr^{-1}\,kpc^{-2}$) values. Individual ^{13}CO galaxy detections from Davis (2014) are also over-plotted. Concerning the dependencies of $L'(^{12}CO)/L'(^{13}CO)$ as a function of Σ_{H_2}, when we split into low ($10^{0.8}$–$10^{1.3}\,M_\odot\,pc^{-2}$) and high ($10^{1.3}$–$10^{-2}\,M_\odot\,pc^{-2}$) values, a moderate trend is found.

We applied a Student's t-test to evaluate the probability that the null hypothesis (i.e. that the $L'(^{12}CO)/L'(^{13}CO)$ line luminosity ratio variations between the low and high SFR, SFE, Σ_{SFR} and Σ_{H_2} populations are not statistically significant), is true. We find supporting evidence that $L'(^{12}CO)/L'(^{13}CO)$ variations between low and high SFR and SFE populations are statistically significant. On the other hand, we do not find evidence that supports that $L'(^{12}CO)/L'(^{13}CO)$ variations between low and high Σ_{SFR}, Σ_{H_2} populations are not statistically significant (see Table 3.5). The lack of a significant difference of $L'(^{12}CO)/L'(^{13}CO)$ with both Σ_{SFR} and Σ_{H_2} shown in the lower panels of Figure 3.8 is most probably due to the reduced number of galaxies used

TABLE 3.8: ^{13}CO stacked continuum emission split into low and high SFR populations.

	SFR [$M_\odot yr^{-1}$]		
Parameter	All	low	high
	N = 27	N = 15	N = 12
		[1.8-9.5]	[10.3-83.4]
SNR	13	6	15
$S_{^{13}CO}\Delta v$ [μJy km s^{-1}]	82 ± 6	64 ± 10	110 ± 7

for Σ_{SFR} and Σ_{H_2} stacks and the relatively small range of surface densities explored in this work. Finally, we note that we did not find any significant variations of $L'(^{12}CO)/L'(^{13}CO)$ with redshift and stellar mass, as with Σ_{H_2}. This might be caused by the relatively small range of redshift ([0.025-0.195]) and stellar masses ($\log(M/M_\odot)$=9.8-10.9) explored in this work.

^{13}CO Individual detections

We have included the $L'(^{12}CO)/L'(^{13}CO)$ line luminosity ratios of the individual ^{13}CO detections (see Table 3.2) in Figures 3.5, 3.7, and 3.8. Galaxy J085748.0+004641 is classified as merger (M) while galaxy J083831.8+000044 is classified as a galaxy with a projected companion (DBC), they both show high $L'(^{12}CO)/L'(^{13}CO)$ line luminosity ratios, in good agreement with previous findings. On the other hand, galaxies J085346.4+001252, J084139.6+015346, J084350.8+005534 and J090633.6+001526 are classified as galaxies that do not show any apparent projected companion and present low $L'(^{12}CO)/L'(^{13}CO)$ line luminosity ratios, in agreement with those expected from galaxies with low L_{IR} values. Finally, galaxy J090949.6+014847 seems to be a peculiar galaxy showing a low $L'(^{12}CO)/L'(^{13}CO)$ line luminosity ratio but with low SFE $= 1\,Gyr^{-1}$ and high $L_{IR} = 10^{12}\,L_\odot$ values. Thus, we identify J090949.6+014847 as an outlier and exclude it from the Spearman rank tests in the previous analyses. Stacking results are robust against the removal of this peculiar source from the sample.

110.201 GHz stacked continuum emission.

As discussed in section 3.2.2 we do not detect continuum emission at ∼110GHz above 5σ significance down to a rms noise of 4μJy beam^{-1} in any of the 27 galaxies of our sample. However, we could detect a high signal-to-noise ratio (SNR=13) emission after stacking the individual continuum emission of our 27 galaxy sample coming from the ^{13}CO datasets. As with the ^{12}CO, ^{13}CO and C^{18}O stacks, we split our sample by low and high SFR populations (see Table 3.8). Similar to what we found for the $L'(^{12}CO)/L'(^{13}CO)$ ratio, galaxies with higher SFR show the higher continuum emission compared with galaxies with low SFR. The detected continuum emission does not show any discrepancy with the expected average continuum emission at ∼110 GHz extrapolated from the spectral energy distributions presented in Villanueva et al. (2017). However, further analyses at these frequencies are needed to uncover the origin of the continuum emission (*e.g. free-free, dust, ionized gas emission*) contributing to the SEDs of these galaxies and its relation with their star formation activity.

3.4.2 $L'(^{13}CO)/L'(C^{18}O)$ correlations.

Our ALMA Band-3 observations helped with the exploration of the $C^{18}O(1-0)$ emission line for 24 VALES galaxies. Following a similar approach as before, in this section we only use these 24 galaxies with simultaneous C^{18}O, ^{13}CO and ^{12}CO observations. Figures 3.9 and 3.10 show the trends for $L'(^{12}CO)/L'(^{13}CO)$ and $L'(^{13}CO)/L'(C^{18}O)$ as a function of L_{IR}, SFR and

TABLE 3.9: Average $L'(^{12}CO)/L'(^{13}CO)$ and $L'(^{13}CO)/L'(C^{18}O)$ line luminosity ratios for the sample of 24 VALES galaxies with $C^{18}O$ observations split into low and high L_{IR}, SFR, SFE, values (see Figs. 3.9 and 3.10). Column 1: parameter of interest; column 2: range explored; column 3: number of galaxies in the explored range; column 4: average value for parameter of interest; columns 5 and 8: the average stacked R_1=$L'(^{12}CO)/L'(^{13}CO)$ and R_2=$L'(^{13}CO)/L'(C^{18}O)$ line luminosity ratios respectively. Finally the Student's t-test statistical reports (t, p) to asses the probability that the null hypothesis ($L'(^{12}CO)/L'(^{13}CO)$ and $L'(^{13}CO)/L'(C^{18}O)$ line luminosity ratios variations between low and high L_{IR}, SFR, SFE populations are not statistically significant) is true, located in columns 6 and 9 (t coefficient) and columns 7 and 10 (probability p-value) respectively.

Parameter	Range	N	Average	R_1	t-test		R_2	t-test	
					t	p		t	p
1	2	3	4	5	6	7	8	9	10
$\log[L_{IR}/L_\odot]$	[10.1 - 11.0]	13	10.5 ± 0.1	13.0 ± 2.5	-4.4	0.002	3.3 ± 0.8	-2.8	0.01
	[11.1 - 11.8]	11	11.3 ± 0.1	18.8 ± 3.7			2.5 ± 0.6		
SFR ($M_\odot yr^{-1}$)	[1.3 - 9.5]	13	3.7 ± 0.5	13.0 ± 2.6	-4.2	0.0003	3.3 ± 0.8	-2.8	0.01
	[10.3 - 68.5]	11	23.6 ± 4.0	18.8 ± 3.8			2.5 ± 0.6		
SFE (Gyr^{-1})	[0.4 - 0.9]	11	0.6 ± 0.1	12.4 ± 2.8	-4.8	7E-5	4.4 ± 1.2	-5.9	5E-6
	[1.1 - 11.8]	13	3.3 ± 0.6	19.4 ± 4.2			2.1 ± 0.5		

SFE respectively and Table 3.9 for average $L'(^{12}CO)/L'(^{13}CO)$ and $L'(^{13}CO)/L'(C^{18}O)$ values. The average $L'(^{13}CO)/L'(C^{18}O)$ line luminosity ratio found is 2.5±0.6, which is in good agreement with the $I(^{13}CO)/I(C^{18}O)$ line intensity ratio found for starburst galaxies (3.4±0.9) but slightly lower than the average ratio found in nearby normal spiral galaxies (6.0±0.9) reported by Jiménez-Donaire et al. (2017). The central panel of Figure 3.10 shows the $L'(^{13}CO)/L'(C^{18}O)$ line luminosity ratio as a function of SFR (see Table 3.10) and also includes values reported in the literature gathered by Romano et al. 2017 and split into normal, starburts and ultra luminous infrarred galaxies (ULIRGs).

As with $L'(^{12}CO)/L'(^{13}CO)$ trends discussed in Section 3.4.1, we implemented a Student's t-test to evaluate the significance of the $L'(^{12}CO)/L'(^{13}CO)$ and $L'(^{13}CO)/L'(C^{18}O)$ variations with L_{IR}, SFR and SFE considering the 24 galaxies with $C^{18}O$ coverage. We find that the differences found in the $L'(^{12}CO)/L'(^{13}CO)$ and $L'(^{13}CO)/L'(C^{18}O)$ variations between low and high L_{IR}, SFR, SFE populations are statistically significant (see Table 3.9). We also applied a KS test to assess the probability that the null hypothesis (low and high: SFR, SFE, L_{IR}, $M_{H_2}/M_\odot$, $M_{H_2}/M_\star$, and f_{H_2} populations were drawn from the same parent population) is true, considering the reduced 24 galaxy sample with $C^{18}O$ coverage. Table 3.10 shows the average values of redshift, $M_{H_2}/M_\odot$, $M_{H_2}/M_\star$), and f_{H_2} split into low and high SFR values and the Kolmogorov-Smirnov statistics (D, p). We find supporting evidence to reject the null hypothesis that the low and high SFR populations were drawn from the same parent population. Therefore, galaxies with high $L'(^{12}CO)/L'(^{13}CO)$ ratio (Figure 3.9) and low $L'(^{13}CO)/L'(C^{18}O)$ ratio (Figure 3.10) also show relatively high L_{IR}, SFR, SFE and high reservoirs of molecular gas (see Table 3.10). These line ratios can be explained by overabundances of ^{12}CO and $C^{18}O$ (both produced in high mass stars), with respect ^{13}CO, that could be understood as a result of selective nucleosynthesis where high-mass stars enrich the ISM of these galaxies.

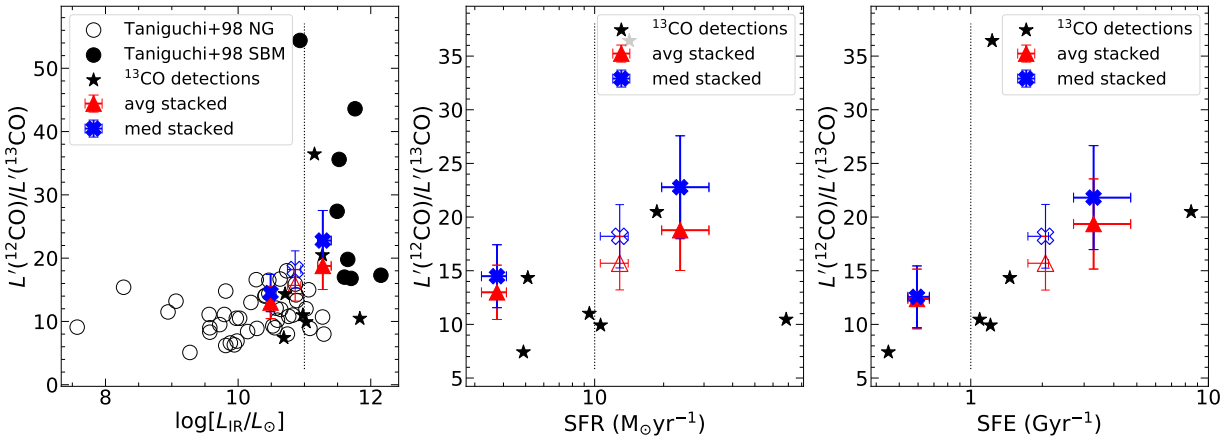

FIGURE 3.9: Average (red triangles) stacked $L'(^{12}\mathrm{CO})/L'(^{13}\mathrm{CO})$ line luminosity ratio for low and high L_{IR} (left panel), SFR (middle panel) and SFE (right panel), subsets (triangles). As reference average and median line luminosity ratio considering all galaxies in open symbols and dashed lines indicating the boundary between low and high L_{IR}, SFR and SFE populations are included. Error bars correspond to 1σ confidence intervals for average (or median) values based on Monte-Carlo simulations. $L'(^{12}\mathrm{CO})/L'(^{13}\mathrm{CO})$ line ratios of normal galaxies (open circles), starburst mergers (filled circles) are scaled by a 1.75 factor to convert from far-IR to IR luminosities (see Appendix E from Herrera-Camus et al. 2015). Data from Taniguchi and Ohyama (1998) and individual ^{13}CO detections (stars) are also included.

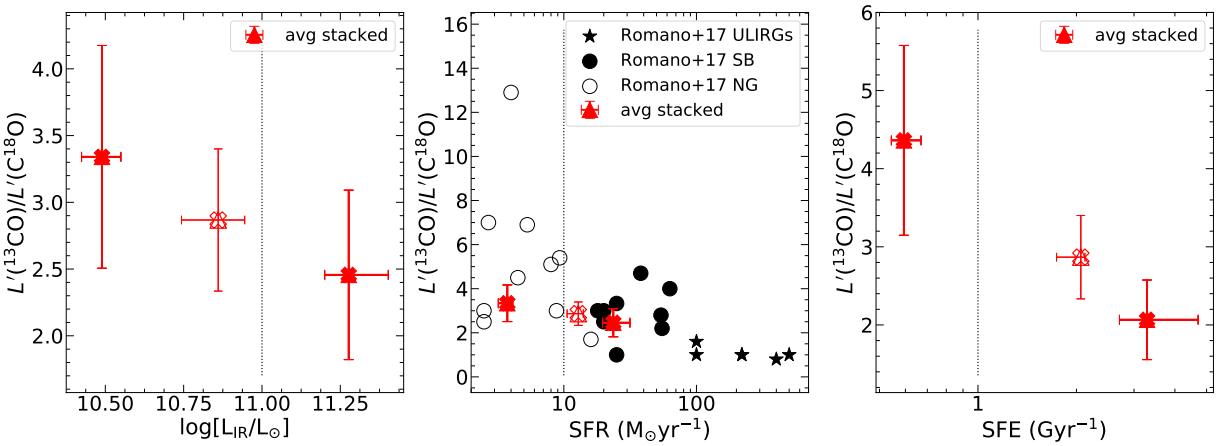

FIGURE 3.10: Average (red triangles) stacked $L'(^{13}\mathrm{CO})/L'(\mathrm{C}^{18}\mathrm{O})$ line luminosity ratio for low and high L_{IR} (left panel), SFR (middle panel) and SFE (right panel), subsets (triangles). As reference, average line luminosity ratio considering all 24 galaxies with $\mathrm{C}^{18}\mathrm{O}$ coverage are shown in open symbols and dashed lines indicating the boundary between low and high L_{IR}, SFR and SFE populations are included. Error bars correspond to 1σ confidence intervals for average values based on Monte-Carlo simulations. $I(^{13}\mathrm{CO})/I(\mathrm{C}^{18}\mathrm{O})$ ratios reported in the literature and gathered by (Romano et al., 2017) split into normal galaxies (NG open circles), starburst galaxies (SB filled circles) and ULIRGs (stars) as a function of SFR are also included. We note that median $L'(^{13}\mathrm{CO})/L'(\mathrm{C}^{18}\mathrm{O})$ line luminosities stacks are not included in our analyses due to low significance in these values.

TABLE 3.10: Average values of different parameters (column 1): redshift, molecular gas mass (M_{H_2}), molecular gas mass to stellar mass ratio ($M_{H_2}/M_\star$), and molecular gas fraction ($f_{H_2} = M_{H_2} / (M_{H_2}+M_\star)$) considering 24 galaxies with $C^{18}O$ coverage split into low (column 2) and high SFR values (column 3) . Columns 4 and 5 contain the Kolmogorov-Smirnov statistical reports (D, p) to asses the probability that low and high (z, M_{H_2}, $M_{H_2}/M_\star$, and f_{H_2}) populations were drawn from populations with identical distributions.

	SFR [$M_\odot yr^{-1}$]			
Parameter	low	high	KS	
	N = 15 [1.3-9.5]	N = 12 [10.3-68.5]	D	p
1	2	3	4	5
<z>	0.04 ± 0.01	0.10 ± 0.04	0.8	7E-5
<log[$M_{H_2}/M_\odot$]>	8.8 ± 0.1	9.9 ± 0.1	0.8	0.01
<$M_{H_2}/M_\star$>	0.15 ± 0.04	0.36 ± 0.05	0.6	0.02
<f_{H_2}>	0.12 ± 0.07	0.24 ± 0.09	0.6	0.02

3.5 Discussion

The $L'(^{12}CO)/L'(^{13}CO)$ line luminosity ratios presented in this work can be affected by optical depth effects or by the different physical processes that have been invoked to explain large and low $I(^{12}CO)/I(^{13}CO)$ line intensity ratios. The most relevant ones are: i) selective photodissociation: ^{12}CO molecules are more abundant than ^{13}CO molecules and hence due to their higher density they are self-shielded against strong interstellar UV radiation fields, unlike less abundant ^{13}CO molecules which are more easily photo-dissociated leading to a ^{13}CO under abundance and hence a higher $I(^{12}CO)/I(^{13}CO)$ line intensity ratio in regions with strong UV radiation fields, ii) chemical isotope-dependent fractionation: where gas kinetic temperatures elevates ^{13}CO abundance through the isotopic charge exchange reaction (Watson, 1977), where $^{12}CO + {}^{13}C^+ \rightarrow {}^{12}C^+ + {}^{13}CO + \Delta E$, and iii) selective nucleosynthesis where massive stars in star forming regions produce significantly higher amounts of ^{12}C compared to ^{13}C leading to a high $I(^{12}CO)/I(^{13}CO)$ line intensity ratio (Henkel and Mauersberger, 1993; Aalto et al., 1995).

The higher $L'(^{12}CO)/L'(^{13}CO)$ line luminosity ratio found for galaxies with close companions may be explained by interaction activity. For example, during the early stages of a merger event, part of the gas escapes and disperses into the intergalactic medium (Mirabel and Sanders, 1989). The remaining gas shrinks to the center, becomes denser and converted partially into molecular H_2 gas. This fresh molecular gas with relatively low metallicity and, hence, a high $^{12}C/^{13}C$ luminosity ratio will trigger new starburst events boosting the $^{12}CO/^{13}CO$ abundance ratio (Casoli, Dupraz, and Combes, 1992b; Langer and Penzias, 1990). On the other hand, the opposite scenario occurs in galaxies in denser environments, like galaxy clusters, where a deficit in ^{12}CO is linked to the low $I(^{12}CO)/I(^{13}CO)$ line ratios observed. Galaxies in clusters have lived long enough to enrich the ISM with ^{13}C atoms from low mass stellar nucleosynthesis, while at the same time, the evaporation or stripping of low density GMCs as galaxies enter into the cluster moving through the intracluster medium (ICM), possibly reducing the presence of new starburst events and therefore would lead to a reduced $I(^{12}CO)/I(^{13}CO)$ intensity ratio (Alatalo et al., 2015). In summary, the enhanced $L'(^{12}CO)/L'(^{13}CO)$ line luminosity ratios observed in galaxy mergers (M) and galaxies with a projected companion (BC, DC) which got relatively high SFR (34 ± 6.9 and 17.6 ± 5.9, respectively) could be explained by a new starburst activity in these systems. Galaxies without any projected companion (B, D) with low SFRs present a relatively low $L'(^{12}CO)/L'(^{13}CO) = 3.4\pm0.5$ line luminosity ratio, which could be explained by ^{13}C enrichment of their ISM induced by low and intermediate mass stars in the absence of young

starburst events.

The trends of $L'(^{12}CO)/L'(^{13}CO)$ with L_{IR}, SFR, and SFE (see Figures 3.7, 3.8 and 3.9) found in this work provide the evidence that galaxies with low SFR, SFE and L_{IR}, also show low $L'(^{12}CO)/L'(^{13}CO)$ line luminosity ratios in agreement to the idea that normal star forming galaxies have larger gas consumption times to enrich with ^{13}C the ISM from low and intermediate mass stars. On the other hand, galaxies with high SFR, SFE and L_{IR} present high $L'(^{12}CO)/L'(^{13}CO)$ line luminosity ratios most probably due to younger starburst activity. These higher ratios found here are in good agreement with scenarios in which galaxies with higher fractions of dense molecular gas (see Tables 3.7 and 3.10) show higher L_{IR} and higher SFE (Solomon and Vanden Bout, 2005; Solomon, Downes, and Radford, 1992), probably induced by the triggering of a recent starburst episode after the in-fall, of unprocessed gas to the central galaxy regions (Henkel and Mauersberger, 1993; Casoli, Dupraz, and Combes, 1992a; König et al., 2016).

Similarly, the $I(^{13}CO)/I(C^{18}O)$ line intensity ratios are explained in terms of either a ^{13}CO deficit or an overabundance of $C^{18}O$. Recently, low $I(^{13}CO)/I(C^{18}O)$ line intensity ratios have been reported for different type of galaxies (Danielson et al., 2013; Sliwa et al., 2017; Jiménez-Donaire et al., 2017; Brown and Wilson, 2019). In all these cases, the low ratios have been attributed to the presence of massive stars in a recent starburst. Our trends found for $L'(^{13}CO)/L'(C^{18}O)$ (Figure 3.10) are in good agreement with previous ratios reported for starburst galaxies (Zhang et al., 2018; Jiménez-Donaire et al., 2017). Considering the 24 VALES galaxies with $C^{18}O$ spectral coverage, we show moderate trends of $L'(^{13}CO)/L'(C^{18}O)$ with L_{IR}, SFR, and SFE. Galaxies with higher L_{IR}, SFR and SFE are found to show high $L'(^{12}CO)/L'(^{13}CO)$ (Figure 3.9), low $L'(^{13}CO)/L'(C^{18}O)$ (Figure 3.10) luminosity ratios, and relatively high reservoirs of molecular gas (see Table 3.10). Similar results have been associated to a top heavy IMF (Danielson et al. 2013; Sliwa et al. 2017; Zhang et al. 2018; Brown and Wilson 2019), however, in order to break the degeneracy between young starburst and top-heavy IMF, an independent determination of the age of the starburst is needed.

3.5.1 Optical depth, selective photodissociation and chemical fractionation effects.

Aalto et al. (1995) pointed out the difficulties interpreting the ^{12}CO and ^{13}CO abundances from $I(^{12}CO)/I(^{13}CO)$ line intensity ratios as these might be affected by surface density, optical depth, and gas temperature. They suggested that the high $I(^{12}CO)/I(^{13}CO)$ line intensity ratios observed in mergers and interacting galaxies (Casoli, Dupraz, and Combes, 1992b; Henkel and Mauersberger, 1993) are produced by the in-falling of unprocessed gas which could affect the gas elemental abundances, only if the ISM has moderate optical depths ($\tau \approx 1$). More recently, Zhang et al. (2018) presented how ^{13}CO and $C^{18}O$ opacity affects $I(^{12}CO)/I(^{13}CO)$ and $I(^{13}CO)/I(C^{18}O)$ line intensity ratios in local thermodynamic equilibrium (LTE) and non LTE conditions assuming: representative Galactic abundance ratios ($^{13}CO/C^{18}O = 7$–10, $^{12}CO/^{13}CO=70$), and typical ULIRGs and SMGs conditions (*e.g.* $\tau_{^{12}CO} \approx 2$, $T_{kin} = 30$K). They found that the high $I(^{12}CO)/I(^{13}CO)$ ratios ≥ 30 observed in high redshift galaxies, would need extremely low optical depths for ^{13}CO ($\tau < 0.03$), meaning that $I(^{12}CO)/I(^{13}CO)$ line intensity ratios are affected by optical depth effects. In order to properly account the optical depths in $I(^{12}CO)/I(^{13}CO)$ intensity ratios, multiple line transitions observations are needed to measure excitation conditions and derive the optical depths of the ISM in these galaxies, which is beyond the scope this work and hence, the $L'(^{12}CO)/L'(^{13}CO)$ luminosity ratios reported here should be taken as a lower limit of the $^{12}CO/^{13}CO$ abundance ratio (Henkel et al., 2010; Martín et al., 2019). On the other hand, Zhang et al. (2018) found that even moderate ^{13}CO optical depths ($\tau_{^{13}CO} \sim 0.2$-0.5) do not cause the $I(^{13}CO)/I(C^{18}O)$ line intensity ratio to deviate significantly from more typical values ($^{13}CO/C^{18}O \sim 7$), meaning that the low $I(^{13}CO)/I(C^{18}O)$ found in high-redshift starbursts

and local ULIRGs reflect the intrinsic isotopologue abundance ratios (*i.e.* $I(^{13}CO)/I(C^{18}O) \approx {}^{13}CO/C^{18}O \approx {}^{13}C/{}^{18}O$).

If chemical fractionation is the main physical mechanism controlling the observed line ratios, the ^{13}CO abundance would be boosted with respect to ^{12}CO (and $C^{18}O$) at low temperatures (T $\approx$ 10 K, Watson, Anicich, and Huntress 1976). Nevertheless, considering a mean temperature T > 20 K (Ibar et al., 2015; Hughes et al., 2017) for our VALES sample, we can reject chemical fractionation as the main mechanism controlling the $L'(^{12}CO)/L'(^{13}CO)$ ratios. On the other hand, selective photodissociation can affect the less abundant ^{13}CO and $C^{18}O$ molecules compared to ^{12}CO, however, extreme conditions with high gas densities ($> 10^{26}cm^{-3}$) are required (Zhang et al., 2018; Romano et al., 2017). However, with an average gas density of 10^4cm^{-3} (Hughes et al., 2017), our sample of galaxies do not fulfill such conditions. Moreover, knowing that $C^{18}O$ is even more sensitive to selective dissociation than ^{13}CO, $C^{18}O$ molecules would be more dissociated than ^{13}CO molecules, resulting in high $L'(^{13}CO)/L'(C^{18}O)$ ratios, which is inconsistent with results shown in Figure 3.10 where galaxies with more intense UV radiation fields associated with high L_{IR} and SFR show low $L'(^{13}CO)/L'(C^{18}O)$ ratios. Thus, the $(L'^{12}CO)/(L'^{13}CO)$ and $(L'^{13}CO)/L'(C^{18}O)$ variations found here are not compatible with a scenario in which selective photodissociation or chemical fractionation play a dominant role.

3.5.2 Insights from Galactic Chemical Evolution

Recently Romano et al. (2017) used Galactic Chemical Evolution (GCE) models to compute the the abundances of numerous elements including ^{12}C, ^{16}O, ^{13}C and ^{18}O in the ISM of galaxies, assuming that i) stars form from raw material with primordial chemical composition, ii) outflows remove stellar ejecta and a fraction of the surrounding ISM, iii) star formation follows a canonical Kennicutt-Schmidt law (Schmidt, 1959; Kennicutt, 1998b), iv) stars release the synthesized elements during their lifetime, and v) stellar eject are homogeneously mixed in the ISM, allowing to follow multiple isotopic ratios and trace their abundance ratios on different isotopes and different elements. They have shown that neither selective photodissociation nor chemical isotope-dependent fractionation can significantly perturb globally averaged isotopologue abundance ratios, since these processes will typically affect only small mass fractions of individual molecular clouds in galaxies. Using these models, Zhang et al. (2018) was able to compare the effects of assuming different IMF of young starbursts by incorporating the appropriate timescales at which different stellar populations enrich the ISM, and conclude that a canonical IMF can not reproduce the observed low $I(^{13}CO)/I(C^{18}O)$ ratios in ULIRGs and SMGs. Thus, assuming that the velocity integrated line flux densities coming from average stacks are not affected by these two other effects, we propose that these emission line ratios could be induced by selective nucleosynthesis.

3.6 Conclusions

Here we present a stacking analysis of $^{12}CO(1-0)$, $^{13}CO(1-0)$ emission lines of 27 galaxies, and $C^{18}O$ $(1-0)$ in 24 galaxies, belonging to the VALES survey. We have detected 6 individual ^{13}CO (1-0) line signals from 6 galaxies in moment-0 maps, with SNR > 5. We have successfully demonstrated that it is possible to detect the signal coming from faint emission lines (^{13}CO and $C^{18}O$) in low-redshift galaxies through stacking analysis, pushing the current ALMA detectability limits. Therefore, the analysis presented here can be applied to detect faint signals from different molecules coming from low, intermediate and high redshift galaxies, exploiting radio interferometric datasets from ALMA.

We have explored three different independent stacking analysis, two of them in the "image plane" i) 2D-moment-0 stacking and ii) 3D-image stacking, while a third one in visibility's space

iii) *uv*-plane stacking. We found that for bright emission line (as the case for ^{12}CO) *uv*-plane stacks produce the highest signal-to-noise compared to 2D-moment-0, and 3D-image stacks. Moment-zero stacked maps for faint lines, like ^{13}CO, shows the highest signal to noise compared with 3D-image and *uv*-plane stackings.

We found an overall $L'(^{12}\mathrm{CO})/L'(^{13}\mathrm{CO})$ line luminosity ratio of 16.1±2.5. We also detect a dependence of $L'(^{12}\mathrm{CO})/L'(^{13}\mathrm{CO})$ line luminosity ratio on optical morphology/environment where galaxies showing a close projected companion and mergers show boosted $L'(^{12}\mathrm{CO})/L'(^{13}\mathrm{CO})$ line luminosity ratios. Mergers show, at low significance, a $L'(^{12}\mathrm{CO})/L'(^{13}\mathrm{CO})$ line luminosity ratio which is 2 times higher than the one found in galaxies without a projected companion. We also detect positive trends between $L'(^{12}\mathrm{CO})/L'(^{13}\mathrm{CO})$ line luminosity ratio and SFR, SFE, L_{IR}, $\Sigma_{\mathrm{H_2}}$ and Σ_{SFR}.

We also provide C^{18}O stacking analysis for 24 VALES galaxies. We detect signal coming from the 2D moment-0 stacked images at a significance of $\sim 5\sigma$ with an average $L'(^{13}\mathrm{CO})/L'(\mathrm{C}^{18}\mathrm{O})$ line luminosity ratio of 2.5±0.6. This average value is in good agreement to the $I(^{13}\mathrm{CO})/I(\mathrm{C}^{18}\mathrm{O})$ = 3.4±0.9 line ratio for starburst galaxies found by Jiménez-Donaire et al. (2017). We find negative trends of $L'(^{13}\mathrm{CO})/L'(\mathrm{C}^{18}\mathrm{O})$ as a function of L_{IR}, SFR and SFE.

We recall that our L$'(^{12}\mathrm{CO})/\mathrm{L}'(^{13}\mathrm{CO})$ ratios can be affected by optical depth effects, and hence the $L'(^{12}\mathrm{CO})/L'(^{13}\mathrm{CO})$ luminosity ratios reported here should be taken as a lower limit for the ^{12}CO/^{13}CO abundance ratio. To assess the optical depth effects on $I(^{12}\mathrm{CO})/I(^{13}\mathrm{CO})$ intensity ratios, multiple line transitions observations are needed to measure excitation conditions and derive the optical depths of the ISM.

Neither chemical fractionation nor selective photo-dissociation are expected to be responsible for the trends found in this work as the required low temperatures ($\leq 10K$) and high densities ($> 10^{26}\mathrm{cm}^{-3}$) are not fulfilled by our sample of galaxies. The combined $L'(^{12}\mathrm{CO})/L'(^{13}\mathrm{CO})$ and $L'(^{13}\mathrm{CO})/L'(\mathrm{C}^{18}\mathrm{O})$ variations provide additional evidence inconsistent with selective photodissociation as the responsible agents behind the results shown here. This, leaves selective nucleosythesis to be the most probable mechanism for the high $L'(^{12}\mathrm{CO})/L'(^{13}\mathrm{CO})$ and low $L'(^{13}\mathrm{CO})/L'(\mathrm{C}^{18}\mathrm{O})$ ratios found in bright far-IR luminosity galaxies. The scenario might be that higher molecular gas reservoirs can trigger new starburst events where high mass stars enrich their ISM.

Future analyses using ALMA observations of these and other CNO isotoplogue molecules (C^{17}O, ^{12}CN, ^{13}CN) on larger samples, sampling different galaxy populations covering wider ranges in SFR, SFE, and molecular gas contents at different epochs could fill in the gap of these molecular line observations between nearby galaxies and lensed galaxies at high redshift, shedding light on the physical processes behind their star formation activity.

Chapter 4

The CMG of star-forming galaxies at $\langle z \rangle \sim 2.6$.

The following chapter presents the results on the stacking analysis on 238 pairs of close star-forming galaxies from the VIMOS Ultra Deep Survey. These results have been submitted for publication to Astronomy and Astrophysics journal under reference number: **AA/2021/42553**. (Méndez-Hernández et al., 2021).

4.1 Introduction

The circumgalactic medium (CGM, 10kpc-$\sim$300 kpc) is the gas reservoir between the interstellar medium (ISM, $\lesssim$ 10kpc) and the intergalactic medium (IGM, $\gtrsim$ 300kpc). It is characterized as an active interface where galaxies reprocess their baryonic material. In fact, up to $\sim$50% of the total baryonic mass is found in the CGM at both, low-redhshift ($z \sim 0.2$) (Wolfe, Gawiser, and Prochaska, 2005; Werk et al., 2014; Zheng et al., 2015) and high-redshift (Hafen et al., 2019), thus representing a significant gas reservoir which can, for example, feed the ISM with gas to form new stars (Zhu and Ménard, 2013; Thom et al., 2012; Richter et al., 2016). Supernovae explosions or strong stellar winds can deposit metals in the surrounding medium, gas which is mixed with pristine gas accreted from the intergalactic medium(IGM; Prochaska and Wolfe 2009; Bauermeister, Blitz, and Ma 2010; Tumlinson et al. 2011; Tumlinson, Peeples, and Werk 2017; Kacprzak 2017).

Since the first discoveries of circumgalactic gas around star-forming galaxies (Boksenberg and Sargent, 1978; Kunth and Bergeron, 1984; Bergeron, 1986), its study by direct detection of emission has been a challenge (van de Voort and Schaye, 2013; Burchett et al., 2021). The CGM has been primarily detected via the absorption features that it produces on light from *background* sources. In a pioneering study at high-redshift ($z \gtrsim 1.5$), Adelberger et al., 2003; Adelberger et al., 2005 studied the dependence of the absorption strength on the projected angular separation between *foreground* and *background* galaxies(i.e., impact parameter b), reporting absorption detection at impact parameters up to 40 kpc and noticed that absorption strength weakens significantly at larger separations. Thanks to their brightness, quasars are typically used as *background* sources to probe the CGM around *foreground* galaxies (Bergeron and Boissé, 1991; Steidel, Dickinson, and Persson, 1994; Kacprzak et al., 2010), allowing to identify the signal produced by extremely low column densities ($N_{HI} \simeq 10^{12}$ cm^{-2}), independent of the properties of the targeted galaxy (e.g., luminosity and/or redshift) (Tumlinson, Peeples, and Werk, 2017; Péroux and Howk, 2020). This technique has been successful to probe the CGM of galaxies up to redshifts $z \sim$5 (Matejek and Simcoe, 2012) and has led to the discovery that the CGM is gas rich and has a multi-phase nature (Adelberger et al., 2003; Steidel, Dickinson, and Persson, 1994; Steidel, 1995; Songaila, 2001; Tripp, Lu, and Savage, 1998; Kacprzak et al., 2010; Werk et al., 2016).

The CGM has been also characterized using the so-called "down-the-barrel technique", which uses the targeted galaxy itself as *background* source. Absorption lines redshifted with respect to

the galaxy rest-frame evidence the presence of gas flowing towards the galaxy. This result has been interpreted as a strong indication of inflowing material onto the host galaxy (Sato et al., 2009; Rubin et al., 2012; Martin et al., 2012), while outflows have been identified as blueshifted absorptions in galaxy spectra (Martin, 2005; Chen et al., 2010). Although the location of the gas producing the detected absorption is unconstrained, this technique has been successful in studying galactic inflows and outflows from the spectroscopy of star-forming galaxies up to $z \sim 2-3$ (Kornei et al., 2012; Rudie et al., 2012; Heckman et al., 2015; Heckman and Borthakur, 2016).

Recently three more techniques have been used to explore the CGM. The first one takes advantage of strong gravitational lensing, the so-called "gravitational-arc tomography", which uses giant bright lensed arcs as background sources to map the CGM of *foreground* galaxies providing a tomographic view of the absorbing gas (Lopez et al., 2018; Claeyssens et al., 2019; Lopez et al., 2020; Tejos et al., 2021; Mortensen et al., 2021). The second one takes advantage of deep three-dimensonal datacubes observations to study the cold CGM of high-redhisft ($z > 2$) star-forming galaxies, and have reported the ubiquitous presence of Lyα haloes in these galaxies (Steidel et al., 2011; Matsuda et al., 2012; Momose et al., 2014; Wisotzki et al., 2016; Leclercq et al., 2017; Chen et al., 2020), whose line properties are correlated to their spatial location (Leclercq et al., 2020) and that can extend up to 4Mpc beyond the CGM (Chen et al., 2020; Bacon et al., 2021). The third one uses the spectra of bright afterglows of long gamma-ray bursts (GRBs) to derive the kinematic properties of the CGM gas around their host galaxies and constrain the physical properties (Gatkine, Veilleux, and Cucchiara, 2019; Gatkine et al., 2022).

Alongside these diverse techniques to study the CGM, the large spectroscopic extragalactic surveys have allowed for the statistical extraction and analysis of the weak signals from different metal absorption using the stacking of hundreds of spectra (Steidel et al., 2010). These large datasets have been helpful to overcome the limitations of finding galaxy-QSOs pairs at concordant redshifts (Steidel, Dickinson, and Persson, 1994; Bouché et al., 2007), increasing statistics and facilitating vast parameter space exploration (York et al., 2006; Bordoloi et al., 2011; Zhu and Ménard, 2013). At low-redshift ($z_{\rm med}$ ~0.5) CGM analyses have been focused on the study of Lyα (Chen et al., 2001), C IV (Chen, Lanzetta, and Webb, 2001), O VI (Tumlinson et al., 2011), Mg II (Bowen, Blades, and Pettini, 1995; Bouché et al., 2007; Steidel, Dickinson, and Persson, 1994) absorption lines, and their dependence with stellar mass (Bordoloi et al., 2011), inclination (Kacprzak et al., 2010), and azimuthal angle (Shen et al., 2012; Bordoloi et al., 2014a). At higher redshifts, the observed metal absorption lines are mostly limited to Si II, C II, C IV and Si IV, where the first two are called low-ionization state (LIS, T=$10^{4-4.5}$K) lines, while the last two high-ionization state (HIS, T=$10^{4.5-5.5}$K) lines (Steidel et al., 2010). At high redshift (z>2) several authors have reported the presence of high-velocity outflows. Lehner et al., 2014 demonstrated that O VI successfully probe outflows in star-forming galaxies and reported velocity widths in the range 200-400kms^{-1}. Next, Du et al., 2016 analysed several ionization lines (e.g. Si II, Fe II, Al II, Ni II, Al III, C IV) to probe the multiphase nature of the CGM and deteceted C IV blueshifted offsets concordant with 76kms^{-1} velocity outflows. Their results show a direct link between C IV absorption and star formation rate. Later on, Jones, Stark, and Ellis, 2018 reported velocity outflows of ~150km^{-1} as shown by several LIS and HIS absorptions in nine gravitationally lensed star-forming galaxies($z \simeq 2-3$), suggesting that galaxy outflows regulate the galaxy chemical evolution. Similar outflows detections inferred from different ionization absorption lines have been reported, and where stellar mass and star-formation rate have been invoked as their main drivers (Zhu and Ménard, 2013; Turner et al., 2014; Trainor et al., 2015; Gatkine, Veilleux, and Cucchiara, 2019; Price et al., 2020). However, as suggested by Dutta et al., 2021 LIS and HIS absorption detections (from which velocity outflows can be inferred), could be affected by large-scale environmental processes (Dutta et al., 2021; Wang et al., 2021) or their available neutral gas content (Berry et al., 2012; Oyarzún et al., 2016; Du et al., 2018), and their correlation with stellar mass and star-formation rate in fact might be a consequence of a main-sequence offset,

rather than simply correlated with their star-formation rate or stellar mass (Cicone, Maiolino, and Marconi, 2016; Gatkine et al., 2022).

Numerical simulations consider that the CGM comes from gas accreted from the intergalactic medium (IGM), followed by stellar winds from the central galaxy and the gas ejected or stripped from satellites (Hafen et al., 2019; Christensen et al., 2018). Simulations reveal that the accretion efficiency depends on the galaxy stellar mass, decreasing from ∼80 per cent for $M_\star \sim 10^6 M_\odot$ galaxies to ∼60 per cent for $M_\star \sim 10^{10} M_\odot$ galaxies (Dekel et al., 2005; Kereš et al., 2005; Hafen et al., 2020). Once accreted, this material can remain in the CGM for billions of years leading to a well mixed-halo gas before it interacts with the ejected large-scale stellar winds produced by starbursts (Martin, 2005; Weiner et al., 2009). At $z = 2$, most metals are found to be located in the interstellar medium (ISM) or stars of the central galaxy and by $z = 0.25$ most of it will end up in the CGM and IGM(e.g., Peeples et al. 2014; Anglés-Alcázar et al. 2017; Hafen et al. 2020; Oppenheimer et al. 2016; Nelson et al. 2021.)

The way in which this pristine material is accreted into galaxies may depend on its location relative to the galaxy disk plane defined by the azimuthal angle (ϕ). Various observational studies highlight a correlation between the strength of the Mg II LIS absorption line and the azimuthal angle (Bordoloi et al., 2011; Bordoloi et al., 2014a; Kacprzak et al., 2011; Bouché et al., 2012; Bouché et al., 2013). Although weak Mg II detections along the minor axis have been reported (e.g., Lan, Ménard, and Zhu 2014), it has been found that strong Mg II absorptions are preferentially detected along the major-axis of galaxies, suggesting the presence of inflowing material potentially feeding future star formation. On the other hand, C IV and O VI (HIS lines) absorptions seem stronger along the minor axis, probably evidencing strong stellar winds enriching the CGM (Tumlinson et al., 2011; Kacprzak et al., 2015). Recently, Péroux et al., 2020 used cosmological hydrodynamical simulations to examine the physical properties of the gas located in the CGM of star-forming galaxies ($z < 1$) as a function of angular orientation. They found that the CGM properties vary strongly with the impact parameter, stellar mass, and redshift. They reported a higher average CGM metallicity at large impact parameters (b >100kpc) along the minor versus major axes. Moreover, they tentatively found that the average metallicity of the CGM depends on the azimuthal angle, showing that the low metallicity gas is preferentially inflowing along the galaxy major axis, while outflows are commonly located along the minor axis, concordant with previous observations (Bordoloi et al., 2011; Bouché et al., 2012; Kacprzak, Churchill, and Nielsen, 2012; Kacprzak et al., 2015). These results frame a picture where star-forming galaxies accrete co-planar gas within narrow stream-flows providing fresh fuel for the new generation of stars; later, this population will produce metal-enriched galactic scale outflows along the minor axis (Kacprzak, 2017). However, even though the presence of bipolar outflows collimated along the minor axis is expected to evolve with redshift (expected to be ubiquitous at z = 1), it has been difficult to demonstrate its presence at z = 2, mostly due to the absence of gaseous galactic discs sculpting the outflows (Nelson et al., 2019)

In order to better understand the mechanisms of galaxy growth in earlier phases of the history of the Universe, and to investigate a possible cosmic evolution of such mechanisms, similar studies at higher redshifts are needed. Observations along different lines of sight (l.o.s.) can probe different parts of the CGM, and the identification of low and high ionization metal absorption lines can give information on the possible multi-phase nature of the CGM. However, using QSO-galaxy pairs to study the CGM, is not an straightforward, as the identification of the galaxies responsible for the metal absorptions detected on the spectra of background quasars, is not an easy task. Stacking analysis of *background* galaxy spectra that are located in the vicinity of *foreground* galaxies provides an alternative tool to overcome sensitivity limitations, exploiting large extra-galactic surveys containing a large number of individual spectra. In this work, we seek to characterize the presence of low- (LIS: O I+Si II, C II, Si II, Fe II), intermediate- (IIS: Al III) and high-ionization (HIS: Si IV, C IV) state metal absorption (see Table 4.2) in the CGM of a star-forming galaxy population at $\langle z \rangle \sim 2.6$ using UV spectra obtained from the large VIMOS Ultra

Deep Survey (VUDS; Le Fèvre et al. 2015). We use thousands of galaxies with the most reliable redshift measurements and the highest S/N spectra (with reliability flags 3 and 4; see Le Fèvre et al. 2015; Tasca et al. 2017), a sample broadly representative of the bulk of the star-forming galaxy population at these redshifts (Lemaux et al., 2020). To detect the dim signal coming from low- and high ionization line absorptions produced in the CGM of these star-forming galaxies, we stack the spectra of close (in projection) *background* galaxies to establish the metal distribution in the CGM and explore their dependence on the physical and morphological properties of star-forming galaxies (e.g., impact parameter b, star formation rate, stellar mass, galaxy effective radius and azimuthal angle) at the peak epoch of cosmic star formation activity in the Universe.

This chapter is organized as follows. Section 4.2 summarizes the VUDS survey properties relevant for our analyses. Section 4.3 presents our stacking analysis method for measuring the metal equivalent widths (W_0), while Section 4.4 presents our W_0 results for Lyα, and multiple LIS and HIS metal lines observed our star-forming galaxy sample across different physical and morphological properties. We discuss our results in Section 4.5, and finally we present our conclusions in Section 4.6. Throughout the text, we use ΛCDM cosmology with $H_0 = 70\,\mathrm{km\,s^{-1}\,Mpc^{-1}}$, Ω_M=0.3 and Ω_Λ=0.7, and distances are given in physical units (kpc).

4.2 Data

VUDS has obtained spectra of 5590 galaxies in the redshift range $1.5 < z < 4.5$. A detailed description of the survey observations, the methods applied to process the data, and the derived parameters including the spectroscopic redshifts $z_{\rm spec}$ is given in Le Fèvre et al., 2015. A description of the VUDS-DR1 first data release can be found in Tasca et al., 2017. The VUDS spectroscopic targets are selected based on their photometric redshifts and observed optical flux; the targets have $z_{phot} + 1\sigma_z \geq 2.4$ and $i_{AB} \leq 25$. The wavelength range of each spectrum is between $3600 < \lambda / < 9350$, accumulating 14 hrs of integration time in each of the LRBLUE and LRRED grisms of the VIMOS spectrograph on the ESO Very Large Telescope (Le Fèvre et al., 2003), with a spectral resolution $R \sim 230$ (~ 7) and reaching a S/N=5 on the continuum at 8500 Å. We note that the VUDS observations were taken using the VIMOS low-resolution multi-slit mode with a minimum slit length optimized to 6 arcsec, maximizing the number of observed slits per mask (see Bottini et al. 2005).

Standard data processing was performed using the VIPGI environment (Scodeggio et al., 2005), followed by redshift measurements using the EZ package (Garilli et al., 2010). The final UV rest-frame flux limited sample is broadly representative of the bulk of the star-forming galaxy population at these redshifts ($2 < z < 5$) (Lemaux et al., 2020). A critical aspect of VUDS is the large comoving volume covered, totaling of 1 deg^2 in three fields: COSMOS (Scoville et al., 2007), ECDFS (Giacconi et al., 2002), and VVDS02h (Le Fèvre et al., 2005; Le Fèvre et al., 2013).

For the purposes of this study, the instrumental setup translates into the ability to follow lines redder than Lyα ($\geq$ 1215.6) at redshifts larger than 1.5. We decided to restrict the VUDS sample to 2100 galaxies, selected in the redshift range $1.5 < z < 4.5$ ($z_{\rm flag} = 3, 4$, i.e. $95 - 100\%$ probability of being correct). We note that the velocity accuracy of redshift measurements is expected to be in the range $dz\ /\ (1 + z) = 0.0005$–0.0007, or an absolute velocity (σ_v^{-1}) accuracy 150–200 km (Le Fèvre et al., 2013; Le Fèvre et al., 2015; Tasca et al., 2017). The rich broadband imaging available for galaxies in VUDS is used for spectral energy distribution (SED) fitting (Tasca et al., 2015; Thomas et al., 2017) using the Galaxy Observed-Simulated SED Interactive Program (GOSSIP; Franzetti et al. 2008) to derive various global galaxy properties (e.g., stellar mass, SFR, dust extinction E(B-V), age, or metallicity).

GOSSIP is a tool that performs SED fitting by using a combination of spectro-photometric measurements from different bands to match a set of synthetic galaxy spectra based on emission

TABLE 4.1: Number of objects belonging: VUDS parent sample, star-forming galaxies at $z > 1.5$, star-forming galaxies with morphological parameters available, close *fg-bg* galaxy pairs, and close *fg-bg* galaxy pairs with morphological parameters available extracted from the VUDS parent sample.

.

Sample	N
Galaxies $z > 1.5$, $z_{\rm flag}$=3,4,2,9	5590
Galaxies $z > 1.5$, $z_{\rm flag}$=3,4	2100
fg-bg galaxy pairs, $z_{\rm flag}$=3,4	238
Galaxies fit with GALFIT, $z_{\rm flag}$=3,4,2,9	1242
fg-bg galaxy pairs, $z_{\rm flag}$=3,4 + GALFIT	97

from stellar populations. GOSSIP uses model spectra from galaxy population synthesis models (Bruzual and Charlot, 2003; Maraston, 2005) and uses the probability distribution function (PDF) of each galaxy parameter to determine the best SED fit. Figure 4.1 shows SFR versus stellar mass for 5590 star-forming galaxies at: $z > 1.5$ selected from the VUDS survey (gray squares), $2 < z < 3.5$ (yellow crosses) and the 238 star-forming galaxies (blue stars) which we finally selected and scrutinized in this work (see Section 4.3). These 238 galaxies have stellar masses and star formation rates of $\log[M_\star/M_\odot]=9.73 \pm 0.4$ and $\log[SFR/(M_\odot yr^{-1})]=1.38 \pm 0.39$, respectively.

Exploiting the Hubble Space Telescope (HST) *F814W* images (Koekemoer et al., 2007) that are available as part of the COSMOS Survey (Scoville et al., 2007), morphological parameters have been estimated for 1242 star-forming galaxies($z_{\rm flag} = 4, 3, 2, 9$, i.e. 75% probability of being correct) with $9.5<\log[M_\star/M_\odot]<11.5$. In particular, Ribeiro et al., 2016 run GALFIT (Peng et al., 2002; Peng et al., 2010), a standard parametric profile-fitting tool, estimating Sersic indices (n), azimuthal angles, major to minor axis ratios (q) and effective radii ($r_{\rm eff}$). Figure 4.2 shows the distribution of the 97 selected galaxy pairs (see Section 4.3) with available morphological parameters. Table 4.1 shows the detailed number of subsets of galaxies.

4.3 Analysis

In this work, we seek to probe the CGM around galaxies at $z \sim 2.6$, near the epoch at which the cosmic star formation rate density of the Universe reaches its peak, by using the spectra of *background (bg)* galaxies as "spotlights" illuminating the CGM. At these redshifts individual *bg* galaxies are not bright enough to individually detect low- and high-ionization state metal absorption lines. Thus, we stack spectra of *bg* galaxies to look for absorption lines produced by the CGM around *foreground (fg)* star-forming galaxies. To select a sample of close galaxy pairs(*fg-bg*) out of the VUDS survey, we have imposed similar criteria as those described by Steidel et al., 2010: (i) galaxy spectra for the *fg* and *bg* galaxies must possess an accurately determined redshift ($95-100\%$ see Le Fèvre et al. 2015; Tasca et al. 2017 for details), (ii) a redshift separation $0.1 < z_{\rm bg} - z_{\rm fg} \leqslant 1.0$ between *fg-bg* galaxy pairs to ensure that each spectrum contains a significant common spectral coverage after shifting to the rest-frame of the *fg* galaxy and avoid an overlap between the fg CGM and the *bg* galaxy absorptions., and iii) a maximum projected angular separation of $23''$.

Stacking the *fg* spectra provides the absorptions at the foreground galaxy's rest-frame. Figure 4.3 shows the redshift distributions of the *foreground* (red) and *background* (blue) galaxy pairs and the *fg-bg* pairs redshift difference($\Delta z = z_{bg} - z_{fg}$) distribution on the top-right corner. The spectroscopic sample includes 238 spectra within the redshift range $1.5 < z \lesssim 4.43$ ($\langle z \rangle = 2.6 \pm 0.41$)

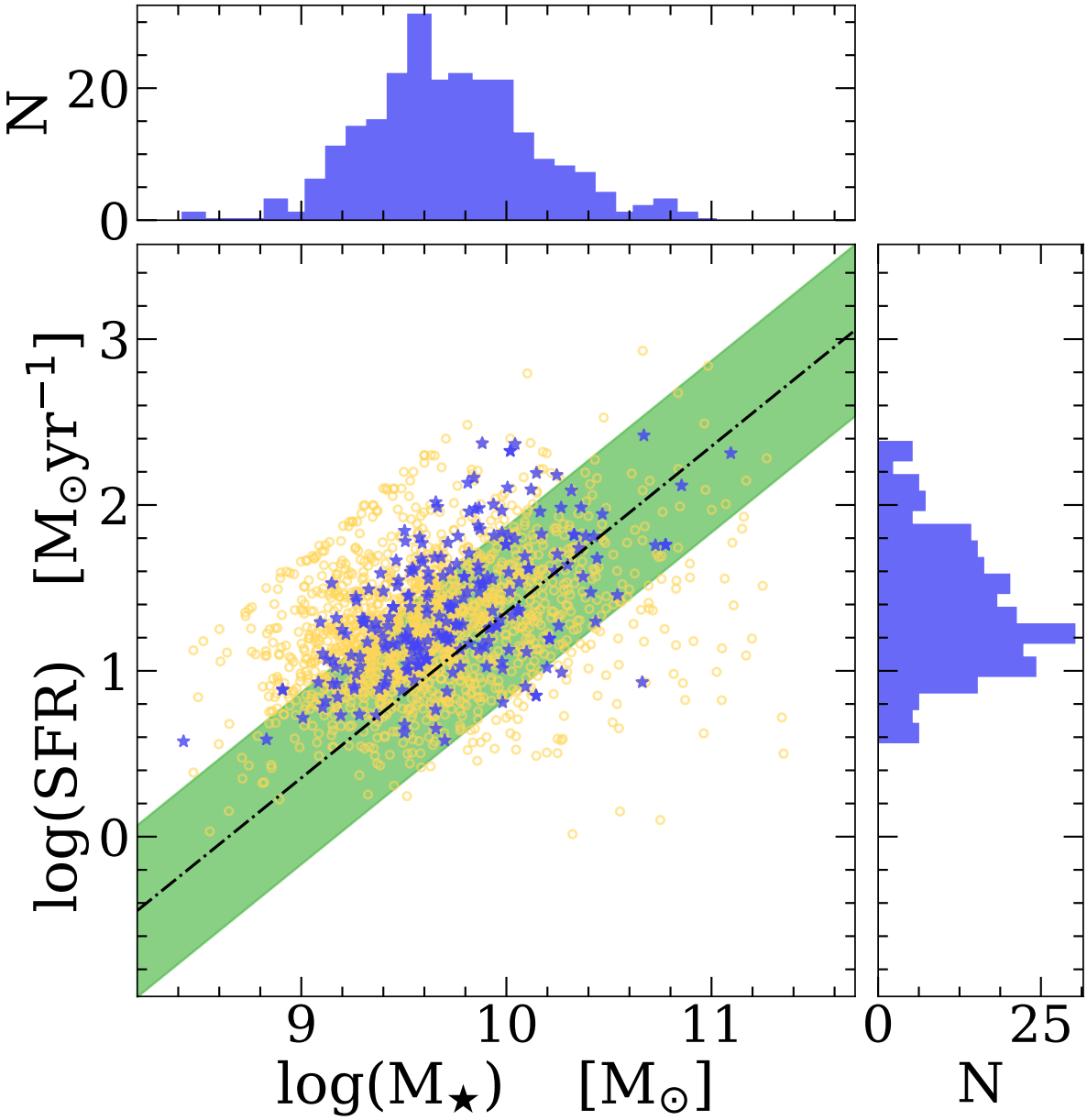

FIGURE 4.1: SFR versus stellar mass for star-forming galaxies at $z > 1.5$ selected from the VUDS survey (yellow circles) and the 238 star-forming galaxies (blue stars) analyzed in this work. The black dot-dashed line shows the main sequence of star-forming galaxies (SFG) for $1.5 < z < 2.5$ including its $\pm$3dex width represented by the green shaded region, as defined by (Tasca et al., 2015).

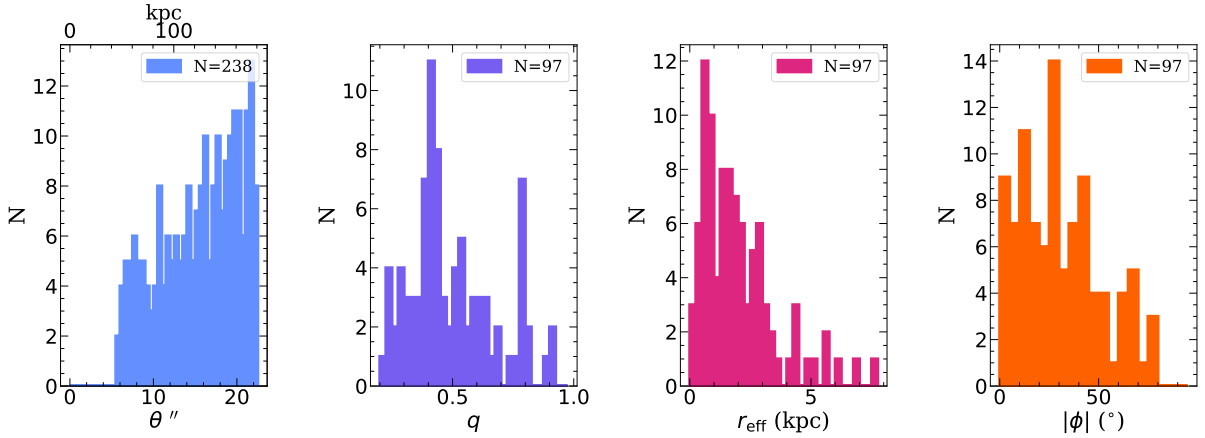

FIGURE 4.2: Projected angular separation (θ) among galaxy *foreground-background* galaxy pairs, axial ratio (q), effective radius (r_{eff}) and azimuthal angle (ϕ) distributions of the star-forming (*foreground*) galaxies used in our analyses. Morphological parameters were obtained from the parametric measures of Ribeiro et al., 2016, see section 4.2 for details.

and is limited to a 23″ maximum projected angular separation distance among galaxy pairs, which correspond to 187.2 kpc at z=2.6. This sample is then split into four different bins according to their angular projected separation: $\theta \leqslant 11\farcs8$, $11\farcs8 < \theta \leqslant 16\farcs5$, $16\farcs5 < \theta \leqslant 20''$ and $20'' < \theta \leqslant 23''$, identified as samples S1, S2, S3, and S4 respectively and were defined in such a way that each bin contains approximately the same number of galaxies(see Table 4.3) providing a comparable S/N for each composite spectra. These angular projected separation bins correspond to projected physical distances (hereafter impact parameters) b: $\leqslant$ 68.6 kpc, 68.6 kpc $< b \leqslant$113.5 kpc, 113.5 kpc $< b \leqslant$ 146.2 kpc, and 146.2 kpc $< b \leqslant$ 172.8 kpc for samples S1, S2, S3, and S4, respectively. We note that the conversion from angular separation to physical impact parameter varies $\pm$3% over the full redshift range $(1.5 < z < 4.5)$ of the *foreground* galaxy sample, thus in the following impact parameter b and projected angular separation θ will be interchangeably used. Table 4.3 contains a summary of the statistical properties of the galaxy pair samples.

To generate our *fg* and *bg* composite spectra we co-added individual spectra as follows. For each pair of galaxies, the spectrum of the *fg* was:

1. shifted to its own rest-frame;
2. continuum-normalized using the full wavelength range[1];
3. resampled[2] to a common wavelength resolution $\Delta\lambda$, defined by the maximum of the shifted wavelength resolution ($\Delta\lambda_{shf\_fg}$) distribution of the galaxy sample used to generate the composite spectra (e.g. $\Delta\lambda \sim 2$ for fg composite spectra as shown in Figure 4.4);
4. smoothed with a Gaussian kernel with width size $\Delta\lambda$ defined before.

A similar approach was used to produce stacked spectra of the *bg* galaxies, each individual *bg* galaxy spectrum was:

[1]Full observed wavelength coverage: $3650 < \lambda < 9350$ [] which at $z \sim$2.6 translates into a rest-frame wavelength coverage: $1013 < \lambda < 2597$ []

[2]We have made use of PYSYNPHOT (Blagorodnova et al., 2014) to resample our spectra.

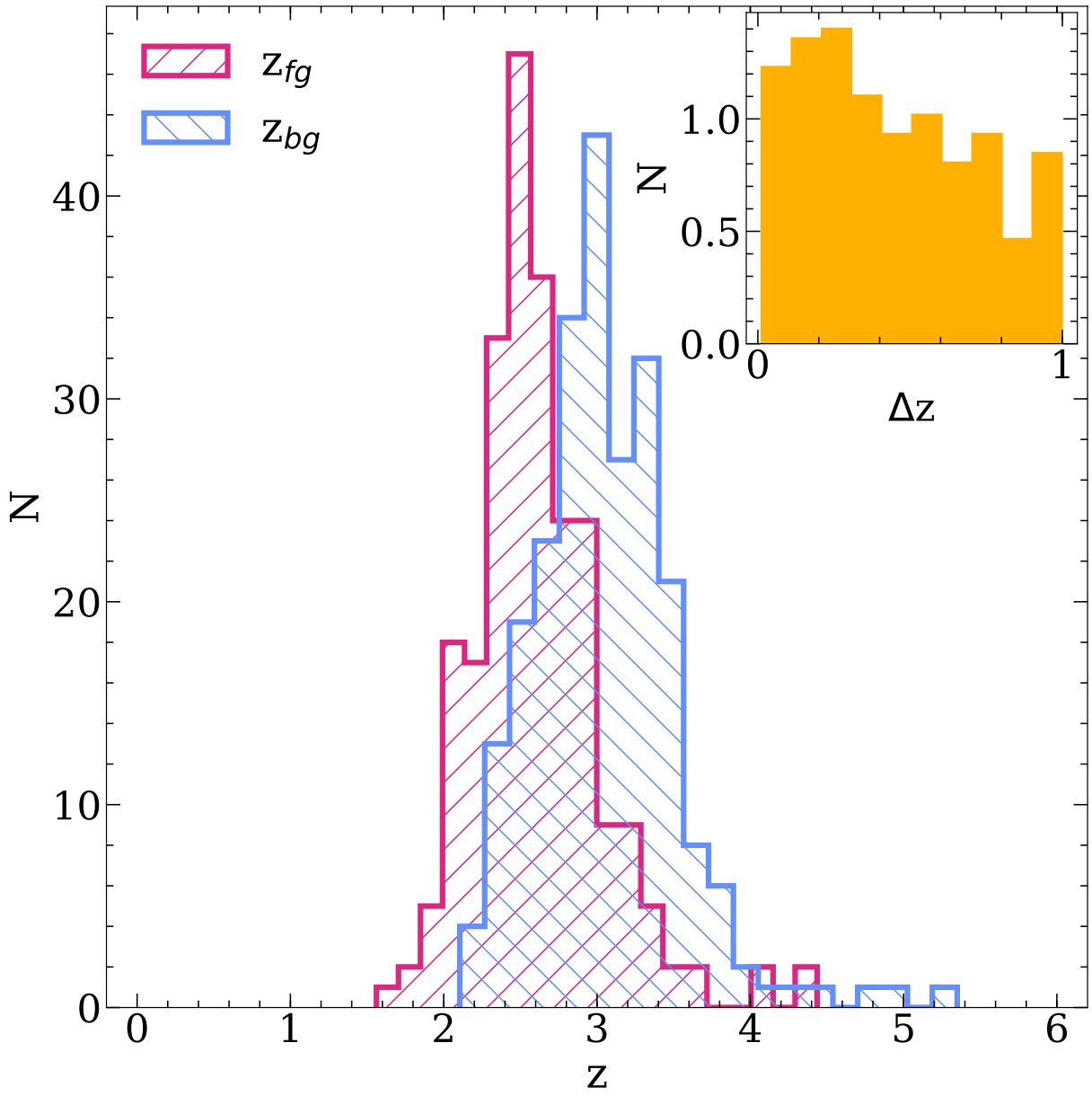

FIGURE 4.3: Redshift distribution of the star-forming galaxy pairs (*foreground* and *background*) selected in this work. The $\Delta z = z_{bg}$-z_{fg} distribution is also included in the top-right corner.

1. shifted into the *fg* galaxy's rest-frame using the same systemic redshift applied to their corresponding *fg* galaxy spectrum;
2. continuum normalized using the full wavelength range[1];
3. resampled to a common wavelength resolution $\Delta\lambda$, defined by the maximum of the shifted wavelength resolution ($\Delta\lambda_{shf\_bg}$) distribution of the galaxy sample used to generate the composite spectra;
4. smoothed with $\Delta\lambda$ Gaussian kernel as defined before;
5. masked the strong interstellar absorption features (see Fig 4.4 and Table 4.2) located at the redshift of each *bg* rest-frame which can potentially contaminate the composite signal at the *fg* rest-frame.

Finally the *foreground* and *background* spectra were co-added independently to produce composite stacked spectra; in all cases, for each spectral bin, we calculated both the average and the median value, eventually producing both an average and median coadded spectrum.

4.4 Results

Rest-frame UV spectra of star-forming galaxies at redshift $z \sim 3$ are commonly dominated by the emission of O and B stars; the CGM and/or IGM media imprint absorption features on top of this UV continuum (Sargent et al., 1980; Bergeron, 1986; Bergeron and Boissé, 1991; Lanzetta et al., 1995). Composite spectra can provide different l.o.s. of the average absorption strength produced by the gas located in these media (Adelberger et al., 2005; Shapley et al., 2003). Figure 4.4 shows the median and average composite spectra by stacking the 238 *foreground* galaxies. The lower panel shows a histogram of the fraction of galaxies contributing to each spectral bin of the co-added spectrum. In our analysis, the separation zero ($b = 0$) l.o.s. defines the interstellar medium properties of the *foreground* galaxies, while larger separations ($b > 0$) l.o.s. define the properties of the CGM around the *foreground* galaxies at different separations.

While the l.o.s that we use to study the CGM cross through the whole CGM at a given separation, the information about the ISM comes only from the absorptions produced by the gas located in the half galaxy that is the closest to the observer. For this reason, in order to compare the strength of the absorptions at separation 0 (e.g. the ISM) and at separation > 0 (e.g. the CGM), the former need to be corrected for this incompleteness. Following Steidel et al., 2010, we apply the following factors: 1.45 for low-ionization species(Si II, C II), 1.70 for Si IV and ~ 2 for C IV. The different l.o.s. probed by the *background* galaxy's light passing through the *foreground* CGM help us to trace neutral and ionized gas in HII star-forming regions and the large-scale stellar winds produced by star-formation activity (Shapley et al., 2003). The main spectral features identified in our *fg* composite spectra (Figure 4.4) in the 1100-2000Å range are summarized in Table 4.2 and include: H I(Lyα) emission/absorption (blue), low-ionization state metal absorption lines (cyan), intermediate-ionization state metal absorption lines (peach), high-ionization state metal absorption lines (magenta), interstellar fine-structure emission line (green), absorption stellar photospheric lines (gold), emission nebular lines (lime), and emission/absorption lines associate with stellar winds (indigo)(Halliday et al. 2008; Le Fèvre et al. 2015; Shapley et al. 2003; OTELO [3]).

In the 900–1900 Å range, we have explored the following absorption lines: Lyα (λ 1215.7 Å), O I+Si II ($\lambda\lambda$ 1303.2 Å), C II (λ 1334.5 Å), Si IV ($\lambda\lambda$ 1393-1402 Å), Si II (λ 1526.7 Å), C IV ($\lambda\lambda$ 1548.2-1550.8 Å), Fe II (λ 1608.5 Å), Al II (λ 1670.8 Å) and Al III (λ 1862.8 Å). First we present

[3]OSIRIS Tunable Emission Line Object survey http://research.iac.es/proyecto/otelo/pages/data-tools/spectral-line-summary.php

TABLE 4.2: Main spectral features observed in our VUDS stacked spectra in the 1100-2000 Å rest-frame range.

Spectral line	[Å]	Type
1176 1206 C III	1192	IIS absorption
Si II	1192	LIS absorption
Si III	1192	IIS absorption
Lyα	1215.7	H I
N V	1238/1242	Photospheric
Si II	1260	LIS absorption
Si II*	1264.0	Interstellar
O I+Si II	1303.2	LIS absorption
Si II*	1309.0	Interstellar
C II	1334.5	LIS absorption
O IV	1343.0	Photospheric
Si IV	1393.8/1402.8	HIS absorption
Si III	1417	Photospheric
S V	1501.8	Photospheric
Si II	1526.7	LIS absorption
C IV	1548.2/1550.8	HIS absorption
Fe II	1608,	LIS absorption
Fe II	1610,	LIS absorption
He II	1640	Stellar wind
O III]	1660/1666	Nebular
Al II	1670.7	LIS absorption
Ni II	1709.6	LIS absorption
N IV	1718.5	Stellar wind
Ni II	1741.5/1751.9	LIS absorption
Si II	1808	LIS absorption
Al III	1854.7/1862.7	IIS absorption
Si III]	1889	Nebular
C III]	1908.7	Nebular

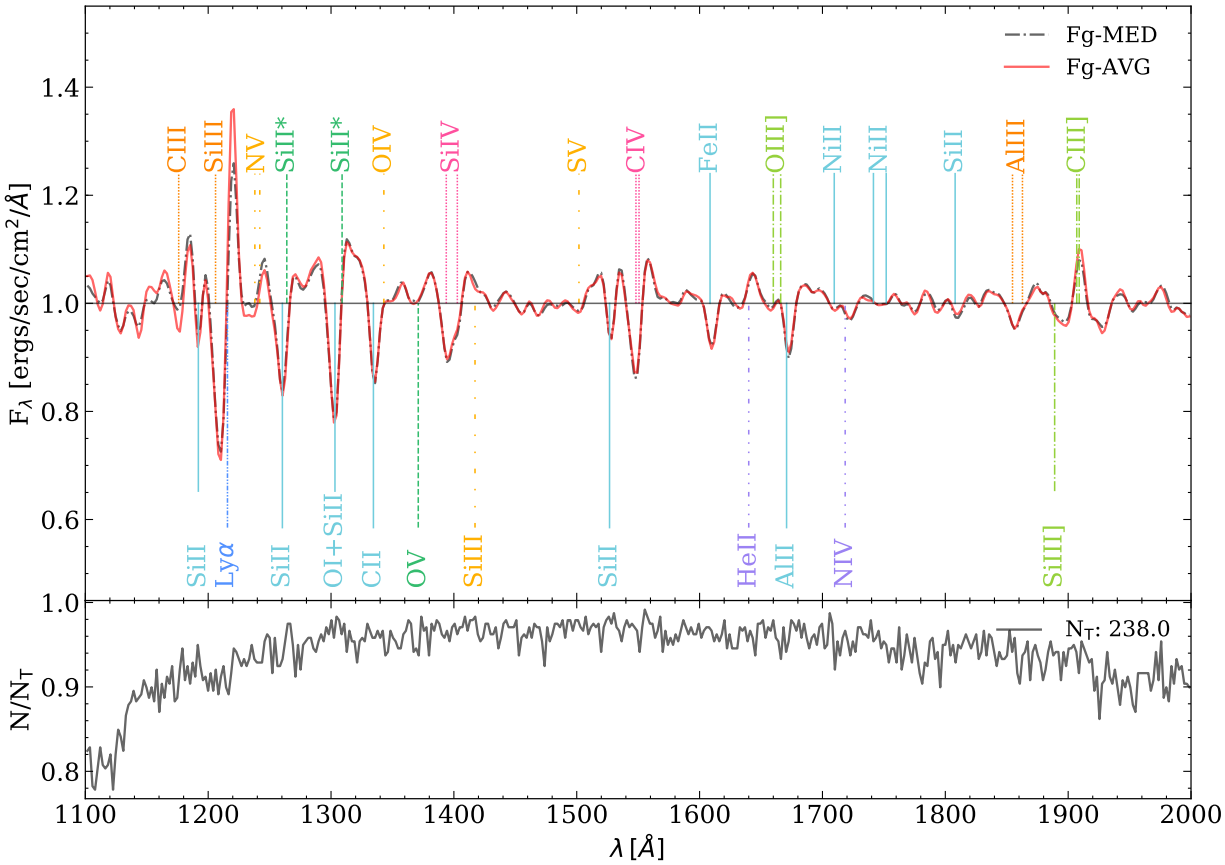

FIGURE 4.4: Top: Median (black) and average (red) composite spectra shifted to rest-frame of 238 *foreground* galaxies with projected angular separations $< 23''$ ($b < 187.2$ kpc at z=2.6). Bottom: The fraction of contributing individual spectra to the composite spectra per unit wavelength. Several spectral lines of interest are marked: H I (Lyα) emission/absorption (blue), low-ionization state metal absorption lines (cyan), intermediate-ionization state metal absorption lines (peach), high-ionization state metal absorption lines (magenta), interstellar fine-structure emission line (green), absorption stellar photospheric lines (gold), emission nebular lines (lime), and emission/absorption lines associated with stellar winds (indigo).

TABLE 4.3: *Foreground-background* (*fg-bg*) galaxy pair statistics according to their projected angular separation (θ). Column 1: Sample ID; column 2: number of galaxies per sample; column 3: range of angular separation of the *fg-bg* pairs; column 4: mean angular separation of the *fg-bg* pairs within the θ range; column 5: range of the impact parameter in kpc assuming z_{med} within the projected separation bin for conversion; column 6: mean impact parameter within the θ range in kpc; column 7 and 8: redshift ranges and mean redshift of the *foreground* galaxies sample within their respectively θ range, and columns 9 and 10: redshift ranges and mean redshift of the *background* galaxies sample within their respectively θ range.

ID	N	θ	$\langle\theta\rangle$	b (kpc)	$\langle b \rangle$ (kpc)	z_{fg}	$\langle z_{fg} \rangle$	z_{bg}	$\langle z_{bg} \rangle$
c1	c2	c3	c4	c5	c6	c7	c8	c9	c10
ALL	238	<23″	15.″7 ± 4.″9	13.8 - 187.2	125.0 ± 39.5	1.5-4.4	2.60	2.1-5.3	3.04
S1	59	<11.″8	8.″7 ± 2.″0	13.8 - 97.8	68.6 ± 16.3	1.5-4.3	2.55	2.1-4.9	2.98
S2	62	11.″8-16.″5	14.″4 ± 1.″4	92.6 - 135.9	113.5 ± 12.8	1.7-4.3	2.62	2.1-4.9	3.08
S3	60	16.″5-20″	18.″4 ± 0.″9	127.1 - 164.6	146.2 ± 8.8	1.9-3.6	2.66	2.3-4.5	3.11
S4	57	20″-23″	21.″5 ± 0.″8	146.7 - 187.2	172.8 ± 8.4	1.8-4.4	2.59	2.1-5.3	3.02

their equivalent widths as a function of the angular separation between galaxy pairs (θ) (see sec. 4.4.1). We then examine the correlations between the strength of Lyα, LIS (C II, Si II) and HIS (C IV, Si IV) lines as a function of different galaxy properties, including stellar mass, star formation rate (see sec. 4.4.2), effective radius ($r_{\rm eff}$) and the azimuthal angle (ϕ) (see sec. 4.4.3). We also explore the C II/C IV line ratio (see sec. 4.4.4) as a function of the projected angular separation, stellar mass, and star formation rate.

4.4.1 Radial Dependence

Here we present absorptions line produced by gas located in the CGM of star-forming galaxies at $z \sim 2.6$. Figure 4.5 shows the average absorption spectra obtained after stacking the *background* galaxy spectra at the redshift of the *foreground* galaxy as a function of their projected angular separation: $<$ 11.″8, 11.″8–16.″5, 16.″5–20″ and 20″–23″. We note that as a consequence of VUDS design and selection criteria, the number of galaxies with small projected angular separations($<$ 6″) is scarce. The strengths of the line absorptions were measured by fitting a single Gaussian profile to the stacked spectra. Equivalent widths (W_0) of each line profile are obtained by integrating the gaussian fit of each stacked spectrum around the central wavelength of the Gaussian fit to the line using an integration window within the $\pm 5\sigma$ range.

All equivalent width measurements are given in the rest-frame and we use positive (negative) equivalent widths to indicate absorption (emission). The errors on the equivalent width measurements are determined using a bootstrap approach. For each set of galaxy *background* spectra, a thousand co-added spectra are generated from random selections, with replacement, from that same sample, preserving the number of evaluated sources. For each of these co-adds, the line absorption equivalent widths are estimated. The 16th/84th percentiles of the distribution of equivalent widths are taken as error intervals for the original measurement. We note that due to the nature of star-forming galaxies, which show a diversity of spectral features (e.g., ISM absorption lines, photospheric stellar lines/nebular lines, and Lyα emission), the absorption lines in our composite spectra show both an emission and absorption component. The emission components can be produced by the same transition responsible for producing the absorption line (e.g. Lyα), produced by nearby fine-structure transitions or in some cases they can be completely absent.

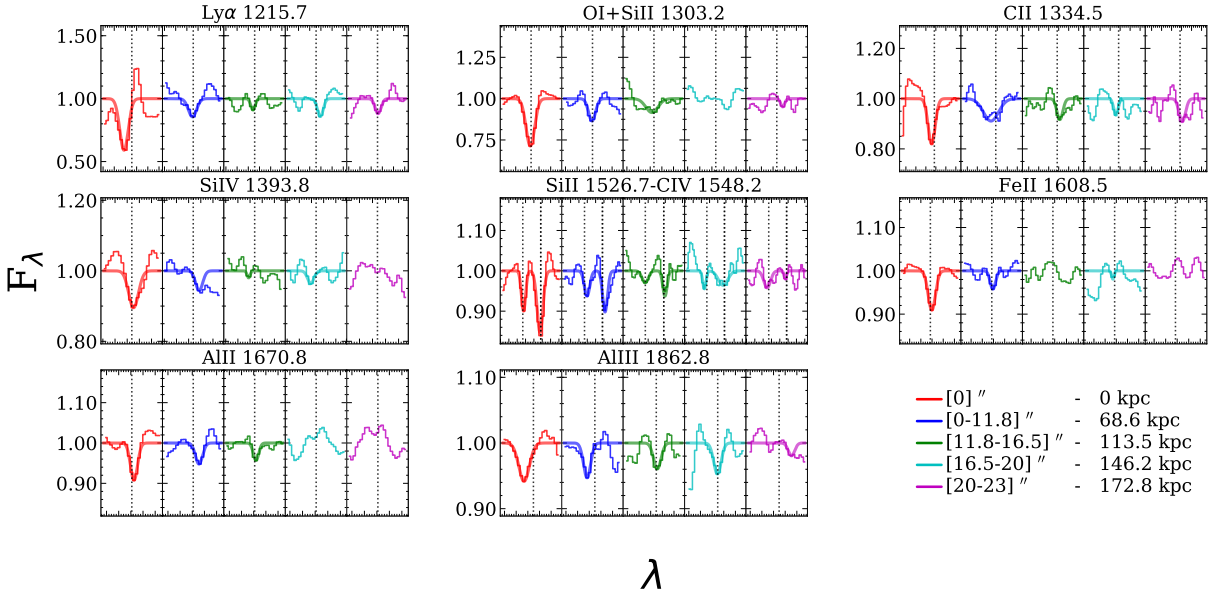

FIGURE 4.5: Median absorption lines (thin lines) detected from the *foreground* (red) and *background* galaxy composite spectra split into their corresponding projected angular separations: <11.″8 (blue), 11.″8-16.″5 (green), 16.″5-20″ (cyan) and 20″-23″ (magenta); bold lines indicate the gaussian profile fit to measure the strength of the line absorptions (see text).

Figure 4.6 shows the radial profiles of the absorption rest-frame equivalent width obtained from the average (red) and median (blue) stacked absorption specra presented in Figure 4.5. Median composite spectra are expected to be free of artifacts and contamination such as sky residuals, unexpected absorption/emission features in the *background* galaxy spectra. On the other hand, the average composite spectra could be affected by strong absorption lines coming from individual l.o.s. Median and average composite spectra are in general concordant, tracing similar trends. We also tested other combination techniques, including straight average, average-sigma-clipping and average-continuum-weighted, which produce very similar composite spectra. Table 4.4 contains a summary of the measured equivalent widths as a function of the projected angular separation, including the significance (in terms of S/N) of the detections. Noise estimations were computed with the DER_SNR[4] algorithm (Stoehr et al., 2008) on continuum bandpass adjacent to each central absorption line. We limit our analyses to detections with S/N ≥ 3, however, upper limits with $S/N < 3$ are also included and highlighted using solid black symbols and arrows in Figure 4.6, as these detections are useful to outline the possible correlations/trends of the profiles. We note that some precautions should be taken when interpreting the absorption strenghts of these spectral features as they could not reflect the true conditions of the cold and hot gas CGM components. For instance, the balances among singly ionized species of some elements (e.g. Al, Cl) can be altered by dielectronic recombination (Black and Dalgarno, 1973; Watson, 1973; Jura, 1974) or ion-molecule reactions (charge exchange reactions of ionized species with neutral hydrogen and helium Steigman 1975). In fact, while the abundances relative to neutral hydrogen of some elements (e.g. O, N, P, Cl, Si, Cr, Mn, Fe, Ni) can be affected by factors of 2-10, Al is depleted by a factor of $\sim$ 100 (York and Kinahan, 1979), making Al II a biased tracer of the neutral gas phase. In addition, Fe II is contaminated by Fe IV (λ 1610 Å) and Fe II (λ 1611.5 Å) lines (Judge, Jordan, and Feldman, 1992; Shull, van Steenberg, and Seab, 1983; Pickering et al., 2002), making difficult to determine accurately its absorption strength. Subsequently, double ionized species (e.g. Si III, Al III) are intermediate-ionization

[4] http://www.stecf.org/software/ASTROsoft/DER_SNR/

state (IIS) tracers of moderately photoionized warm gas sensitive to both diffuse ionized gas (traced by HIS) as well as denser, partly neutral gas. Depending on the species they can be correlated with cold (e.g. Si III Richter et al. 2016) or hot gas component (e.g. Al III Vladilo et al. 2001) and they can be used to infer the relative mix of neutral and ionized material (Howk, Savage, and Fabian, 1999).

We note, that the composite spectra considering *foreground* (down-the-barrel) galaxies from our $fg-bg$ galaxy pairs split by separation, do not show any significant dependency of the W_0 of absorption lines with impact parameter b, which show an average variance of $\leq 15\%$ among the absorption lines included in 4.6. This is in agreement, with the $< 10\%$ variance that Steidel et al., 2010 reported for their brightest absorption lines. Considering the *background* galaxies from our $fg-bg$ galaxy pairs split by separation, our radial profiles show a general negative gradient as reported by previous works. As the impact parameter increases, the strength of the detected absorption feature decreases. This is the case for all the spectral lines considered in our analysis. Recently, Kacprzak et al., 2021 compiled measurements of low-ionization state absorption lines (O I, C II, N II, Si II), and high-ionization state absorption lines(C III, N III, Si III, C IV, Si IV, NV, and OVI) in the CGM of low-redshift ($z \lesssim 0.3$) galaxies with $9 \leq \log[M_\star/M_\odot] \leq 11$, using quasars as background spotlights. Measurements at low redshift (Bordoloi et al., 2018; Borthakur et al., 2015; Johnson et al., 2017; Liang and Chen, 2014; Prochaska et al., 2011; Werk et al., 2013) and high-redshift ($z \sim 2.3$) galaxies (Steidel et al., 2010) are also overplotted in Figure 4.6.

Although at low redshift these lines can be detected at distances up to 300 kpc, at high redshift using galaxy-galaxy pairs, Steidel et al., 2010 reported detections that are limited to 100 kpc; including 42 additional bright quasars-galaxy pairs that provide access to the low density gas in the CGM, they extended their Lyα detections up to 280 kpc. More recently, using galaxy images at $\langle z \rangle \sim 2.4$, Chen et al., 2020 measured the Lyα excess relative to the background intergalactic medium, probing the CGM gas up to impact parameters of 2000 kpc. Here, for star-forming galaxies at a mean redshift $\langle z \rangle = 2.6$, we report detections at distances up to 146 kpc and 172 kpc for HIS and LIS/Lyα, respectively. These results include Al III, which is detected for the first time in the CGM of high-redshift star-forming galaxies up to distances of $\sim$150 kpc. Low-ionization state lines (C II, Si II, Al II) show less steep radial profiles compared with high ionization lines. The LIS radial profile shows an abrupt decay at smaller radii. From separation zero to $\langle b \rangle \sim 68$ kpc, the strengths of C II, Si II and Al II are reduced by a factor of 1.7, 2.5 and 3.2, while Si IV and C IV are reduced by a factor of 6.8 and 4.5, respectively.

Steidel et al., 2010 reported that at a separation of $\langle b \rangle = 103$ kpc, lines can be hardly detected in their stacked spectra, low-ionization state metal absorption lines cannot be detected and C IV is detected with marginal significance. Here we are able to detect LIS (C II and Si II) and HIS (Si IV, C IV) both with S/N$\geq$ 3 up to $\langle b \rangle = 172$ kpc and 146 kpc separations, respectively. We note that beyond this separation ($\theta > 23''$=172 kpc) we are unable to detect any significant signal from the *background* composite spectra. This might be caused by differences in the S/N and resolution of the individual spectra used in the two analyses. The spectral line features considered here are more difficult to detect in our low resolution spectra compared to a high resolution spectra at the same S/N level. Higher resolution spectra could allow to resolve spectral lines that are blended (e.g. O I-Si II: $\lambda\lambda$ 1303-1307 Å, Si IV: $\lambda\lambda$ 1393-1402 Å), or that are affected by close photospheric/interstellar/nebular spectral lines(e.g. Fe II-Fe IV:$\lambda\lambda$1608-1610, Si II-Si II*: $\lambda\lambda$ 1260-1264), disentangling the spectral features and thus provide a more accurate W_0 measurements. Another possibility to explain these discrepancies, is that they might be the result of differences in the SNR of both parent dataset samples. We know that both parent samples adopted opposite observational strategies. On one hand, Steidel et al., 2004 deliberately kept short the total exposure times on their observations to maximize the number of galaxies for which redshifts could be measured. This led to a dataset with spectral quality (S/N) that varies considerably among their spectra (Steidel et al., 2004; Steidel et al., 2010), and that could be affecting their redshift determinations. On the other, VUDS provide an homogeneous dataset with integration times of

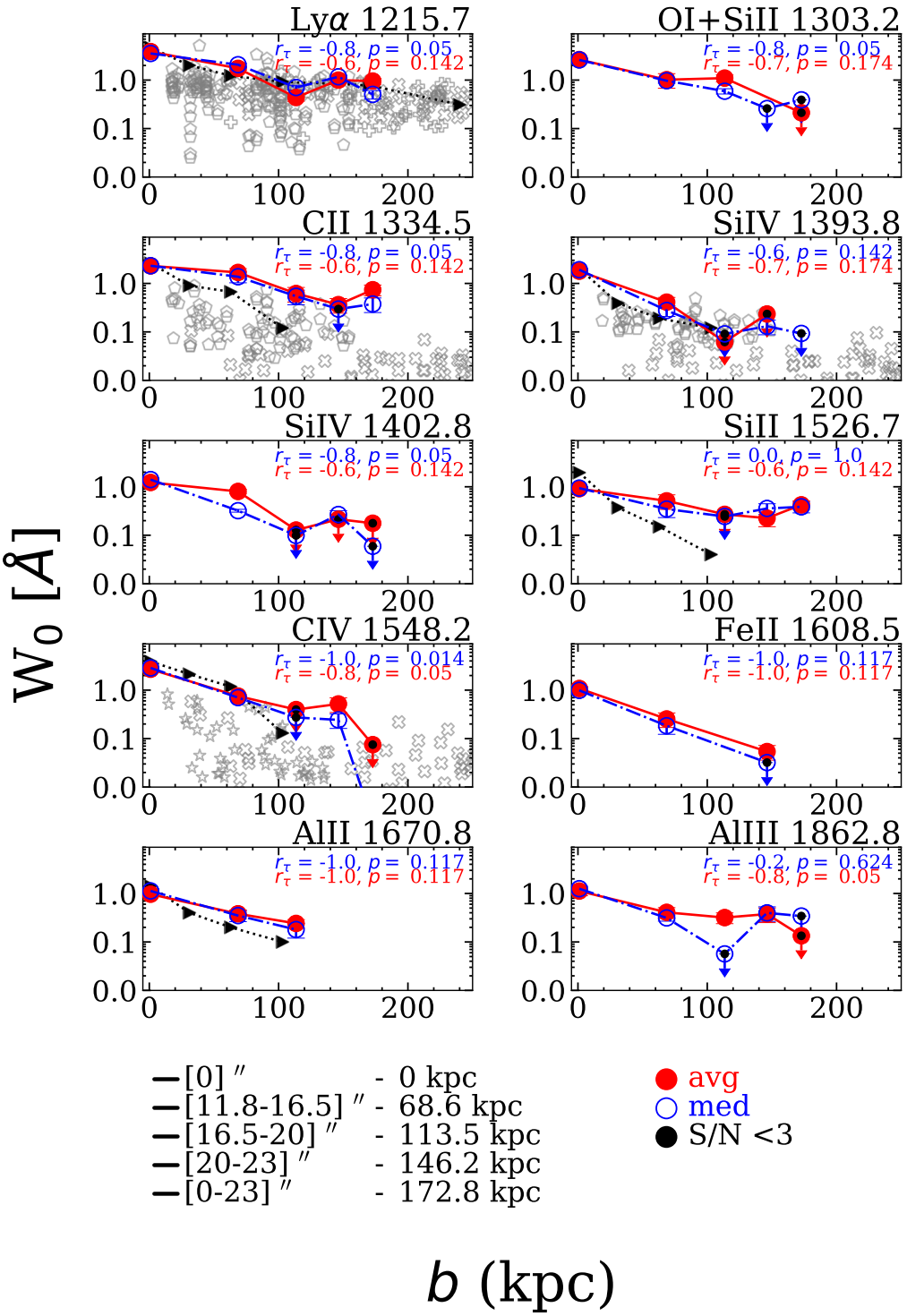

FIGURE 4.6: Rest equivalent width (W_0) as a function of the impact parameter (b) obtained from the line profiles in Fig 4.5, corresponding to the *foreground* composite spectra (0 kpc) and the *background* composite spectra at $\langle b \rangle$: 68.6 kpc (8.″7), 113.5 kpc (14.″4), 146.2 kpc (18.″4) and 172.8 kpc (21.″5). Average and median W_0 are shown in solid-red and open-blue symbols respectively, solid black symbols correspond to tenative detections with 2≤ SNR <3. Reported values from the literature including low-redshift values (open-gray symbols): Bordoloi et al. 2018 (stars), Borthakur et al. 2015 (pentagons), Liang and Chen 2014 (crosses), Prochaska et al. 2011 (diamonds), Werk et al. 2013 (pluses), and high-redshift values Steidel et al. 2010 black triangles. Error bars correspond to 1σ confidence intervals for average (red filled circles) or median (blue unfilled circles) values based on a bootstrap analysis. Additionally, the results from the Kendall-Tau correlation test, the correlation coefficients r_τ and their corresponding p-value (probability of no correlation) are also included.

$\simeq$14h per target, allowing to reach a S/N on the continuum at 8500 Å of S/N=5 (Le Fèvre et al., 2015). Moreover, for the purposes of this work we have considered galaxies with reliability flags (z_f = 3, 4) with 95-100% probability of being correct. However, it is not clear if similar constraints on their redshift determinations were adopted by Steidel et al., 2010 to define their galaxy-galaxy pair sample. This is crucial, as composite spectra can be affected by spectral offsets in the individual spectra. LIS and HIS spectral absorptions could be washed out or artificially boosted by considering individual spectra with low SNR and low reliability redshift determinations to generate composite spectra. In fact, it is possible that the spectra considered to generate our stacked spectra show an average SNR larger than the average SNR of the spectra considered by Steidel et al., 2010. If similar separations $\langle b \rangle$ are considered, Steidel's P3 sample at $\langle b \rangle$ = 103 kpc ($\langle \theta \rangle$ = 12.″5) and this work S2 sample b = 113.5 kpc ($\langle \theta \rangle$ = 14.″4), Steidel's P3 sample considers $\sim$ 5 times the number of objects (N=306) considered in our S2 sample (N=62). This would imply that our individual spectra have in average higher individual SNR compared to the average SNR of the dataset used by Steidel et al., 2010, allowing us to detect similar/weaker spectral absorptions at larger separations.

To asses the correlation between W_0 and b, we implemented a Kendall-Tau correlation test. The correlation coefficients r_τ and their corresponding p-value (the probability of no correlation) are provided in the same figure. In all cases we find a robust anticorrelation of the strength of the absorption line as a function of the impact parameter: in particular, Lyα, C II, C IV, and Fe II all show a strong correlation ($p < 0.05$), while we find that O I, Si IV, Si II, Al II and Al III present a flatter radial profile with that results in a lower significance of the anti-correlation($p \sim 0.1$). To asses the scale of the relationship between W_0 and b, we compute the slopes of the radial profiles shown in Fig 4.6. We find that Ly show a slope of -1.20. $\pm$ 0.01, LIS: O I+Si II, C II, Si II, Fe II, and Al II absorption lines show slopes -1.34 $\pm$ 0.01 -1.31 $\pm$ 0.01, -1.53 $\pm$ 0.02, -1.50 $\pm$ 0.07, and -1.44 $\pm$ 0.05 respectively, Al III show a slope of -1.38 $\pm$ 0.06, and HIS: Si IV and C IV absorption lines show, -1.10 $\pm$ 0.04 and -1.24 $\pm$ 0.01 respectively. If we focus to low and high ionization lines of the same species, and considered Si II–Si IV and C II–C IV absorption line pairs, we find that the slopes of these absorption lines are different at $\geq 5\sigma$ level. Compared with Steidel et al., 2010 radial profiles, our results show slopes that are different at a 5σ level for Si II and 3σ level for C II and Al II absorption lines. These differences suggest that within the CGM, cold and dense gas is more spatially extended in galaxies at $z \sim 2.6$ compared with galaxies at $z \sim 2.3$ and lower redshifts, as probed by Si II C II, in agreement to the expected higher covering factors of neutral gas at higher redshifts (Reddy et al., 2016; Du et al., 2018; Sanders et al., 2021). Compared with low-redshift CGM studies(see Figure 4.6), our Lyα, LIS and HIS rest-frame equivalent width radial profiles are at the upper envelope of the equivalent width measurements at lower redshifts, suggesting a potential redshift evolution for the CGM gas content that produces these absorptions.

4.4.2 Star formation and Stellar Mass Dependence

To explore the dependence of low- and high-ionization state absorptions with physical and morphological properties (i.e. star formation rate, stellar mass, galaxy effective radius and azimuthal angle) produced in the CGM of our high-redhift star-forming galaxy sample, we considered galaxy pairs at all projected distances ($b < 23''$) split by the corresponding galaxy property. A summary of the statistical properties of the galaxy pair subsamples divided by these properties can be found in the Appendix **??**. We note that Fe II, Al III, and Al II lines were excluded from our following analyses (see sec 4.4.1) Figure 4.7 (upper panels) shows the equivalent width of the absorption features as a function of stellar mass and SFR for LIS (C II, Si II), HIS (Si IV, C IV) and Lyα. We find that galaxies with high stellar masses (log[$M_\star/M_\odot$]>10.30) and high star formation rates (log[SFR/($M_\odot yr^{-1}$)]>1.93) show C IV (HIS) metal absorption with larger equivalent widths. On the other hand, galaxies with low stellar masses (log[$M_\star/M_\odot$]<9.26) and low SFRs

TABLE 4.4: Median absorption line strengths measured (W_0) in stacked spectra as a function of the average impact parameter ($\langle b \rangle$) of the sample: 68.6 kpc (N=60), 113.5 kpc (N=62), 146.2 kpc (N=60), and 172.8 kpc (N=57). The errors on the equivalent width (W_0) measurements correspond to 1σ confidence intervals based on a Bootstrap analysis (see sec. 4.4.1).

$\langle b \rangle$ (kpc) c1	W_0 [Å] c2	S/N c3	W_0 [Å] c4	S/N c5	W_0 [Å] c6	S/N c7	W_0 [Å] c8	S/N c9
Lyα 1215.7			O I-Si III 1303.2		C II 1334.5		Si IV 1393.8	
0.0	3.54 ± 0.02	58	2.61 ± 0.15	17	2.31 ± 0.08	20	1.91 ± 0.01	18
68.6	1.71 ± 0.13	14	0.97 ± 0.10	9	1.37 ± 0.02	4	0.28 ± 0.06	4
113.5	0.75 ± 0.05	9	0.59 ± 0.07	8	0.54 ± 0.01	3	0.09 ± 0.04	2
146.2	1.08 ± 0.13	13	<0.26	<2	0.30 ± 0.09	2	0.13 ± 0.19	3
172.8	0.46 ± 0.14	5	<0.39	<2	0.38 ± 0.10	3	<0.09	<2
Si IV 1402.8			Si II 1526.7		C IV 1548.2		Fe II 1608.5	
0.0	1.40 ± 0.05	67	0.94 ± 0.02	18	2.87 ± 0.11	20	0.99 ± 0.01	6
68.6	0.32 ± 0.06	15	0.35 ± 0.03	3	0.70 ± 0.04	13	0.18 ± 0.03	3
113.5	<0.10	<2	0.24 ± 0.09	2	0.27 ± 0.04	2	<0.03	<2
146.2	0.27 ± 0.31	5	0.36 ± 0.05	4	0.24 ± 0.02	3	—-	—
172.8	<0.06	<2	0.39 ± 0.04	4	<0.05	<2	—-	—
Al II 1670.8			Al III 1862.8					
0.0	1.13 ± 0.03	10	1.25 ± 0.01	8				
68.6	0.35 ± 0.03	4	0.31 ± 0.11	7				
113.5	0.18 ± 0.03	3	<0.06	<2				
146.2	—-	—	0.40 ± 0.02	3				
172.8	—-	—	<0.34	<2				

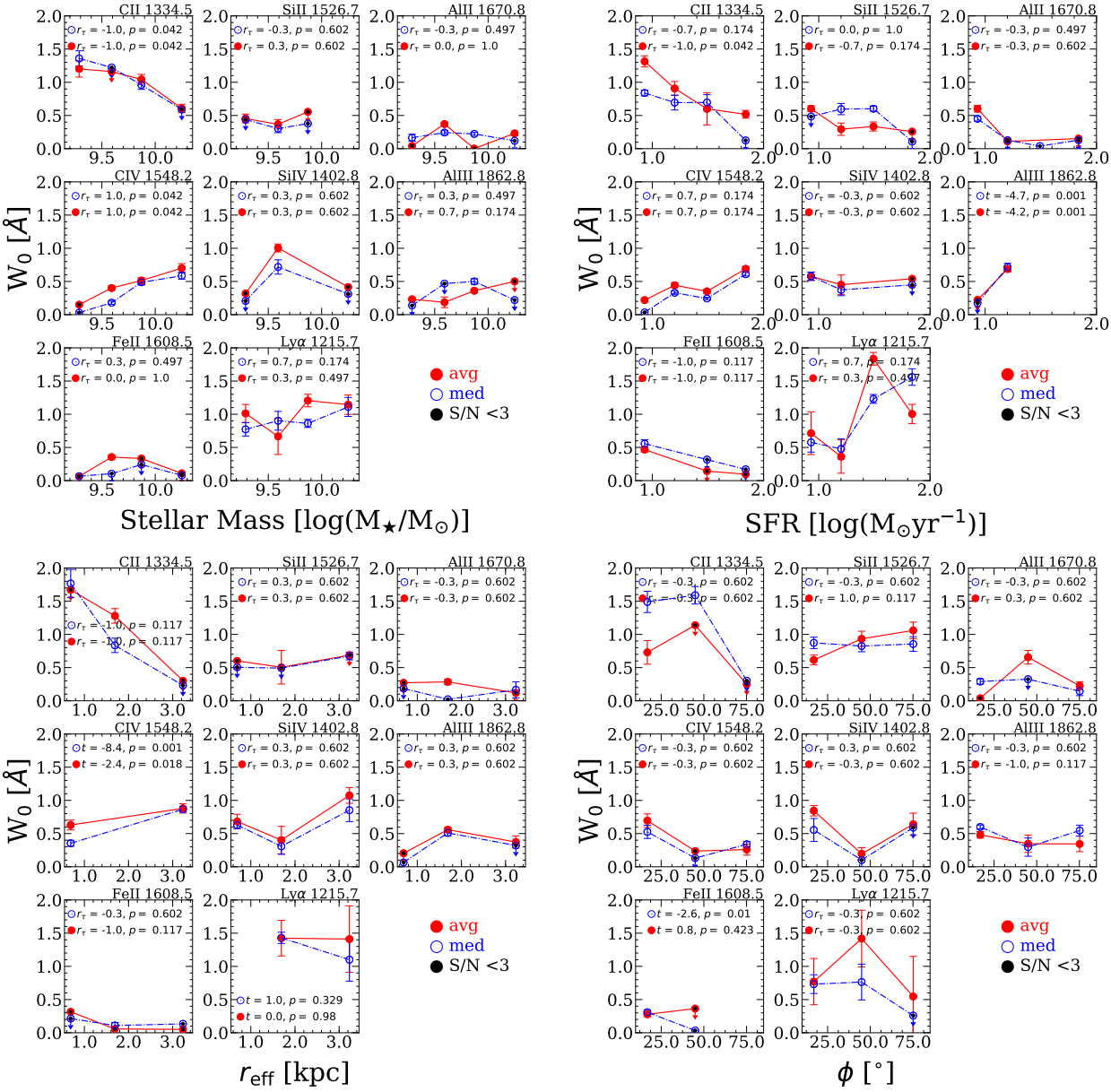

FIGURE 4.7: Rest equivalent width (W_0) of the absorption lines as a function of the *foreground* galaxy's stellar mass (log[$M_\star/M_\odot$]), SFR (log[$M_\odot yr^{-1}$]), effective radius ($r_{\rm eff}$) and azimuthal angle(ϕ). The W_0 measurements come from composite spectra taking into account galaxy pairs at all projected distances ($b < 23''$) and split by the corresponding galaxy property.

Stellar mass and SFR W_0 were obtained from composite spectra considering 238 *bg* galaxies, while $r_{\rm eff}$ and ϕ come from composite spectra considering 97 *bg* galaxies(see sec. 3.2 and Table 4.1). Average and median W_0 are shown in solid-red and open-blue symbols respectively, solid black symbols correspond to upper limits with SNR <3. Error bars correspond to 1σ confidence intervals for average or median values based on a Bootstrap analysis. The panels include the results from the Kendall-Tau correlation test: the correlation coefficients r_τ and their corresponding p-value (the probability of no correlation). The panels of absorption lines with detections in only two subsamples also show the results from Student's t-test: the difference between a pair of mean values given by the t coefficient and their corresponding p-value (the probability of significant difference among means).

(log[SFR/($M_\odot yr^{-1}$)] < 0.9) show C II (LIS) metal absorptions with stronger equivalent widths. Nevertheless, Si II and Si IV do not show a similar trend. This might be caused by the fact that we do not have Si II and Si IV detections with S/N>3 in all of our SFR and stellar mass bins.

In order to quantify the robustness of the trends highlighted in Figure 4.7, we ran a Kendall-Tau rank test for the absorption lines that are detected in at least 3 bins. We find that SFR and stellar mass are anti-correlated with C II, but they correlate positively with C IV. This would imply that C II is located preferentially in galaxies with low stellar mass(log[$M_\star/M_\odot$]<9.26) and low SFR (log[SFR/($M_\odot yr^{-1}$)] < 0.9) while C IV is detected in galaxies with high stellar mass (log[$M_\star/M_\odot$]>10.2) and high SFR (log[SFR/($M_\odot yr^{-1}$)] > 1.5). In fact, the slopes of the W_0 relationships with stellar mass and SFR for C II and C IV are 0.79 ± 0.13 , 0.61 ± 0.05 and 0.73 ± 0.08 , 0.55 ± 0.04, which are significantly different at $\geq 5\sigma$ level. We do not find any robust correlation between SFR and stellar mass with Si II, Si IV Fei II, Al II, Al III or Ly$_\alpha$, yielding a probability of no correlation above 60% in all cases. We also explored the combined effect of impact parameter with stellar mass and SFR; however, no clear conclusion was reached due to low-number statistics resulting in composite spectra with low S/N line detection.

4.4.3 Morphological Dependence

The strength of the observed metal absorption signatures in the CGM can be explored as a function of the azimuthal angle ϕ between the l.o.s. and the projected major/minor axis of the *foreground* galaxy. Here we define the azimuthal angle (ϕ) as the projected angle between the *background* galaxy l.o.s. and the projected minor axis of the *foreground* galaxy. Small azimuthal angles($\phi \sim 0°$) refer to l.o.s. passing along projected minor axis of the *foreground* galaxy, while large azimuthal angles ($\phi = 90°$) refer to l.o.s. passing along the projected major axis of the *foreground* galaxy. The effective radius ($r_{\rm eff,circ} = r_{\rm eff}\sqrt{q}$ [5]) was obtained by fitting a single Sérsic profile with no constraints in the parameters and then was circularized using the galaxy ellipticity (Ribeiro et al., 2016). Alongside the effective radius, GALFIT provides other structural parameters: Sérsic index (n), the axis ratio of the ellipse (b/a) and the position angle, $\theta_{\rm PA}$. Out of the 238 galaxies evaluated in this paper, only 97 are in the COSMOS field, covered by HST imaging, and therefore have morphological parameters. To inspect the dependency of the LIS-HIS absorption strengths with the azimuthal angle (ϕ), we split our sample into three ϕ bins: [0-30]°, [30-60]° and [60-90]°. Figure 4.7 (lower panels) reports the equivalent width of different spectral features in bins of $r_{\rm eff}$ and ϕ.

To check and assess the robustness of possible correlations between the morphological parameters and the equivalent widths measured in the composite spectra for LIS, HIS and Ly$_\alpha$, we ran a Kendall-Tau rank test between W_0 and $\phi/r_{\rm eff}$. For lines detected in only two bins the correlation can not be assessed, therefore we estimated the significance of the difference between their absorption strength (W_0). To do so, we applied a Student's t-test to determine the probability that the W_0 variations between the low- and high $r_{\rm eff}/\phi$ populations are not statistically significant. According to the Student's statistics (t) a large p-value indicates that a large probability of the null hypothesis to be correct (the two samples are not statistically significant); a small p-value suggests that the difference is significant. Both, Kendall-Tau and Student's t-test results are quoted in Figure 4.7 in the corresponding panels.

Regarding the effective radius ($r_{\rm eff}$) of the galaxy, the Kendall-Tau test shows a mild anti-correlation with C II ($p < 0.117$), while it does not show any significant correlation with Si II and Si IV ($p >0.602$). We find a significant difference ($p < 0.01$) in the W_0 variations between small and large $r_{\rm eff}$ as shown by the Student's t-test. However, no correlation is found for Lyα. This suggests that C IV gas is preferentially located in the CGM of larger galaxies while C II gas is located in the CGM of smaller galaxies. Concerning the azimuthal angle, we do not find any significant correlation with ϕ in any of the spectral lines inspected, in agreement to what has been

[5] q is the axis ratio (b/a) of the elliptical isophotes that best fit the galaxy.

reported by (Chen et al., 2021) who inspected the azimuthal dependence of Lyα emission of 59 star-forming galaxies ($z_{med} \sim 2.3$). This is opposed to the low-redshift scenario, where galaxies show high-velocity biconical outflows oriented along the minor-axis and accreting material along the major-axis. This result could be linked to the metal distribution along the disk of star-forming galaxies as metal absorption systems are often compact and poorly mixed, where cool low-ionization metal absorbers have typical sizes of $\sim$ 1 kpc (Faucher-Giguère, 2017a), while high-ionization gas seen in absorption arises in multiple, extended structures spread over $\sim$100 kpc (Churchill et al., 2015; Peeples et al., 2019)

4.4.4 CII/CIV line ratio

A further inspection of the differences between LIS and HIS on the different galaxy parameters come from the C II/C IV equivalent width line ratio. We focus on Carbon ions as they provide stronger absorptions with higher S/N compared to aluminum or silicate ones. Figure 4.8 shows C II/C IV line ratio as a function of impact parameter, stellar mass, and star formation rate. C II/C IV line ratio appears to anticorrelate with impact parameter (b), stellar mass and star formation rate. Similarly to the analyses for individual line absorptions, we ran a Kendall-Tau to assess possible correlations for C II/C IV line ratio, and included in all panels of Figure 4.8. We confirm that the anticorrelations between C II/C IV ratio and impact parameter, stellar mass, and star formation rate are statistically robust. This suggests that C II is more important than C IV in the inner regions of these star-forming galaxies, while the opposite occurs in the outskirts at large separations.

On the other hand, star-forming galaxies and low-stellar mass with low-star formation rates show higher CII/CIV line ratio compared with galaxies that have high stellar mass and high star formation rates. Our results suggests that galaxies with higher star formation rates and large stellar masses are capable to sweep out the highly ionized gas (traced by C IV) farther away from the galaxy with respect to less star-forming and less massive galaxies. Another possible explanation is that more active and massive galaxies have stronger ionizing fluxes, able to ionize gas at larger distances compared with less massive and less star-forming galaxies. Recent studies have shown that fast and energetic outflows can push material away from the central regions in star-forming galaxies, more effectively in galaxies with large SFR (with a weaker dependence on stellar mass; Heckman et al. 2015; Cicone, Maiolino, and Marconi 2016; Trainor et al. 2015; Feltre et al. 2020.) The presence of an AGN can make this effect even more dramatic, as shown by an enhanced gas budgets in H I and low-ionization gas in high-redshift ($z > 2$) galaxies (Prochaska, Lau, and Hennawi, 2014), suggesting larger accretion rates or a net gain of cold gas in the CGM in these star-forming galaxies (Faucher-Giguère et al., 2016). However, the physical mechanism through which the AGN removes and/or heats the gas and suppresses accretion is not clear (Tumlinson, Peeples, and Werk, 2017). Determining the nature of the source responsible for ionizing the gas in the CGM is crucial to improve our understanding of the multi-phase CGM, but is beyond the scope of this paper.

4.4.5 Lyα-emission

As we already noted in section 4.4.1 (Figure 4.5), the Lyα emission component is clearly detected in our composite spectra. Figure 4.9 shows the Ly$\alpha_{\rm em}$ rest equivalent width as a function of the impact parameter. We find that Ly$\alpha_{\rm em}$ decreases as a function of the impact parameter b similarly to what Chen et al., 2021 reported from 2D Ly$\alpha_{\rm em}$ maps. We also explore the Ly$\alpha_{\rm em}$ equivalent width strength as a function of the galaxy stellar mass, star formation rate and azimuthal angle. However, we do not find any significant correlation in these cases. This might be caused by the fact that at $z \sim$2 the Ly$\alpha_{\rm em}$-stellar mass relation is weaker compared with galaxies at higher redshifts (Du et al., 2018). Another possibility is the fact that our Ly$\alpha_{\rm em}$ measurements come

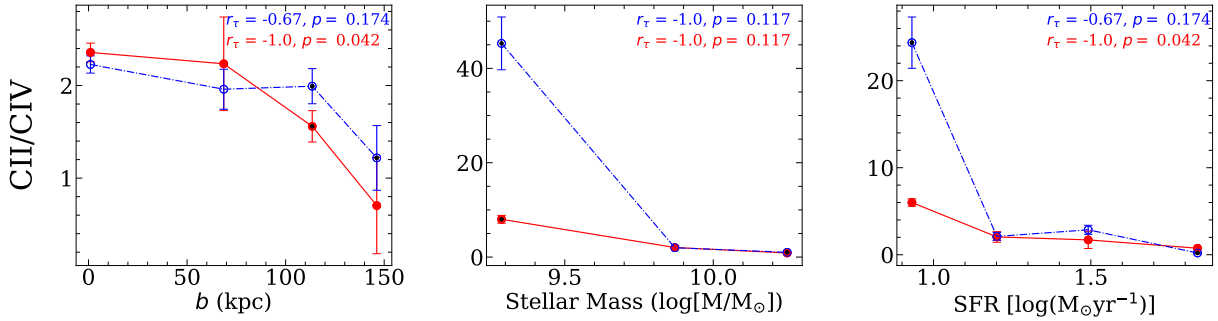

FIGURE 4.8: CII/CIV W_0 line ratio as a function of the impact parameter b, and the *foreground* galaxy's stellar mass and SFR. CII/CIV W_0 were obtained considering the exact same set of *fg-bg* galaxy pairs. Average and median W_0 are shown in solid-red and open-blue symbols respectively, solid black symbols correspond to tentative detections with 2$\leq$ SNR <3. Error bars correspond to 1σ confidence intervals for average or median values based on a Bootstrap analysis.

from composite spectra, hence coming from star-forming galaxies with and without direct Lyα_{em} detections (EW$\leq$ 0, EW$>$ 0 and EW$\geq$ 20 Le Fèvre et al. 2015; Hathi et al. 2016), covering a wide range of stellar masses and star formation rates which may have diluted a real Lyα_{em} signal (Steidel et al., 2011).

4.5 Discussion

Analyses of low and high-ionization state absorption features and their dependence on stellar mass, star formation rate, and galaxy inclination have been widely explored at $\lesssim$ 0.5 (see Tumlinson, Peeples, and Werk 2017; Kacprzak 2017). At high-redshift however, the studies of the CGM are limited. Steidel et al., 2010 used 512 close ($< 15'' = 124$kpc) angular pairs of z ~2–3 (z_{bg} ~2.3) galaxies to map the cool and diffuse gas around galaxies. They found strong evidence suggesting the presence of superwind outflows and proposed a simple model of the gas in the CGM, where cool gas is distributed symmetrically around every galaxy, accelerating radially outward with the outflow velocity increasing with radius. Later, Turner et al., 2014 and Lau, Prochaska, and Hennawi, 2016 reported detections that suggest that in galaxies at $\langle z \rangle = 2.4$ the CGM extends at least up to 180 kpc. Moreover, the mass in metals found within the halo is substantial and equivalent to ~25% of the metal mass within the interstellar medium (Rudie et al., 2019). This is, however, a lower percentage than what has been reported from studies in low-redshift galaxies (Werk et al., 2014), which suggests a considerable redistribution of the metal content of galaxies in an inside out fashion over the last ~8.5 Gyr. We note that eight of the nine resonance Si II transitions fall within the [900-1900]Å wavelength range considered here: λ989, λ1020 , λλ1190 − 1193, λ1260, λ1304 λ1526, and λ1808 (Shull, York, and Snow, 1981). Lines located blueward to Ly$_\alpha$ are not included in our analyses, due to the low coverage of our composite spectra at this wavelength range and because UV continuum level blueward to Ly$_\alpha$ is particularly sensitive to the dust content, metallicity and the age of the stellar population (Trainor et al., 2015) and their strength could be affected by IGM absorptions (Shapley et al., 2003). The λ1304 component is blended with O I λ1302 absorption line and is close to excited fine-structure emission transitions that could lower W_0 measurements (Trainor et al., 2015). Finally, λ1526 is the least resonance component affected by blends (Shapley et al., 2003) and is the strongest Si II line among their counterparts. In this work, we chose λ1526 for our Si II W_0 computations as this component is free of blending effects due in our low spectral resolution dataset. However, as noted by Jones, Stark, and Ellis, 2018 Si II transitions probe diverse optical depths,

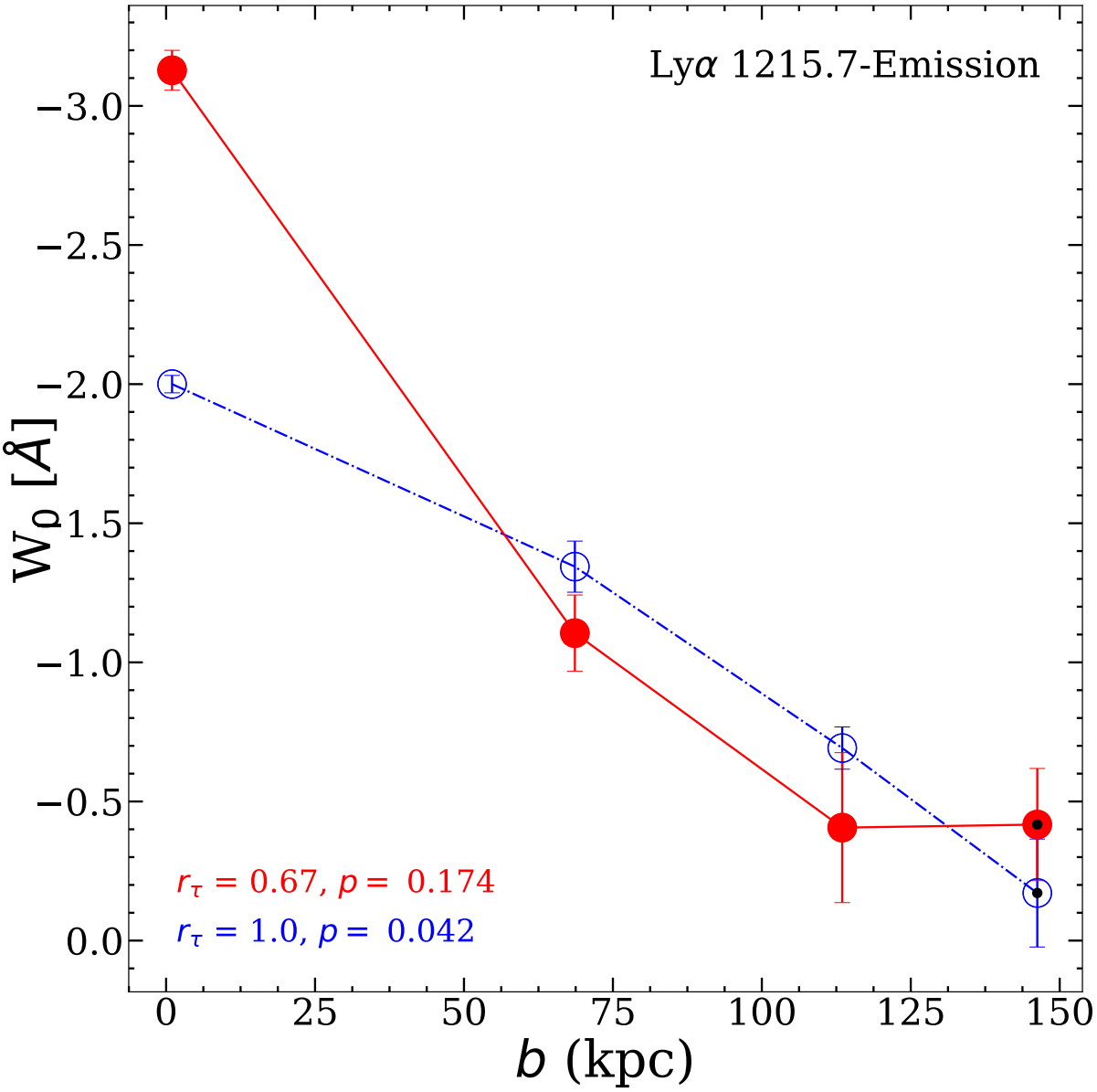

FIGURE 4.9: Rest equivalent width (W_0) for the Lyα emission as a function of the impact parameter (b) obtained from the average (solid red-line) and median (dot-dashed blue-line) composite spectra. Error bars correspond to 1σ CIs for average or median values based on a Bootstrap analysis.

and hence the most accurate way to compute Si II absorption strength is to consider the contributions of all the Si II resonance components (λλλ1260, 1304, 1526) within the analysed range, by averaging their strenghts and deblending them from nearby spectral features that could affect their individual W_0 measurements. Nevertheless, different studies have adopted diverse strategies to compute the LIS (including Si II resonance components) W_0 strength. For example Jones, Stark, and Ellis, 2018 averaged Si II λλλ1260, 1304, 1526, O I λ1302, C II λ1334, Al II λ1670, Fe II λ2382 and Mg II λλ2796 − 2803 components, Ranjan et al., 2022 considered the average of the eight Si II resonance components to estimate the W_0 Si II absorption in high-z Damped Lyman α (DLA) systems, Du et al., 2016 averaged λ1526, Si II, Al II λ1670 Ni II λλ1741 − 1751, Si II λ1808 and Fe II λ2382 absorption lines to compute an overall LIS average absorption estimation, while later-on Du et al., 2018 considered λ1260, O I-Si II λλ1302 − 1304, C II λ1334, and Si II λ1526, for similar computations. The differences on the number of Si II resonance components considered for W_0 computations could be the reason why similar Si II trends as those of C II with SFR and stellar mass shown in Fig. 4.7 are not appreciated. In fact, as shown by Jones, Stark, and Ellis, 2018 different low-ions transitions(Si II , Fe II and Ni II) show a non-uniform covering fractions in the CGM of star-forming galaxies at high redshift ($z \simeq 2 - 3$).

In this work we have used a sample of 238 galaxy close pairs to probe the CGM around star-forming galaxies at $z \sim 2.6$. Our results show an anticorrelation between the equivalent width of the absorption lines and the impact parameter (b) for this high redshift star-forming galaxy sample, and are consistent with previous results at lower redshift. Here we detect Lyα/LIS and HIS absorption at distances up to 172 kpc and 146 kpc respectively. Our low-ionization state (C II, Si II), and high-ionization state (C IV Si IV) absorption lines detections shape an upper envelope of the equivalent width distribution coming from studies at low redshift (see Figure 4.6). This is further evidenced by the differences in the slopes of the W_0 radial profiles between low- and high-ionization state absorptions of the same ion species, where Si II–Si IV and C II–C IV absorption line pairs are different at $\geq 5\sigma$ level. Moreover, when compared with galaxies at $z \sim 2.3$ (Steidel et al., 2010) our results show a significance difference in their slopes at a 5σ level for Si II and 3σ level for C II and Al II absorption lines. These discrepancies between LIS and HIS suggest that, within the CGM, cold (T$< 10^{4.5}$K) and dense gas is more extended in galaxies at $z \sim 2.6$ compared with galaxies at $z \sim 2.3$ and lower redshifts, as probed by Si II, C II, Si IV C IV. These results suggests a potential redshift evolution for the CGM gas content which produce these absorptions. As higher covering factors of neutral gas lead to stronger absorption lines (Du et al., 2018), this suggests a higher content of neutral gas in high redshift galaxies compared with low-redshift galaxies. This concentration of neutral gas could represent a reservoir of gas that can be later accreted onto the galaxies to fuel future star formation (Hafen et al., 2019; Hafen et al., 2020).

We note that it is possible to increase the maximum angular projected separation($\geq 23''$) allowing to probe larger distances closer to the CGM and IGM boundary following Chen et al., 2020. However, we have limited our analyses to $23''$ ∼170kpc and galaxy spectra with highly reliable redshifts to guarantee detection with good S/N. Spectra with unreliable redshift measurements could wash out the expected metal absorptions and/or produce spurious features in the final composite spectra. This is further supported by the observed metallicity dependence with impact parameter, where LIS are preferentially located in the inner CGM (close to the galaxy; Lau, Prochaska, and Hennawi 2016) while HIS (e.g. O VI are expected to dominate the CGM at larger separations Shen et al. 2013) making it difficult to detect weak LIS absorptions at larger separations given their expected W_0.

4.5.1 LIS/HIS absorption dependencies.

At $\lesssim 1$, Churchill et al., 2000 explored a sample of 45 Mg II absorption systems in high resolution QSO spectra, and studied their spectra, together with the C IV and Fe II absorption profiles,

suggesting that the gas responsible for Mg II and C IV absorptions arises from gas in different phases, (i.e. gas producing HIS absorption features have typical temperatures T>10^5K Tumlinson, Peeples, and Werk 2017). Moreover, they observed an evolution of the absorbing gas, which is consistent with scenarios of galaxy evolution in which mergers and accretion of "protogalactic clumps" provide gas reservoirs responsible for the elevated star formation activity at high-redshift, while at intermediate and lower redshifts ($z \leq 1$), the balance of high- and low-ionization state CGM gas may be related to the presence of star-forming regions in the host galaxy (Churchill et al., 2000). Later on, Zibetti et al., 2007 found that early-type (quiescent, red) galaxies ($0.37 < z < 1$) are associated with weaker Mg II absorptions while stronger systems are located in late-type (star-forming, blue) galaxies. These results provided evidence that the SFR correlates with Mg II absorption strength caused by the presence of outflows from star-forming/bursting galaxies. This scenario is also supported by subsequent studies that demonstrated that SFR correlates with outflow velocity deduced from the Mg II absorption strength (Weiner et al., 2009; Martin et al., 2012; Tremonti, Moustakas, and Diamond-Stanic, 2007; Rubin et al., 2010), and by the correlation between the stellar mass and Lyα absorption strength (Bordoloi et al., 2018; Wilde et al., 2021).

Our detection of LIS and HIS absorption lines suggests that at $\langle z \rangle \sim 2.6$ C II and C IV features are correlated with star formation rate and stellar mass. C II is stronger in galaxies with low star formation rates and low stellar masses, while C IV is stronger in galaxies with high SFR and large stellar masses. These results are consistent with what has been reported for low-redshift galaxies in scenarios where LIS and HIS absorbers have different spatial distributions. Low-ionization state metal absorbers probe the gas that is less ionized than high-ionization state metal absorbers (Nagao, Marconi, and Maiolino, 2006) and thus they are expected to be located in gas regions with different density conditions (Burchett et al., 2016). Moreover, studies of low-redshift galaxies ($z \leq 0.5$) have shown that as a consequence of the interaction between a starburst-driven wind and the preexisting CGM at radii as large as 200 kpc, the CGM around star-forming galaxies with high star formation rates differs systematically compared to galaxies with lower SFRs, as probed by Lyα, Mg II, Si II, C IV, and O VI absorption lines (Tumlinson et al., 2011; Borthakur et al., 2013; Lan, Ménard, and Zhu, 2014; Heckman et al., 2017). However, as suggested by Cicone, Maiolino, and Marconi, 2016 and Gatkine et al., 2022, their correlation with stellar mass and star-formation rate in fact might be a consequence of a main-sequence offset, rather than simply a correlation with star-formation rate or stellar mass and as LIS/HIS covering factors can be affeceted by environmental processes (Dutta et al., 2021). Hence, caution should be taken when interpreting LIS/HIS correlations with SFR and/or stellar mass.

The origin of the reservoir of cold neutral gas around low stellar mass galaxies and low SFRs at these distances($\langle b \rangle \approx$ 120kpc see Appendix **??**) is quite uncertain. One explanation come from a soft radiation field unable to ionize HIS (i.e. C IV, Si IV), as the production of C IV, Si IV absorption features in the CGM, requires photons with energies >45 eV associated with hard ionizing radiation fields from massive stars, AGN, and radiative shocks Feltre et al., 2020; Trainor et al., 2015. In fact as shown by Gatkine et al., 2022 HIS are more affected by high-velocity outflows, they show a strong correlation with SFR and are ubiquitous in high-SFR systems. Another possible explanation comes from the galactic fountain scenario, predicted by cosmological galaxy formation simulations (Oppenheimer et al., 2010; Vogelsberger et al., 2013), and where the presence of cold low-ionization gas result from metal-rich gas ejected in previous star-formation episodes that fall back to the disk (Fraternali and Binney, 2006; Hobbs, Read, and Nicola, 2015). Moreover, we know that stellar winds are dominant in the inner region of the CGM <60kpc (Chen et al., 2020), and depending on their velocity, stellar winds in low mass galaxies might be able to expel material or be reaccreted as recycled material (Sánchez Almeida, 2017). However, if the velocity outflow is insufficient to eject material out into the IGM, the recycle time-scales in low-mass galaxies in which gas returns to the galaxy can be small as those in high-mass systems (van de Voort, 2017). In fact, Martin et al., 2012 detected Fe II Doppler shifts and the V_{max}-Mg II

values that suggest that outflows reach the circumgalactic medium with Mg II absorption at blueshifts as high as 700 km s^{-1}, reaching 70 kpc in 100 Myr, a short enough time period for the host galaxy to sustain SFR even if the SFR declines due to the outflow. Nevertheless, our measurements do not allow us to break-down the multiple components of the absorption features in our foreground galaxy ("down-the-barrel") composite spectra and detect blue-shifted offsets that could be related to high-velocity outflows. We note that it is possible to combine down-the-barrel and QSO/galaxy-galaxy pairs to unambiguously detect blue-shifted absorptions relative to the galaxy systemic velocity, and quantify independently the main properties of the detected outflow (Kacprzak et al., 2014; Bouché et al., 2016; Lehner, 2017)

Fig 4.7 (lower panels) shows the dependence of line absorption strength with galaxy's effective radius ($r_{\rm eff}$) and azimuthal angle (ϕ). Concerning the dependence of the absorption strength (W_0) with the size of the galaxy given by the effective radius ($r_{\rm eff}$), we find that LIS are stronger in smaller galaxies compared to HIS absorptions which are shown to be stronger in larger galaxies, in agreement with Rudie et al., 2019 who reported that LIS absorption occurs spatially closer to the galaxy, and gas producing HIS absorptions can be located well beyond the virial radius. Regarding the dependence with azimuthal angle, we do not find any significant correlation with ϕ for both LIS and HIS. However, these results are based on the fraction of galaxies for which we have morphological measurements ($\sim$ 40% of the parent sample). Thus, these similar morphological analysis using larger samples at these high redshifts, as galaxy orientation plays a major role in the measured strength of LIS and HIS. This has been shown at low-redshift from studies using down the barrel (Rubin et al., 2014; Bordoloi et al., 2014b) and QSO-galaxy pairs (Kacprzak et al., 2011; Bordoloi et al., 2011) analyses. Moreover, at z $\gtrsim$ 2 star-forming galaxies have clumpy morphologies (Förster Schreiber et al., 2011), with galactic winds that are mainly driven by outflows from prominent star-forming clumps (Genzel et al., 2011), and haven't formed yet an stable disk (if any) capable of collimate galactic winds into bipolar outflows (Faucher-Giguère, 2017b), indicating that the minor/major axis dichotomy, associated with rotation present at low-redshift (z<1) is not broadly applicable at z$\sim$2-3 (Law et al., 2012; Nelson et al., 2019; Price et al., 2020). Therefore, it is not obvious that, at high-redshift ($z \gtrsim 2$) the azimuthal angle can be determined and, if it can, it has any physical meaning.

The dependence of LIS and HIS absorption strength on the azimuthal angle has been explored in the literature to prove/disprove theories on how galaxies accrete gas from the intergalactic medium. Inflowing material along filaments in the IGM is expected to be the largest source of accretion (Kereš et al., 2005). Simulations have shown that accretion of metal-poor gas inflows occurs along the major axis of galaxies, where outflows are preferentially located along the semi-minor axis form bipolar outflows (Putman, 2017), and gas being accreted onto galaxies which later can trigger star formation has been supported from evidence collected by multiple CGM studies at low-redshift (Kacprzak et al., 2010; Kacprzak, Churchill, and Nielsen, 2012; Kacprzak et al., 2015; Kacprzak et al., 2019; Lan and Mo, 2018; Martin et al., 2019; Nielsen et al., 2015; Rubin et al., 2018; Zhu and Ménard, 2013; Tumlinson et al., 2011; Bordoloi et al., 2014a; Lan, Ménard, and Zhu, 2014). Recent cosmological hydrodynamical simulations examine the physical properties of the gas located in the CGM of star-forming galaxies as a function of angular orientation (Péroux et al., 2020). They found that the CGM varies strongly with impact parameter, stellar mass, and redshift. Moreover they suggest that the inflow rate of gas is more substantial along the galaxy major axis, while the outflow is strongest along the minor axis.

The correlations between C II and C IV with impact parameter, star formation rate, and stellar mass scenario of a multi-phase CGM where LIS absorptions are produced by denser gas located closer to the galaxy, whether this dense neutral gas component is part of an outflow or material falling back to the galaxy taking part of a galactic fountain that eventually could be funneled to the galaxy to sustain star formation activity (Kereš et al., 2005) is not clear and can not be assessed by our datasets. low-metallicity gas is funneled to the galaxies to sustain star formation activity (Kereš et al., 2005). On the other hand, HIS absorption features associated with strong stellar

winds produced by high star formation activity capable to ionize radiation in high stellar mass galaxies with high star formation activity sweeping out material to the outer regions of these galaxies (Putman, 2017; Bower et al., 2016; Oppenheimer et al., 2016; Voit et al., 2015).

Similar analyses including observations at different redshifts coming from different complementary surveys (e.g. VANDELS (McLure et al., 2018; Pentericci et al., 2018), zCOSMOS (Lilly et al., 2007; Lilly et al., 2009), VVDS(Le Fèvre et al., 2013), DEIMOS10K (Hasinger et al., 2018)), can help to increase the number of galaxy pairs with close angular separations($b < 6''$), deblend close spectral line features (e.g. C II-O IV λλ 1334.5-1343.0 Å; Si IV λλ 1393.8-1402.8 Å), and cover different low- and high-ionization state lines(e.g. O VI λλ 1032-1038 Å, Mg II λ 2798 Å). Additionally, as it has been shown AGN activity is dependent on stellar mass and SFR (e.g. Lemaux et al. 2014; Bongiorno et al. 2016; Magliocchetti et al. 2020), thus, studies considering *bg*/QSO−AGN galaxy pairs (Hennawi et al., 2006; Prochaska, Lau, and Hennawi, 2014) are needed to study the effect that the presence of an AGN has on feedback and quenching in star-forming galaxies at low- and high-redshifts.

4.5.2 C II / C IV line ratio.

A further inspection of the differences between LIS and HIS on the different galaxy parameters explored comes from C II/C IV line ratio. We found that C II/C IV line ratio anti-correlates with impact parameter, stellar mass and star formation rate. This implies that C IV is preferentially located at larger distances in more massive galaxies with higher star formation rates, while C II dominates at smaller impact parameters and is found preferentially in low stellar mass galaxies with low star formation rates. These results further support the picture of a multi-phase CGM where LIS line absorptions are produced by denser gas with lower temperatures (T$< 10^{4.5}$K) that is located close to the central galaxy while HIS line absorptions are produced by warm gas located at larger distances from the central galaxy. Simulations have shown that much of the ongoing gas accretion occurs towards the edges of the galaxies to avoid the dominant feedback(outflows) from the central regions (Stewart et al., 2011; Fernández, Joung, and Putman, 2012; Putman, 2017), however, we do not find supporting evidence of the low-redshift scenario where low-ionization state gas infalls along the major axis of star-forming galaxies, accompanied by large-scale outflows along the minor axis forming bipolar outflows. On the contrary our results suggest that this scenario is not broadly applicable at z∼2. We note that, we have also explored Si II / Si IV and Al II / Al III equivalent width line ratios, however, we did not detect any significant correlations. On one hand, Si IV predominantly arise in denser gas closer to galaxies more similar to other LIS state lines like Mg II than to that of higher ions (Ford et al., 2013; Ford et al., 2014), and hence Si II and Si IV line absorption might be probing gas with similar physical conditions. On the other, Al III is an intermediate-ionization state(IIS) tracer of moderately photoionized warm gas generally associated with neutral phase gas (Savage, Meade, and Sembach, 2001; Knauth et al., 2003; Vladilo et al., 2001). In fact, Al III absorption is associated with low-ions as shown by the significant correlation between the velocity widths of Al III and low-ionization species (e.g. Si II, Fe II, Zn II, Howk, Savage, and Fabian 1999), suggesting that a substantial fraction of the low-ionization ions may be associated with moderately ionized gas traced by Al III, Fe III (Wolfe, Gawiser, and Prochaska, 2005) and that, doubly ionized species (e.g. Al III, Fe III, C III, Si III) often have comparable column densities to the singly ionized (e.g. Al II, Fe II, C II, Si II) ones (Mas-Ribas et al., 2017).

4.5.3 Lyα-emission.

Regarding Lyα_{em}, several studies have been carried out to explore the relation with galaxy properties. At low-redshift Runnholm et al., 2020, used the Lyman Alpha Reference Sample (LARS)

correlations between Lyα and different galaxy properties (i.e. star formation rate, dust extinction, compactness, and the gas covering fraction) At high-redshiftit has been found that bluer galaxies show stronger Lyα_{em} (Shapley et al., 2003; Pentericci et al., 2010; Berry et al., 2012; Erb et al., 2016), and that low-stellar mass galaxies with lower SFRs show stronger Lyα_{em} than high-stellar mass galaxies with higher SFRs (Vanzella et al., 2009; Stark et al., 2010; Erb et al., 2006; Jones, Stark, and Ellis, 2012; Shapley et al., 2003; Kornei et al., 2010; Hathi et al., 2016). Additionally Lyα_{em} is correlated with LIS absorption: stronger LIS absorptions correspond to weaker Lyα_{em}, as high concentrations of neutral gas responsible for strong LIS absorption are also responsible for scattering out of the l.o.s. Lyα photons (Shapley et al., 2003; Vanzella et al., 2009; Jones, Stark, and Ellis, 2012). More recently Du et al., 2018, (Trainor et al., 2019) and Pahl et al., 2020 studied the spectroscopic properties of star-forming galaxies at z ∼2-5 through composite spectra grouped through different galaxy properties. They detected stronger Lyα_{em} at higher redshift at fixed stellar mass, SFR and UV Luminosity, and found that the LIS-Lyα_{em} relation is redshift independent suggesting that this is caused by the variations of the neutral gas covering fraction favoring Ly escape and production and/or dust content in the ISM and CGM. Moreover Oyarzún et al., 2016; Oyarzún et al., 2017 shown that at high-redhfit ($3 < z < 4.6$) Lyα_{em} anticorrelations with stellar mass, star formation rate and UV luminosity are stronger in low-stellar-mass populations explained by the rapidly increasing neutral gas fraction of the universe at higher redshifts (Du et al., 2021).

4.6 Conclusions

In this paper we present stacks of 238 background galaxy spectra to probe the CGM content and extent around star-forming galaxies at $\langle z \rangle \sim 2.6$. We use only spectra with highly reliable spectroscopic redshifts ($95 - 100\%$ probability of being correct) to identify the low-ionization state (LIS: Si II, C II) and high-ionization state (HIS: C IV, Si IV) metal absorption lines, and constrain their spatial distribution, and their dependence with stellar mass, star formation rate, azimuthal angle and effective radius.

We summarize our maiWe summarize our main results below:

1. We detect LIS and HIS metal absorption lines in the CGM around star-forming galaxies at distances up to 172 kpc and 146 kpc, respectively. The limitations due to the size of our sample do not allow us to follow metal lines beyond these distances. The strength of these absorptions decreases at increasing distance from the galaxy, consistently with results published in literature. At any fixed distance from the galaxy, the strength of all absorption lines that we identify in our sample at $z \sim 2.6$ is larger than any other measurement at lower redshift, providing evidence of a redshift evolution of the CGM gas content responsible for producing these absorptions.

2. We do no find any significant correlation of the LIS/HIS absorptions with the azimuthal angle (ϕ). This is opposed to the scenario at low-redshift where, cold gas (traced by LIS line) is infalling onto galaxies along the plane containing the disk, while the gas heated and processed by star-formation (traced by HIS lines) is outflowing perpendicularly to the plane. This can be explained by the fact that high-redshift galaxies haven't formed a stable disk capable of collimate galactic winds into bipolar outflows. However, due to the small sample of close pairs with available morphological features, these trends need to be confirmed applying a similar analysis on larger samples at these high redshifts.

3. We find an anticorrelation between Lyα_{em} and the impact parameter b, in agreement with previous results at high-redshift.

4. To assess the relative importance of LIS and HIS absorptions, we compute the CII/CIV equivalent width line ratio, and found that it correlates with impact parameter b, stellar mass and star formation rate. CII/CIV W_0 line ratio is higher at small separations, mainly detected in star-forming galaxies ($\langle z \rangle \sim 2.6$) with low stellar masses and low star formation rates. Conversely small CII/CIV line ratios are defined by stronger CIV line absorption compared to CII and observed at large separations in star-forming galaxies with higher stellar masses and star formation rates.

The results presented here provide observational evidence consistent with a scenario where star-forming galaxies at $\langle z \rangle \sim 2.6$ possess a multi-phase CGM where LIS metal absorptions are produced by denser gas, which is more extended in these star-forming galaxies. Our results suggests that galaxies with higher star formation rates and large stellar masses have stronger ionizing fluxes, able to ionize gas at larger distances and/or are capable to sweep out the highly ionized gas(traced by C IV) farther away from the galaxy compared with less massive and less star-forming galaxies. Subsequently, star-forming galaxies with low SFR and low stellar mass show larger reservoirs of cold gas as probed by their CII, CIV and their CII/CIV equivalent width line ratio. This large reservoirs of cold gas could be funneled into the galaxies and eventually provide the necessary fuel to sustain star formation activity. Recently, Wang et al., 2021 has demonstrated that large-scale environment modulates star-formation by regulating the way in which galaxies breath in/out (accrete/expell) material by exchanging material within the CGM. This process is synchronized with star-formation rate events ocurring within a galaxy, and is related to maxima (minima) of SFR associated with a previous decrease (increase) of the cold circumgalactic gas phase, which halts a further rise (decline), and lead to fall (rise) of the star formation rate in later stages. Our results from CII-peaks and CIV-troughs detected in low-mass galaxies (low SFRs) and high-mass galaxies (high SFRs) could be interpreted as the snapshots of these two different stages of the complex interplay between the ISM/CGM/IGM in which galaxies exchange material. However, we emphasize that high resolution observations are required to detect the presence of outflows expelling out material or inflows accreting cold material back to the galaxy as recycled material. We highlight that although stacking increases the S/N of the background *spotlights*, allowing to detect the faint signal produced by gas in the CGM, it also smears out the information about the spatial, kinematic and ionization properties of the CGM. Thus we reiterate the necessity to perform deeper observations with higher resolutions at this and higher redshift of multiple LIS and HIS metal lines to provide better constraints on the properties of the multiphase CGM. It is likely that future and ongoing observations from large and deep spectroscopic surveys like VANDELS (McLure et al., 2018; Pentericci et al., 2018), zCOSMOS (Lilly et al., 2007; Lilly et al., 2009), VVDS(Le Fèvre et al., 2013) or DEIMOS10K (Hasinger et al., 2018) and Integral Field Unit observations from MUSE/KMOS/JWST will help us understand more about the multiphase nature of the CGM. Future work should points towards a resolved view to the velocity field of the in-falling/out-flowing gas of galaxies at redshift $z > 2$.

Chapter 5

Conclusions

This thesis has aimed to tackle some of the physical processes controlling the star-formation activity in galaxies at different redshifts. The main tool used in this work is the stacking technique. I developed the Valparaíso Stacking Analysis Tool, composed of a series of python tools to select, pre-process, combine, measure and analyze spectra coming from different astronomical datasets. My research is presented in two first author papers (Méndez-Hernández et al., 2020; Méndez-Hernández et al., 2021) and is based on the exploitation of two different galaxy samples to probe the molecular gas and the ionized gas in the interstellar and circumgalactic medium. To analyse the molecular gas content, we make use of the Valparaíso ALMA/APEX Line Emission Survey (VALES), while for characterising the ionized gas we exploit the The Vimos Ultra Deep Survey (VUDS). Something in common between both analyses (Chapters 3 and 4) is that the signals in emission and absorption coming from the cold dense molecular gas and the circumgalactic gas, respectively, are too weak to be seen as individual detections. The Valparaíso Stacking Analysis Tool is thus used to generate composite spectra by stacking the signal of individual spectra, hence raising the signal to noise ratio to obtain clear detections of the combined signal of these objects. Below I present the main results from each of the published papers.

5.1 Results Paper I

I analyzed the ^{12}CO, ^{13}CO, and C^{18}O ($\nu_{^{12}\mathrm{CO(1\text{-}0)}} = 115.271\,\mathrm{GHz}$, $\nu_{^{13}\mathrm{CO(1\text{-}0)}} = 110.201\,\mathrm{GHz}$, and $\nu_{\mathrm{C}^{18}\mathrm{O(1\text{-}0)}} = 109.782\,\mathrm{GHz}$ rest-frame frequencies), emission lines to study the cool and dense molecular gas of dusty star-forming galaxies at low-redshift. For these purposes I used 27 star-forming dusty galaxies ($0.02 < z < 0.2$) belonging to the VALES survey. I detected six individual ^{13}CO line emission through moment-0 maps with SNR>5. Using the 27 sources, I explored and compared three different stacking analyses for interferometric datasets: two of them in the "image plane": (i) 2D-moment-0 stacking and (ii) 3D-image stacking analyzed with VSAT, and the third one in visibility's space (iii) uv-plane stacking. I found that for bright emission lines like ^{12}CO uv-plane stack produce composite images with the highest SNR. However for faint line emission like ^{13}CO or CO^{18}O composite images obtained by stacking individual moment-zero images have the highest SNR.

I found a L' (^{12}CO) / L' (^{13}CO) luminosity line ratio that depends on optical morphology and environment, where mergers and galaxies accompanied by a close projected companion show a higher L' (^{12}CO) / L' (^{13}CO) line luminosity ratio by a factor of 2 compared to the L' (^{12}CO) / L' (^{13}CO) line luminosity ratio of galaxies without a projected companion. I also found positive trends between L' (^{12}CO) / L' (^{13}CO) line luminosity ratio with SFR, SFE, L_{IR}, $\Sigma_{\mathrm{H_2}}$ and Σ_{SFR}. By including in the analyses the C^{18}O isotopologue emission line coming from the composite images of 24 VALES galaxies with C^{18}O coverage, I detect a 5σ emission from the 2D moment-o stacked images. The former resulted in an average L' (^{13}CO) / L' (C^{18}O) line luminosity ratio of 2.5 ± 0.6, in agreement with has been reported for nearby starbust galaxies. I also found negative

trends of $L'(^{13}CO)/L'(C^{18}O)$ as a function of L_{IR}, SFR and SFE.

$I(^{12}CO)$ / $I(^{13}CO)$ line intensity ratios are affected by opacity, surface density and gas temperature making difficult the intepretation of ^{12}CO / ^{13}CO abundances derived from this luminosity ratio. Thus, the $L'(^{12}CO)$ / $L'(^{13}CO)$ luminosity ratios reported here should be taken as a lower limit of the ^{12}CO / ^{13}CO abundance ratio. On the other hand, it has been reported that even moderate ^{13}CO optical depths ($\tau_{^{13}CO} \sim 0.2 - 0.5$) do not produce a deviation from the typical values of ^{13}CO / $C^{18}O \sim 7$ abundance ratios, meaning that the low $I(^{13}CO)$ / $I(C^{18}O)$ found in high-redshift starburst and local ULIRGs truly reflect the intrinsic isotopologue abundance ratios [i.e. $I(^{13}CO)/I(C^{18}O) \approx {}^{13}CO$ / $C^{18}O \approx {}^{13}C$ / ^{18}O].

Chemical fractionation and selective photo-dissociation are usually called as responsible of these ratios, however our sample of galaxies do not fulfill the required low temperatures ($\leq 10K$) and high densities ($> 10^{26}cm^{-3}$). The combined $L'(^{12}CO)$ / $L'(^{13}CO)$ and $L'(^{13}CO)$ / $L'(C^{18}O)$ variations provide additional evidence to dismiss photo-dissociation as responsible of our results. Thus, selective nucleosythesis is the most probable mechanism for the high $L'(^{12}CO)$ / $L'(^{13}CO)$ and low $L'(^{13}CO)$ / $L'(C^{18}O)$ ratios found in bright far-IR luminosity galaxies. Suggesting that higher molecular gas reservoirs can trigger new starburst events where high mass stars enrich their ISM.

5.2 Results Paper II

We characterize the presence of low- and high-ionization state metal absorption (e.g. O I+Si II, Si II, Si IV, C II, C IV, Al II, Al III) in the CGM of a star-forming galaxy population at $\langle z \rangle \sim 2.6$ using UV spectra obtained from the large VIMOS Ultra Deep Survey (VUDS; Le Fèvre et al. 2015). We use galaxies with the most reliable redshift measurements and the highest S/N spectra (with reliability flags 3 and 4; see Le Fèvre et al. 2015; Tasca et al. 2017), a sample broadly representative of the bulk of the star-forming galaxy population at these redshifts (Lemaux et al., 2020). To detect the dim signal coming from low- and high ionization line absorptions produced in the CGM of these star-forming galaxies, we stack the spectra of close (in projection) *background* galaxies to establish the metal distribution in the CGM and explore their dependence on the physical and morphological properties of star-forming galaxies (e.g., impact parameter b, star formation rate, stellar mass, galaxy effective radius and azimuthal angle) at the peak epoch of cosmic star formation activity in the Universe.

We detect LIS and HIS metal absorption lines to distances up to 172 kpc and 146 kpc respectively. This is in good agreement with an anti-correlation between impact parameter b and metal absorption line previously reported in the literature. At any fixed distance from the galaxy, the strength of all absorption lines that we identify in our sample at $z \sim 2.6$ is larger than any other measurement at lower redshift, providing evidence of a redshift evolution of the CGM gas content responsible for producing these absorptions. For the first time a LIS/HIS metal absorption correlation with stellar mass and star formation rates at this redshift is presented. I found that more massive galaxies ($\log[M_\star/M\odot]>10.2$) with higher star formation rates ($\log[M_\star yr^{-1}]>1.5$) show stronger HIS absorption features in contrast with their LIS counterparts which are stronger in low mass ($\log[M_\star/M\odot]<9.2$) star-forming galaxies with lower SFRs ($\log[SFR/(M_\star yr^{-1})] < 0.9$). I identify trends of the strength of the LIS/HIS absorptions with the azimuthal angle (ϕ) and effective radius (r_{eff}). However, due to the small sample of close pairs with available morphological features, these trends need to be confirmed applying a similar analysis on larger samples at these high redshifts.

To assess the LIS/HIS correlations, I compute C II/C IV equivalent width line ratio and found correlations with impact parameter b, stellar mass and star formation rate. CII/C IV W_0 line ratio is higher at close separations, mainly produced by star-forming galaxies ($\langle z \rangle \sim 2.6$) with low stellar masses and low star formation rates. Conversely small C II/C IV line ratios are defined by stronger C IV line absorption compared to C II and observed at large separations in star-forming galaxies with higher stellar masses and star formation rates.

These results provide observational evidence consistent with a scenario where star-forming galaxies at $\langle z \rangle \sim 2.6$ possess a multi-phase CGM. This multi-phase CGM posses dense gas located closer to the galaxies preferentially along the major axis producing LIS metal absorptions. In this scenario, low-metal gas is funneled to the galaxies that could eventually provide the necessary fuel to sustain star formation activity. These new episodes of star-formation would be able to produce large-scale bipolar outflows preferentially along the minor axis and expelling high ionization material to the outer regions of these galaxies.

5.2.1 Linking molecular with ionized gas phases.

Observations of molecular gas content have revealed that its evolution mirrors the global star-formation rate density of the Universe (Hafen et al., 2020; Péroux et al., 2020). Thus, the SFRHU is mainly driven by the cosmic evolution of the gas reservoir. At low-redshift the steep decline of the SFRH is caused by a deficit of molecular gas supply and a drop in the accretion rate fueling galaxies with unprocessed gas indispensable for new episodes of star-formation. High-redshift galaxies near the peak of star-formation rate of the Universe forming stars vigorously are uncapable to deposit processed material into the IGM. This processed material is then reaccreted into the central galaxy by galactic fountains, which will eventually cool down feeding a new generation of stars and sustaining star-formation at lower redshifts.

5.3 Future prospects.

In this work it has been demonstrated that stacking analysis is a powerful tool to further exploit the current observational capabilities. We have positively detect the faint signal coming from the molecular and ionized gas in low- and high-redshift star-forming galaxies. The flexibility of VSAT allows us to further exploit public archival databases from different observatories ALMA, NOEMA, SKA, VLT, KECK. Moreover, VSAT can be used to further push the detection limits of the upcoming JWST/ELT/GMT/EVLA missions, in the near future.

VALES cycle I observations are composed by star-forming galaxies at higher redshift ($0.14 < z < 0.34$) with higher $L_{\rm IR}$, SFR, $\Sigma_{\rm gas}$, and $\Sigma_{\rm SFR}$. Additional observations of the ^{13}CO and C^{18}O alongside the existent ^{12}CO datasets of the VALES cycle I sample could provide a bridge on the molecular gas content between low-reshift and lensed galaxies at high redshifts, shedding light on the physical processes behind their star formation activity. Moreover, they can be used to widen the stellar mass and redshift ranges and could be helpful to identify L' (^{12}CO) / L' (^{13}CO) and L' (^{13}CO) / L' (C^{18}O) stellar mass and redshift trends.

On the other hand, future analyses using interferometric observations of different CNO isotopologue molecules (CN, HCN, HNC, C^{17}O, ^{12}CN, and ^{13}CN) on larger samples, sampling different galaxy populations covering wider ranges in SFR, SFE, and molecular gas contents at different epochs, could fill in the existing gap of molecular line observations between nearby

galaxies intermediate- and high-redshift galaxies. Recently several studies have suggested the possibility of a modified IMF as responsible of the observed low $I(^{13}CO)/I(C^{18}O)$ line intensity ratios (Sliwa et al., 2017; Zhang et al., 2018; Brown and Wilson, 2019). However to break the degeneracy between a recent starburst and a top-heavy IMF, independent determination of the age of the starburst is needed. This can be achieved by reconstructing the star formation histories of starburst galaxies candidates with high-resolution observations (Cortijo-Ferrero et al., 2017). It is also possible to use observations of multiple low-J CO lines [$^{12}CO(1-0, 2-1, 3-2$ and $^{13}CO(1-0, 2-1)$] and dense gas tracers (e.g. HCN$(1-0)$, HCO+$(1-0)$, CN) to study in detail the physical and kinematic properties of molecular gas in star-forming galaxies. For example, Tang et al. (2019) reported ^{12}CN and ^{13}CN detections concordant with inflow material into the central region of a nearby starburst galaxy, Topal (2021) found evidence suggesting a higher star-formation activity in the central regions of nearby galaxies, while Young et al. (2021) found $^{12}CO/^{13}CO$ and $^{13}CO/C^{18}O$ line ratios consistent with molecular (and atomic) gas accreted from a spiral galaxy.

Studies on the multiphase-nature of the CGM can be extended by using VSAT and including observations at different redshifts coming from different complementary surveys (e.g. VANDELS (McLure et al., 2018; Pentericci et al., 2018), zCOSMOS (Lilly et al., 2007; Lilly et al., 2009), VVDS (Le Fèvre et al., 2013), DEIMOS10K (Hasinger et al., 2018)). For example, VANDELS provide high resolution spectra of star-forming galaxies at higher redshifts ($4 < z < 7$). At this moment, I am carrying out a similar analysis to detect LIS and HIS absorption features in star-forming galaxies from VANDELS. These detections will be helpful to detect inflows or outflows in these galaxies by measuring blue- and red-shift offsets of absorption lines. These complementary surveys can help to increase the number of galaxy pairs with close angular separations ($b < 6''$), cover different low- and high-ionization state lines (e.g. O VI λλ 1032-1038 , Mg II λ 2798), and deblend close spectral line features (e.g. C II-O IV λλ 1334.5-1343.0 ; Si IV λλ 1393.8-1402.8) to identify outflows and inflows in the CGM of star-forming galaxies. It is also possible to choose close pairs of galaxies at different redshifts observed in different spectral regimes that could provide a multi-wavelength perspective of the CGM. For example, (Fu et al., 2016) used VLA observations of sub-millimeter galaxies (SMGs) - Quasars (QSOs) pairs to study the cool gas component of the CGM of SMGs at $z \sim 2$.

Additionally, to better understand the metal spatial distribution in the CGM, deep spatially resolved observations (e.g. VLT-MUSE, Keck-KCWI-OSIRIS) can be used to determine morphological properties and disentangle the kinematic properties of the gas accreting into the galaxy or being expelled to the CGM/IGM (Strom et al., 2021; Zabl et al., 2021; Burchett et al., 2021; Mortensen et al., 2021). For these purposes follow up campaigns of close pairs showing strong Lyα, LIS and HIS absorptions provide ideal candidates for detailed physical and kinematic analyses.

In both cases, these observational efforts have to be accompanied by detailed models of the ISM/CGM gas properties to better understand the physics underlying the complex interplay that star-formation has at low- and high redshifts. Alongside, simulations have to be included as they have proved to be an important tool in the study of the ISM and CGM properties by providing predictions of the their properties that can be better constrained by observations.

Bibliography

Aalto, S. et al. (Sept. 1991). "Large 12CO/13CO intensity ratios in luminous mergers." In: 249, p. 323.

Aalto, S. et al. (Aug. 1995). "Molecular gas in starburst galaxies: line intensities and physical conditions". In: 300, p. 369.

Adelberger, Kurt L. et al. (Feb. 2003). "Galaxies and Intergalactic Matter at Redshift z$\sim$3: Overview". In: 584.1, pp. 45–75. DOI: 10.1086/345660. arXiv: astro-ph/0210314 [astro-ph].

Adelberger, Kurt L. et al. (Aug. 2005). "The Connection between Galaxies and Intergalactic Absorption Lines at Redshift 2<<$\sim$3". In: 629.2, pp. 636–653. DOI: 10.1086/431753. arXiv: astro-ph/0505122 [astro-ph].

Adelman-McCarthy, Jennifer K. et al. (2008). "The Sixth Data Release of the Sloan Digital Sky Survey". In: *The Astrophysical Journal Supplement Series* 175.2, pp. 297–313. DOI: 10.1086/524984. URL: https://doi.org/10.1086/524984.

Alatalo, Katherine et al. (May 2015). "Evidence of boosted 13CO/12CO ratio in early-type galaxies in dense environments". In: *Monthly Notices of the Royal Astronomical Society* 450.4, pp. 3874–3885. ISSN: 0035-8711. DOI: 10.1093/mnras/stv837. eprint: https://academic.oup.com/mnras/article-pdf/450/4/3874/5797291/stv837.pdf. URL: https://doi.org/10.1093/mnras/stv837.

Anglés-Alcázar, Daniel et al. (Oct. 2017). "The cosmic baryon cycle and galaxy mass assembly in the FIRE simulations". In: 470.4, pp. 4698–4719. DOI: 10.1093/mnras/stx1517. arXiv: 1610.08523 [astro-ph.GA].

Ashton, E. (2015). "The Detection of Faint Asteroids by the Shifting and Stacking of Difference Images." In:

Baba, N. et al. (May 1985). "Stellar speckle reconstruction by the shift-and-add method." In: 24, pp. 1403–1405. DOI: 10.1364/AO.24.001403.

Bacon, R. et al. (Mar. 2021). "The MUSE Extremely Deep Field: The cosmic web in emission at high redshift". In: 647, A107, A107. DOI: 10.1051/0004-6361/202039887. arXiv: 2102.05516 [astro-ph.CO].

Bagnuolo W. G., Jr. (Sept. 1982). "The Application of Bate's Algorithm to Binary Stars". In: 200, p. 1113. DOI: 10.1093/mnras/200.4.1113.

Bagnuolo W. G., Jr. and H. A. McAlister (Dec. 1983). "The true nodal quadrant of Capella." In: 95, pp. 992–995. DOI: 10.1086/131279.

Bahcall, John N. and Jr. Spitzer Lyman (May 1969). "Absorption Lines Produced by Galactic Halos". In: 156, p. L63. DOI: 10.1086/180350.

Bartelmann, M. and S. D. M. White (Sept. 2003). "Stacking clusters in the ROSAT All-Sky Survey". In: 407, pp. 845–854. DOI: 10.1051/0004-6361:20030991. arXiv: astro-ph/0210067 [astro-ph].

Bates, R. H. T. and F. M. Cady (Mar. 1980). "Towards true imaging by wideband speckle interferometry." In: *Optics Communications* 32, pp. 365–369. DOI: 10.1016/0030-4018(80)90261-8.

Bauermeister, Amber, Leo Blitz, and Chung-Pei Ma (July 2010). "The Gas Consumption History to Redshift 4". In: 717.1, pp. 323–332. DOI: 10.1088/0004-637X/717/1/323. arXiv: 0909.3840 [astro-ph.CO].

Bera, Apurba et al. (2018). "Probing Star Formation in Galaxies at z ≈ 1 via a Giant Metrewave Radio Telescope Stacking Analysis". In: *The Astrophysical Journal* 865.1, p. 39. DOI: 10.3847/1538-4357/aad698. URL: https://doi.org/10.3847/1538-4357/aad698.

Bergeron, J. (Jan. 1986). "The MG II absorption system in the QSO PKS 2128-12 : a galaxy disc/halo with a radius of 65 kpc." In: 155, pp. L8–L11.

Bergeron, J. and P. Boissé (Mar. 1991). "A sample of galaxies giving rise to Mg II quasar absorption systems." In: 243, p. 344.

Bergin, Edwin A. and Mario Tafalla (2007). "Cold Dark Clouds: The Initial Conditions for Star Formation". In: *Annual Review of Astronomy and Astrophysics* 45.1, pp. 339–396. DOI: 10.1146/annurev.astro.45.071206.100404. eprint: https://doi.org/10.1146/annurev.astro.45.071206.100404. URL: https://doi.org/10.1146/annurev.astro.45.071206.100404.

Berry, Michael et al. (2012). "STACKED REST-FRAME ULTRAVIOLET SPECTRA OF Lyα-EMITTING AND CONTINUUM-SELECTED GALAXIES AT 2 z 3.5". In: *The Astrophysical Journal* 749.1, p. 4. DOI: 10.1088/0004-637x/749/1/4. URL: https://doi.org/10.1088/0004-637x/749/1/4.

Bigiel, F. et al. (2008). "THE STAR FORMATION LAW IN NEARBY GALAXIES ON SUB-KPC SCALES". In: *The Astronomical Journal* 136.6, pp. 2846–2871. DOI: 10.1088/0004-6256/136/6/2846. URL: https://doi.org/10.1088/0004-6256/136/6/2846.

Black, J. H. and A. Dalgarno (Sept. 1973). "The Cosmic Abundance of Deuterium". In: 184, p. L101. DOI: 10.1086/181299.

Blagorodnova, Nadejda et al. (July 2014). "GS-TEC: the Gaia spectrophotometry transient events classifier". In: 442.1, pp. 327–342. DOI: 10.1093/mnras/stu837. arXiv: 1404.7150 [astro-ph.IM].

Bland-Hawthorn, Joss et al. (Dec. 2007). "The Source of Ionization along the Magellanic Stream". In: 670.2, pp. L109–L112. DOI: 10.1086/524657. arXiv: 0711.0247 [astro-ph].

Boksenberg, A. and W. L. W. Sargent (Feb. 1978). "The existence of Ca II absorption lines in the spectrum of the quasar 3C 232 due to the galaxy NGC 3067." In: 220, pp. 42–46. DOI: 10.1086/155880.

Bolatto, Alberto D., Mark Wolfire, and Adam K. Leroy (2013). "The CO-to-H2 Conversion Factor". In: *Annual Review of Astronomy and Astrophysics* 51.1, pp. 207–268. DOI: 10.1146/annurev-astro-082812-140944. eprint: https://doi.org/10.1146/annurev-astro-082812-140944. URL: https://doi.org/10.1146/annurev-astro-082812-140944.

Bongiorno, A. et al. (Apr. 2016). "AGN host galaxy mass function in COSMOS. Is AGN feedback responsible for the mass-quenching of galaxies?" In: 588, A78, A78. DOI: 10.1051/0004-6361/201527436. arXiv: 1601.02091 [astro-ph.GA].

Bordoloi, R. et al. (Dec. 2011). "The Radial and Azimuthal Profiles of Mg II Absorption around 0.5 < z < 0.9 zCOSMOS Galaxies of Different Colors, Masses, and Environments". In: 743.1, 10, p. 10. DOI: 10.1088/0004-637X/743/1/10. arXiv: 1106.0616 [astro-ph.CO].

Bordoloi, R. et al. (Apr. 2014a). "Modeling the Distribution of Mg II Absorbers around Galaxies Using Background Galaxies and Quasars". In: 784.2, 108, p. 108. DOI: 10.1088/0004-637X/784/2/108. arXiv: 1211.3774 [astro-ph.CO].

Bordoloi, R. et al. (Oct. 2014b). "The Dependence of Galactic Outflows on the Properties and Orientation of zCOSMOS Galaxies at z ∼1". In: 794.2, 130, p. 130. DOI: 10.1088/0004-637X/794/2/130. arXiv: 1307.6553 [astro-ph.CO].

Bordoloi, Rongmon et al. (Sept. 2018). "On the CGM Fundamental Plane: The Halo Mass Dependency of Circumgalactic H I". In: 864.2, 132, p. 132. DOI: 10.3847/1538-4357/aad8ac. arXiv: 1712.02348 [astro-ph.GA].

Borthakur, Sanchayeeta et al. (May 2013). "The Impact of Starbursts on the Circumgalactic Medium". In: 768.1, 18, p. 18. DOI: 10.1088/0004-637X/768/1/18. arXiv: 1303.1183 [astro-ph.CO].

Borthakur, Sanchayeeta et al. (Nov. 2015). "Connection between the Circumgalactic Medium and the Interstellar Medium of Galaxies: Results from the COS-GASS Survey". In: 813.1, 46, p. 46. DOI: 10.1088/0004-637X/813/1/46. arXiv: 1504.01392 [astro-ph.GA].

Bottini, D. et al. (Sept. 2005). "The Very Large Telescope Visible Multi-Object Spectrograph Mask Preparation Software". In: 117.835, pp. 996–1103. DOI: 10.1086/432150.

Bouché, N. et al. (Oct. 2012). "Physical properties of galactic winds using background quasars". In: 426.2, pp. 801–815. DOI: 10.1111/j.1365-2966.2012.21114.x. arXiv: 1110.5877 [astro-ph.CO].

Bouché, N. et al. (July 2013). "Signatures of Cool Gas Fueling a Star-Forming Galaxy at Redshift 2.3". In: *Science* 341.6141, pp. 50–53. DOI: 10.1126/science.1234209. arXiv: 1306.0134 [astro-ph.CO].

Bouché, N. et al. (Apr. 2016). "Possible Signatures of a Cold-flow Disk from MUSE Using a z ∼ 1 Galaxy-Quasar Pair toward SDSS J1422-0001". In: 820.2, 121, p. 121. DOI: 10.3847/0004-637X/820/2/121. arXiv: 1601.07567 [astro-ph.GA].

Bouché, Nicolas et al. (Nov. 2007). "The SINFONI Mg II Program for Line Emitters (SIMPLE): Discovering Starbursts near QSO Sight Lines". In: 669.1, pp. L5–L8. DOI: 10.1086/523594. arXiv: 0709.4248 [astro-ph].

Bowen, David V., J. Chris Blades, and Max Pettini (Aug. 1995). "Interstellar MG II Absorption Lines from Low-Redshift Galaxies". In: 448, p. 634. DOI: 10.1086/175993.

Bower, Richard G. et al. (Oct. 2016). "The dark nemesis of galaxy formation: why hot haloes trigger black hole growth and bring star formation to an end". In: *Monthly Notices of the Royal Astronomical Society* 465.1, pp. 32–44. ISSN: 0035-8711. DOI: 10.1093/mnras/stw2735. eprint: https://academic.oup.com/mnras/article-pdf/465/1/32/8593464/stw2735.pdf. URL: https://doi.org/10.1093/mnras/stw2735.

Brandt, W. N. et al. (Sept. 2001a). "The Chandra Deep Field-North Survey. VII. X-Ray Emission from Lyman Break Galaxies". In: 558.1, pp. L5–L9. DOI: 10.1086/323570. arXiv: astro-ph/0107392 [astro-ph].

Brandt, W. N. et al. (July 2001b). "The Chandra Deep Survey of the Hubble Deep Field North Area. IV. An Ultradeep Image of the HDF-N". In: 122.1, pp. 1–20. DOI: 10.1086/321135. arXiv: astro-ph/0102411 [astro-ph].

Brown, Toby and Christine D. Wilson (2019). "Extreme CO Isotopologue Line Ratios in ULIRGS: Evidence for a Top-heavy IMF". In: *The Astrophysical Journal* 879.1, p. 17. DOI: 10.3847/1538-4357/ab2246. URL: https://doi.org/10.3847/1538-4357/ab2246.

Bruzual, G. and S. Charlot (Oct. 2003). "Stellar population synthesis at the resolution of 2003". In: 344.4, pp. 1000–1028. DOI: 10.1046/j.1365-8711.2003.06897.x. arXiv: astro-ph/0309134 [astro-ph].

Burchett, Joseph N. et al. (2016). "A DEEP SEARCH FOR FAINT GALAXIES ASSOCIATED WITH VERY LOW REDSHIFT C iv ABSORBERS. III. THE MASS- AND ENVIRONMENT-DEPENDENT CIRCUMGALACTIC MEDIUM". In: *The Astrophysical Journal* 832.2, p. 124. DOI: 10.3847/0004-637x/832/2/124. URL: https://doi.org/10.3847/0004-637x/832/2/124.

Burchett, Joseph N. et al. (Mar. 2021). "Circumgalactic Mg II Emission from an Isotropic Starburst Galaxy Outflow Mapped by KCWI". In: 909.2, 151, p. 151. DOI: 10.3847/1538-4357/abd4e0. arXiv: 2005.03017 [astro-ph.GA].

Cady, F. M. and R. H. T. Bates (Oct. 1980). "Speckle processing gives diffraction-limited true images from severely aberrated instruments". In: *Optics Letters* 5.10, pp. 438–440. DOI: 10.1364/OL.5.000438.

Carvajal, R. et al. (Jan. 2020). "The ALMA Frontier Fields Survey. V. ALMA Stacking of Lyman-Break Galaxies in Abell 2744, Abell 370, Abell S1063, MACSJ0416.1-2403 and MACSJ1149.5+2223". In: 633, A160, A160. DOI: 10.1051/0004-6361/201936260. arXiv: 1912.02916 [astro-ph.GA].

Casoli, F., C. Dupraz, and F. Combes (Oct. 1992a). "A molecular line survey of the merger NGC 3256". In: 264, pp. 49–54.

— (Oct. 1992b). "The case of missing 13CO in mergers." In: 264, pp. 55–67.

Chabrier, Gilles (2003). "The Galactic Disk Mass Function: Reconciliation of the [ITAL]Hubble Space Telescope[/ITAL] and Nearby Determinations". In: *The Astrophysical Journal* 586.2, pp. L133–L136. DOI: 10.1086/374879. URL: https://doi.org/10.1086/374879.

Chen, Hsiao-Wen, Kenneth M. Lanzetta, and John K. Webb (July 2001). "The Origin of C IV Absorption Systems at Redshifts z < 1: Discovery of Extended C IV Envelopes around Galaxies". In: 556.1, pp. 158–163. DOI: 10.1086/321537. arXiv: astro-ph/0104403 [astro-ph].

Chen, Hsiao-Wen et al. (May 1998). "The Gaseous Extent of Galaxies and the Origin of Lyα Absorption Systems. III. Hubble Space Telescope Imaging of Lyα-absorbing Galaxies at z < 1". In: 498.1, pp. 77–94. DOI: 10.1086/305554. arXiv: astro-ph/9710310 [astro-ph].

— (Oct. 2001). "The Gaseous Extent of Galaxies and the Origin of Lyα Absorption Systems. V. Optical and Near-Infrared Photometry of Lyα-absorbing Galaxies at z<1". In: 559.2, pp. 654–674. DOI: 10.1086/322414. arXiv: astro-ph/0107137 [astro-ph].

Chen, Yan-Mei et al. (Aug. 2010). "Absorption-line Probes of the Prevalence and Properties of Outflows in Present-day Star-forming Galaxies". In: 140.2, pp. 445–461. DOI: 10.1088/0004-6256/140/2/445. arXiv: 1003.5425 [astro-ph.GA].

Chen, Yuguang et al. (Sept. 2020). "The Keck Baryonic Structure Survey: using foreground/background galaxy pairs to trace the structure and kinematics of circumgalactic neutral hydrogen at z $\sim$ 2". In: 499.2, pp. 1721–1746. DOI: 10.1093/mnras/staa2808. arXiv: 2006.13236 [astro-ph.GA].

Chen, Yuguang et al. (Apr. 2021). "The KBSS-KCWI Survey: The connection between extended Lyα halos and galaxy azimuthal angle at $z \sim 2-3$". In: *arXiv e-prints*, arXiv:2104.10173, arXiv:2104.10173. arXiv: 2104.10173 [astro-ph.GA].

Cheng, C et al. (Dec. 2017). "VALES – IV. Exploring the transition of star formation efficiencies between normal and starburst galaxies using APEX/SEPIA Band-5 and ALMA at low redshift". In: *Monthly Notices of the Royal Astronomical Society* 475.1, pp. 248–256. ISSN: 0035-8711. DOI: 10.1093/mnras/stx3183. eprint: https://academic.oup.com/mnras/article-pdf/475/1/248/23388368/stx3183.pdf. URL: https://doi.org/10.1093/mnras/stx3183.

Christensen, Charlotte R. et al. (Nov. 2018). "Tracing Outflowing Metals in Simulations of Dwarf and Spiral Galaxies". In: 867.2, 142, p. 142. DOI: 10.3847/1538-4357/aae374. arXiv: 1808.07872 [astro-ph.GA].

Christou, J. C. et al. (Feb. 1986). "Self-calibrating shift-and-add technique for speckle imaging". In: *Journal of the Optical Society of America A* 3, pp. 204–209. DOI: 10.1364/JOSAA.3.000204.

Churchill, Christopher W. et al. (Nov. 2000). "Low- and High-Ionization Absorption Properties of Mg II Absorption-selected Galaxies at Intermediate Redshifts. II. Taxonomy, Kinematics, and Galaxies". In: 543.2, pp. 577–598. DOI: 10.1086/317120. arXiv: astro-ph/0005586 [astro-ph].

Churchill, Christopher W. et al. (Mar. 2015). "Direct Insights Into Observational Absorption Line Analysis Methods of the Circumgalactic Medium Using Cosmological Simulations". In: 802.1, 10, p. 10. DOI: 10.1088/0004-637X/802/1/10. arXiv: 1409.0914 [astro-ph.GA].

Cicone, C., R. Maiolino, and A. Marconi (Apr. 2016). "Outflows and complex stellar kinematics in SDSS star-forming galaxies". In: 588, A41, A41. DOI: 10.1051/0004-6361/201424514. arXiv: 1601.04715 [astro-ph.GA].

Claeyssens, A et al. (Sept. 2019). "Spectral variations of Lyman

alpha

emission within strongly lensed sources observed with MUSE". In: *Monthly Notices of the Royal Astronomical Society* 489.4, pp. 5022–5029. ISSN: 0035-8711. DOI: 10.1093/mnras/stz2492. eprint: https://academic.oup.com/mnras/article-pdf/489/4/5022/30047592/stz2492.pdf. URL: https://doi.org/10.1093/mnras/stz2492.

Cochran, Anita L. et al. (Dec. 1995). "The Discovery of Halley-sized Kuiper Belt Objects Using the Hubble Space Telescope". In: 455, p. 342. DOI: 10.1086/176581. arXiv: astro-ph/9509100 [astro-ph].

Condon, James J. and Scott M. Ransom (2016). *Essential Radio Astronomy*.

Cormier, D et al. (Jan. 2018). "Full-disc 13CO(1–0) mapping across nearby galaxies of the EMPIRE survey and the CO-to-H2 conversion factor". In: *Monthly Notices of the Royal Astronomical Society* 475.3, pp. 3909–3933. ISSN: 0035-8711. DOI: 10.1093/mnras/sty059. eprint: https://academic.oup.com/mnras/article-pdf/475/3/3909/23965800/sty059.pdf. URL: https://doi.org/10.1093/mnras/sty059.

Cortijo-Ferrero, C. et al. (Nov. 2017). "The spatially resolved star formation history of mergers. A comparative study of the LIRGs IC 1623, NGC 6090, NGC 2623, and Mice". In: 607, A70, A70. DOI: 10.1051/0004-6361/201731217. arXiv: 1707.05324 [astro-ph.GA].

Croton, Darren J. et al. (Jan. 2006). "The many lives of active galactic nuclei: cooling flows, black holes and the luminosities and colours of galaxies". In: 365.1, pp. 11–28. DOI: 10.1111/j.1365-2966.2005.09675.x. arXiv: astro-ph/0508046 [astro-ph].

Daddi, E. et al. (2010). "DIFFERENT STAR FORMATION LAWS FOR DISKS VERSUS STARBURSTS AT LOW AND HIGH REDSHIFTS". In: *The Astrophysical Journal* 714.1, pp. L118–L122. DOI: 10.1088/2041-8205/714/1/l118. URL: https://doi.org/10.1088/2041-8205/714/1/l118.

Danielson, A. L. R. et al. (Dec. 2013). "^{13}CO and C^{18}O emission from a dense gas disc at z = 2.3: abundance variations, cosmic rays and the initial conditions for star formation". In: 436.3, pp. 2793–2809. DOI: 10.1093/mnras/stt1775. arXiv: 1309.5952 [astro-ph.CO].

Davé, Romeel, Kristian Finlator, and Benjamin D. Oppenheimer (Mar. 2012). "An analytic model for the evolution of the stellar, gas and metal content of galaxies". In: 421.1, pp. 98–107. DOI: 10.1111/j.1365-2966.2011.20148.x. arXiv: 1108.0426 [astro-ph.CO].

Davis, Timothy A. (Dec. 2014). "Systematic variation of the ^{12}CO/^{13}CO ratio as a function of star formation rate surface density". In: 445.3, pp. 2378–2384. DOI: 10.1093/mnras/stu1850. arXiv: 1409.1732 [astro-ph.GA].

Dekel, A. and J. Silk (Apr. 1986). "The Origin of Dwarf Galaxies, Cold Dark Matter, and Biased Galaxy Formation". In: 303, p. 39. DOI: 10.1086/164050.

Dekel, A. et al. (Sept. 2005). "Lost and found dark matter in elliptical galaxies". In: 437.7059, pp. 707–710. DOI: 10.1038/nature03970. arXiv: astro-ph/0501622 [astro-ph].

Dole, H. et al. (May 2006). "The cosmic infrared background resolved by Spitzer. Contributions of mid-infrared galaxies to the far-infrared background". In: 451.2, pp. 417–429. DOI: 10.1051/0004-6361:20054446. arXiv: astro-ph/0603208 [astro-ph].

Driver, Simon P. et al. (Feb. 2016). "Galaxy And Mass Assembly (GAMA): Panchromatic Data Release (far-UV-far-IR) and the low-z energy budget". In: 455.4, pp. 3911–3942. DOI: 10.1093/mnras/stv2505. arXiv: 1508.02076 [astro-ph.GA].

Du, Xinnan et al. (Oct. 2016). "The Kinematics of C IV in Star-forming Galaxies at z $\approx$ 1.2". In: 829.2, 64, p. 64. DOI: 10.3847/0004-637X/829/2/64. arXiv: 1604.03945 [astro-ph.GA].

Du, Xinnan et al. (June 2018). "The Redshift Evolution of Rest-UV Spectroscopic Properties in Lyman-break Galaxies at z $\sim$ 2-4". In: 860.1, 75, p. 75. DOI: 10.3847/1538-4357/aabfcf. arXiv: 1803.05912 [astro-ph.GA].

Du, Xinnan et al. (Oct. 2021). "The MOSDEF-LRIS Survey: Probing the ISM/CGM Structure of Star-forming Galaxies at z 2 Using Rest-UV Spectroscopy". In: 920.2, 95, p. 95. DOI: 10.3847/1538-4357/ac1273. arXiv: 2103.15824 [astro-ph.GA].

Duivenvoorden, S. et al. (Jan. 2020). "Have we seen all the galaxies that comprise the cosmic infrared background at 250 μm $\leq \lambda \leq$ 500 μm?" In: 491.1, pp. 1355–1368. DOI: 10.1093/mnras/stz3110. arXiv: 1911.01437 [astro-ph.GA].

Dutta, Rajeshwari et al. (Dec. 2021). "Metal-enriched halo gas across galaxy overdensities over the last 10 billion years". In: 508.3, pp. 4573–4599. DOI: 10.1093/mnras/stab2752. arXiv: 2109.10927 [astro-ph.GA].

Eales, S. et al. (May 2010). "The Herschel ATLAS". In: 122.891, p. 499. DOI: 10.1086/653086. arXiv: 0910.4279 [astro-ph.CO].

Elbaz, D. et al. (Sept. 2011). "GOODS-Herschel: an infrared main sequence for star-forming galaxies". In: 533, A119, A119. DOI: 10.1051/0004-6361/201117239. arXiv: 1105.2537 [astro-ph.CO].

Encrenaz, P. J. et al. (Sept. 1979). "Observations of carbon monoxide isotopes in external galaxies." In: 78.1, pp. L1–L4.

Erb, Dawn K. et al. (July 2006). "The Stellar, Gas, and Dynamical Masses of Star-forming Galaxies at z ∼2". In: 646.1, pp. 107–132. DOI: 10.1086/504891. arXiv: astro-ph/0604041 [astro-ph].

Erb, Dawn K. et al. (Oct. 2016). "A High Fraction of Lyα Emitters among Galaxies with Extreme Emission Line Ratios at z ∼2". In: 830.1, 52, p. 52. DOI: 10.3847/0004-637X/830/1/52. arXiv: 1605.04919 [astro-ph.GA].

Evans Neal J., II (Jan. 1999). "Physical Conditions in Regions of Star Formation". In: 37, pp. 311–362. DOI: 10.1146/annurev.astro.37.1.311. arXiv: astro-ph/9905050 [astro-ph].

Faucher-Giguère, Claude-André (2017a). "Observational Diagnostics of Gas Flows: Insights from Cosmological Simulations". In: *Gas Accretion onto Galaxies*. Ed. by Andrew Fox and Romeel Davé. Vol. 430, p. 271. DOI: 10.1007/978-3-319-52512-9_12.

— (Jan. 2017b). "Observational Diagnostics of Gas Flows: Insights from Cosmological Simulations". In: *Gas Accretion onto Galaxies*. Ed. by Andrew Fox and Romeel Davé. Vol. 430. Astrophysics and Space Science Library, p. 271. DOI: 10.1007/978-3-319-52512-9_12. arXiv: 1612.00448 [astro-ph.GA].

Faucher-Giguère, Claude-André et al. (Sept. 2016). "A stellar feedback origin for neutral hydrogen in high-redshift quasar-mass haloes". In: 461.1, pp. L32–L36. DOI: 10.1093/mnrasl/slw091. arXiv: 1601.07188 [astro-ph.GA].

Feltre, Anna et al. (Sept. 2020). "The MUSE Hubble Ultra Deep Field Survey. XV. The mean rest-UV spectra of Lyα emitters at z > 3". In: 641, A118, A118. DOI: 10.1051/0004-6361/202038133. arXiv: 2007.01878 [astro-ph.GA].

Fernández, Ximena, M. Ryan Joung, and Mary E. Putman (Apr. 2012). "The Origin and Distribution of Cold Gas in the Halo of a Milky-Way-mass Galaxy". In: 749.2, 181, p. 181. DOI: 10.1088/0004-637X/749/2/181. arXiv: 1203.0306 [astro-ph.GA].

Ferrarese, Laura and David Merritt (Aug. 2000). "A Fundamental Relation between Supermassive Black Holes and Their Host Galaxies". In: 539.1, pp. L9–L12. DOI: 10.1086/312838. arXiv: astro-ph/0006053 [astro-ph].

Finlator, Kristian and Romeel Davé (Apr. 2008). "The origin of the galaxy mass-metallicity relation and implications for galactic outflows". In: 385.4, pp. 2181–2204. DOI: 10.1111/j.1365-2966.2008.12991.x. arXiv: 0704.3100 [astro-ph].

Ford, Amanda Brady et al. (June 2013). "Hydrogen and metal line absorption around low-redshift galaxies in cosmological hydrodynamic simulations". In: 432.1, pp. 89–112. DOI: 10.1093/mnras/stt393. arXiv: 1206.1859 [astro-ph.CO].

Ford, Amanda Brady et al. (Oct. 2014). "Tracing inflows and outflows with absorption lines in circumgalactic gas". In: 444.2, pp. 1260–1281. DOI: 10.1093/mnras/stu1418. arXiv: 1309.5951 [astro-ph.CO].

Förster Schreiber, N. M. et al. (Apr. 2011). "Constraints on the Assembly and Dynamics of Galaxies. I. Detailed Rest-frame Optical Morphologies on Kiloparsec Scale of z ∼2 Star-forming Galaxies". In: 731.1, 65, p. 65. DOI: 10.1088/0004-637X/731/1/65. arXiv: 1011.1507 [astro-ph.CO].

Fox, Andrew J. et al. (June 2014). "The COS/UVES Absorption Survey of the Magellanic Stream. III. Ionization, Total Mass, and Inflow Rate onto the Milky Way". In: 787.2, 147, p. 147. DOI: 10.1088/0004-637X/787/2/147. arXiv: 1404.5514 [astro-ph.GA].

Franzetti, P. et al. (Aug. 2008). "GOSSIP, a New VO Compliant Tool for SED Fitting". In: *Astronomical Data Analysis Software and Systems XVII*. Ed. by R. W. Argyle, P. S. Bunclark, and J. R. Lewis. Vol. 394. Astronomical Society of the Pacific Conference Series, p. 642. arXiv: 0801.2518 [astro-ph].

Fraternali, F. and J. J. Binney (Feb. 2006). "A dynamical model for the extraplanar gas in spiral galaxies". In: 366.2, pp. 449–466. DOI: 10.1111/j.1365-2966.2005.09816.x. arXiv: astro-ph/0511334 [astro-ph].

Fried, D. L. (1966). "Optical Resolution Through a Randomly Inhomogeneous Medium for Very Long and Very Short Exposures". In: *J. Opt. Soc. Am.* 56.10, pp. 1372–1379. DOI: 10.1364/JOSA.56.001372. URL: http://www.osapublishing.org/abstract.cfm?URI=josa-56-10-1372.

Fu, Hai et al. (Nov. 2016). "The Circumgalactic Medium of Submillimeter Galaxies. I. First Results from a Radio-identified Sample". In: 832.1, 52, p. 52. DOI: 10.3847/0004-637X/832/1/52. arXiv: 1607.00016 [astro-ph.GA].

Fudamoto, Yoshinobu et al. (Feb. 2020). "A3COSMOS: the dust attenuation of star-forming galaxies at z = 2.5-4.0 from the COSMOS-ALMA archive". In: 491.4, pp. 4724–4734. DOI: 10.1093/mnras/stz3248. arXiv: 1910.12885 [astro-ph.GA].

Fuentes, Cesar I., Matthew R. George, and Matthew J. Holman (May 2009). "A Subaru Pencil-Beam Search for $m_R \sim 27$ Trans-Neptunian Bodies". In: 696.1, pp. 91–95. DOI: 10.1088/0004-637X/696/1/91. arXiv: 0809.4166 [astro-ph].

Fujimoto, Seiji et al. (July 2018). "ALMA 26 Arcmin^2 Survey of GOODS-S at One Millimeter (ASAGAO): Average Morphology of High-z Dusty Star-forming Galaxies in an Exponential Disk (n 1)". In: 861.1, 7, p. 7. DOI: 10.3847/1538-4357/aac6c4. arXiv: 1802.02136 [astro-ph.GA].

Fujimoto, Seiji et al. (Dec. 2019). "First Identification of 10 kpc [C II] 158 μm Halos around Star-forming Galaxies at z = 5-7". In: 887.2, 107, p. 107. DOI: 10.3847/1538-4357/ab480f. arXiv: 1902.06760 [astro-ph.GA].

Gao, Yu and Philip M. Solomon (May 2004). "The Star Formation Rate and Dense Molecular Gas in Galaxies". In: 606.1, pp. 271–290. DOI: 10.1086/382999. arXiv: astro-ph/0310339 [astro-ph].

Garilli, B. et al. (July 2010). "EZ: A Tool For Automatic Redshift Measurement". In: 122.893, p. 827. DOI: 10.1086/654903. arXiv: 1005.2825 [astro-ph.IM].

Gatkine, Pradip, Sylvain Veilleux, and Antonino Cucchiara (Oct. 2019). "The CGM-GRB Study. I. Uncovering the Circumgalactic Medium around GRB Hosts at Redshifts 2-6". In: 884.1, 66, p. 66. DOI: 10.3847/1538-4357/ab31ae. arXiv: 1907.05903 [astro-ph.GA].

Gatkine, Pradip et al. (Feb. 2022). "The CGM-GRB Study. II. Outflow-Galaxy Connection at z 2-6". In: 926.1, 63, p. 63. DOI: 10.3847/1538-4357/ac408e. arXiv: 2010.10540 [astro-ph.GA].

Gatto, A. et al. (Aug. 2013). "Unveiling the corona of the Milky Way via ram-pressure stripping of dwarf satellites". In: 433.4, pp. 2749–2763. DOI: 10.1093/mnras/stt896. arXiv: 1305.4176 [astro-ph.GA].

Genzel, R. et al. (June 2011). "The Sins Survey of z $\sim$2 Galaxy Kinematics: Properties of the Giant Star-forming Clumps". In: 733.2, 101, p. 101. DOI: 10.1088/0004-637X/733/2/101. arXiv: 1011.5360 [astro-ph.CO].

Gezari, D. Y., A. Labeyrie, and R. V. Stachnik (Apr. 1972). "Speckle Interferometry: Diffraction-Limited Measurements of Nine Stars with the 200-INCH Telescope". In: 173, p. L1. DOI: 10.1086/180906.

Giacconi, Riccardo et al. (Apr. 2002). "Chandra Deep Field South: The 1 Ms Catalog". In: 139.2, pp. 369–410. DOI: 10.1086/338927.

Graham, Alister W. (Feb. 2012). "Breaking the Law: The M_{bh}-$M_{spheroid}$ Relations for Core-Sérsic and Sérsic Galaxies". In: 746.1, 113, p. 113. DOI: 10.1088/0004-637X/746/1/113. arXiv: 1202.1878 [astro-ph.CO].

Hafen, Zachary et al. (Sept. 2019). "The origins of the circumgalactic medium in the FIRE simulations". In: 488.1, pp. 1248–1272. DOI: 10.1093/mnras/stz1773. arXiv: 1811.11753 [astro-ph.GA].

Hafen, Zachary et al. (Apr. 2020). "The fates of the circumgalactic medium in the FIRE simulations". In: 494.3, pp. 3581–3595. DOI: 10.1093/mnras/staa902. arXiv: 1910.01123 [astro-ph.GA].

Halfen, D. T., N. J. Woolf, and L. M. Ziurys (Aug. 2017). "The $^{12}C/^{13}C$ Ratio in Sgr B2(N): Constraints for Galactic Chemical Evolution and Isotopic Chemistry". In: 845.2, 158, p. 158. DOI: 10.3847/1538-4357/aa816b.

Halliday, C. et al. (Feb. 2008). "GMASS ultradeep spectroscopy of galaxies at z ~2 . I. The stellar metallicity". In: 479.2, pp. 417–425. DOI: 10.1051/0004-6361:20078673. arXiv: 0801.1193 [astro-ph].

Hasinger, G. et al. (May 2018). "The DEIMOS 10K Spectroscopic Survey Catalog of the COSMOS Field". In: 858.2, 77, p. 77. DOI: 10.3847/1538-4357/aabacf. arXiv: 1803.09251 [astro-ph.GA].

Hathi, N. P. et al. (Apr. 2016). "The VIMOS Ultra Deep Survey: Lyα emission and stellar populations of star-forming galaxies at $2 < z < 2.5$". In: 588, A26, A26. DOI: 10.1051/0004-6361/201526012. arXiv: 1503.01753 [astro-ph.GA].

Heckman, Timothy et al. (Sept. 2017). "COS-burst: Observations of the Impact of Starburst-driven Winds on the Properties of the Circum-galactic Medium". In: 846.2, 151, p. 151. DOI: 10.3847/1538-4357/aa80dc. arXiv: 1707.05933 [astro-ph.GA].

Heckman, Timothy M. and Sanchayeeta Borthakur (May 2016). "The Implications of Extreme Outflows from Extreme Starbursts". In: 822.1, 9, p. 9. DOI: 10.3847/0004-637X/822/1/9. arXiv: 1603.03036 [astro-ph.GA].

Heckman, Timothy M. et al. (Aug. 2015). "The Systematic Properties of the Warm Phase of Starburst-Driven Galactic Winds". In: 809.2, 147, p. 147. DOI: 10.1088/0004-637X/809/2/147. arXiv: 1507.05622 [astro-ph.GA].

Heitsch, Fabian and Mary E. Putman (June 2009). "The Fate of High-Velocity Clouds: Warm or Cold Cosmic Rain?" In: 698.2, pp. 1485–1496. DOI: 10.1088/0004-637X/698/2/1485. arXiv: 0904.1995 [astro-ph.GA].

Henkel, C. and R. Mauersberger (July 1993). "C and O nucleosynthesis in starbursts : the connection between distant mergers, the galaxy and the solar system." In: 274, pp. 730–742.

Henkel, C. et al. (June 2010). "Weak ^{13}CO in the Cloverleaf quasar: evidence for a young, early generation starburst". In: 516, A111, A111. DOI: 10.1051/0004-6361/200912889. arXiv: 1004.2699 [astro-ph.CO].

Hennawi, Joseph F. et al. (Nov. 2006). "Quasars Probing Quasars. I. Optically Thick Absorbers near Luminous Quasars". In: 651.1, pp. 61–83. DOI: 10.1086/507069. arXiv: astro-ph/0603742 [astro-ph].

Herrera-Camus, R. et al. (Feb. 2015). "[C II] 158 μm Emission as a Star Formation Tracer". In: 800.1, 1, p. 1. DOI: 10.1088/0004-637X/800/1/1. arXiv: 1409.7123 [astro-ph.GA].

Herwig, Falk and Sam M. Austin (Sept. 2004). "Nuclear Reaction Rates and Carbon Star Formation". In: 613.1, pp. L73–L76. DOI: 10.1086/424872. arXiv: astro-ph/0408394 [astro-ph].

Hobbs, Alexander, Justin Read, and Andrina Nicola (Oct. 2015). "Growing galaxies via superbubble-driven accretion flows". In: 452.4, pp. 3593–3609. DOI: 10.1093/mnras/stv1469. arXiv: 1410.3827 [astro-ph.GA].

Hopkins, Philip F., Eliot Quataert, and Norman Murray (Apr. 2012). "Stellar feedback in galaxies and the origin of galaxy-scale winds". In: 421.4, pp. 3522–3537. DOI: 10.1111/j.1365-2966.2012.20593.x. arXiv: 1110.4638 [astro-ph.CO].

Hornschemeier, A. E. et al. (Sept. 2000). "X-Ray Sources in the Hubble Deep Field Detected by Chandra". In: 541.1, pp. 49–53. DOI: 10.1086/309431. arXiv: astro-ph/0004260 [astro-ph].

Howk, J. Christopher, Blair D. Savage, and Dirk Fabian (Nov. 1999). "Abundances and Physical Conditions in the Warm Neutral Medium toward μ Columbae". In: 525.1, pp. 253–293. DOI: 10.1086/307888. arXiv: astro-ph/9905187 [astro-ph].

Hughes, T. M. et al. (June 2017). "VALES. II. The physical conditions of interstellar gas in normal star-forming galaxies up to z = 0.2 revealed by ALMA". In: 602, A49, A49. DOI: 10.1051/0004-6361/201629588. arXiv: 1611.05867 [astro-ph.GA].

Huynh, Minh T. et al. (Oct. 2005). "Radio Observations of the Hubble Deep Field-South Region. II. The 1.4 GHz Catalog and Source Counts". In: 130.4, pp. 1373–1388. DOI: 10.1086/432873. arXiv: astro-ph/0506047 [astro-ph].

Ibar, E. et al. (Oct. 2013). "Herschel reveals the obscured star formation in HiZELS Hα emitters at z = 1.47". In: 434.4, pp. 3218–3235. DOI: 10.1093/mnras/stt1258. arXiv: 1307.3556 [astro-ph.CO].

Ibar, E. et al. (May 2015). "A multiwavelength exploration of the [C II]/IR ratio in H-ATLAS/GAMA galaxies out to z = 0.2". In: 449.3, pp. 2498–2513. DOI: 10.1093/mnras/stv439. arXiv: 1503.01128 [astro-ph.GA].

Jeong, Wooyoung et al. (2019). "Suppression algorithm of speckle noise for parallel phase-shift digital holography". In: *Optics Laser Technology* 112, pp. 93–100. ISSN: 0030-3992. DOI: https://doi.org/10.1016/j.optlastec.2018.10.053. URL: https://www.sciencedirect.com/science/article/pii/S0030399218307047.

Jiménez-Donaire, María J. et al. (Feb. 2017). "^{13}CO/C^{18}O Gradients across the Disks of Nearby Spiral Galaxies". In: 836.2, L29, p. L29. DOI: 10.3847/2041-8213/836/2/L29. arXiv: 1701.01734 [astro-ph.GA].

Johnson, Sean D. et al. (2017). "The Extent of Chemically Enriched Gas around Star-forming Dwarf Galaxies". In: *The Astrophysical Journal* 850.1, p. L10. DOI: 10.3847/2041-8213/aa9370. URL: https://doi.org/10.3847/2041-8213/aa9370.

Jones, Tucker, Daniel P. Stark, and Richard S. Ellis (May 2012). "Keck Spectroscopy of Faint 3 < z < 7 Lyman Break Galaxies. III. The Mean Ultraviolet Spectrum at z $\sim$= 4". In: 751.1, 51, p. 51. DOI: 10.1088/0004-637X/751/1/51. arXiv: 1111.5102 [astro-ph.CO].

— (Aug. 2018). "Dust in the Wind: Composition and Kinematics of Galaxy Outflows at the Peak Epoch of Star Formation". In: 863.2, 191, p. 191. DOI: 10.3847/1538-4357/aad37f. arXiv: 1805.01484 [astro-ph.GA].

Joung, M. Ryan, Greg L. Bryan, and Mary E. Putman (Feb. 2012). "Gas Condensation in the Galactic Halo". In: 745.2, 148, p. 148. DOI: 10.1088/0004-637X/745/2/148. arXiv: 1105.4639 [astro-ph.CO].

Judge, P. G., C. Jordan, and U. Feldman (Jan. 1992). "Fe II Emission Lines. II. Excitation Mechanisms in Cool Stars". In: 384, p. 613. DOI: 10.1086/170903.

Jura, M. (July 1974). "Formation and destruction rates of interstellar H_2." In: 191, pp. 375–379. DOI: 10.1086/152975.

Kacprzak, Glenn G. (2017). "Gas Accretion in Star-Forming Galaxies". In: *Gas Accretion onto Galaxies*. Ed. by Andrew Fox and Romeel Davé. Vol. 430, p. 145. DOI: 10.1007/978-3-319-52512-9_7.

Kacprzak, Glenn G., Christopher W. Churchill, and Nikole M. Nielsen (Nov. 2012). "Tracing Outflows and Accretion: A Bimodal Azimuthal Dependence of Mg II Absorption". In: 760.1, L7, p. L7. DOI: 10.1088/2041-8205/760/1/L7. arXiv: 1205.0245 [astro-ph.CO].

Kacprzak, Glenn G. et al. (Mar. 2010). "Halo Gas and Galaxy Disk Kinematics Derived from Observations and ΛCDM Simulations of Mg II Absorption-selected Galaxies at Intermediate Redshift". In: 711.2, pp. 533–558. DOI: 10.1088/0004-637X/711/2/533. arXiv: 0912.2746 [astro-ph.CO].

Kacprzak, Glenn G. et al. (Oct. 2011). "Morphological properties of z$\sim$ 0.5 absorption-selected galaxies: the role of galaxy inclination". In: 416.4, pp. 3118–3137. DOI: 10.1111/j.1365-2966.2011.19261.x. arXiv: 1106.3068 [astro-ph.CO].

Kacprzak, Glenn G. et al. (Sept. 2014). "New Perspective on Galaxy Outflows from the First Detection of Both Intrinsic and Traverse Metal-line Absorption". In: 792.1, L12, p. L12. DOI: 10.1088/2041-8205/792/1/L12. arXiv: 1407.4126 [astro-ph.GA].

Kacprzak, Glenn G. et al. (Dec. 2015). "The Azimuthal Dependence of Outflows and Accretion Detected Using O VI Absorption". In: 815.1, 22, p. 22. DOI: 10.1088/0004-637X/815/1/22. arXiv: 1511.03275 [astro-ph.GA].

Kacprzak, Glenn G. et al. (Dec. 2019). "The Relationship between Galaxy ISM and Circumgalactic Gas Metallicities". In: 886.2, 91, p. 91. DOI: 10.3847/1538-4357/ab4c3c. arXiv: 1910.04310 [astro-ph.GA].

Kacprzak, Glenn G. et al. (Jan. 2021). "Evidence for galaxy quenching in the green valley caused by a lack of a circumgalactic medium". In: 500.2, pp. 2289–2301. DOI: 10.1093/mnras/staa3461. arXiv: 2011.02589 [astro-ph.GA].

Kennicutt Robert C., Jr. (Jan. 1998a). "Star Formation in Galaxies Along the Hubble Sequence". In: 36, pp. 189–232. DOI: 10.1146/annurev.astro.36.1.189. arXiv: astro-ph/9807187 [astro-ph].

— (May 1998b). "The Global Schmidt Law in Star-forming Galaxies". In: 498.2, pp. 541–552. DOI: 10.1086/305588. arXiv: astro-ph/9712213 [astro-ph].

Kereš, Dušan et al. (Oct. 2005). "How do galaxies get their gas?" In: 363.1, pp. 2–28. DOI: 10.1111/j.1365-2966.2005.09451.x. arXiv: astro-ph/0407095 [astro-ph].

Knauth, David C. et al. (Aug. 2003). "On the Origin of the High-Ionization Intermediate-Velocity Gas toward HD 14434". In: 592.2, pp. 964–974. DOI: 10.1086/375767. arXiv: astro-ph/0304196 [astro-ph].

Knudsen, K. K. et al. (Oct. 2005). "Submillimeter Observations of Distant Red Galaxies: Uncovering the 1 mJy 850 μm Population". In: 632.1, pp. L9–L12. DOI: 10.1086/497636. arXiv: astro-ph/0509104 [astro-ph].

Kobayashi, Chiaki, Amanda I. Karakas, and Hideyuki Umeda (July 2011). "The evolution of isotope ratios in the Milky Way Galaxy". In: 414.4, pp. 3231–3250. DOI: 10.1111/j.1365-2966.2011.18621.x. arXiv: 1102.5312 [astro-ph.GA].

Koekemoer, A. M. et al. (Sept. 2007). "The COSMOS Survey: Hubble Space Telescope Advanced Camera for Surveys Observations and Data Processing". In: 172.1, pp. 196–202. DOI: 10.1086/520086. arXiv: astro-ph/0703095 [astro-ph].

König, S. et al. (Oct. 2016). "Deep ALMA imaging of the merger NGC 1614. Is CO tracing a massive inflow of non-starforming gas?" In: 594, A70, A70. DOI: 10.1051/0004-6361/201628535. arXiv: 1603.05405 [astro-ph.GA].

Kornei, Katherine A. et al. (Mar. 2010). "The Relationship between Stellar Populations and Lyα Emission in Lyman Break Galaxies". In: 711.2, pp. 693–710. DOI: 10.1088/0004-637X/711/2/693. arXiv: 0911.2000 [astro-ph.CO].

Kornei, Katherine A. et al. (Oct. 2012). "The Properties and Prevalence of Galactic Outflows at z $\sim$1 in the Extended Groth Strip". In: 758.2, 135, p. 135. DOI: 10.1088/0004-637X/758/2/135. arXiv: 1205.0812 [astro-ph.CO].

Krumholz, Mark R., Avishai Dekel, and Christopher F. McKee (2011). "A UNIVERSAL, LOCAL STAR FORMATION LAW IN GALACTIC CLOUDS, NEARBY GALAXIES, HIGH-REDSHIFT DISKS, AND STARBURSTS". In: *The Astrophysical Journal* 745.1, p. 69. DOI: 10.1088/0004-637x/745/1/69. URL: https://doi.org/10.1088/0004-637x/745/1/69.

Kunth, D. and J. Bergeron (Oct. 1984). "Strong NaI D absorption in the spectrum of the QSO PKS 1327-206 due to the galaxy MCG 03-34-085." In: 210, pp. 873–882. DOI: 10.1093/mnras/210.4.873.

Kuwamura, Susumu et al. (Mar. 2008). "Image Restoration of Io by Shift-and-Add Method and Deconvolution". In: 120.865, p. 348. DOI: 10.1086/529550.

Labeyrie, A. (May 1970). "Attainment of Diffraction Limited Resolution in Large Telescopes by Fourier Analysing Speckle Patterns in Star Images". In: 6, p. 85.

Lan, Ting-Wen, Brice Ménard, and Guangtun Zhu (Nov. 2014). "The Properties of the Cool Circumgalactic Gas Probed with the SDSS, WISE, and GALEX Surveys". In: 795.1, 31, p. 31. DOI: 10.1088/0004-637X/795/1/31. arXiv: 1404.5301 [astro-ph.GA].

Lan, Ting-Wen and Houjun Mo (Oct. 2018). "The Circumgalactic Medium of eBOSS Emission Line Galaxies: Signatures of Galactic Outflows in Gas Distribution and Kinematics". In: 866.1, 36, p. 36. DOI: 10.3847/1538-4357/aadc08. arXiv: 1806.05786 [astro-ph.GA].

Langer, William D. and Arno A. Penzias (July 1990). "12C/ 13C Isotope Ratio across the Galaxy from Observations of 13C 18O in Molecular Clouds". In: 357, p. 477. DOI: 10.1086/168935.

Lanzetta, Kenneth M. et al. (Apr. 1995). "The Gaseous Extent of Galaxies and the Origin of Lyman-Alpha Absorption Systems: A Survey of Galaxies in the Fields of Hubble Space Telescope Spectroscopic Target QSOs". In: 442, p. 538. DOI: 10.1086/175459.

Lau, Marie Wingyee, J. Xavier Prochaska, and Joseph F. Hennawi (Oct. 2016). "Quasars Probing Quasars. VIII. The Physical Properties of the Cool Circumgalactic Medium Surrounding z ∼2-3 Massive Galaxies Hosting Quasars". In: 226.2, 25, p. 25. DOI: 10.3847/0067-0049/226/2/25. arXiv: 1510.06018 [astro-ph.GA].

Law, David R. et al. (Nov. 2012). "A HST/WFC3-IR Morphological Survey of Galaxies at z = 1.5-3.6. II. The Relation between Morphology and Gas-phase Kinematics". In: 759.1, 29, p. 29. DOI: 10.1088/0004-637X/759/1/29. arXiv: 1206.6889 [astro-ph.CO].

Le Fèvre, O. et al. (Sept. 2005). "The VIMOS VLT deep survey. First epoch VVDS-deep survey: 11 564 spectra with 17.5 ≤ IAB ≤ 24, and the redshift distribution over 0 ≤ z ≤ 5". In: 439.3, pp. 845–862. DOI: 10.1051/0004-6361:20041960. arXiv: astro-ph/0409133 [astro-ph].

Le Fèvre, O. et al. (Nov. 2013). "The VIMOS VLT Deep Survey final data release: a spectroscopic sample of 35 016 galaxies and AGN out to z ∼6.7 selected with 17.5 ≤ i_{AB} ≤ 24.75". In: 559, A14, A14. DOI: 10.1051/0004-6361/201322179. arXiv: 1307.0545 [astro-ph.CO].

Le Fèvre, O. et al. (Apr. 2015). "The VIMOS Ultra-Deep Survey: ∼10 000 galaxies with spectroscopic redshifts to study galaxy assembly at early epochs 2 < z 6". In: 576, A79, A79. DOI: 10.1051/0004-6361/201423829. arXiv: 1403.3938 [astro-ph.CO].

Le Fèvre, Oliver et al. (Mar. 2003). "Commissioning and performances of the VLT-VIMOS instrument". In: *Instrument Design and Performance for Optical/Infrared Ground-based Telescopes*. Ed. by Masanori Iye and Alan F. M. Moorwood. Vol. 4841. Society of Photo-Optical Instrumentation Engineers (SPIE) Conference Series, pp. 1670–1681. DOI: 10.1117/12.460959.

Leclercq, Floriane et al. (Dec. 2017). "The MUSE Hubble Ultra Deep Field Survey. VIII. Extended Lyman-α haloes around high-z star-forming galaxies". In: 608, A8, A8. DOI: 10.1051/0004-6361/201731480. arXiv: 1710.10271 [astro-ph.GA].

Leclercq, Floriane et al. (Mar. 2020). "The MUSE Hubble Ultra Deep Field Survey. XIII. Spatially resolved spectral properties of Lyman α haloes around star-forming galaxies at z > 3". In: 635, A82, A82. DOI: 10.1051/0004-6361/201937339. arXiv: 2002.05731 [astro-ph.GA].

Lehmer, B. D. et al. (Mar. 2007). "The X-Ray Evolution of Early-Type Galaxies in the Extended Chandra Deep Field-South". In: 657.2, pp. 681–699. DOI: 10.1086/511297. arXiv: astro-ph/0612003 [astro-ph].

Lehner, N. et al. (June 2014). "Galactic and Circumgalactic O VI and its Impact on the Cosmological Metal and Baryon Budgets at 2 < z <∼3.5". In: 788.2, 119, p. 119. DOI: 10.1088/0004-637X/788/2/119. arXiv: 1401.1811 [astro-ph.CO].

Lehner, Nicolas (Jan. 2017). "Gas Accretion via Lyman Limit Systems". In: *Gas Accretion onto Galaxies*. Ed. by Andrew Fox and Romeel Davé. Vol. 430. Astrophysics and Space Science Library, p. 117. DOI: 10.1007/978-3-319-52512-9_6. arXiv: 1612.00458 [astro-ph.GA].

Lemaux, B. C. et al. (Dec. 2014). "Hidden starbursts and active galactic nuclei at 0 < z < 4 from the Herschel-VVDS-CFHTLS-D1 field: Inferences on coevolution and feedback". In: 572, A90, A90. DOI: 10.1051/0004-6361/201323089. arXiv: 1311.5228 [astro-ph.CO].

Lemaux, B. C. et al. (Sept. 2020). "The VIMOS Ultra Deep Survey: The Reversal of the Star Formation Rate – Density Relation at 2 < z < 5". In: *arXiv e-prints*, arXiv:2009.03324, arXiv:2009.03324. arXiv: 2009.03324 [astro-ph.GA].

Liang, Cameron J. and Hsiao-Wen Chen (Oct. 2014). "Mining circumgalactic baryons in the low-redshift universe". In: *Monthly Notices of the Royal Astronomical Society* 445.2, pp. 2061–2081. ISSN: 0035-8711. DOI: 10.1093/mnras/stu1901. eprint: https://academic.oup.com/mnras/article-pdf/445/2/2061/18755276/stu1901.pdf. URL: https://doi.org/10.1093/mnras/stu1901.

Lilly, S. J. et al. (Sept. 2007). "zCOSMOS: A Large VLT/VIMOS Redshift Survey Covering 0 < z < 3 in the COSMOS Field". In: 172.1, pp. 70–85. DOI: 10.1086/516589. arXiv: astro-ph/0612291 [astro-ph].

Lilly, Simon J. et al. (Oct. 2009). "The zCOSMOS 10k-Bright Spectroscopic Sample". In: 184.2, pp. 218–229. DOI: 10.1088/0067-0049/184/2/218.

Lindroos, L. et al. (Feb. 2015). "Stacking of large interferometric data sets in the image- and uv-domain - a comparative study". In: 446.4, pp. 3502–3515. DOI: 10.1093/mnras/stu2344. arXiv: 1411.1410 [astro-ph.GA].

Liske, J. et al. (Sept. 2015). "Galaxy And Mass Assembly (GAMA): end of survey report and data release 2". In: 452.2, pp. 2087–2126. DOI: 10.1093/mnras/stv1436. arXiv: 1506.08222 [astro-ph.GA].

Longair, Malcolm S. (2008). *Galaxy Formation*.

Loomis, Ryan A. et al. (Apr. 2018). "Detecting Weak Spectral Lines in Interferometric Data through Matched Filtering". In: 155.4, 182, p. 182. DOI: 10.3847/1538-3881/aab604. arXiv: 1803.04987 [astro-ph.IM].

Lopez, S. et al. (Jan. 2020). "Slicing the cool circumgalactic medium along the major axis of a star-forming galaxy at z = 0.7". In: 491.3, pp. 4442–4461. DOI: 10.1093/mnras/stz3183. arXiv: 1911.04809 [astro-ph.GA].

Lopez, Sebastian et al. (Feb. 2018). "A clumpy and anisotropic galaxy halo at redshift 1 from gravitational-arc tomography". In: 554.7693, pp. 493–496. DOI: 10.1038/nature25436. arXiv: 1801.10175 [astro-ph.GA].

Lynds, C. R., S. P. Worden, and J. W. Harvey (July 1976). "Digital image reconstruction applied to Alpha Orionis." In: 207, pp. 174–180. DOI: 10.1086/154481.

Madau, Piero and Mark Dickinson (Aug. 2014). "Cosmic Star-Formation History". In: 52, pp. 415–486. DOI: 10.1146/annurev-astro-081811-125615. arXiv: 1403.0007 [astro-ph.CO].

Magliocchetti, M. et al. (Apr. 2020). "The role of galaxy mass on AGN emission: a view from the VANDELS survey". In: 493.3, pp. 3838–3853. DOI: 10.1093/mnras/staa410. arXiv: 2002.02980 [astro-ph.GA].

Magorrian, John et al. (June 1998). "The Demography of Massive Dark Objects in Galaxy Centers". In: 115.6, pp. 2285–2305. DOI: 10.1086/300353. arXiv: astro-ph/9708072 [astro-ph].

Maraston, Claudia (Sept. 2005). "Evolutionary population synthesis: models, analysis of the ingredients and application to high-z galaxies". In: 362.3, pp. 799–825. DOI: 10.1111/j.1365-2966.2005.09270.x. arXiv: astro-ph/0410207 [astro-ph].

Martin, Crystal L. (Mar. 2005). "Mapping Large-Scale Gaseous Outflows in Ultraluminous Galaxies with Keck II ESI Spectra: Variations in Outflow Velocity with Galactic Mass". In: 621.1, pp. 227–245. DOI: 10.1086/427277. arXiv: astro-ph/0410247 [astro-ph].

Martin, Crystal L. et al. (Dec. 2012). "Demographics and Physical Properties of Gas Outflows/Inflows at 0.4 < z < 1.4". In: 760.2, 127, p. 127. DOI: 10.1088/0004-637X/760/2/127. arXiv: 1206.5552 [astro-ph.CO].

Martin, Crystal L. et al. (June 2019). "Kinematics of Circumgalactic Gas: Feeding Galaxies and Feedback". In: 878.2, 84, p. 84. DOI: 10.3847/1538-4357/ab18ac. arXiv: 1901.09123 [astro-ph.GA].

Martín, S. et al. (Apr. 2019). "Spatially resolved carbon and oxygen isotopic ratios in NGC 253 using optically thin tracers". In: 624, A125, A125. DOI: 10.1051/0004-6361/201935106. arXiv: 1903.03244 [astro-ph.GA].

Mas-Ribas, Lluís et al. (Sept. 2017). "The Mean Metal-line Absorption Spectrum of Damped Lyα Systems in BOSS". In: 846.1, 4, p. 4. DOI: 10.3847/1538-4357/aa81cf. arXiv: 1610.02711 [astro-ph.GA].

Matejek, Michael S. and Robert A. Simcoe (Dec. 2012). "A Survey of Mg II Absorption at 2 < z < 6 with Magellan/FIRE. I. Sample and Evolution of the Mg II Frequency". In: 761.2, 112, p. 112. DOI: 10.1088/0004-637X/761/2/112. arXiv: 1201.3919 [astro-ph.CO].

Matsuda, Y. et al. (Sept. 2012). "Diffuse Lyα haloes around Lyα emitters at z=3: do dark matter distributions determine the Lyα spatial extents?" In: 425.2, pp. 878–883. DOI: 10.1111/j.1365-2966.2012.21143.x. arXiv: 1204.4934 [astro-ph.CO].

McLure, R. J. et al. (Sept. 2018). "The VANDELS ESO public spectroscopic survey". In: 479.1, pp. 25–42. DOI: 10.1093/mnras/sty1213. arXiv: 1803.07414 [astro-ph.GA].

Méndez-Hernández, H. et al. (Sept. 2020). "VALES VI: ISM enrichment in star-forming galaxies up to z $\sim$ 0.2 using ^{12}CO(1-0), ^{13}CO(1-0), and C^{18}O(1-0) line luminosity ratios". In: 497.3, pp. 2771–2785. DOI: 10.1093/mnras/staa1964. arXiv: 2007.01182 [astro-ph.GA].

Méndez-Hernández, H. et al. (2021). "The metal content of the Circumgalactic medium around star-forming galaxies at z $\sim$ 2.6 as revealed by the VIMOS Ultra-Deep Survey." In: submitted.ref. AA/2021/42553.

Milam, S. N. et al. (Dec. 2005). "The ^{12}C/^{13}C Isotope Gradient Derived from Millimeter Transitions of CN: The Case for Galactic Chemical Evolution". In: 634.2, pp. 1126–1132. DOI: 10.1086/497123.

Millard, Jenifer S. et al. (May 2020). "S2COSMOS: Evolution of gas mass with redshift using dust emission". In: 494.1, pp. 293–315. DOI: 10.1093/mnras/staa609. arXiv: 2003.01727 [astro-ph.GA].

Miller, Neal A. et al. (Nov. 2008). "The VLA 1.4 GHz Survey of the Extended Chandra Deep Field-South: First Data Release". In: 179.1, pp. 114–123. DOI: 10.1086/591054. arXiv: 0804.2375 [astro-ph].

Miller, Neal A. et al. (Apr. 2013). "The Very Large Array 1.4 GHz Survey of the Extended Chandra Deep Field South: Second Data Release". In: 205.2, 13, p. 13. DOI: 10.1088/0067-0049/205/2/13. arXiv: 1301.7004 [astro-ph.CO].

Mirabel, I. F. and D. B. Sanders (May 1989). "The Ratio of Molecular to Atomic Gas in Infrared Luminous Galaxies". In: 340, p. L53. DOI: 10.1086/185437.

Momose, Rieko et al. (July 2014). "Diffuse Lyα haloes around galaxies at z = 2.2-6.6: implications for galaxy formation and cosmic reionization". In: 442.1, pp. 110–120. DOI: 10.1093/mnras/stu825. arXiv: 1403.0732 [astro-ph.CO].

Mortensen, Kris et al. (June 2021). "Kinematics of the Circumgalactic Medium of a z = 0.77 Galaxy from Mg II Tomography". In: 914.2, 92, p. 92. DOI: 10.3847/1538-4357/abfa11. arXiv: 2006.00006 [astro-ph.GA].

Münch, Guido and Harold Zirin (Jan. 1961). "Interstellar Matter at Large Distances from the Galactic Plane." In: 133, p. 11. DOI: 10.1086/146999.

Nagao, T., A. Marconi, and R. Maiolino (Feb. 2006). "The evolution of the broad-line region among SDSS quasars". In: 447.1, pp. 157–172. DOI: 10.1051/0004-6361:20054024. arXiv: astro-ph/0510385 [astro-ph].

Nandra, K. et al. (Sept. 2002). "X-Ray Properties of Lyman Break Galaxies in the Hubble Deep Field-North Region". In: 576.2, pp. 625–639. DOI: 10.1086/341888. arXiv: astro-ph/0205215 [astro-ph].

Nelson, Dylan et al. (Dec. 2019). "First results from the TNG50 simulation: galactic outflows driven by supernovae and black hole feedback". In: 490.3, pp. 3234–3261. DOI: 10.1093/mnras/stz2306. arXiv: 1902.05554 [astro-ph.GA].

Nelson, Dylan et al. (Nov. 2021). "The cold circumgalactic medium in emission: Mg II haloes in TNG50". In: 507.3, pp. 4445–4463. DOI: 10.1093/mnras/stab2177. arXiv: 2106.09023 [astro-ph.GA].

Nielsen, Nikole M. et al. (Oct. 2015). "MAGIICAT V. Orientation of Outflows and Accretion Determine the Kinematics and Column Densities of the Circumgalactic Medium". In: 812.1, 83, p. 83. DOI: 10.1088/0004-637X/812/1/83. arXiv: 1505.07167 [astro-ph.GA].

Oppenheimer, Benjamin D. et al. (Aug. 2010). "Feedback and recycled wind accretion: assembling the z = 0 galaxy mass function". In: 406.4, pp. 2325–2338. DOI: 10.1111/j.1365-2966.2010.16872.x. arXiv: 0912.0519 [astro-ph.CO].

Oppenheimer, Benjamin D. et al. (Aug. 2016). "Bimodality of low-redshift circumgalactic O VI in non-equilibrium EAGLE zoom simulations". In: 460.2, pp. 2157–2179. DOI: 10.1093/mnras/stw1066. arXiv: 1603.05984 [astro-ph.GA].

Oyarzún, Grecco A. et al. (Apr. 2016). "How Lyman Alpha Emission Depends on Galaxy Stellar Mass". In: 821.1, L14, p. L14. DOI: 10.3847/2041-8205/821/1/L14. arXiv: 1604.03113 [astro-ph.GA].

Oyarzún, Grecco A. et al. (July 2017). "A Comprehensive Study of Lyα Emission in the High-redshift Galaxy Population". In: 843.2, 133, p. 133. DOI: 10.3847/1538-4357/aa7552. arXiv: 1706.01886 [astro-ph.GA].

Pagel, Bernard E. J. (1997). *Nucleosynthesis and Chemical Evolution of Galaxies*.

Pahl, Anthony J. et al. (Apr. 2020). "The redshift evolution of rest-UV spectroscopic properties to z $\sim$ 5". In: 493.3, pp. 3194–3211. DOI: 10.1093/mnras/staa355. arXiv: 1910.04179 [astro-ph.GA].

Peeples, Molly S. et al. (May 2014). "A Budget and Accounting of Metals at z $\sim$0: Results from the COS-Halos Survey". In: 786.1, 54, p. 54. DOI: 10.1088/0004-637X/786/1/54. arXiv: 1310.2253 [astro-ph.CO].

Peeples, Molly S. et al. (Mar. 2019). "Figuring Out Gas & Galaxies in Enzo (FOGGIE). I. Resolving Simulated Circumgalactic Absorption at 2 $\leq$ z $\leq$ 2.5". In: 873.2, 129, p. 129. DOI: 10.3847/1538-4357/ab0654. arXiv: 1810.06566 [astro-ph.GA].

Peng, Chien Y. et al. (July 2002). "Detailed Structural Decomposition of Galaxy Images". In: 124.1, pp. 266–293. DOI: 10.1086/340952. arXiv: astro-ph/0204182 [astro-ph].

— (June 2010). "Detailed Decomposition of Galaxy Images. II. Beyond Axisymmetric Models". In: 139.6, pp. 2097–2129. DOI: 10.1088/0004-6256/139/6/2097. arXiv: 0912.0731 [astro-ph.CO].

Pentericci, L. et al. (May 2010). "Physical and morphological properties of z $\sim$3 Lyman break galaxies: dependence on Lyα line emission". In: 514, A64, A64. DOI: 10.1051/0004-6361/200913425. arXiv: 1002.2068 [astro-ph.CO].

Pentericci, L. et al. (Sept. 2018). "The VANDELS ESO public spectroscopic survey: Observations and first data release". In: 616, A174, A174. DOI: 10.1051/0004-6361/201833047. arXiv: 1803.07373 [astro-ph.GA].

Penzias, A. A. (Oct. 1981). "The isotopic abundances of interstellar oxygen." In: 249, pp. 518–523. DOI: 10.1086/159311.

Penzias, A. A., K. B. Jefferts, and R. W. Wilson (May 1971). "Interstellar {12}C{16}O, {13}C{16}O, and {12}C{18}O". In: 165, p. 229. DOI: 10.1086/150893.

Perger, Krisztina et al. (Dec. 2019). "Unveiling the weak radio quasar population at z$\geq$4". In: 490.2, pp. 2542–2549. DOI: 10.1093/mnras/stz2723. arXiv: 1909.11012 [astro-ph.GA].

Péroux, Céline and J. Christopher Howk (Aug. 2020). "The Cosmic Baryon and Metal Cycles". In: 58, pp. 363–406. DOI: 10.1146/annurev-astro-021820-120014. arXiv: 2011.01935 [astro-ph.GA].

Péroux, Céline et al. (Sept. 2020). "Predictions for the angular dependence of gas mass flow rate and metallicity in the circumgalactic medium". In: 499.2, pp. 2462–2473. DOI: 10.1093/mnras/staa2888. arXiv: 2009.07809 [astro-ph.GA].

Pickering, J. C. et al. (Dec. 2002). "The FERRUM Project: Experimental oscillator strengths of the UV 8 multiplet and other UV transitions from the y^{6}P levels of Fe II". In: 396, pp. 715–722. DOI: 10.1051/0004-6361:20021388.

Planck Collaboration et al. (Sept. 2020). "Planck 2018 results. VI. Cosmological parameters". In: 641, A6, A6. DOI: 10.1051/0004-6361/201833910. arXiv: 1807.06209 [astro-ph.CO].

Prantzos, N., O. Aubert, and J. Audouze (May 1996). "Evolution of the carbon and oxygen isotopes in the Galaxy." In: 309, pp. 760–774.

Price, Sedona H. et al. (May 2020). "The MOSDEF Survey: Kinematic and Structural Evolution of Star-forming Galaxies at $1.4 \leq z \leq 3.8$". In: 894.2, 91, p. 91. DOI: 10.3847/1538-4357/ab7990. arXiv: 1902.09554 [astro-ph.GA].

Prochaska, J. Xavier, Marie Wingyee Lau, and Joseph F. Hennawi (Dec. 2014). "Quasars Probing Quasars. VII. The Pinnacle of the Cool Circumgalactic Medium Surrounds Massive z ~2 Galaxies". In: 796.2, 140, p. 140. DOI: 10.1088/0004-637X/796/2/140. arXiv: 1409.6344 [astro-ph.GA].

Prochaska, J. Xavier and Arthur M. Wolfe (May 2009). "On the (Non)Evolution of H I Gas in Galaxies Over Cosmic Time". In: 696.2, pp. 1543–1547. DOI: 10.1088/0004-637X/696/2/1543. arXiv: 0811.2003 [astro-ph].

Prochaska, J. Xavier et al. (Oct. 2011). "Probing the Intergalactic Medium/Galaxy Connection. V. On the Origin of Lyα and O VI Absorption at $z < 0.2$". In: 740.2, 91, p. 91. DOI: 10.1088/0004-637X/740/2/91. arXiv: 1103.1891 [astro-ph.CO].

Putman, Mary E. (2017). "An Introduction to Gas Accretion onto Galaxies". In: *Gas Accretion onto Galaxies*. Ed. by Andrew Fox and Romeel Davé. Vol. 430, p. 1. DOI: 10.1007/978-3-319-52512-9_1.

Ranjan, A. et al. (Jan. 2022). "Multi-phase gas properties of extremely strong intervening DLAs towards quasars". In: *arXiv e-prints*, arXiv:2201.06413, arXiv:2201.06413. arXiv: 2201.06413 [astro-ph.GA].

Reddy, Naveen A. et al. (Sept. 2016). "The Connection Between Reddening, Gas Covering Fraction, and the Escape of Ionizing Radiation at High Redshift". In: 828.2, 108, p. 108. DOI: 10.3847/0004-637X/828/2/108. arXiv: 1606.03452 [astro-ph.GA].

Ribeiro, B. et al. (Aug. 2016). "Size evolution of star-forming galaxies with $2 < z < 4.5$ in the VIMOS Ultra-Deep Survey". In: 593, A22, A22. DOI: 10.1051/0004-6361/201628249. arXiv: 1602.01840 [astro-ph.GA].

Richter, P. (July 2017). "Gas Accretion onto the Milky Way". In: *Whereabouts and Physics of the Roaming Baryons in the Universe*, p. 30.

Richter, P. et al. (May 2016). "An HST/COS legacy survey of intervening Si III absorption in the extended gaseous halos of low-redshift galaxies". In: 590, A68, A68. DOI: 10.1051/0004-6361/201527038. arXiv: 1507.06317 [astro-ph.CO].

Rickard, L. J. and L. Blitz (May 1985). "Carbon monoxide isotope ratios in galactic center and disks." In: 292, pp. L57–L60. DOI: 10.1086/184472.

Rickard, L. J. et al. (July 1975). "Detection of extragalactic carbon monoxide at millimeter wavelengths." In: 199, pp. L75–L78. DOI: 10.1086/181852.

Rigby, J. R. et al. (Jan. 2018). "The Magellan Evolution of Galaxies Spectroscopic and Ultraviolet Reference Atlas (MegaSaura). II. Stacked Spectra". In: 853.1, 87, p. 87. DOI: 10.3847/1538-4357/aaa2fc. arXiv: 1710.07499 [astro-ph.GA].

Rodighiero, G. et al. (2011). "THE LESSER ROLE OF STARBURSTS IN STAR FORMATION AT z = 2". In: *The Astrophysical Journal* 739.2, p. L40. DOI: 10.1088/2041-8205/739/2/l40. URL: https://doi.org/10.1088/2041-8205/739/2/l40.

Rodighiero, G. et al. (Feb. 2015). "Relationship between Star Formation Rate and Black Hole Accretion At Z = 2: the Different Contributions in Quiescent, Normal, and Starburst Galaxies". In: 800.1, L10, p. L10. DOI: 10.1088/2041-8205/800/1/L10. arXiv: 1501.04634 [astro-ph.GA].

Romano, D. et al. (Sept. 2017). "The evolution of CNO isotopes: a new window on cosmic star formation history and the stellar IMF in the age of ALMA". In: 470.1, pp. 401–415. DOI: 10.1093/mnras/stx1197. arXiv: 1704.06701 [astro-ph.GA].

Rubin, Kate H. R. et al. (Aug. 2010). "The Persistence of Cool Galactic Winds in High Stellar Mass Galaxies between z ~1.4 and ~1". In: 719.2, pp. 1503–1525. DOI: 10.1088/0004-637X/719/2/1503. arXiv: 0912.2343 [astro-ph.CO].

Rubin, Kate H. R. et al. (Mar. 2012). "The Direct Detection of Cool, Metal-enriched Gas Accretion onto Galaxies at z ∼0.5". In: 747.2, L26, p. L26. DOI: 10.1088/2041-8205/747/2/L26. arXiv: 1110.0837 [astro-ph.CO].

Rubin, Kate H. R. et al. (Oct. 2014). "Evidence for Ubiquitous Collimated Galactic-scale Outflows along the Star-forming Sequence at z ∼0.5". In: 794.2, 156, p. 156. DOI: 10.1088/0004-637X/794/2/156. arXiv: 1307.1476 [astro-ph.CO].

Rubin, Kate H. R. et al. (Dec. 2018). "Galaxies Probing Galaxies in PRIMUS. II. The Coherence Scale of the Cool Circumgalactic Medium". In: 868.2, 142, p. 142. DOI: 10.3847/1538-4357/aad566. arXiv: 1806.08801 [astro-ph.GA].

Rudie, Gwen C. et al. (May 2012). "The Gaseous Environment of High-z Galaxies: Precision Measurements of Neutral Hydrogen in the Circumgalactic Medium of z ∼2-3 Galaxies in the Keck Baryonic Structure Survey". In: 750.1, 67, p. 67. DOI: 10.1088/0004-637X/750/1/67. arXiv: 1202.6055 [astro-ph.CO].

Rudie, Gwen C. et al. (Nov. 2019). "Column Density, Kinematics, and Thermal State of Metal-bearing Gas within the Virial Radius of z ∼ 2 Star-forming Galaxies in the Keck Baryonic Structure Survey". In: 885.1, 61, p. 61. DOI: 10.3847/1538-4357/ab4255. arXiv: 1903.00004 [astro-ph.GA].

Runnholm, Axel et al. (Mar. 2020). "The Lyman Alpha Reference Sample. X. Predicting Lyα Output from Star-forming Galaxies Using Multivariate Regression". In: 892.1, 48, p. 48. DOI: 10.3847/1538-4357/ab7a91. arXiv: 2002.12378 [astro-ph.GA].

Sánchez Almeida, Jorge (Jan. 2017). "Gas Accretion and Star Formation Rates". In: *Gas Accretion onto Galaxies*. Ed. by Andrew Fox and Romeel Davé. Vol. 430. Astrophysics and Space Science Library, p. 67. DOI: 10.1007/978-3-319-52512-9_4. arXiv: 1612.00776 [astro-ph.GA].

Sanders, Ryan L. et al. (June 2021). "The MOSDEF Survey: The Evolution of the Mass-Metallicity Relation from z = 0 to z 3.3". In: 914.1, 19, p. 19. DOI: 10.3847/1538-4357/abf4c1. arXiv: 2009.07292 [astro-ph.GA].

Sargent, W. L. W. et al. (Jan. 1980). "The distribution of Lyman-alpha absorption lines in the spectra of six QSOs: evidence for an intergalactic origin." In: 42, pp. 41–81. DOI: 10.1086/190644.

Sato, Taro et al. (May 2009). "AEGIS: The Nature of the Host Galaxies of Low-Ionization Outflows at z < 0.6". In: 696.1, pp. 214–232. DOI: 10.1088/0004-637X/696/1/214. arXiv: 0804.4312 [astro-ph].

Savage, Blair D., Marilyn R. Meade, and Kenneth R. Sembach (Oct. 2001). "IUE Absorption-Line Observations of the Moderately and Highly Ionized Interstellar Medium toward 164 Early-Type Stars". In: 136.2, pp. 631–702. DOI: 10.1086/322537.

Schinnerer, E. et al. (Sept. 2007). "The VLA-COSMOS Survey. II. Source Catalog of the Large Project". In: 172.1, pp. 46–69. DOI: 10.1086/516587. arXiv: astro-ph/0612314 [astro-ph].

Schmidt, Maarten (Mar. 1959). "The Rate of Star Formation." In: 129, p. 243. DOI: 10.1086/146614.

Scodeggio, M. et al. (Nov. 2005). "The VVDS Data-Reduction Pipeline: Introducing VIPGI, the VIMOS Interactive Pipeline and Graphical Interface". In: 117.837, pp. 1284–1295. DOI: 10.1086/496937. arXiv: astro-ph/0409248 [astro-ph].

Scott, Robert (Lauchie) and Alex Ellery (2015). "An approach to ground based space surveillance of geostationary on-orbit servicing operations". In: *Acta Astronautica* 112, pp. 56–68. ISSN: 0094-5765. DOI: https://doi.org/10.1016/j.actaastro.2015.03.010. URL: https://www.sciencedirect.com/science/article/pii/S0094576515001095.

Scoville, N. et al. (Sept. 2007). "The Cosmic Evolution Survey (COSMOS): Overview". In: 172.1, pp. 1–8. DOI: 10.1086/516585. arXiv: astro-ph/0612305 [astro-ph].

Seibert, Mark, Timothy M. Heckman, and Gerhardt R. Meurer (July 2002). "The Starburst Nature of Lyman Break Galaxies: Testing Ultraviolet Extinction with X-Rays". In: 124.1, pp. 46–52. DOI: 10.1086/341043. arXiv: astro-ph/0204047 [astro-ph].

Shapley, Alice E. et al. (May 2003). "Rest-Frame Ultraviolet Spectra of z∼3 Lyman Break Galaxies". In: 588.1, pp. 65–89. DOI: 10.1086/373922. arXiv: astro-ph/0301230 [astro-ph].

Shen, Sijing et al. (Nov. 2012). "The Origin of Metals in the Circumgalactic Medium of Massive Galaxies at z = 3". In: 760.1, 50, p. 50. DOI: 10.1088/0004-637X/760/1/50. arXiv: 1109.3713 [astro-ph.CO].

Shen, Sijing et al. (Mar. 2013). "The Circumgalactic Medium of Massive Galaxies at z ∼3: A Test for Stellar Feedback, Galactic Outflows, and Cold Streams". In: 765.2, 89, p. 89. DOI: 10.1088/0004-637X/765/2/89. arXiv: 1205.0270 [astro-ph.CO].

Shull, J. M., M. van Steenberg, and C. G. Seab (Aug. 1983). "Observationally determined Fe II oscillator strenghts." In: 271, pp. 408–414. DOI: 10.1086/161207.

Shull, J. M., D. G. York, and Jr. Snow T. P. (June 1981). "Observationally determined silicon II oscillator strengths". In: 246, pp. 549–553. DOI: 10.1086/158955.

Silk, Joseph and Martin J. Rees (Mar. 1998). "Quasars and galaxy formation". In: 331, pp. L1–L4. arXiv: astro-ph/9801013 [astro-ph].

Sliwa, Kazimierz et al. (May 2017). "Luminous Infrared Galaxies with the Submillimeter Array. V. Molecular Gas in Intermediate to Late-stage Mergers". In: 840.1, 8, p. 8. DOI: 10.3847/1538-4357/aa689b. arXiv: 1703.07121 [astro-ph.GA].

Solomon, P. M., D. Downes, and S. J. E. Radford (Mar. 1992). "Dense Molecular Gas and Starbursts in Ultraluminous Galaxies". In: 387, p. L55. DOI: 10.1086/186304.

Solomon, P. M. and P. A. Vanden Bout (Sept. 2005). "Molecular Gas at High Redshift". In: 43.1, pp. 677–725. DOI: 10.1146/annurev.astro.43.051804.102221. arXiv: astro-ph/0508481 [astro-ph].

Songaila, Antoinette (Nov. 2001). "The Minimum Universal Metal Density between Redshifts of 1.5 and 5.5". In: 561.2, pp. L153–L156. DOI: 10.1086/324761. arXiv: astro-ph/0110123 [astro-ph].

Spilker, J. S. et al. (Apr. 2014). "The Rest-frame Submillimeter Spectrum of High-redshift, Dusty, Star-forming Galaxies". In: 785.2, 149, p. 149. DOI: 10.1088/0004-637X/785/2/149. arXiv: 1403.1667 [astro-ph.GA].

Stark, Daniel P. et al. (Nov. 2010). "Keck spectroscopy of faint 3 < z < 7 Lyman break galaxies - I. New constraints on cosmic reionization from the luminosity and redshift-dependent fraction of Lyman α emission". In: 408.3, pp. 1628–1648. DOI: 10.1111/j.1365-2966.2010.17227.x. arXiv: 1003.5244 [astro-ph.CO].

Steidel, C. C. (Jan. 1995). "The Nature and Evolution of Absorption-Selected Galaxies". In: *QSO Absorption Lines*. Ed. by Georges Meylan, p. 139. arXiv: astro-ph/9509098 [astro-ph].

Steidel, Charles C., Mark Dickinson, and S. E. Persson (Dec. 1994). "Field Galaxy Evolution Since Z approximately 1 from a Sample of QSO Absorption–selected Galaxies". In: 437, p. L75. DOI: 10.1086/187686. arXiv: astro-ph/9410025 [astro-ph].

Steidel, Charles C. et al. (Apr. 2004). "A Survey of Star-forming Galaxies in the 1.4<<∼2.5 Redshift Desert: Overview". In: 604.2, pp. 534–550. DOI: 10.1086/381960. arXiv: astro-ph/0401439 [astro-ph].

Steidel, Charles C. et al. (July 2010). "The Structure and Kinematics of the Circumgalactic Medium from Far-ultraviolet Spectra of z ∼= 2-3 Galaxies". In: 717.1, pp. 289–322. DOI: 10.1088/0004-637X/717/1/289. arXiv: 1003.0679 [astro-ph.CO].

Steidel, Charles C. et al. (Aug. 2011). "Diffuse Lyα Emitting Halos: A Generic Property of High-redshift Star-forming Galaxies". In: 736.2, 160, p. 160. DOI: 10.1088/0004-637X/736/2/160. arXiv: 1101.2204 [astro-ph.CO].

Steigman, G. (Aug. 1975). "Charge transfer reactions in multiply charged ion-atom collisions." In: 199, pp. 642–646. DOI: 10.1086/153732.

Stewart, Kyle R. et al. (Sept. 2011). "Orbiting Circumgalactic Gas as a Signature of Cosmological Accretion". In: 738.1, 39, p. 39. DOI: 10.1088/0004-637X/738/1/39. arXiv: 1103.4388 [astro-ph.CO].

Stoehr, F. et al. (Aug. 2008). "DER_SNR: A Simple & General Spectroscopic Signal-to-Noise Measurement Algorithm". In: *Astronomical Data Analysis Software and Systems XVII*. Ed. by R. W. Argyle, P. S. Bunclark, and J. R. Lewis. Vol. 394. Astronomical Society of the Pacific Conference Series, p. 505.

Strom, Allison L. et al. (Nov. 2021). "Chemical abundance scaling relations for multiple elements in z$_\sim$2-3 star-forming galaxies". In: *arXiv e-prints*, arXiv:2111.06410, arXiv:2111.06410. arXiv: 2111.06410 [astro-ph.GA].

Tan, Qing-Hua et al. (July 2011). "^{12}CO, ^{13}CO and C^{18}O observations along the major axes of nearby bright infrared galaxies". In: *Research in Astronomy and Astrophysics* 11.7, pp. 787–810. DOI: 10.1088/1674-4527/11/7/005. arXiv: 1103.5540 [astro-ph.CO].

Tang, X. D. et al. (Sept. 2019). "ALMA view of the ^{12}C/^{13}C isotopic ratio in starburst galaxies". In: 629, A6, A6. DOI: 10.1051/0004-6361/201935603. arXiv: 1906.06638 [astro-ph.GA].

Taniguchi, Yoshiaki and Youichi Ohyama (Nov. 1998). "^{13}CO (J = 1-0) Depression in Luminous Starburst Mergers". In: 507.2, pp. L121–L124. DOI: 10.1086/311696. arXiv: astro-ph/9809252 [astro-ph].

Taniguchi, Yoshiaki, Youichi Ohyama, and D. B. Sanders (Sept. 1999). "^{13}CO (J=1-0) Depression in Luminous Starburst Mergers, Revisited". In: 522.1, pp. 214–219. DOI: 10.1086/307650. arXiv: astro-ph/9904066 [astro-ph].

Tasca, L. A. M. et al. (Sept. 2015). "The evolving star formation rate: M$_\star$ relation and sSFR since z 5 from the VUDS spectroscopic survey". In: 581, A54, A54. DOI: 10.1051/0004-6361/201425379. arXiv: 1411.5687 [astro-ph.GA].

Tasca, L. A. M. et al. (Apr. 2017). "The VIMOS Ultra Deep Survey first data release: Spectra and spectroscopic redshifts of 698 objects up to z_{spec} 6 in CANDELS". In: 600, A110, A110. DOI: 10.1051/0004-6361/201527963. arXiv: 1602.01842 [astro-ph.GA].

Tejos, N. et al. (May 2021). "Telltale signs of metal recycling in the circumgalactic medium of a $z \sim 0.77$ galaxy". In: *arXiv e-prints*, arXiv:2105.01673, arXiv:2105.01673. arXiv: 2105.01673 [astro-ph.GA].

Tepper-García, Thor, Joss Bland-Hawthorn, and Ralph S. Sutherland (Nov. 2015). "The Magellanic Stream: Break-up and Accretion onto the Hot Galactic Corona". In: 813.2, 94, p. 94. DOI: 10.1088/0004-637X/813/2/94. arXiv: 1505.01587 [astro-ph.GA].

Thom, Christopher et al. (Oct. 2012). "Not Dead Yet: Cool Circumgalactic Gas in the Halos of Early-type Galaxies". In: 758.2, L41, p. L41. DOI: 10.1088/2041-8205/758/2/L41. arXiv: 1209.5442 [astro-ph.CO].

Thomas, R. et al. (June 2017). "The extended epoch of galaxy formation: Age dating of 3600 galaxies with 2 < z < 6.5 in the VIMOS Ultra-Deep Survey". In: 602, A35, A35. DOI: 10.1051/0004-6361/201628141. arXiv: 1602.01841 [astro-ph.GA].

Timmes, F. X., S. E. Woosley, and Thomas A. Weaver (June 1995). "Galactic Chemical Evolution: Hydrogen through Zinc". In: 98, p. 617. DOI: 10.1086/192172. arXiv: astro-ph/9411003 [astro-ph].

Tinsley, B. M. (Jan. 1980). "Evolution of the Stars and Gas in Galaxies". In: 5, pp. 287–388.

Topal, Selçuk (July 2021). "Molecular line ratio diagnostics and gas kinematics in the AGN host Seyfert galaxy NGC 5033". In: 504.4, pp. 5941–5953. DOI: 10.1093/mnras/stab1269. arXiv: 2105.11198 [astro-ph.GA].

Trainor, Ryan F. et al. (Aug. 2015). "The Spectroscopic Properties of Lyα-Emitters at z $\sim$2.7: Escaping Gas and Photons from Faint Galaxies". In: 809.1, 89, p. 89. DOI: 10.1088/0004-637X/809/1/89. arXiv: 1506.08205 [astro-ph.GA].

Trainor, Ryan F. et al. (Dec. 2019). "Predicting Lyα Emission from Galaxies via Empirical Markers of Production and Escape in the KBSS". In: 887.1, 85, p. 85. DOI: 10.3847/1538-4357/ab4993. arXiv: 1908.04794 [astro-ph.GA].

Tremonti, Christy A., John Moustakas, and Aleksandar M. Diamond-Stanic (July 2007). "The Discovery of 1000 km s^{-1} Outflows in Massive Poststarburst Galaxies at z=0.6". In: 663.2, pp. L77–L80. DOI: 10.1086/520083. arXiv: 0706.0527 [astro-ph].

Tripp, Todd M., Limin Lu, and Blair D. Savage (Nov. 1998). "The Relationship between Galaxies and Low-Redshift Weak Lyα Absorbers in the Directions of H1821+643 and PG 1116+215". In: 508.1, pp. 200–231. DOI: 10.1086/306397. arXiv: astro-ph/9806036 [astro-ph].

Tumlinson, J. et al. (Nov. 2011). "The Large, Oxygen-Rich Halos of Star-Forming Galaxies Are a Major Reservoir of Galactic Metals". In: *Science* 334.6058, p. 948. DOI: 10.1126/science.1209840. arXiv: 1111.3980 [astro-ph.CO].

Tumlinson, Jason, Molly S. Peeples, and Jessica K. Werk (Aug. 2017). "The Circumgalactic Medium". In: 55.1, pp. 389–432. DOI: 10.1146/annurev-astro-091916-055240. arXiv: 1709.09180 [astro-ph.GA].

Turner, Monica L. et al. (Nov. 2014). "Metal-line absorption around z $\approx$ 2.4 star-forming galaxies in the Keck Baryonic Structure Survey". In: 445.1, pp. 794–822. DOI: 10.1093/mnras/stu1801. arXiv: 1403.0942 [astro-ph.CO].

van de Voort, Freeke (Jan. 2017). "The Effect of Galactic Feedback on Gas Accretion and Wind Recycling". In: *Gas Accretion onto Galaxies*. Ed. by Andrew Fox and Romeel Davé. Vol. 430. Astrophysics and Space Science Library, p. 301. DOI: 10.1007/978-3-319-52512-9_13. arXiv: 1612.00591 [astro-ph.GA].

van de Voort, Freeke and Joop Schaye (Apr. 2013). "Soft X-ray and ultraviolet metal-line emission from the gas around galaxies". In: 430.4, pp. 2688–2702. DOI: 10.1093/mnras/stt115. arXiv: 1207.5512 [astro-ph.CO].

Vanzella, E. et al. (Apr. 2009). "Spectroscopic Observations of Lyman Break Galaxies at Redshifts ~4, 5, and 6 in the Goods-South Field". In: 695.2, pp. 1163–1182. DOI: 10.1088/0004-637X/695/2/1163. arXiv: 0901.4364 [astro-ph.CO].

Vigroux, L., J. Audouze, and J. Lequeux (Oct. 1976). "Isotopes of C, N and O and chemical evolution of galaxies (II)." In: 52.1, pp. 1–9.

Villanueva, V. et al. (Oct. 2017). "VALES I: the molecular gas content in star-forming dusty H-ATLAS galaxies up to z = 0.35". In: 470.4, pp. 3775–3805. DOI: 10.1093/mnras/stx1338. arXiv: 1705.09826 [astro-ph.GA].

Vladilo, Giovanni et al. (Aug. 2001). "Ionization Properties and Elemental Abundances in Damped Lyα Systems". In: 557.2, pp. 1007–1020. DOI: 10.1086/321650. arXiv: astro-ph/0104298 [astro-ph].

Vogelsberger, Mark et al. (Dec. 2013). "A model for cosmological simulations of galaxy formation physics". In: 436.4, pp. 3031–3067. DOI: 10.1093/mnras/stt1789. arXiv: 1305.2913 [astro-ph.CO].

Voit, G. Mark et al. (July 2015). "Precipitation-regulated Star Formation in Galaxies". In: 808.1, L30, p. L30. DOI: 10.1088/2041-8205/808/1/L30. arXiv: 1505.03592 [astro-ph.GA].

Wang, Feige et al. (Jan. 2021). "A Luminous Quasar at Redshift 7.642". In: *arXiv e-prints*, arXiv:2101.03179, arXiv:2101.03179. arXiv: 2101.03179 [astro-ph.GA].

Watson, W. D. (1977). "Isotope Fractionation in Interstellar Molecules". In: *CNO Isotopes in Astrophysics*. Ed. by J. Audouze. Vol. 67, p. 105. DOI: 10.1007/978-94-010-1232-4_15.

Watson, W. D., V. G. Anicich, and Jr. Huntress W. T. (May 1976). "Measurement and significance of the reaction $^{13}C^{+}$+^{12}CO ü $^{12}C^{+}$+^{13}CO for alteration of the $^{13}C/^{12}C$ ratio in interstellar molecules." In: 205, pp. L165–L168. DOI: 10.1086/182115.

Watson, William D. (June 1973). "Formation of the HD Molecule in the Interstellar Medium". In: 182, p. L73. DOI: 10.1086/181222.

Webb, T. M. et al. (Jan. 2003). "The Canada-United Kingdom Deep Submillimeter Survey. V. The Submillimeter Properties of Lyman Break Galaxies". In: 582.1, pp. 6–16. DOI: 10.1086/344608. arXiv: astro-ph/0201181 [astro-ph].

Wechsler, Risa H. and Jeremy L. Tinker (Sept. 2018). "The Connection Between Galaxies and Their Dark Matter Halos". In: 56, pp. 435–487. DOI: 10.1146/annurev-astro-081817-051756. arXiv: 1804.03097 [astro-ph.GA].

Weiner, Benjamin J. et al. (Feb. 2009). "Ubiquitous Outflows in DEEP2 Spectra of Star-Forming Galaxies at z = 1.4". In: 692.1, pp. 187–211. DOI: 10.1088/0004-637X/692/1/187. arXiv: 0804.4686 [astro-ph].

Werk, Jessica K. et al. (2013). "THE COS-HALOS SURVEY: AN EMPIRICAL DESCRIPTION OF METAL-LINE ABSORPTION IN THE LOW-REDSHIFT CIRCUMGALACTIC MEDIUM". In: *The Astrophysical Journal Supplement Series* 204.2, p. 17. DOI: 10.1088/0067-0049/204/2/17. URL: https://doi.org/10.1088/0067-0049/204/2/17.

Werk, Jessica K. et al. (2014). "THE COS-HALOS SURVEY: PHYSICAL CONDITIONS AND BARYONIC MASS IN THE LOW-REDSHIFT CIRCUMGALACTIC MEDIUM". In: *The Astrophysical Journal* 792.1, p. 8. DOI: 10.1088/0004-637x/792/1/8. URL: https://doi.org/10.1088/0004-637x/792/1/8.

Werk, Jessica K. et al. (Dec. 2016). "The COS-Halos Survey: Origins of the Highly Ionized Circumgalactic Medium of Star-Forming Galaxies". In: 833.1, 54, p. 54. DOI: 10.3847/1538-4357/833/1/54. arXiv: 1609.00012 [astro-ph.GA].

Wilde, Matthew C. et al. (May 2021). "CGM^2 I: The Extent of the Circumgalactic Medium Traced by Neutral Hydrogen". In: 912.1, 9, p. 9. DOI: 10.3847/1538-4357/abea14. arXiv: 2008.08092 [astro-ph.GA].

Wilson, R. W., K. B. Jefferts, and A. A. Penzias (July 1970). "Carbon Monoxide in the Orion Nebula". In: 161, p. L43. DOI: 10.1086/180567.

Wisotzki, L. et al. (Mar. 2016). "Extended Lyman α haloes around individual high-redshift galaxies revealed by MUSE". In: 587, A98, A98. DOI: 10.1051/0004-6361/201527384. arXiv: 1509.05143 [astro-ph.GA].

Wolfe, Arthur M., Eric Gawiser, and Jason X. Prochaska (Sept. 2005). "Damped Ly α Systems". In: 43.1, pp. 861–918. DOI: 10.1146/annurev.astro.42.053102.133950. arXiv: astro-ph/0509481 [astro-ph].

Yang, G. et al. (Apr. 2018). "Linking black hole growth with host galaxies: the accretion-stellar mass relation and its cosmic evolution". In: 475.2, pp. 1887–1911. DOI: 10.1093/mnras/stx2805. arXiv: 1710.09399 [astro-ph.GA].

Yen, Hsi-Wei et al. (Dec. 2016). "Stacking Spectra in Protoplanetary Disks: Detecting Intensity Profiles from Hidden Molecular Lines in HD 163296". In: 832.2, 204, p. 204. DOI: 10.3847/0004-637X/832/2/204. arXiv: 1610.01780 [astro-ph.SR].

York, D. G. and B. F. Kinahan (Feb. 1979). "The interstellar medium near the sun. II. The line of sight to alpha Virginis." In: 228, pp. 127–146. DOI: 10.1086/156830.

York, Donald G. et al. (Apr. 2006). "Average extinction curves and relative abundances for quasi-stellar object absorption-line systems at 1 <=z_{abs} < 2". In: 367.3, pp. 945–978. DOI: 10.1111/j.1365-2966.2005.10018.x. arXiv: astro-ph/0601279 [astro-ph].

Young, J. S. and D. B. Sanders (Mar. 1986). "Distributions of 13CO Emission in the Disks of Late-Type Spiral Galaxies". In: 302, p. 680. DOI: 10.1086/164029.

Young, Lisa M. et al. (Mar. 2021). "The Evolution of NGC 7465 as Revealed by Its Molecular Gas Properties". In: 909.2, 98, p. 98. DOI: 10.3847/1538-4357/abe126. arXiv: 2101.11652 [astro-ph.GA].

Zabl, Johannes et al. (Nov. 2021). "MusE GAs FLOw and Wind (MEGAFLOW) VIII. Discovery of a MgII emission halo probed by a quasar sightline". In: 507.3, pp. 4294–4315. DOI: 10.1093/mnras/stab2165. arXiv: 2105.14090 [astro-ph.GA].

Zhang, Zhi-Yu et al. (June 2018). "Stellar populations dominated by massive stars in dusty starburst galaxies across cosmic time". In: 558.7709, pp. 260–263. DOI: 10.1038/s41586-018-0196-x. arXiv: 1806.01280 [astro-ph.GA].

Zheng, Y. et al. (July 2015). "The Circumgalactic Medium of the Milky Way is Half Hidden". In: 807.1, 103, p. 103. DOI: 10.1088/0004-637X/807/1/103. arXiv: 1504.05594 [astro-ph.GA].

Zhu, Guangtun and Brice Ménard (2013). "THE JHU-SDSS METAL ABSORPTION LINE CATALOG: REDSHIFT EVOLUTION AND PROPERTIES OF Mg II ABSORBERS". In: *The Astrophysical Journal* 770.2, p. 130. DOI: 10.1088/0004-637x/770/2/130. URL: https://doi.org/10.1088/0004-637x/770/2/130.

Zibetti, Stefano et al. (Mar. 2007). "Optical Properties and Spatial Distribution of Mg II Absorbers from SDSS Image Stacking". In: 658.1, pp. 161–184. DOI: 10.1086/511300. arXiv: astro-ph/0609760 [astro-ph].